Multi-level contactless motion system

Document Version:
Publisher's PDF, also known as Version of Record (includes final page, issue and volume numbers)

Please check the document version of this publication:

• A submitted manuscript is the version of the article upon submission and before peer-review. There can be important differences between the submitted version and the official published version of record. People interested in the research are advised to contact the author for the final version of the publication, or visit the DOI to the publisher's website.
• The final author version and the galley proof are versions of the publication after peer review.
• The final published version features the final layout of the paper including the volume, issue and page numbers.

Link to publication

Download date: 22. Aug. 2022

Multi-Level Contactless Motion System

PROEFSCHRIFT

ter verkrijging van de graad van doctor aan de
Technische Universiteit Eindhoven, op gezag van de
Rector Magnificus, prof.dr.ir. C.J. van Duijn, voor een
commissie aangewezen door het College voor
Promoties in het openbaar te verdedigen
op donderdag 29 januari 2009 om 16.00 uur

door

Jeroen de Boeij

geboren te Vlijmen

Dit proefschrift is goedgekeurd door de promotoren:

prof.dr.ir. P.P.J. van den Bosch
en
prof.dr.ir. J.H. Blom

Copromotor:
dr. E.A. Lomonova MSc

prof.dr.ir. P.P.J. van den Bosch vervult namens wijlen
prof.dr.ir. A.J.A. Vandenput de rol van 1^e promotor.

to my father

ABSTRACT

Multi-Level Contactless Motion System

In machine design, the acceleration and velocity of moving parts are often constrained by mechanical bearings for guidance and cables for transferring power and information. These factors not only limit the stroke and functionality of the machine, but additionally disturb the motion of the mover, thereby reducing reliability, speed and accuracy. This thesis focusses on the removal of these constraints and its effect on the system level design of the machine. Three different contactless techniques can be incorporated in the motion system design to overcome the limitations of bearings and cables:

- Six DOF electromagnetic suspension and propulsion,

- Contactless power transfer,

- Wireless motion control.

Each contactless technique operates in a different frequency level of the electromagnetic spectrum, hence the title "Multi-Level Contactless Motion System". The electromagnetic bearings and actuators use permanent magnets and coils with a current loop up to several kHz. The power transfer uses inductive coupling and AC currents of 50-200 kHz and finally, the data is transmitted using a RF-transceiver operating at 2.4 GHz. Even higher frequencies are possible, especially if optical systems are used for data transmission.

This thesis presents the theory and technology necessary to describe and build a multi-level contactless motion system consisting of three subsystems and to model their interaction within this global system, i.e. six DOF contactless planar actuator with moving magnets with a long stroke movement in the x-y plane, contactless power transfer to the moving platform and wireless real-time communication between the ground controller and the plant processes on the platform. The plant on the platform is a manipulator with two linear motors driving a beam and a rotary motor driving an arm and each motor is equipped with an incremental encoder.

The electromagnetic interaction between the coils and the magnet array is modeled to predict the coupling of each coil, i.e. the force and torque that each coil can produce per unit current. If this coupling is known for all coils, the currents necessary to realize the desired forces and torques on the planar actuator can be modeled and calculated using the pseudo-inverse of the coupling matrix. Based upon this model, a look-up table based commutation algorithm is presented that can perform these calculations in real-time. With this method, it is also possible to predict the coupling of coils at the perimeter of the magnet array, which behave differently due to end-effects of the magnetic field, in real-time. In addition, it can realize full rotation around the z-axis, when round coils are used. A thermal model is presented that can estimate the worst-case steady-state temperature in the coil for a given current.

The contactless power transfer is investigated with a focus on the effect of long stroke mechanical movement on the electrical system. The power transfer is based upon an inductive coupling between a primary coil and a secondary coil. The primary coil is the coil that either applies force and torque on the planar actuator, if it is in range of the magnet array, or acts as a primary coil of an aircore transformer when it is in range of the secondary coil. Due to the high frequency of the contactless power transfer, the primary coil has to be made of litz wire, which reduces the AC resistance but increases the DC resistance, thereby increasing the thermal stresses in the planar actuator. By keeping the variation of the inductive coupling between the primary coil and the secondary coil small in a large area, while keeping the mean value high enough for a significant power transfer, it is possible to transfer power efficiently and continuously throughout the workspace of the contactless planar actuator.

With the models that describe the contactless planar actuator and the contactless power transfer it is possible to find a suitable topology of a contactless planar actuator with contactless power transfer within the thermal and geometrical constraints. The final topology is selected not only based upon these thermal and geometrical constraints but also on electrical properties of the contactless power transfer, controllability and mechanical considerations such as stiffness and levitated mass of the platform including the manipulator. Since this is the first time that litz wire is used for electromechanical actuation systems, a conservative estimate of the properties is used in the analysis.

The system dynamics are derived using Lagrange, both for the mechanical and the electromagnetic domain. This set of equations provides a complete description of the electromechanical system and has been used for verification purposes. It is recommended for analysis and design of future similar systems in combination with a real-time commutation algorithm, since it provides a transient analysis, which can include motion profiles, control laws, coil currents and power amplifier voltages. The system dynamics can be extended with non-rigid body modes or non-linear electromagnetic effects.

Existing wireless communication links suffer from a delay of several milliseconds, which is unacceptable for real-time control in high performance motion systems. The cause of this significant delay is the protocol, which is usually optimized for high data throughput, not for small delays. A new protocol is proposed and implemented on an FPGA and 2.4 GHz transceivers that significantly reduces the communication delay with a factor 10 compared to the fastest existing wireless radio link protocols.

A prototype of a multi-level contactless motion system is built and has been successfully tested. The feasibility of this concept is demonstrated.

Contents

CHAPTER 1

INTRODUCTION

Freedom is generally associated with being able to go wherever you like without being constrained by factors other than your own imagination. Often, physical boundaries prevent us from pursuing this mindset as it becomes clear from expressions like: "*free as a bird*" and "*no strings attached*", which emphasize that these constraints are considered a nuisance.

The same holds for machine design, where the acceleration and velocity of moving parts are often constrained by mechanical bearings for guidance and cables for transferring power and information. These factors not only limit the stroke and functionality of the machine, but additionally disturb the motion of the mover, thereby reducing reliability, speed and accuracy. This thesis focusses on the removal of these constraints and its effect on the system level design of the machine.

1.1 High Precision Machines

In industrial applications, high precision machines are becoming more and more common nowadays. First, precision machines were limited to a few niche areas such as lithography, wire bonding and advanced optics. However, due to the ongoing demand for integration and miniaturization, high precision is becoming standard in many applications, such as pick and place machines for component placement and material handling or medical and manufacturing robots.

Most high precision machines are positioning stages with multiple degrees of freedom (DOF), which often consist of cascaded long stroke linear or rotary actuators that are supported by mechanical or air bearings. Examples are depicted in Figure 1.1, where a Kuka pick and place robot arm is presented and in Figure 1.2, which shows the interior of an Assembléon AX201 surface mount machine. The AX201 consists of a long stroke motion system with three linear motors in an H-configuration, which is therefore sometimes referred to as an H-drive.

Both machines have cables with power and communication connecting the stationary frame and the moving parts, which usually have a micrometer range accuracy. If submicron accuracy is required, this is realized by additional short stroke actuators with nanometer resolution.

To build a high precision machine, as much disturbances as possible should be eliminated. Disturbances that can not be eliminated should be known exactly so they can be countered by advanced feedforward controls. Common sources of disturbances are vibrations, Coulomb and viscous friction in bearings, crosstalk of multiple cascaded actuators and cable slabs that guide the power and sensor cables to the moving parts of the machine. Additionally, there is a continuous push for

Figure 1.1: Kuka 5-axis pick and place robot

Figure 1.2: Interior of an Assembléon AX201 surface mount machine

increasing throughput to lower production costs and processing time. There are two common methods to improve the productivity of a machine.

1. Develop faster machines, which require higher accelerations and velocities.

2. Increase the batch size of production processes, e.g. use a larger wafer so more chips fit on one wafer, so more dies are produced in a single process step.

Both methods compromise the accuracy of the machine. By increasing the acceleration, more force or torque is necessary, which introduces heavier motors and larger vibrations. To reduce this effect more stiffness is needed, which is created by adding more mass, thereby further increasing the force or torque required for the desired acceleration. The use of more powerful motors at higher speeds increases vibrations and disturbances that result from the larger cables to the motor.

Increasing the stroke of the actuator makes it more difficult to align all components, thus making the actuator more expensive or less accurate. In addition, the stiffness of the machine cannot be compromised by the larger stroke, which generally requires more mass, thus more force or torque for the same acceleration. The vicious circle of increasing force, higher vibrations, more stiffness, additional mass, which again results in higher forces is especially a problem when several actuators are cascaded. As a result of this vicious circle, the machine in Figure 1.2 has a moving mass of about 60 kg to place components with a mass below 60 grams.

Another possibility to increase productivity is to use parallel processing, i.e. movement and positioning in parallel with inspection, calibration, assembling, scanning, etc. With parallel processing it is possible to improve the performance of the machine without the need of increasing the machine size or speed. However, it makes a high precision machine more complex since it requires synchronization of multiple actuator and sensor systems to ensure proper operation.

Finally, vacuum operation becomes necessary for the next generation of wafer-scanners, since the technique currently used in lithography is reaching its limits. Further significant reductions in feature size on silicon wafers requires a projection source that is beyond the wavelength of visible light. At these wavelengths operation must be in high vacuum, which requires the actuator and all mechanical or air bearings to be sealed. Proper sealing of the actuator is difficult especially at long strokes. Furthermore, guiding power and data cables from a non-vacuum to a vacuum is tedious, since normal cable isolation is unsuitable to prevent contamination of the vacuum.

1.2   Multi-Level Contactless Motion System

Three different contactless techniques can be incorporated in the motion system design to overcome the problems discussed in Section 1.1:

- Six DOF electromagnetic suspension and propulsion,

- Contactless power transfer,

- Wireless motion control.

1.2.1   Six DOF Electromagnetic Suspension and Propulsion

The cross-talk between cascaded actuators and disturbances in mechanical bearings can be removed by creating a single stage machine that has long or infinite stroke movement capabilities in the x-y plane and short stroke movement in the other DOF. Such a system is a contactless planar actuator, which is already extensively discussed in literature [1, 2, 3, 4, 5, 6, 7, 8, 9, 10, 11, 12][1], where they are presented as the next step in lithography machines. This work is a continuation of research of planar or spherical actuators with two or three DOF [13, 14, 15, 16, 17] and additional mechanical or air bearings.

There are two main levitation techniques [10, 18] in the field of electrical machines: electromagnetic suspension with a static magnetic field and electrodynamic suspension, based upon induced currents. The contactless planar actuator is of the electromagnetic type, which uses repulsive forces between permanent magnets and coils to create a floating platform. Furthermore, it is attractive for applications in vacuum, due to the absence of mechanical or air bearings. The main disadvantage is the additional control complexity compared to mechanical bearings.

When coils are used in the mover in combination with a permanent magnet stator a cable slab is necessary to provide power and cooling to the moving coils, thus limiting the flexibility of the system [5, 6]. In addition, the cable slab is a source of disturbances such as friction and vibrations that reduces the accuracy of the mover. Therefore, a system with moving magnets and stationary coils is more attractive for high-accuracy applications since the cable slab can be omitted. A thorough and comprehensive discussion of a magnetically levitated planar actuator with moving magnets is found in [10, 12], including theory, modeling, design rules, optimization, control, performance and test results. The other references are mainly from patent literature, so theory, performance and test results are mostly absent in the discussion.

To control the movement of the contactless planar actuator, it is necessary to be able to calculate the coil currents that are required to realize the desired force and torque to act on the actuator. This is called commutation. The amount of force or torque that each coil can exert on the mover per unit current is strongly position dependent [10, 12], so in a control system these values need to be calculated every sample time. This implies that the time necessary to calculate the varying interaction between stationary coils and the moving permanent magnets must be in the order of 100 μs. In [10, 12], a simplified analytical model of the planar actuator is used to calculate the mapping that converts desired force and torque into coil currents. However, the validity of the model is limited to coils that are completely overlapped by the magnet array and excludes coils on the perimeter. This requires additional weighing functions in the commutation algorithm to smoothly force the coil currents to zero before switching the coil of when it comes close to the perimeter of the magnet array.

In case a significant additional mass will have to be levitated, it is beneficial to include the coils on the outer perimeter of the magnet array in the mapping as well, since more coils can share the load. Additionally, it enables greater flexibility in the design of the planar actuator if end-effects are included, e.g. odd-shaped

---

[1]The citations are grouped per topic as it is explained in the bibliography

magnet arrays and a reduction in the total number of coils necessary to realize a controllable topology.

Although no power on the mover is required for the electromagnetic suspension and propulsion in the case of a moving magnet contactless planar actuator, still power will be necessary for processes on top of the floating platform, e.g. small actuators to fix the wafer or for sensor systems on top of the platform.

1.2.2   Contactless Power Transfer

A great deal of disturbances in high precision machines can be removed by making cable slabs obsolete, which requires the transfer of power and information without cable between the moving parts and the stationary frame. In the case of x-y long stroke movement, the contactless power transfer should be able to function within that workspace, including possible short stroke movements in other directions.

Inductive coupling is a well known technique to transfer power without conductive contacts by means of mutual inductance between two circuits. Nicolas Tesla was working on this in the beginning of the twentieth century, as it becomes clear from one of his patents [32]. On the primary side a time varying current is forced into the primary coil, which induces a voltage in the secondary coil. In most applications (e.g. [33, 34, 35, 36, 37, 38]), the coils have to be aligned and can tolerate only slight misalignments of the center axes of the coils. The use of this type of contactless power transfer is often motivated by safety, e.g. in the case of the electric toothbrush.

Besides safety, contactless power transfer is used in machines and transport systems to eliminate wear and disturbances due to friction and cables. One of the first applications of contactless power transfer in machines is published in [33, 34], which allows contactless power transfer in a rotating joint. Other examples are contactless power transfer between stationary and rotating parts as described in [35, 38], eliminating the need of slip rings. Contactless power transfer from a stationary part to translating part is also feasible either by using elongated coils with cores as discussed in [39, 40], a grid of primary coils [41, 42, 43] or by using charging bays [44, 45]. These systems either have the disadvantage of limited stroke or they cannot supply power at any possible position.

Systems exist that can transfer power without electrical contact to any object on top of a grid of primary coils as discussed in [46] and [47]. However, these systems cannot supply power to moving loads.

Ideally, a contactless power transfer system should have, in principle, unlimited stroke and can efficiently transfer power continuously, at any position in the x-y plane. In addition, this system should be tolerant for variations of several millimeters of the airgap between the primary and secondary coil and small angle deviations (+/- 10 mrad). Finally, the power available on the mover should be sufficient to operate a motion system, which is specified as several hundred Watts.

1.2.3   Wireless Motion Control

For a true cableless machine, the data transmission between the moving part and the stationary frame should be wireless. In motion systems, the position

measurement is usually done at the moving part, where the sensor moves along a static reference. The position measurement has to be sent to the motion controller without any delay, since time delay will compromise the performance of the feedback loop. In case of more advanced controller strategies, feedforward controllers are implemented that may depend on the position of the mover or the feedback controller is position dependent, e.g. gain scheduling.

As is the case in the machine shown in Figure 1.2, several placement heads are located on the mover which need to be controlled in synchronization with the movement of the machine. Commands for those systems are sent from the machine controller to the placement heads through the cable slabs.

Finally, if electric drives are present on the moving part either a position command or a current command should be sent to the mover. Usually a machine consists of several moving parts and to realize the desired behavior all this communication needs to be synchronized, which excludes uncertain time delays.

Many wireless techniques exist that can reliably transmit data, such as WLAN TCP/IP, WLAN UDP/IP, Bluetooth, DECT and Zigbee [55, 57, 58, 61]. These protocols, based on radio communication in the 2.4 GHz ISM band, are designed to transmit large amounts of data and are optimized for high data throughput. The only exception is DECT, which works in the 1.9 GHz band. With the exception of WLAN UDP/IP and DECT all protocols guarantee that the data arrives correctly at the receiving side. Since the time between sending and receiving is not critical for sending large data files such as website information, music and movies, the delay is in the order of several milliseconds for WLAN UDP/IP and up to 20 ms for the other protocols [56, 59, 65, 67]. Although latencies as low as several hundreds of microseconds are estimated for WLAN UDP/IP in [67], measured data in [59] shows that the projected best case performance is not met in real situations. Moreover, this delay is not constant but it has considerable variation or jitter [59, 65]. In some applications such a delay poses no problem like sensor systems to monitor temperatures in buildings [70], however, for high precision machines, delays of several milliseconds are unacceptable for fast servo loops.

A lot of work is done to deal with this delay with observers and predictors [64, 69, 71, 72, 74] and to prove the stability of systems suffering from variable transmission delays [73, 75]. However, all these contributions use the standard protocols that are not developed for data transmission with a minimal delay. Moreover, using a wireless data transmission with delay in combination with observers and predictors will never work as well as removing, or greatly reducing, the delay itself. The inverted pendulum wireless control loops discussed in [59, 65] show errors in the range of 10 degrees (0.2 rad) or worse, which is not realistic for a high precision application. Therefore, a new protocol, specially developed to minimize delays in the transmission should be the starting point of wireless motion control.

1.2.4 Contactless Planar Actuator with Manipulator

Each contactless technique operates in a different frequency level of the electromagnetic spectrum. The electromagnetic suspension and propulsion use permanent magnets and coils with a current loop up to several kHz. The power transfer utilizes inductive coupling and AC currents of 50-200 kHz and finally, the data is transmitted with a RF-transceiver operating at 2.4 GHz. Even higher frequencies

Six DOF electromagnetic   Contactless   Wireless

suspension and propulsion   power transfer   motion control

10^0 10^1 10^2 10^3 10^4 10^5 10^6 10^7 10^8 10^9 10^{10} 10^{11}
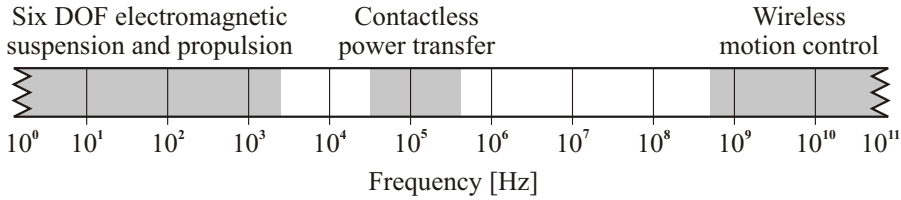
Frequency [Hz]

Figure 1.3: The location of the contactless techniques in the electromagnetic frequency spectrum

are possible, especially if optical systems are used for data transmission. This is depicted in Figure 1.3, which clearly shows that each technique operates within a separate part of the spectrum.

Due to the different location of the contactless techniques in the electromagnetic frequency spectrum it is possible to integrate the three into one multi-level contactless motion system. A combination of contactless power transfer and wireless communication is documented for a rotary movement [34, 38] and linear movement [66]. However, no data is available about delay in the wireless communication and the reliability and accuracy of the data transmission.

Since the movement requirements of the planar actuator match well with the workspace of the contactless power transfer as discussed in Section 1.2.2, it would be challenging to research the possibility to integrate both systems. Moreover, some power transfer to the planar actuator will be required anyway to operate sensors or actuators on the platform. Finally, a planar actuator already requires an array of coils on the fixed world that can be used for power transfer. The integration of electromagnetic suspension and propulsion with contactless power transfer has not been documented before, unlike the combination of power and data transfer.

To demonstrate the contactless power transfer and the real-time wireless motion control, a robot or manipulator can be placed on top of the floating platform. The movement of the manipulator results in disturbance forces and torques acting on the platform that have to be countered by the magnetic suspension. The controller of the electromagnetic suspension and propulsion should be able to anticipate the disturbance forces. On the other side, the movement of the platform will exert disturbance forces on the manipulator, which should be countered by the manipulator controller. This requires a model of the multi-body dynamics of the platform and the manipulator that predicts the disturbance forces on the platform and the manipulator, depending on the movement.

To allow the use of a model of the system dynamics by the controllers, information of the moving manipulator should be sent from the platform to the controllers using real-time wireless communication. Furthermore, controller commands should be sent to the manipulator on the platform, so wireless motion control is, therefore, essential.

The combination of all three wireless techniques results in a contactless planar actuator with manipulator of which a CAD drawing is shown in Figure 1.4. It consists of a contactless planar actuator with moving permanent magnets and sta-
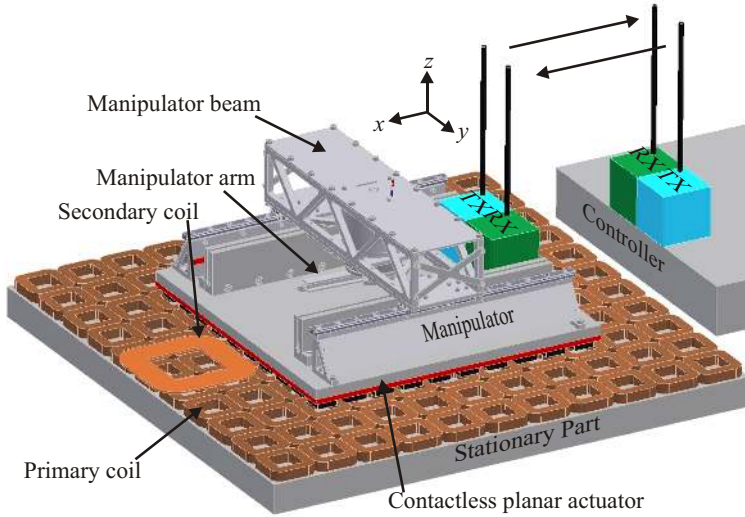
Figure 1.4: Multi-level contactless motion system

tionary coils. Furthermore, a secondary coil is attached to the floating permanent magnet platform that can pick up power from the stationary primary coil underneath the secondary coil. Finally, a real-time wireless communication unit enables the wireless motion control. These three techniques together create a multi-level contactless motion system that integrates three different levels of contactless operation into one system.

1.3 Thesis Goal

The goal of this thesis is to create the theory and technology necessary to describe and build a multi-level contactless motion system consisting of three subsystems and to model their interaction within this global system, i.e. six DOF contactless planar actuator with moving magnets, contactless power transfer to the moving platform and wireless real-time communication between the ground controller and the plant processes on the platform.

For the contactless planar actuator technology, the work presented in [10, 12] will be the starting point. The contactless planar actuator technology needs to be extended to realize the integration of contactless power transfer and wireless motion control. In addition, models and topologies for contactless power transfer with infinite stroke in the x-y plane should be investigated. Furthermore, real-time wireless data transfer must be researched, which is necessary to realize wireless motion control of a contactless planar actuator with the dynamic load of the manipulator. Finally, the models of the contactless power transfer, the contactless planar actuator, wireless motion control and the dynamics are to be linked together to investigate the interaction of these subsystems in the system.

To meet the global goal, several objectives are formulated:

1. **System integration**
   Research into the interaction between the six DOF electromagnetic suspension and propulsion, the contactless power transfer and wireless motion control and into the integration of the three contactless techniques into a single motion system.

2. **Contactless power transfer**
   Modeling of contactless power transfer including mechanical movement to find suitable topologies which realize an efficient contactless power transfer with unlimited stroke in the x-y plane and short stroke movement in the other directions.

3. **Real-time wireless communication**
   Research into the characteristics of wireless communication techniques and protocols to find a communication scheme that is suitable for wireless motion control.

4. **Contactless planar actuator**
   Research into commutation strategies and algorithms that include end-effects in real-time, which allows coils on the perimeter of the magnet array to contribute to the force and torque acting on the actuator.

5. **Realization of a prototype**
   Build a test setup to verify the models and to show the behavior of the subsystems and their interaction within the system.

1.4   Outline of the Thesis

The models necessary to describe the contactless planar actuator and a commutation algorithm that includes end-effects as well as a thermal model are discussed in Chapter 2.

Chapter 3 deals with modeling of the various topics associated with contactless power transfer, such as coupling between coils, topologies and power electronics. Furthermore, an experimental setup is presented that proves the principle of contactless power transfer with infinite stroke in the x-y plane.

The integration of the contactless planar actuator with the contactless power transfer is explained in Chapter 4, where several optimal planar actuator topologies are found that are suitable for integrating both functions. Considerations that concern the full system finally determine which topology is most appropriate for the final prototype.

The dynamics of the contactless planar actuator with manipulator are derived in Chapter 5 based on the total energy in the system. Using the approach of Lagrange, the equations of the multi-body dynamics are derived and are extended into the electromagnetic domain. The result is a single set of equations that describes the system dynamics in the mechanical as well as the electromagnetic domain and the interaction of both domains. This set of equations is linked to the models and discussion in the Chapters 2, 3 and 4. Finally, the rigid body

dynamics of the manipulator are validated and the occurrence non-rigid body modes is identified by measurements.

In Chapter 6, it is analyzed why currently available wireless communication protocols are infeasible for real-time motion control. The requirements for a wireless control system are defined and a new approach is presented that yields a real-time wireless communication system with significantly reduced delay compared to existing techniques.

The prototype is presented in Chapter 7, which discusses the design choices in the realization process first. The behavior of the subsystems and their interaction in the system as a whole is shown with measurements.

Finally, conclusions and recommendations are given in Chapter 8.

CHAPTER 2

MODELING THE PLANAR ACTUATOR

In this chapter, the models are discussed that describe the behavior of the contactless planar actuator both in the electromechanical and thermal domain. The models are used to calculate the characteristics and performance indices, that will be used later to optimize the design in Chapter 4. Furthermore, the model for calculating the force and torque on the planar actuator depending on the coil currents is used to derive a look-up table based commutation algorithm that includes end-effects. The model describing forces and torques is published in [85] and the commutation algorithm is published in [88]. Finally, a thermal model is introduced to estimate the worst-case temperature in a coil.

2.1 Modeling of Force and Torque

The design of a planar actuator is a complex 3D problem, especially when a topology is used with stationary coils and moving magnets, where end-effects in the magnetic field on the perimeter of the magnet array play a significant role. A CAD drawing of a contactless planar actuator with stationary coils and moving magnets is shown in Figure 2.1. Finite element models can be used to evaluate performance but these calculations are time consuming. Existing analytical models based on spatial harmonics of the magnetic field often do not include end-effects of the magnet or coil arrays [9, 10, 22].

In this section a model is described that allows fast and flexible computation of the performance of planar actuator structures by combining analytical solutions of the Maxwell equations with numerical techniques. The model is very useful for design and optimization purposes of planar actuators e.g. comparing different magnet array and coil array topologies and it is a modified version of the surface charge model presented in [9, 10].
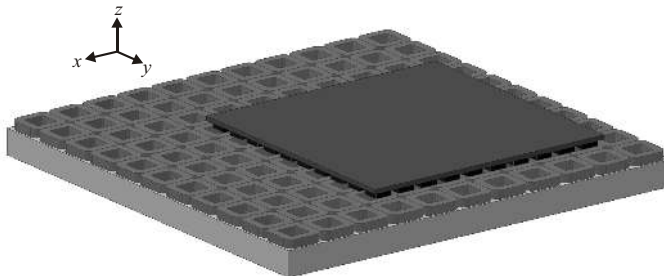
Figure 2.1: Contactless planar actuator

2.1.1 Comparing Virtual Work Force and Lorentz Force

There are three common methods for calculating forces in electromechanical systems, i.e. Maxwell stress tensor, virtual work based on variation of energy and Lorentz force [19, 20, 21]. In finite element packages. forces are usually calculated using Maxwell stress tensor or the virtual work method, since these methods can calculate forces accurately between both current carrying objects (e.g. coils, Lorentz force) and non-current carrying objects (e.g. iron, reluctance force). The Lorentz force method can only be used to calculate forces on current carrying objects in free space and is therefore limited in its use. However, the Lorentz force method is computationally much faster for force calculations than Maxwell stress tensor (integral) and especially the virtual work method (differential) so the Lorentz force method is therefore preferable. To compare Lorentz force and virtual work force values, the force between a filamentary coil and a permanent magnet array is calculated analytically using both methods.

Virtual Work

The virtual work principle is based on the conservation of energy [26]. The electromagnetic energy input in a coil (U_{in}, [J]) is equal to the dissipated energy (U_{diss}, [J]), the electromagnetic energy stored in the system (U_{em}, [J]) and the mechanical output energy (U_{mech}, [J]):

$$U_{in} \quad = \quad U_{diss} + U_{em} + U_{mech}. \tag{2.1}$$

When a conservative system is considered, i.e. no losses and no external input, the total energy in the system does not change:

$$U_{em} \quad = \quad \frac{1}{2}\Lambda_c i_c + \Lambda_m i_c, \tag{2.2}$$

$$0 \quad = \quad \frac{1}{2}\Lambda_c i_c + \Lambda_m i_c + U_{mech}, \tag{2.3}$$

where i_c [A] is the current in the coil, Λ_m [J/A] the flux linkage of the coil due to the magnetic field of the magnet array, Λ_c [J/A] the flux linkage of the coil due to the current flowing through the coil. When this system is subject to an infinitesimal (virtual) displacement dx [m] this can be rewritten to:

$$\frac{i_c d\Lambda_c}{2} + d\Lambda_m i_c + F_{em}dx = 0, \tag{2.4}$$

with F_{em} [N] the force applied by the magnetic field on the coil. Rewriting Eq. 2.4 and generalizing for three dimensions yields:

$$\underline{F}_c \quad = \quad -i_c \nabla \Lambda_m - \frac{i_c}{2}\nabla \Lambda_c, \tag{2.5}$$

where $\underline{F}_c$ [N] is the force vector acting on the coil and ∇ is the vector differential operator. Under the assumption that the coil behavior is linear ($\Lambda_c = Li_c$) and the self-inductance L [H] does not depend on the position of the coil with respect to the magnet array the force equation reduces to:

$$\underline{F}_c \quad = \quad -i_c \nabla \Lambda_m. \tag{2.6}$$
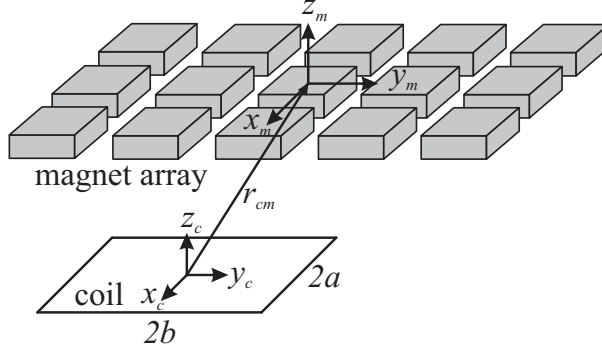
Figure 2.2: Magnet array with filamentary coil in local Cartesian coordinate system

These assumptions are reasonable when the current density in the coil is not too high and, since there is no iron core, the self-inductance does not change when the magnets move. The effect of the magnets having a μ_r [-] slightly higher than unity (for NdFeB magnets $1.0 \leq \mu_r \leq 1.1$, [28, 29]) on the self-inductance is assumed negligible.

Lorentz Force

The Lorentz force is calculated according to:

$$\underline{F}_c = \int_{V_c} \underline{J}_c \times \underline{B}_m dV_c, \tag{2.7}$$

where $\underline{J}_c$ [A/m^2]is the current density vector in the coil, V_c the volume of the coil and $\underline{B}_m$ [T] the magnetic flux density vector generated by the magnet array. For a wire filament $\underline{dl}$ [m] with current i_c this reduces to:

$$\underline{dF}_c = i_c \underline{dl} \times \underline{B}_m. \tag{2.8}$$

Consider a rectangular coil with dimensions $2a \times 2b$ located in the local reference frame (x_c, y_c, z_c) in x-y plane as shown in Figure 2.2. Above the coil is a magnet array with reference frame x_m, y_m, z_m and pole pitch τ [m]. The displacement r_{cm} between the two reference frames is (x_{cm}, y_{cm}, z_{cm}), so $x_m = x_c + x_{cm}$, $y_m = y_c + y_{cm}$, $z_m = z_c + z_{cm}$. Finally, it is assumed that the two reference frames are aligned, i.e. all angles are zero.

The magnetic field underneath the array can be written as an infinite sum of spatial harmonics [9, 10, 22]:

$$\underline{B}_m(x_m, y_m, z_m) = \sum_{n=1}^{\infty} B_n \exp\left(\frac{-2n\pi(z_c+z_{cm})}{\tau}\right)$$

$$\begin{bmatrix} \sin\left(\frac{n\pi(x_c+x_{cm})}{\tau}\right) \cos\left(\frac{n\pi(y_c+y_{cm})}{\tau}\right) \\ \sin\left(\frac{n\pi(y_c+y_{cm})}{\tau}\right) \cos\left(\frac{n\pi(x_c+x_{cm})}{\tau}\right) \\ \cos\left(\frac{n\pi(x_c+x_{cm})}{\tau}\right) \cos\left(\frac{n\pi(y_c+y_{cm})}{\tau}\right) \end{bmatrix}. \tag{2.9}$$

For this equation to be valid the divergence of the magnetic flux density with respect to x_m, y_m, z_m should be zero, i.e.

$$
\begin{aligned}
\nabla \cdot \underline{B}_m \;=\;& \sum_{n=1}^{\infty} B_n \frac{n\pi}{\tau} \exp\left(\frac{-2n\pi(z_c + z_{cm})}{\tau}\right) \\
& \left\{ \cos\left(\frac{n\pi(x_c + x_{cm})}{\tau}\right) \cos\left(\frac{n\pi(y_c + y_{cm})}{\tau}\right) \right. \\
& + \cos\left(\frac{n\pi(x_c + x_{cm})}{\tau}\right) \cos\left(\frac{n\pi(y_c + y_{cm})}{\tau}\right) \\
& \left. -2 \cos\left(\frac{n\pi(x_c + x_{cm})}{\tau}\right) \cos\left(\frac{n\pi(y_c + y_{cm})}{\tau}\right) \right\} \\
=\;& 0.
\end{aligned}
\tag{2.10}
$$

Now the coil flux linkage due to the magnet array is calculated:

$$
\begin{aligned}
\Lambda_m \;=\;& \int_{-a}^{a} \int_{-b}^{b} B_z \, dx_c dy_c \bigg|_{z_c = 0} \\
=\;& \sum_{n=1}^{\infty} B_n \frac{4\tau^2}{\pi^2 n^2} \exp\left(\frac{-2n z_{cm}\pi}{\tau}\right) \\
& \sin\left(\frac{an\pi}{\tau}\right) \cos\left(\frac{n\pi x_{cm}}{\tau}\right) \sin\left(\frac{bn\pi}{\tau}\right) \cos\left(\frac{n\pi y_{cm}}{\tau}\right).
\end{aligned}
\tag{2.11}
$$

Then, the forces in x-, y- and z-direction can be calculated depending on the position of the magnet with respect to the coil, according to the virtual work method and Eq. 2.6.

$$
\begin{aligned}
\underline{F}_c \;=\;& -i_c \nabla_{cm} \Lambda_m \\
=\;& -i_c \sum_{n=1}^{\infty} B_n \frac{-4\tau}{n\pi} \exp\left(\frac{-2n\pi z_{cm}}{\tau}\right) \\
& \begin{bmatrix} \sin\left(\frac{an\pi}{\tau}\right) \sin\left(\frac{n\pi x_{cm}}{\tau}\right) \sin\left(\frac{bn\pi}{\tau}\right) \cos\left(\frac{n\pi y_{cm}}{\tau}\right) \\ \sin\left(\frac{an\pi}{\tau}\right) \cos\left(\frac{n\pi x_{cm}}{\tau}\right) \sin\left(\frac{bn\pi}{\tau}\right) \sin\left(\frac{n\pi y_{cm}}{\tau}\right) \\ 2\sin\left(\frac{bn\pi}{\tau}\right) \cos\left(\frac{n\pi y_{cm}}{\tau}\right) \sin\left(\frac{an\pi}{\tau}\right) \cos\left(\frac{n\pi x_{cm}}{\tau}\right) \end{bmatrix}.
\end{aligned}
\tag{2.12}
$$

From Eq. 2.8 the Lorentz force on the square filamentary coil is calculated according to:

$$
\begin{aligned}
\underline{F}_c \;=\;& i_c \int_{-a}^{a} \begin{bmatrix} -1 \\ 0 \\ 0 \end{bmatrix} \times \underline{B}_m \, dx_c \bigg|_{\substack{z_c = 0 \\ y_c = -b}} + \\
& i_c \int_{-b}^{b} \begin{bmatrix} 0 \\ -1 \\ 0 \end{bmatrix} \times \underline{B}_m \, dy_c \bigg|_{\substack{z_c = 0 \\ x_c = a}} + \\
& i_c \int_{-a}^{a} \begin{bmatrix} 1 \\ 0 \\ 0 \end{bmatrix} \times \underline{B}_m \, dx_c \bigg|_{\substack{z_c = 0 \\ y_c = b}} + \\
& i_c \int_{-b}^{b} \begin{bmatrix} 0 \\ 1 \\ 0 \end{bmatrix} \times \underline{B}_m \, dy_c \bigg|_{\substack{z_c = 0 \\ x_c = -a}}.
\end{aligned}
\tag{2.13}
$$

which results in exactly the same equations for the force in each direction as the virtual work method. Since any coil can be represented as a bundle of filamentary coils, the Lorentz force method can be used to calculate the forces on the coils as well as the forces on the magnet array using Newton's third law. For a wire filament $\underline{dl}$, the Lorentz force exerted on the magnet array $\underline{dF}_m$ equals:

$$\underline{dF}_m = -i_c\underline{dl} \times \underline{B}_m. \tag{2.14}$$

2.1.2 Torque on the Planar Actuator

The Lorentz force on the magnet array by wire filament $\underline{dl}$ is defined by Eq. 2.14 in Section 2.1.1. The torque $\underline{dT}_m$ [Nm] exerted on the magnet array by the wire filament equals:

$$\begin{aligned} \underline{dT}_m &= \underline{r}_c \times \underline{dF}_m \\ &= -\underline{r}_c \times i_c\underline{dl} \times \underline{B}_m, \end{aligned} \tag{2.15}$$

where $\underline{r}_c$ is the vector from the center of mass of the magnet array to the wire filament. By summing all torque contributions of all wire filaments, the torque on the planar actuator can be determined. Note that the torque arm $\underline{r}_c$ is different for each wire filament. Therefore, the torque contribution of each coil cannot be calculated by the total force acting on the coil times an effective arm. Instead, the whole volume of the coil has to be taken into account when calculating the torque on the planar actuator.

2.1.3 Combined Analytical-Numerical Lorentz Force Model

In this section a fast combined analytical-numerical model is described using the Lorentz force method.

Permanent Magnet Model

To calculate the magnetic flux density vector $\underline{B}_m$ underneath the magnet array, each magnet in the magnet array is assumed to be ideal with a relative permeability $\mu_r = 1$ and is modeled as an equivalent magnetic charge. The magnetic charge model is derived from the Maxwell equations using the magnetic scalar potential Ψ [25, 26]:

$$\nabla \cdot \underline{B}_m = 0, \tag{2.16}$$
$$\underline{B}_m = \mu_0\underline{H} + \mu_0\underline{M}(\underline{H}), \tag{2.17}$$
$$\underline{H} = -\nabla\Psi, \tag{2.18}$$

where $\underline{M}$ [A/m] is the magnetization vector of the magnet and $\underline{H}$ [A/m] the magnetic field strength vector. Substituting Eq. 2.17 and 2.18 into Eq. 2.16 results into:

$$\begin{aligned} \nabla \cdot \underline{B}_m &= \mu_0\nabla \cdot (\underline{H} + \underline{M}) = 0 \\ &= \mu_0(-\nabla^2\Psi + \nabla \cdot \underline{M}) = 0, \end{aligned} \tag{2.19}$$
$$\nabla^2\Psi = \nabla \cdot \underline{M}. \tag{2.20}$$

The vector field $\underline{C}$ is introduced:

$$\Psi \;=\; \nabla \cdot \underline{C}, \tag{2.21}$$

and by substituting Eq. 2.21 into Eq. 2.20 a Poisson equation is obtained:

$$\nabla^2 \underline{C} \;=\; \underline{M}. \tag{2.22}$$

The solution of the Poisson equation is:

$$\underline{C} \;=\; -\frac{1}{4\pi} \int_V \frac{\underline{M}(r')}{|\underline{r} - \underline{r}'|} dV(\underline{r}'), \tag{2.23}$$

where $\underline{r}'$ is the source point vector and $\underline{r}$ the point of evaluation vector. Substituting the solution into Eq. 2.21 yields:

$$
\begin{aligned}
\Psi \;=\; & -\frac{1}{4\pi} \nabla \cdot \int_V \frac{\underline{M}(r')}{|\underline{r} - \underline{r}'|} dV(\underline{r}') \\
\;=\; & -\frac{1}{4\pi} \int_V \frac{\nabla' \cdot \underline{M}(r')}{|\underline{r} - \underline{r}'|} dV(\underline{r}') \\
& +\frac{1}{4\pi} \int_S \frac{\underline{M}(r') \cdot \underline{n}}{|\underline{r} - \underline{r}'|} dS(\underline{r}').
\end{aligned}
\tag{2.24}
$$

Finally, the expression for the magnetic flux density outside the magnet volume is obtained:

$$
\begin{aligned}
\underline{B}_m \;=\; & \mu_0 \underline{H} = -\mu_0 \nabla \Psi \\
\;=\; & \frac{\mu_0}{4\pi} \int_V (-\nabla' \cdot \underline{M}) \frac{(\underline{r} - \underline{r}')}{|\underline{r} - \underline{r}'|^3} dV \\
& +\frac{\mu_0}{4\pi} \int_S (\underline{M} \cdot \underline{n}) \frac{(\underline{r} - \underline{r}')}{|\underline{r} - \underline{r}'|^3} dS,
\end{aligned}
\tag{2.25}
$$

where $-\nabla' \cdot \underline{M}$ represents a magnetic volume charge distribution $\rho_c(\underline{r}')$ and $\underline{M} \cdot \underline{n}$ the magnetic surface charge $\sigma_c(\underline{r}')$. When the magnetization of the magnet is assumed uniform $\nabla' \cdot \underline{M} = 0$, the magnetic field outside the magnet can be represented by the magnetic surface charge $\sigma_c(\underline{r}')$ on the boundary surface of the magnet only. A cuboidal permanent magnet can be represented with two surface charges $\pm\sigma_c$ on the sides of the permanent magnet that are perpendicular to the magnetization direction. For a magnet with its center in position $[x_m \quad y_m \quad z_m]^T$ and sizes $2a$, $2b$ and $2c$ in the $x-$, $y-$ and $z-$direction, respectively, this results in the following expression of the magnetic flux density [25, 26]:

$$B_x \;=\; \frac{B_r}{4\pi} \sum_{i=0}^{1}\sum_{j=0}^{1}\sum_{k=0}^{1} (-1)^{i+j+k} \log\left(R - T\right), \tag{2.26}$$

$$B_y \;=\; \frac{B_r}{4\pi} \sum_{i=0}^{1}\sum_{j=0}^{1}\sum_{k=0}^{1} (-1)^{i+j+k} \log\left(R - S\right), \tag{2.27}$$

$$B_z \;=\; \frac{B_r}{4\pi} \sum_{i=0}^{1}\sum_{j=0}^{1}\sum_{k=0}^{1} (-1)^{i+j+k} \operatorname{atan2}\left(\frac{ST}{RU}\right), \tag{2.28}$$
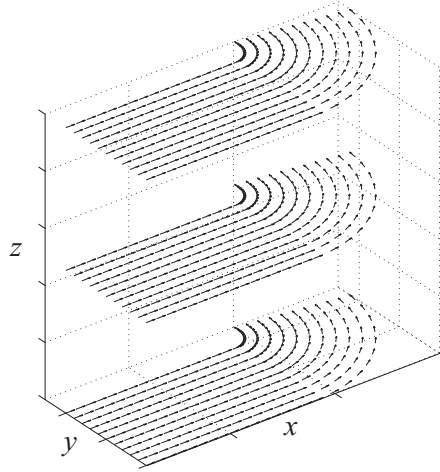
Figure 2.3: Part of coil with vector sequences as filamentary wires.

where atan2 is the four quadrant arctangent function, B_r [T] is the remanent magnetization of the permanent magnet and:

$$R = \sqrt{S^2 + T^2 + U^2}, \tag{2.29}$$
$$S = (x_m - x) - (-1)^i a, \tag{2.30}$$
$$T = (y_m - y) - (-1)^j b, \tag{2.31}$$
$$U = (z_m - z) - (-1)^k c. \tag{2.32}$$

To calculate the magnetic flux density of a magnet array, the magnetic flux density of each magnet can be calculated separately using the charge model. Then, the total magnetic flux density generated by the magnet array is calculated by superposition [10].

Coil Model

The coil is now modeled as a bundle of filamentary wires. Since the current can be taken out of the line integral (Eq. 2.13), the force on the magnet only depends on the geometry of the coil, the magnitude and sign of the Ampère-turns and the magnetic flux density of the magnet array, if a uniform current density is assumed in the coil. Therefore, each filamentary wire can be modeled as a sequence of vectors $\underline{dl}$, making the model very flexible by allowing almost any coil geometry. This is shown in Figure 2.3.

By eliminating the current from the line integral, any commutation scheme can be used and the six DOF equivalent of the motor constant can be calculated for each coil resulting in a matrix that prescribes the force and torque per unit current for each coil. End-effects are included as well, since the charge model is used to calculate the magnetic flux density underneath the magnet array, instead of spatial harmonics.

Model Implementation

The model is implemented using a combination of C and Matlab codes, where a compiled C function is used to improve the calculation time of the magnetic flux density underneath the magnet array. The data is then loaded into the Matlab workspace for the force and torque calculation.

The magnetic flux density is not directly calculated in each coil vector $\underline{dl}$ but in a 3D grid to further save calculation time. The magnet flux density in each coil vector $\underline{dl}$ is then estimated by interpolation. The advantage of this approach is that it is not necessary to recalculate the magnetic flux density underneath the magnet array when the position of the coils changes with respect to the magnet array, when the current in the coil changes or when the shape of the coil changes altogether.

2.1.4   Accuracy of the Lorentz Force Model

The accuracy of this model is limited by the assumption that the magnets do not have a relative permeability μ_r of 1. This causes a higher estimation of the magnetic flux density underneath the magnet array and a slightly more efficient force generation by the coils. Since high quality NdFeB magnets will be used with a relative permeability of about 1.03, the error is estimated to be about 2% [10]. Furthermore, the self-inductance of the coils depends on the position of the magnet array if $\mu_r > 1$, which introduces an error due to reluctance force of 0.3% [10]. Moreover, it is assumed that the magnetization of the magnets is uniform and that the magnetization direction is perfectly perpendicular to the surface of the magnets. Finally, mechanical tolerances also give rise to errors. Based on the experimental results discussed in [10] and the comparison with various models, it can be concluded that the model error is a few percent.

2.2   Coil Currents and Losses

The combined analytical-numerical model of the planar actuator with moving magnets and stationary coils is used to calculate the force and torque acting on the magnet array per Ampère-turn in each coil, which can be written as:

$$\left[\begin{array}{c} \underline{F} \\ \underline{T} \end{array} \right] \;=\; \underline{K} i_{at}, \tag{2.33}$$

here $\underline{F}$ and $\underline{T}$ are the force and torque vector on the magnet array with respect to its center of mass, respectively. The vector $\underline{i}_{at}$ [A] contains the number of Ampère-turns in each coil. There are n coils, so coupling matrix $\underline{K}$ has size $6 \times n$.

To generate a desired force and torque on the moving platform, the currents are calculated by using the pseudo-inverse of the matrix $\underline{K}$ ([10, 11, 12, 27]):

$$\underline{i}_{at} \;=\; \underline{K}^T (\underline{K}\underline{K}^T)^{-1} \left[\begin{array}{c} \underline{F}_d \\ \underline{T}_d \end{array} \right], \tag{2.34}$$

where $\underline{F}_d$ and $\underline{T}_d$ represent the desired force and torque vector, respectively.
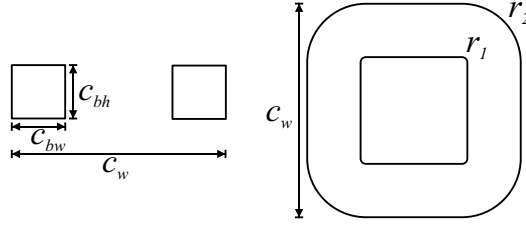
Figure 2.4: Coil geometry parameters

If Eq. 2.34 is substituted in Eq. 2.33, the result is:

$$
\begin{aligned}
\left[\begin{array}{c} \underline{F} \\ \underline{T} \end{array} \right] &= \underline{K}\underline{K}^T (\underline{K}\underline{K}^T)^{-1} \left[\begin{array}{c} \underline{F}_d \\ \underline{T}_d \end{array} \right], \\
\left[\begin{array}{c} \underline{F} \\ \underline{T} \end{array} \right] &= \left[\begin{array}{c} \underline{F}_d \\ \underline{T}_d \end{array} \right].
\end{aligned} \tag{2.35}
$$

These equations are used to determine the currents necessary to levitate and accelerate the platform. The currents in the coil determine the thermal behavior of the coils and the current requirements of the amplifier. The combined analytical-numerical model cannot be used to calculate the coil currents in real-time, since the calculation time is too long. The real-time commutation is discussed separately.

2.2.1 Dissipated Power

The dissipated power depends on the Ampère-turns through the coil and the filling factor of copper in the cross-section (f_c). The resistance of the coil R [Ω] is calculated by:

$$
R = \frac{N^2 \rho l_c}{f_c c_{bh} c_{bw}}, \tag{2.36}
$$

where N [-] is the number of turns in the coil, ρ [Ωm] is the electrical resistivity of the material, l_c [m] is the average length of one turn, c_{bh} [m] is the height of the coil bundle and c_{bw} [m] is the width of the coil bundle as it is shown in Figure 2.4. The power dissipation is:

$$
\begin{aligned}
P &= i_c^2 R \\
&= \frac{i_{at}^2}{N^2} \frac{N^2 \rho l_c}{f_c c_{bh} c_{bw}} \\
&= \frac{i_{at}^2 \rho l_c}{f_c c_{bh} c_{bw}}, \tag{2.37}
\end{aligned}
$$

where i_c is the current in the coil and i_{at} is the number of Ampère-turns in the coil.

2.2.2 Controllability of the Planar Actuator

The commutation law defined by Eq. 2.34 can only be applied if the inverse of $\underline{K}\underline{K}^T$ exists. This implies that $\underline{K}\underline{K}^T$ must be a positive definite matrix and the

rank of $\underline{K}\underline{K}^T$ must be equal to the number of controlled DOFs. Furthermore, the conditioning of $\underline{K}\underline{K}^T$ must be such that a numerical inverse of $\underline{K}\underline{K}^T$ is feasible. If the conditioning is poor, a small model error in an element of $\underline{K}$ can result in a large error in the numerical inverse. The conditioning of a matrix is defined by the condition number, which is derived using the singular value decomposition (SVD) [27]. The SVD decomposes $\underline{K}$ into:

$$\underline{K} \quad = \quad \underline{U}\,[\underline{\Sigma} \quad \underline{0}]\,\underline{V}^T, \tag{2.38}$$

where $\underline{U}$ and $\underline{V}$ are unitary, $\underline{\Sigma}$ is a diagonal matrix and $\underline{0}$ is a zero matrix. The size of $\underline{K}$ is $6 \times n$ so $\underline{U}$ and $\underline{\Sigma}$ have size 6×6, $\underline{0}$ has size $6 \times n\text{-}6$ and $\underline{V}$ has size $n \times n$. The values on the diagonal of $\underline{\Sigma}$ are called the singular values of $\underline{K}$. Since $\underline{K}$ is real, $\underline{U}$ and $\underline{V}$ are orthogonal. The 2-norm of any vector multiplied by an orthogonal matrix remains the same. This means that all the energy conversion from the current vector $\underline{i}_{at}$ to the force and torque vector is defined by $\underline{\Sigma}$.

The condition number c of a non-square matrix is calculated using the singular value decomposition and its value is defined as:

$$c \quad = \quad \frac{\max \operatorname{diag}(\underline{\Sigma})}{\min \operatorname{diag}(\underline{\Sigma})} \tag{2.39}$$

The condition number can vary between one and infinity, where infinity means that the matrix is singular. The condition number should be sufficiently small to ensure numerical stability. The upper bound of the condition number c_{max} is defined by the precision p of the elements in matrix $\underline{K}$. Since the model has an error of a few percent, the entries of $\underline{K}$ are 2 digits accurate ($p = 2$). The upper bound of the condition number is calculated by:

$$c_{max} = 10^p, \tag{2.40}$$

which means that for $p = 2$, the maximum allowable condition number is 100.

2.3   Coil Back-EMF Model

For a coil and a magnet array in an ironless structure, the force and torque on the coil can be calculated using virtual work (see also Section 2.1.1 and Eq. 2.6) according to:

$$\begin{bmatrix} \underline{F}_c \\ \underline{T}_c \end{bmatrix} \quad = \quad -\begin{bmatrix} \frac{d}{dx} & \frac{d}{dy} & \frac{d}{dz} & \frac{d}{d\theta} & \frac{d}{d\psi} & \frac{d}{d\phi} \end{bmatrix}^T \Lambda_m i_c, \tag{2.41}$$

where $\underline{F}_c$ is the force vector and $\underline{T}_c$ the torque vector acting on the coil, Λ_m is the flux linkage of the coil due to the magnet array and i_c is the current flowing though the coil. The coordinates x, y, z, θ, ψ and ϕ correspond to the relative position and orientation of the magnet array with respect to the coil.

When assuming that all coils have the same N number of turns, the current vector of the coils $\underline{i}$ (in amperes) can be related to $\underline{i}_{at}$ (in Ampère-turns) by:

$$\underline{i}_{at} \quad = \quad N\underline{i}. \tag{2.42}$$

Now, Eq. 2.33 is rewritten to:

$$\left[\begin{array}{c} \underline{F} \\ \underline{T} \end{array} \right] \;\; = \;\; \underline{K}N\underline{i}, \tag{2.43}$$

Furthermore, the force and torque acting on the magnet array is the opposite as the force and torque acting on the coils. By generalizing Eq. 2.41 for multiple coils, the scalar flux linkage Λ_m becomes a vector $\underline{\Lambda}_m$ with n flux linkages for n coils. The following can be stated:

$$\left[\begin{array}{cccccc} \frac{d}{dx} & \frac{d}{dy} & \frac{d}{dz} & \frac{d}{d\theta} & \frac{d}{d\psi} & \frac{d}{d\phi} \end{array} \right]^T \underline{\Lambda}_m^T \underline{i} \;\; = \;\; \underline{K}\underline{i}_{at}, \tag{2.44}$$

and:

$$\left[\begin{array}{cccccc} \frac{d}{dx} & \frac{d}{dy} & \frac{d}{dz} & \frac{d}{d\theta} & \frac{d}{d\psi} & \frac{d}{d\phi} \end{array} \right]^T \underline{\Lambda}_m^T \;\; = \;\; \underline{K}N. \tag{2.45}$$

The back-EMF in one coil can be written as:

$$E_{EMF} \;\; = \;\; \frac{d}{dt}\Lambda_m. \tag{2.46}$$

The time derivative of the flux linkages can be written as partial derivatives with respect to position and its time derivative:

$$\begin{aligned} \frac{d}{dt}\Lambda_m \;\; = \;\; & \frac{\partial}{\partial x}\Lambda_m \frac{\partial x}{\partial t} + \frac{\partial}{\partial y}\Lambda_m \frac{\partial y}{\partial t} + \frac{\partial}{\partial z}\Lambda_m \frac{\partial z}{\partial t} \\ & + \frac{\partial}{\partial \theta}\Lambda_m \frac{\partial \theta}{\partial t} + \frac{\partial}{\partial \psi}\Lambda_m \frac{\partial \psi}{\partial t} + \frac{\partial}{\partial \phi}\Lambda_m \frac{\partial \phi}{\partial t}, \end{aligned} \tag{2.47}$$

which can be rewritten as the product of the spatial derivatives of the flux linkage with the relative velocity vector $\underline{v}$ of the magnet array with respect to the stationary coils:

$$\frac{d}{dt}\Lambda_m = \underline{v}^T \left[\begin{array}{cccccc} \frac{d}{dx} & \frac{d}{dy} & \frac{d}{dz} & \frac{d}{d\theta} & \frac{d}{d\psi} & \frac{d}{d\phi} \end{array} \right]^T \Lambda_m. \tag{2.48}$$

Combining these equations results in:

$$\begin{aligned} \underline{E}_{EMF}^T \;\; = \;\; & \underline{v}^T \left[\begin{array}{cccccc} \frac{d}{dx} & \frac{d}{dy} & \frac{d}{dz} & \frac{d}{d\theta} & \frac{d}{d\psi} & \frac{d}{d\phi} \end{array} \right]^T \underline{\Lambda}_m^T, \\ = \;\; & \underline{v}^T \underline{K}N, \end{aligned} \tag{2.49}$$

where $\underline{E}_{EMF}$ is a vector containing the back-EMF voltages of the coils. These equations are used to calculate the back-EMF in the coil for a given speed of the platform, which is necessary to determine the voltage requirements of the power amplifier.

2.4 Real-time Commutation of the Coil Currents

The relationship between the current in each coil and the force-torque vector on the moving platform is highly non-linear [8, 10, 11, 12, 24], so accurate computing

of the interaction between coil currents and the force-torque vector is difficult if closed-loop rates of several kHz are required [10, 12, 24]. The first two problems can be addressed by using an appropriate mapping between the control currents and the dynamics of the planar actuator ([8, 11]). However, the mapping requires a correct calculation of the matrix that couples the currents in the coils to the force-torque vector on the platform. The calculation of the coupling matrix can be done by using simplified models of the real system [10, 23, 24].

First, the magnetic flux density of the planar actuator can be represented as a sum of spatial harmonics as it is discussed in [10, 22]. Second, the coil can be modeled as a number of filaments or surfaces, for which it is possible to find an analytical solution for the Lorentz force and the corresponding torque [9, 10].

The expressions derived in [9, 10] show that the torque acting on the magnet array depends on two components. One component can be expressed as the cross-product between a constant torque arm and the force vector. The other component does not depend on an arm, which indicates that the force does not act on a single point and the force distribution must be taken into account.

Although the analytical expressions provide a good insight in the mechanisms that determine the forces and torques on the planar actuator, the simplifying assumptions compromise the accuracy of the model. To allow real-time calculation of the forces and torques, only the first spatial harmonic of the planar actuator magnet array can be included. Furthermore, coils are reduced to current sheets or a single loop of filament. Moreover, end-effects cannot be included, which implies that the coils on the perimeter of the magnet array cannot be used and the currents in these coils must be forced to zero [11, 12]. Including the end-effects allows the coils on the perimeter to be used in the control of the planar actuator. These coils have the largest arm with respect to the center of the platform, so they can contribute significantly to the applied torque vector. Furthermore, it is possible to reduce the total number of coils underneath the magnet array for a controllable topology.

Another solution is to use a look-up table. The advantage of look-up tables is that effects (e.g. end-effects), which are hard to model, can easily be included. In addition, a look-up table can be very accurate since all time consuming computations are done offline, while accessing a look-up table in real-time is very fast. On the other hand, the large number of coils, the long stroke and multiple DOF of the planar actuator prohibits the use of one look-up table since it has an extremely large size for a DSP and the offline computational effort is enormous. Therefore, a new approach is proposed, which combines the advantages of a look-up table with a feasible size for real-time control of planar actuators.

2.4.1   Position Symmetry of Force and Torque Vector

A planar actuator has a long stroke in the x-y plane and a short stroke in the z-direction. In addition, small angles around all three axes can be realized. If a planar actuator has n coils, the coupling matrix between coil currents and the force-torque vector has dimension $6 \times n$. Since this coupling matrix $\underline{K}$ needs to be calculated at any position in the workspace, a look-up table of the full system with all coils and all six DOF will be enormous, especially if the required accuracy is high. If the stroke is $100 \times 100 \times 2$ mm in the x-, y- and z-direction respectively
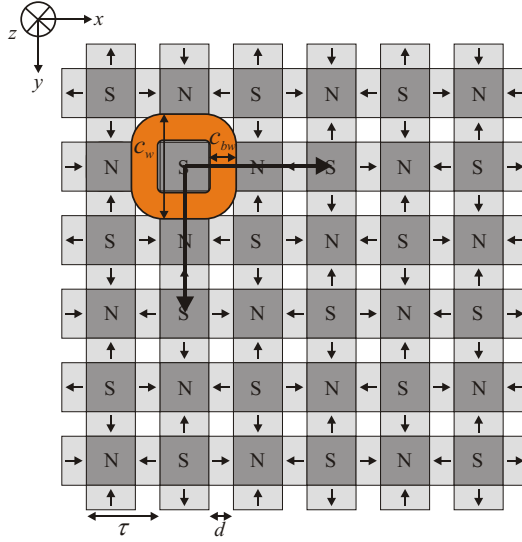
Figure 2.5: Halbach magnet array with a single coil

with a resolution of $1 \times 1 \times 0.050$ mm, 25 active coils and small angles of ± 5 mrad with a 0.5 mrad resolution are assumed, a look-up table with 16 bit precision would require ($100^2 \times 40 \times 20^3 \times 6 \times 25 \times 16 =$) 7.68 Tbits. Therefore, symmetries in the structure and the magnetic flux density distribution must be used to reduce the size of the look-up table. The use of look-up tables is illustrated with a 6×6 Halbach magnet array with square coils. The same principle can be applied to other magnet array and coil topologies.

To investigate the symmetry, a planar actuator with a Halbach array with a single coil is considered, as shown in Figure 2.5. The center of the top-left magnet is defined as the origin of the coordinate-system. The dimensions of the magnet array and the coil are listed in Table 2.1 and the definition of the coil geometry parameters is shown in Figure 2.4. The symmetry is studied for a coil that is completely overlapped by the magnet array. The behavior on the perimeter, i.e. the end-effects, are considered later.

The coil is moved over a distance of 2τ in the plane underneath the magnet array, where the initial position is shown in Figure 2.5 and the movement directions are indicated by the two arrows. In a grid with points every 2 mm the force and torque per Ampère-turn is calculated using the analytical-numerical model that is described in Section 2.1. All angles are assumed to be small enough to be negligible, i.e. <5 mrad. The current in the coil is assumed to have a uniform distribution over the cross-section. Furthermore, the airgap is kept constant. The coupling matrix $\underline{K}$ has six entries for each coil, three for force and three for torque in x-, y- and z-direction, respectively. The vector containing the coupling related to force for a single coil is called $\underline{K}_F$ and it is called $\underline{K}_T$, if torque is considered. Both $\underline{K}_F$ and $\underline{K}_T$ have dimension 3×1.

Table 2.1: Dimensions of magnet array and coil

Parameter	Symbol	Value	Dimension
Pole pitch	τ	30	mm
HB Magnet width	d	10	mm
Magnet height	m_h	8	mm
Coil width	c_w	45	mm
Coil bundle width	c_{bw}	15	mm
Coil bundle height	c_{bh}	10	mm
Airgap	g	2	mm
Inner radius	r_1	1	mm
Outer radius	r_2	11	mm
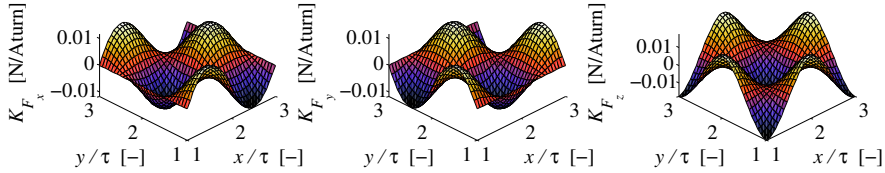
Figure 2.6: Plot of the x-, y- and z-components of $\underline{K}_F$ for different positions

Force Symmetry

The force coupling $\underline{K}_F$ in newton per Ampère-turn is shown in Figure 2.6 for the x-, y- and z-direction. From this figure it is clear that K_{F_y} is simply the transposed of K_{F_x}. Furthermore, there is a symmetry every pole pitch in both the x- and y-direction. This indicates that the forces in x-, y- and z-direction can be characterized by only two look-up tables of one pole pitch. First, the area is divided into four sections:

$$s1 \in \left\{ (x,y) \in \mathbb{R}^2 \mid \tau \leq x \leq 2\tau, \tau \leq y \leq 2\tau \right\}, \tag{2.50}$$

$$s2 \in \left\{ (x,y) \in \mathbb{R}^2 \mid 2\tau < x \leq 3\tau, \tau \leq y \leq 2\tau \right\}, \tag{2.51}$$

$$s3 \in \left\{ (x,y) \in \mathbb{R}^2 \mid \tau \leq x \leq 2\tau, 2\tau < y \leq 3\tau \right\}, \tag{2.52}$$

$$s4 \in \left\{ (x,y) \in \mathbb{R}^2 \mid 2\tau < x \leq 3\tau, 2\tau < y \leq 3\tau \right\}. \tag{2.53}$$

Using the lookup tables $^{s1}K_{F_x}$ and $^{s1}K_{F_z}$ derived from the data of K_{F_x} and
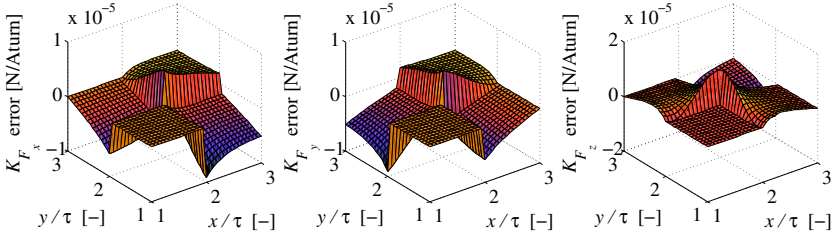
Figure 2.7: Difference between the coupling calculated with the model and the $\underline{K}_F$ look-up table prediction

K_{F_z} in $s1$, respectively, the following holds:

$$^{s2}K_{F_x} = -^{s1}\underline{K}_{F_x}, \tag{2.54}$$

$$^{s3}K_{F_x} = -^{s1}K_{F_x}, \tag{2.55}$$

$$^{s4}K_{F_x} = {}^{s1}K_{F_x}, \tag{2.56}$$

$$^{si}K_{F_y} = \left[{}^{si}K_{F_x}\right]^T \quad \text{for } i = 1, 2, 3, 4, \tag{2.57}$$

$$^{s2}K_{F_z} = -^{s1}K_{F_z}, \tag{2.58}$$

$$^{s3}K_{F_z} = -^{s1}K_{F_z}, \tag{2.59}$$

$$^{s4}K_{F_z} = {}^{s1}K_{F_z}. \tag{2.60}$$

The difference between the coupling $\underline{K}_F$ calculated by the model in the entire area and the coupling constructed from the look-up tables $^{s1}K_{F_x}$ and $^{s1}K_{F_z}$ according to Eqs. 2.54-2.60 is shown in Figure 2.7. In section s_1 the difference is zero since the model predictions from this section is used in the look-up table. In the other sections, the maximum difference is a factor 2500 smaller in x- and y-direction and 1000 smaller in z-direction than the maximum value, which is related to the accuracy of the model, as it is discussed in Section 2.1.

Torque Symmetry

As discussed in the previous section, the torque vector has two components. One can be written as the cross-product of a single torque arm and the force vector, the other cannot. Since the forces are known from the look-up tables and the arm is known from the geometry (e.g. assuming the force attaches in a fixed point of the coil), only the second component needs to be estimated using look-up tables. The second term $\underline{K}_T$ is defined as:

$$\underline{K}_T = \underline{K}_{T_{model}} - \underline{r} \times \underline{K}_{F_{model}}, \tag{2.61}$$

where $\underline{K}_{T_{model}}$ is the torque coupling, predicted by the analytical-numerical model and $\underline{r}$ is the torque arm from the center of mass of the magnet array to a fixed point of the coil, i.e. the geometrical center of the coil.
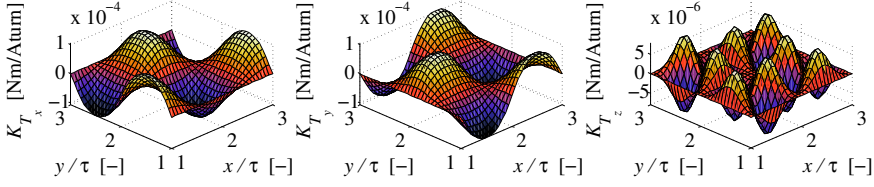
Figure 2.8: Plot of the x-, y- and z-components of $\underline{K}_T$ for different positions
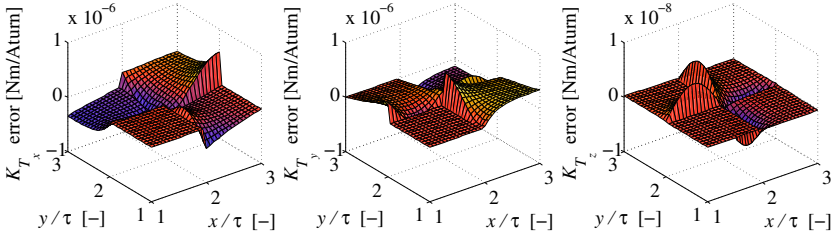
Figure 2.9: Difference between the coupling calculated with the model and the $\underline{K}_T$ look-up table prediction

The torque coupling $\underline{K}_T$ in newton-meter per Ampère-turn is shown in Figure 2.8 for the x-, y- and z-direction. From this figure it is clear that K_{T_y} is the transposed of $-K_{T_x}$. Again, there is a symmetry every pole pitch in both the x- and y-direction. This indicates that the torques in x-, $y-$ and z-direction can be characterized by two look-up tables of one pole pitch. Again, the area is divided into four sections ($s1$, $s2$, $s3$ and $s4$) and the following equations define the torque coupling in each section:

$$^{s2}K_{T_x} = -^{s1}K_{T_x}, \tag{2.62}$$

$$^{s3}K_{T_x} = -^{s1}K_{T_x}, \tag{2.63}$$

$$^{s4}K_{T_x} = {}^{s1}K_{T_x}, \tag{2.64}$$

$$^{si}K_{T_y} = \left[-^{si}K_{T_x}\right]^T \quad \text{for } i = 1, 2, 3, 4, \tag{2.65}$$

$$^{s2}K_{T_z} = \left[^{s1}K_{T_z}\right]^T, \tag{2.66}$$

$$^{s3}K_{T_z} = \left[^{s1}K_{T_z}\right]^T, \tag{2.67}$$

$$^{s4}K_{T_z} = {}^{s1}K_{T_z}. \tag{2.68}$$

The difference between the coupling $\underline{K}_T$ calculated by the model in the entire area and the coupling constructed from the look-up tables $^{s1}K_{T_x}$ and $^{s1}K_{T_z}$ according to Eqs. 2.62-2.68 is shown in Figure 2.9. The maximum difference is a factor 300 smaller in x- and y-direction and 4500 smaller in z-direction than the maximum value. Although the shapes for K_{F_x}, K_{F_y}, K_{T_x} and K_{T_y} look very similar, the relationship between the force and torque profiles is more complicated
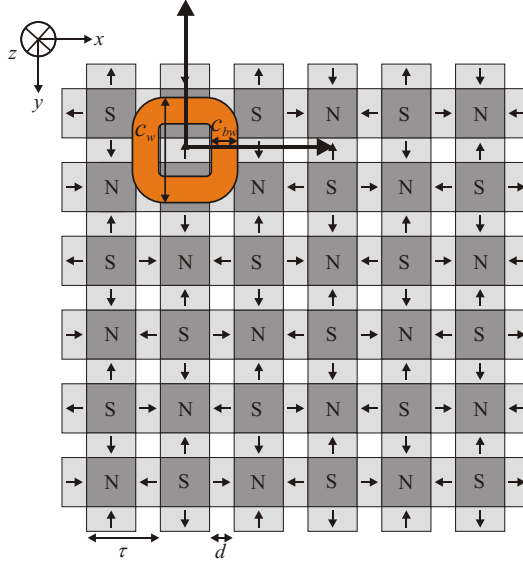
Figure 2.10: Halbach magnet array with a single coil at the top side

than a simple gain.

2.4.2 End-Effects at the Side

At the perimeter of the magnet array the forces and torques will behave differently, so another set of look-up tables is necessary to include the end-effects. In Figures 2.10 and 2.11, a coil is shown that moves inside the magnet array for the x- and y-direction, respectively, and outside the magnet array in the other direction. The $\underline{K}_F$ and $\underline{K}_T$ that correspond with the case depicted in Figure 2.10 are shown in Figure 2.12. There is no symmetry in the y-direction but there is symmetry in the x-direction, because the values of $\underline{K}_F$ and $\underline{K}_T$ change sign every pole pitch. Since there is only symmetry in one direction, the behavior for x and y is different, a look-up table is necessary for all six components of $\underline{K}_F$ and $\underline{K}_T$. The end-effects at the left side, shown in Figure 2.11, can be derived from the plots shown in Figure 2.10 by swapping the values for x and y and transposing the look-up table:

$$^lK_{F_x} = \left[{}^tK_{F_y}\right]^T, \tag{2.69}$$

$$^lK_{F_y} = \left[{}^tK_{F_x}\right]^T, \tag{2.70}$$

$$^lK_{F_z} = \left[{}^tK_{F_z}\right]^T, \tag{2.71}$$

$$^lK_{T_x} = -\left[{}^tK_{T_y}\right]^T, \tag{2.72}$$

$$^lK_{T_y} = -\left[{}^tK_{T_x}\right]^T, \tag{2.73}$$

$$^lK_{T_z} = -\left[{}^tK_{T_z}\right]^T, \tag{2.74}$$
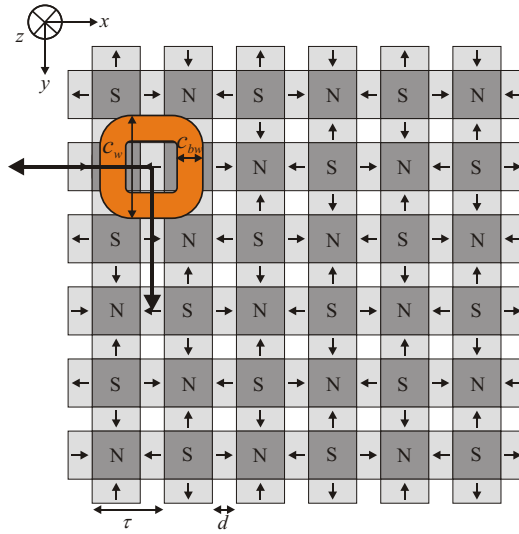
Figure 2.11: Halbach magnet array with a single coil at the left side
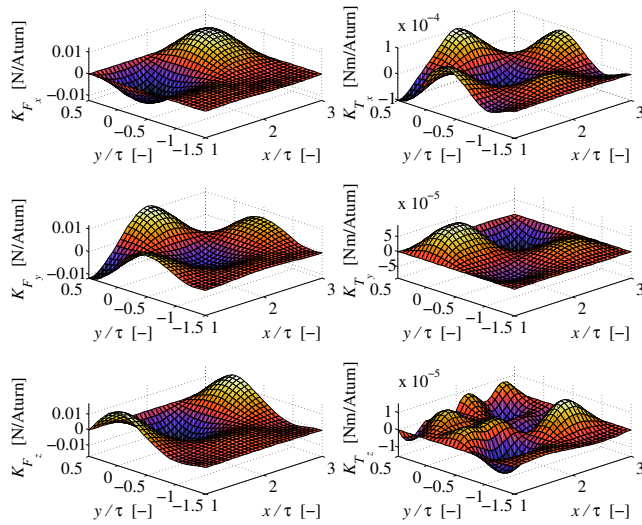
Figure 2.12: Plot of $\underline{K}_F$ and $\underline{K}_T$ at the top side of the magnet array
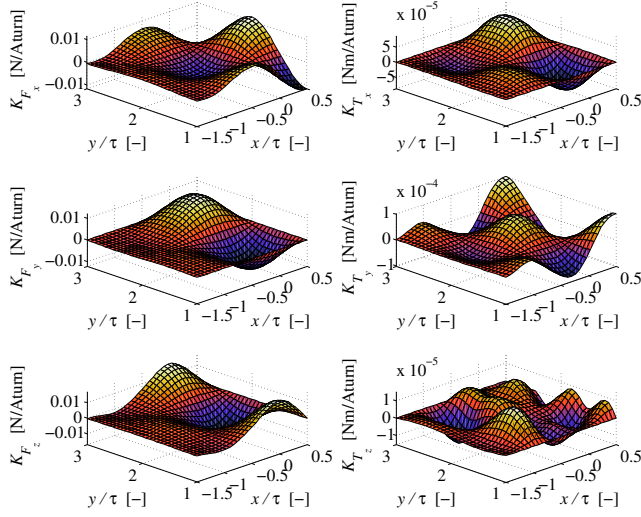
Figure 2.13: Plot of $\underline{K}_F$ and $\underline{K}_T$ at the left side of the magnet array

where l indicates the left side and t the top side. The end-effects at the bottom side b and right side r can be derived by mirroring the top side and left side, respectively:

$$^bK_{F_x} = -\left(^tK_{F_x}\right)_{mx}, \tag{2.75}$$

$$^bK_{F_y} = \left(^tK_{F_y}\right)_{mx}, \tag{2.76}$$

$$^bK_{F_z} = -\left(^tK_{F_z}\right)_{mx}, \tag{2.77}$$

$$^bK_{T_x} = \left(^tK_{T_x}\right)_{mx}, \tag{2.78}$$

$$^bK_{T_y} = -\left(^tK_{T_y}\right)_{mx}, \tag{2.79}$$

$$^bK_{T_z} = \left(^tK_{T_z}\right)_{mx}, \tag{2.80}$$

$$^rK_{F_x} = \left(\left[^tK_{F_y}\right]^T\right)_{my}, \tag{2.81}$$

$$^rK_{F_y} = -\left(\left[^tK_{F_x}\right]^T\right)_{my}, \tag{2.82}$$

$$^rK_{F_z} = -\left(\left[^tK_{F_z}\right]^T\right)_{my}, \tag{2.83}$$

$$^rK_{T_x} = \left(\left[^tK_{T_y}\right]^T\right)_{my}, \tag{2.84}$$

$$^rK_{T_y} = -\left(\left[^tK_{T_x}\right]^T\right)_{my}, \tag{2.85}$$

$$^rK_{T_z} = \left(\left[^tK_{T_z}\right]^T\right)_{my}, \tag{2.86}$$
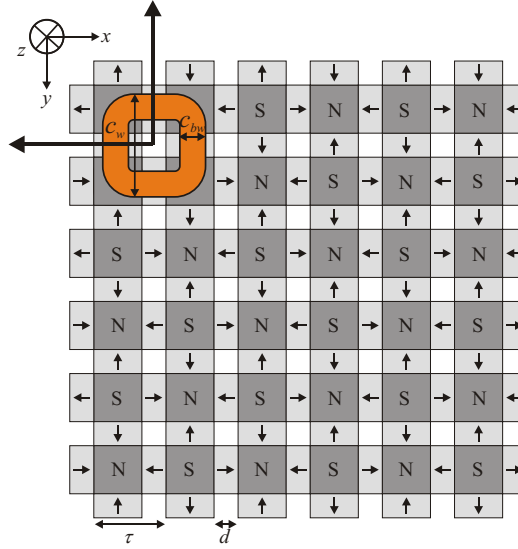
Figure 2.14: Halbach magnet array with a single coil at the top-left corner

where mx and my denote that the look-up table is mirrored along the x- or y-axis. All end-effects can thus be included by six look-up tables, each covering an area of one pole pitch in the direction along the side and approximately two pole pitches, depending on the coil size, perpendicular to the side.

2.4.3 End-Effects at the Corners

In Figure 2.14 the coil is shown at the top-left corner of the magnet array and moved outside the array in the direction of the arrows. The corresponding values of $\underline{K}_F$ and $\underline{K}_T$ are shown in Figure 2.15. At the corner of the magnet array, there is symmetry in both the x- and y-direction, so all end-effects at the corner can be included by four look-up tables, ${}^{tl}K_{F_x}$, ${}^{tl}K_{F_z}$, ${}^{tl}K_{T_x}$ and ${}^{tl}K_{T_z}$, where tl stands for top-left. The look-up tables for the y-components can be derived from the x-components according to:

$$
{}^{tl}K_{F_y} \quad = \quad \left[{}^{tl}K_{F_x}\right]^T ,
\tag{2.87}
$$

$$
{}^{tl}K_{T_y} \quad = \quad \left[{}^{tl}K_{T_x}\right]^T .
\tag{2.88}
$$
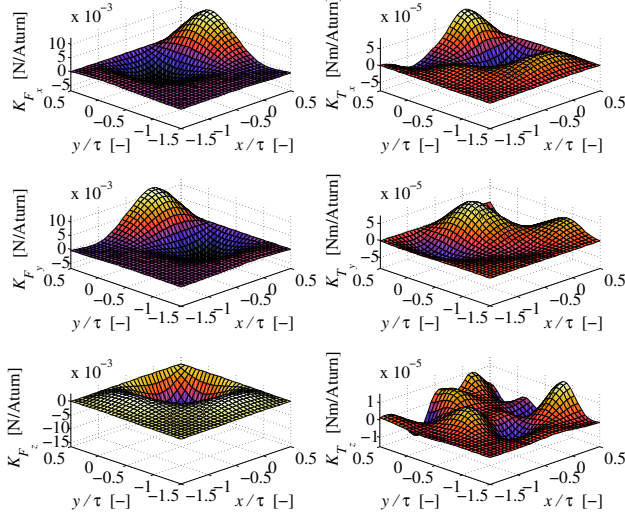
Figure 2.15: Plot of $\underline{K}_F$ and $\underline{K}_T$ at the top-left corner of the magnet array

The values for $\underline{K}_F$ and $\underline{K}_T$ for the top-right corner are found by:

$$^{tr}K_{F_x} = \left(^{tl}K_{F_x}\right)_{my}, \tag{2.89}$$

$$^{tr}K_{F_y} = -\left[\left(^{tl}K_{F_x}\right)_{mx}\right]^T, \tag{2.90}$$

$$^{tr}K_{F_z} = -\left(^{tl}K_{F_z}\right)_{my}, \tag{2.91}$$

$$^{tr}K_{T_x} = -\left(^{tl}K_{T_x}\right)_{my}, \tag{2.92}$$

$$^{tr}K_{T_y} = -\left[\left(^{tl}K_{T_x}\right)_{mx}\right]^T, \tag{2.93}$$

$$^{tr}K_{T_z} = \left(^{tl}K_{T_z}\right)_{my}, \tag{2.94}$$

where tr denotes the top-right corner of the magnet array. Finally, $\underline{K}_F$ and $\underline{K}_T$ in the bottom-left (bl) and bottom-right (br) are calculated:

$$^{bl}K_{F_x} = -\left(^{tl}K_{F_x}\right)_{mx}, \tag{2.95}$$

$$^{bl}K_{F_y} = \left[\left(^{tl}K_{F_x}\right)_{my}\right]^T, \tag{2.96}$$

$$^{bl}K_{F_z} = -\left(^{tl}K_{F_z}\right)_{mx}, \tag{2.97}$$

$$^{bl}K_{T_x} = \left(^{tl}K_{T_x}\right)_{mx}, \tag{2.98}$$

$$^{bl}K_{T_y} = \left[\left(^{tl}K_{T_x}\right)_{my}\right]^T, \tag{2.99}$$

$$^{bl}K_{T_z} = \left(^{tl}K_{T_z}\right)_{mx}, \tag{2.100}$$

$$
{}^{br}K_{F_x} = -\left({}^{tl}K_{F_x}\right)_{mx,my}, \tag{2.101}
$$

$$
{}^{br}K_{F_y} = -\left[\left({}^{tl}K_{F_x}\right)_{mx,my}\right]^T, \tag{2.102}
$$

$$
{}^{br}K_{F_z} = \left({}^{tl}K_{F_z}\right)_{mx,my}, \tag{2.103}
$$

$$
{}^{br}K_{T_x} = -\left({}^{tl}K_{T_x}\right)_{mx,my}, \tag{2.104}
$$

$$
{}^{br}K_{T_y} = \left[\left({}^{tl}K_{T_x}\right)_{mx,my}\right]^T, \tag{2.105}
$$

$$
{}^{br}K_{T_z} = \left({}^{tl}K_{T_z}\right)_{mx,my}. \tag{2.106}
$$

The area covered by the look-up tables is approximately $2\tau \times 2\tau$, depending on the size of the coils.

2.4.4   Look-Up Tables of the Full Planar Actuator

In the previous sections $\underline{K}_F$ and $\underline{K}_T$ are considered at a constant airgap, which result in a 2D look-up table. To cover the entire workspace of the planar actuator, however, variations of the airgap (δz) have to be included resulting in a 3D look-up table. The size of the look-up table increases as the symmetry decreases. For coils completely covered by the magnet array, four look-up tables covering $\tau \times \tau \times \delta z$ are sufficient. To include the coils at the sides another six look-up tables covering $\tau \times 2\tau \times \delta z$ are necessary. Finally, to include the coils at the corners, four more look-up tables of $2\tau \times 2\tau \times \delta z$ are required. The density of the grid points in the look-up tables depends on the required accuracy, the interpolation method used, e.g. nearest point or linear interpolation and the available memory and computation power. For example: the memory required for 30 grid point per pole pitch and 30 grid points in δz is ($30^3 \times 4 \times 16 =$) 1.728 Mbits for the coils that are completely overlapped, ($30^2 \times 60 \times 6 \times 16 =$) 5.184 Mbits for the coils at the sides and ($60^2 \times 30 \times 4 \times 16 =$) 6.912 Mbits for the coils at the corners. An overview of the look-up tables and the sections of the magnet array in which they are applicable is shown in Figure 2.16.

Reducing 3D Look-Up Tables to 2D

Since the variation of the airgap is relatively small, especially compared to the stroke in the x- and y-direction, it might be possible to include the variation of the airgap by a z-dependent gain. With this approach the 2D look-up table does not have to be expanded to a 3D look-up table but the inclusion of an additional 1D look-up table with gains or a fitted function that covers the variation of the airgap will suffice.

To investigate this possibility, the force coupling $\underline{K}_F$ and the torque coupling $\underline{K}_T$ are calculated with an airgap of 1 mm in sections s_1, instead of 2 mm, which was used previously. Next, a gain for the x-, y- and z-component of the force coupling $\underline{K}_F$ and the torque coupling $\underline{K}_T$ is calculated using a least-squares fit of several other data sets.

The difference between the coupling at 2 mm airgap and the coupling at 1 mm airgap corrected by the gain is shown in Figure 2.17. The maximum error is approximately a hundred times smaller than the maximum coupling and within
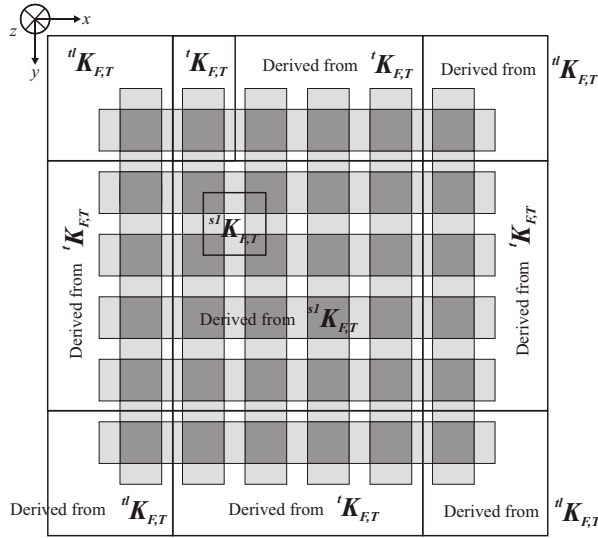
Figure 2.16: Look-up table sections

the limits of the model accuracy. The coupling between the coil and the magnet array can therefore be approximated by a 2D look-up table that contains the x-y variation of the coupling and an independent 1D look-up table or a fitted function that covers the z-dependency of the coupling.

The commutation algorithm based upon 2D look-up tables and linear interpolation can calculate the currents in 81 coils within 104 μs, according to a dSpace benchmark with a DS1005 processor. The use of look-up tables is illustrated with a 6×6 Halbach magnet array with square coils. The same principle can be applied to other magnet array and coil topologies.

2.4.5   Accuracy of the Look-Up Table Commutation

The accuracy of the look-up table commutation algorithm is mainly limited by the model that is used to calculate the look-up tables. In this case, the combined analytical-numerical Lorentz force model is used that is presented in Section 2.1.3, which has errors in the order of a few percent as it is discussed in Section 2.1.4. Since the relative errors of the look-up table method are of the same magnitude or smaller, it is difficult to judge, whether the error is induced by the model or by the commutation method. For instance, if a coil is exactly centered underneath a north magnetic pole it should, based upon logic, have exactly the opposite behavior as if it were exactly centered underneath a south magnetic pole. This is off course valid only, if all other factors such as magnetization, mechanical dimensions etc. are equal. It is expected that by calculating the look-up table with a more accurate method, i.e. FEM, it should be possible to improve the accuracy of the commutation.

On the other hand, there are certain assumptions in the commutation, that limit the accuracy of the model, regardless of the model that is used to calculate
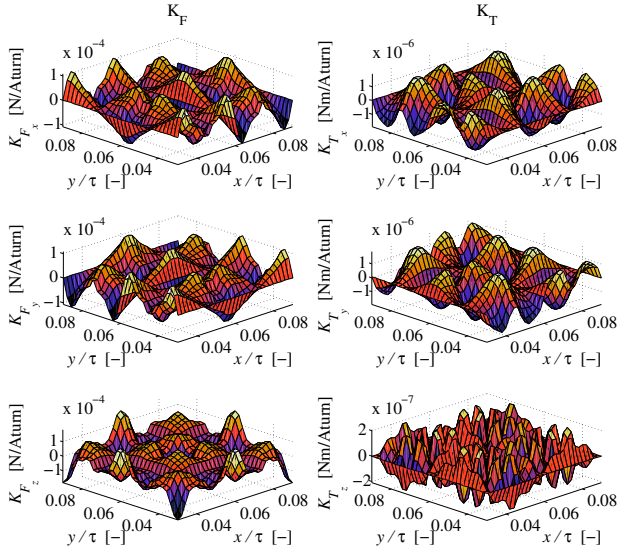
Figure 2.17: Error for $\underline{K}_F$ and $\underline{K}_T$ by using z-dependent gain

the look-up tables. First of all, interpolation between the look-up table entries is necessary to estimate the values of $\underline{K}_F$ and $\underline{K}_T$ at all positions. The values of $\underline{K}_F$ and $\underline{K}_T$ change smoothly with position as it is clear from Figures 2.6, 2.8, 2.12, 2.13 and 2.15. In fact, the results of the experimental verification using linear interpolation presented in Section 7.2 did not improve, if the distance between the points in the look-up table was reduced from 1 mm to 0.5 mm, so the effect of interpolation is invisible in the measurements.

Second, the reduction of the look-up tables from 3D to 2D, by treating the variation of $\underline{K}_F$ and $\underline{K}_T$ in the x-y plane independent from the z-direction also gives rise to an error. It is estimated to introduce a maximum error of 1%, based upon the simulations in Section 2.4.4. However, these errors are in the same range as the model errors itself so they might be slightly larger or smaller. By calculating the look-up tables at the nominal airgap between the coils and the magnet array, this effect can be minimized.

Third, the decay of the magnetic field is asymptotical, which implies that the magnetic field at the edges of the area covered by the end-effect look-up tables is not exactly zero. This gives rise to a discontinuity, which effect depends on the area outside the magnet array that is covered by the look-up tables. The values of $\underline{K}_F$ and $\underline{K}_T$ are not exactly zero at the edges but are assumed zero beyond the edges. The area covered by the look-up tables is chosen to limit the maximum value of these discontinuities to a few percent relative to the maximum values of $\underline{K}_F$ and $\underline{K}_T$, which is the same as the model error used to calculate the look-up tables.

Finally, it is important to know how these errors add up when the resulting force

and torque on the magnet array is considered. The errors plotted in Figures 2.7, 2.9 and 2.17 vary around zero. Moreover, the number of active coils is large (> 25) and these coils are at different positions underneath the magnet array, so it is expected that these errors will average to a value close to zero. Mainly the errors that are related to the model used to calculate the look-up tables will be visible.

2.5   Thermal Model

The planar actuator has a significant weight that must be levitated. The magnets themselves and the plate to which they are glued need to be supported by the magnetic bearings. On top of that, there is an additional mass of the manipulator with power and control electronics. Therefore, the dissipation in the coils, due to the currents to levitate and accelerate the platform will be significant. Moreover, it is anticipated that special wire, called litz wire, is necessary to reduce eddy current effects when transferring power. This type of wire consists of a large number of individually isolated strands that reduces skin and proximity effects. More is explained about litz wire in Chapter 3, Chapter 4 and Chapter 7. The result of this additional isolation is a reduction of the percentage of copper in the cross-section of the coil, which increases the dissipation for a certain number of Ampère-turns in the coil. To effectively remove the heat from the coils, a ceramic disc is used to transport the heat to the aluminum cooling block. The important characteristic of ceramic is that it does conduct heat very well, but is not electrically conductive.

The purpose of this model is to make a first order estimate of the worst-case temperatures that can occur in the coils while levitating the planar actuator at a certain position. If the actuator is moving, the coils are not continuously energized and the dissipation depends on the duty-cycle. However, for a worst-case estimation, the worst-case dissipation in a single coil is considered and it is assumed that there is no heat flow to other coils, i.e. there is no heat flow in the direction perpendicular to the outer surface of the coil. Finally, the worst-case maximum temperatures are of concern, so there are no heat capacities and transients required in the model. All heat transfer due to radiation is neglected.

A 2D cross-section of a coil with a ceramic disc of aluminum-oxide is shown in Figure 2.18, with the thick lines representing glue layers. The thick dotted lines on each side represent adiabatic boundaries, which prevent heat flow outside the perimeter of the coil. This approach ensures that the heat flow of each coil is not effected by the other coils. The structure in Figure 2.18 is analyzed in a FEM simulation to investigate the heat flows. The values of the parameters that are used in the calculation are listed in Table 2.2. It is assumed that the temperature of the air and the temperature of the coolant water is equal to the ambient temperature in the laboratory. For this assumption to be valid, the heat capacity of the water cooling, which is embedded in a large aluminum heat sink with coolant channels, should be sufficient to remove all the heat with only a slight raise in temperature, i.e. 1 K. The water temperature at the inflow of the coil block is certainly equal to the ambient temperature, since it passes through a heat exchange unit with forced air cooling before the water is pumped back to the coilblock. For the water
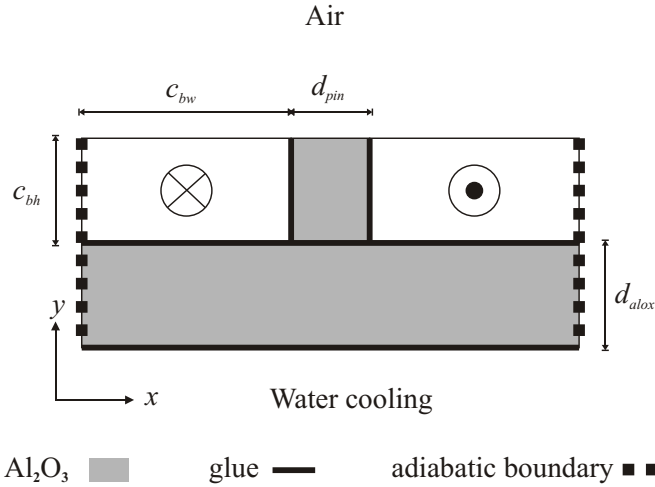
Figure 2.18: 2D cross-section of a coil with a ceramic disc

cooling used in the final setup as discussed in Chapter 7, the flow is 0.2 liters per second and to raise the temperature of this flow by 1 K, a total dissipation in the coils of approximately 830 W is necessary. Since the maximum total dissipation in the coils of the prototype during levitation only is approximately 260 W, The assumption that the water cooling operates at ambient temperature is, therefore, valid.

In Figure 2.19, the steady-state temperature profile is shown according to a FEM simulation in Maxwell 3D 10 ePhysics with the parameters from Table 2.2. From this figure it is clear that most of the heat flow is towards the water cooling and that the hotspot is close to the top surface of the coil. Furthermore, the gradient of the temperature distribution in the ceramic disc is almost zero in the x-direction, which suggests the assumption that there is no heat flow perpendicular to the flow towards the water cooling. Finally, it is clear that the temperature distribution is mainly determined by the limited thermal conductivity of the coil, since its conductivity is a factor 35 lower than the conductivity of the ceramic disc.

A thermal network is used to analyse the heat flows, where three heat flows are assumed to be significant:

1. Heat flow through the top surface of the coil to the air by natural convection Q_1 [W].

2. Heat flow through the bottom surface of the coil and the ceramic disc to the water cooling channel Q_2 [W].

3. Heat flow through the inner surface of the coil, the ceramic pin and the ceramic disc to the water cooling Q_3 [W].

The thermal resistance network that is associated with these three heat flows is shown in Figure 2.20 in which the maximum dissipated heat (P [W]), the three

Table 2.2: Values of heat transfer parameters

Parameter	Value	Unit
k_c	1.0	W/mK
k_g	1.0	W/mK
k_{alox}	35.0	W/mK
h_c	10.0	W/m^{2}K
h_{wc}	1000.0	W/m^{2}K
t_g	0.2	mm
c_{bw}	22.1	mm
c_{bh}	11.3	mm
d_{pin}	8.8	mm
d_{alox}	15.0	mm
A_t	2167	mm^2
A_i	327	mm^2
A_{bp}	67	mm^2
P	27.6	W
T_{amb}	20	$°$C
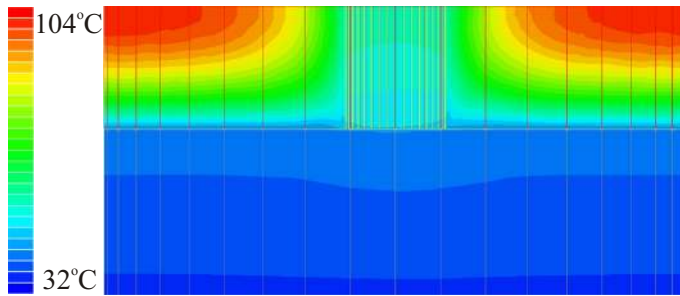
Figure 2.19: Temperature profile of a coil with a ceramic disc according to FEM simulation

heat flows (Q_1, Q_2, Q_3) and the corresponding thermal resistances are shown. Additionally, it is assumed that the heat flow in the ceramic disc has only a component in the y-direction, which is supported by the FEM simulation. Moreover, the water cooling dominates the heat transfer, so it is unlikely that there is a significant heat flow perpendicular to the water cooling surface.

A total of fourteen thermal resistances [W/K] are identified in the network and the parameters are listed in Table 2.2:

1. The thermal resistance of the coil to the top surface:

$$R_{ct} = \frac{c_{bh}}{2k_c A_t},\tag{2.107}$$

where c_{bh} is the coil bundle height, k_c is the conduction coefficient of the coil and A_t is the area of the top surface.

2. The thermal resistance of the top surface to the air by natural convection:

$$R_{nc} \quad = \quad \frac{1}{h_c A_t}, \qquad (2.108)$$

where h_c is the convection coefficient of the top surface.

3. The thermal resistance of the coil to the bottom surface R_{cb} is equal to R_{ct}.

4. The thermal resistance of the glue between the bottom surface of the coil and the ceramic disc:

$$R_{gb1} \quad = \quad \frac{t_g}{k_g A_t}, \qquad (2.109)$$

where t_g is the thickness of the glue layer and k_g is the conduction coefficient of the glue.

5. The thermal resistance of the ceramic disc:

$$R_{cb} \quad = \quad \frac{d_{alox}}{k_{alox} A_t}, \qquad (2.110)$$

where d_{alox} is the height of the ceramic disc and k_{alox} the conduction coefficient of aluminum-oxide.

6. The thermal resistance of the glue between the ceramic disc and the water cooling block R_{gb2} is equal to R_{gb1}.

7. The thermal resistance of the water cooling:

$$R_{wb} \quad = \quad \frac{1}{h_{wc} A_t}, \qquad (2.111)$$

where h_{wc} is the convection coefficient of the water cooling.

8. The thermal resistance of the coil to the inner surface of the coil:

$$R_{ci} \quad = \quad \frac{c_{bw}}{2 k_c A_i}, \qquad (2.112)$$

where A_i is the area of the inner surface, which is assumed equal to the surface of the ceramic pin.

9. The thermal resistance of the glue layer between the coil and the ceramic pin:

$$R_{gi1} \quad = \quad \frac{t_g}{k_g A_i}. \qquad (2.113)$$

10. The thermal resistance of the ceramic pin:

$$R_{ci1} \quad = \quad \frac{1}{k_{alox} \left(2 \frac{A_i}{d_{pin}} + 2 \frac{A_{bp}}{c_{bh}} \right)}, \qquad (2.114)$$

where d_{pin} is the width of the ceramic pin and A_{bp} is the area of the bottom surface of the pin.
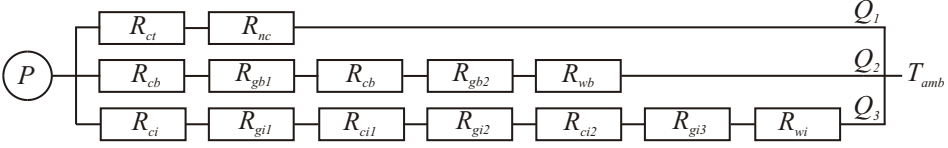
Figure 2.20: Thermal network of a planar actuator coil

11. The thermal resistance of glue between the ceramic pin and the ceramic disc:

$$R_{gi2} = \frac{t_g}{k_g A_{bp}}. \tag{2.115}$$

12. The thermal resistance of the ceramic disc underneath the pin:

$$R_{ci2} = \frac{d_{alox}}{k_{alox} A_{bp}}. \tag{2.116}$$

13. The thermal resistance of the glue layer between the ceramic disc and the water cooling block underneath the pin R_{gi3} is equal to R_{gi2}.

14. The thermal resistance of the water cooling underneath the pin:

$$R_{wi} = \frac{1}{h_{wc} A_{bp}}. \tag{2.117}$$

The total resistances for each heat flow become:

$$R_1 = R_{ct} + R_{nc}, \tag{2.118}$$
$$R_2 = R_{cb} + R_{gb1} + R_{cb} + R_{gb2} + R_{wb}, \tag{2.119}$$
$$R_3 = R_{ci} + R_{gi1} + R_{ci1} + R_{gi2} + R_{ci2} + R_{gi3} + R_{wi}, \tag{2.120}$$

which are associated with Q_1, Q_2 and Q_3, respectively. These heat flows can now be determined:

$$Q_1 = P\frac{R_2 R_3}{R_1 R_3 + R_1 R_2 + R_2 R_3}, \tag{2.121}$$

$$Q_2 = (P - Q_1)\frac{R_3}{R_2 + R_3}, \tag{2.122}$$

$$Q_3 = (P - Q_1)\frac{R_2}{R_2 + R_3}. \tag{2.123}$$

Finally, the temperatures can be calculated:

$$T_{ct} = T_{amb} + Q_1 R_{nc}, \tag{2.124}$$
$$T_{cb} = T_{amb} + Q_2 (R_2 - R_{cb}), \tag{2.125}$$
$$T_{ci} = T_{amb} + Q_3 (R_3 - R_{ci}), \tag{2.126}$$
$$T_{co} = T_{ci} + Q_3 R_{ci}, \tag{2.127}$$
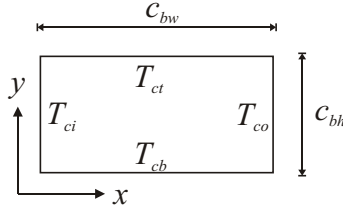
Figure 2.21: Cross-section of the coil bundle

where T_{amb} is the ambient temperature. As defined in Figure 2.21, T_{ct} and T_{cb} are the temperatures at the top and bottom surface of the coil and T_{ci} and T_{co} are the temperatures at the inside and outside surface of the coil, respectively. For a more conservative approach the entire heat transfer can be reduced to a one dimensional problem when the heat transfer Q_3 in the x-direction in the coil is assumed zero ($R_3 = \infty$). The equations for Q_1 and Q_2 then become:

$$Q_1 \quad = \quad P\frac{R_2}{R_1 R_2}, \tag{2.128}$$

$$Q_2 \quad = \quad (P - Q_1), \tag{2.129}$$

while the equations for T_{ct} and T_{cb} remain the same.

To estimate the temperature distribution in the cross-section of the coil, Fourier's law of conduction is used in differential form:

$$q \quad = \quad -k\nabla T, \tag{2.130}$$

where q is the heat flow density in W/m^2, k is the thermal conductivity in W/mK and T the temperature in K. When the temperature is in steady state the following holds:

$$p \quad = \quad \nabla\left(-k\nabla T\right), \tag{2.131}$$

$$p \quad = \quad \frac{P}{A_t c_{bh}}, \tag{2.132}$$

$$k \quad = \quad k_c, \tag{2.133}$$

where p is the heat generation rate in W/m^3. The cross-section of the coil bundle and the temperatures at the surfaces are shown in Figure 2.21, where the bottom-left corner is the origin of the coordinate system. First, only the 1D heat flow in y-direction through the coil is considered. In that case Eq. 2.131 reduces to:

$$p \quad = \quad \frac{d}{dy}\left(-k_c\frac{d}{dy}T\right), \tag{2.134}$$

with solution

$$T(y) \quad = \quad \frac{-P}{2k_c c_{bh} A_t}y^2 + \left(\frac{T_{ct} - T_{cb}}{c_{bh}} + \frac{P}{2k_c A_t}\right)y + T_{cb}. \tag{2.135}$$

The maximum temperature is found by calculating the position at which the derivative of the temperature is zero:

$$\frac{dT}{dy} = \frac{-P}{k_c c_{bh} A_t} y + \left(\frac{T_{ct} - T_{cb}}{c_{bh}} + \frac{P}{2 k_c A_t} \right), \tag{2.136}$$

$$y_{T_{max}} = \frac{(T_{ct} - T_{cb}) A_t k_c}{P} + \frac{c_{bh}}{2}, \tag{2.137}$$

$$T y_{max} = \frac{(T_{ct} - T_{cb})^2 k_c A_t}{2 P c_{bh}} + \frac{T_{ct} + T_{cb}}{2} + \frac{P c_{bh}}{8 k_c A_t}, \tag{2.138}$$

If heat flow Q_3 is assumed zero this is the exact solution of the temperature distribution in the cross-section of the coil. Next the heat flow in both the x- and y-direction is considered, under the assumption that the heat flow in the x-direction is independent from the heat flow in the y-direction. This approximation is not valid, if the 2D temperature distribution in the cross-section of the coil needs to be found. However, the main interest is to find the maximum surface temperatures and the hotspot temperature in the coil, not the exact solution of the temperature distribution in the cross-section. For the x-direction the following holds:

$$T(x) = \frac{-Q_3}{2 k_c c_{bw} A_i} x^2 + \left(\frac{T_{co} - T_{ci}}{c_{bw}} + \frac{Q_3}{2 k_c A_i} \right) x + T_{ci}, \tag{2.139}$$

$$x_{T_{max}} = \frac{(T_{co} - T_{ci}) A_i k_c}{Q_3} + \frac{c_{bw}}{2}, \tag{2.140}$$

$$T x_{max} = \frac{(T_{co} - T_{ci})^2 k_c A_i}{2 Q_3 c_{bw}} + \frac{T_{co} + T_{ci}}{2}. \tag{2.141}$$

Since part of the heat flow (Q_3) occurs in x-direction the heat flow in the y-direction is not P but $Q_1 + Q_2$ in Eqs. 2.136-2.138.

The prediction of the hotspot temperature in the coil with the analytical model is 102°C based upon heat flows Q_1, Q_2 and Q_3. When Q_3 is assumed zero, the predicted hotspot temperature is 105°C. Both predictions agree very well with the FEM calculation shown in Figure 2.19. However, the accuracy of this type of thermal modeling is in the order of 10%, due to the fact that the conductivity of the coil itself (k_c) and the convection coefficients of the water cooling (h_{wc}) and of the natural convection (h_c) are hard to estimate. On the other hand, the large difference in values between the coil conductivity and the ceramics conductivity, as well as the water cooling convection and the natural convection, implies that small errors in the estimate will not effect the end result too much. This makes the model an useful tool to estimate worst-case hotspot temperatures.

2.6 Conclusions

In this chapter, several model have been presented that are used to describe various aspects of the planar actuator. First, a comparison between the virtual work method and Lorentz force method has been made to show which assumptions are necessary in order to be able to use the Lorentz force method only to calculate the forces and torques on the planar actuator.

Second, a model has been presented to calculate the forces and torques on the planar actuator based upon the Lorentz force method using a surface charge representation of the permanent magnets and wire filaments for the coils. The model combines analytical solutions of the Maxwell equations and numerical methods to calculate the forces and torques including the end-effects on the perimeter of the magnet array and has an error of a few percent. The model can also be used to calculate coil currents for a given desired force and torque as well as back-EMF voltages in the coils and controllability aspects of the actuator.

Third, a new commutation algorithm has been presented that is able to calculate the amount of force and torque per Ampère-turn that each coil can generate on the magnet array including the coils on the perimeter of the magnet array in real-time. The accuracy of the commutation algorithm is mainly related to the accuracy of the model used to calculate the look-up tables.

Finally, a thermal model has been presented that is able to estimate the hotspot temperature in the coil. Together, these models can capture all aspects of the planar actuator that are necessary to make a proper design of the planar actuator.

CHAPTER 3
CONTACTLESS POWER TRANSFER

In this chapter, contactless power transfer is analyzed by means of an inductive coupling between a primary coil and a secondary coil. The power transfer should have unlimited stroke in the x-y plane and should allow short stroke movements in the other directions. Moreover, the consequences of mechanical movement and possible integration into the contactless planar actuator are incorporated in the analysis. Furthermore, it is investigated how the power transfer can be continuous and efficient, while moving in the x-y plane. A preliminary design is made to test the models and to verify the practical feasibility. Finally, a power electronics design is presented that can receive and buffer the energy from the secondary coil and convert it to the various DC voltage levels, which are necessary for the operation of the motor power amplifiers and electronics on the secondary side. The models and experiments discussed in this chapter are published in [83, 93, 94, 95].

3.1 CPT Topology

Before a Contactless Power Transfer (CPT) system can be designed the topology of the primary and secondary coil and CPT power supply has to be fixed. For the planar actuator there will be high-inductance coreless coils (> 0.5 mH) on the ground. Each actuator coil is connected to a power amplifier that can supply a current in the coil up to a bandwidth of several kHz. The primary coils of the CPT system have to be integrated into the actuator coil system. There are several options.

1. Actuator coils as primary coils
   Actuator power amplifiers as CPT power supply

2. Actuator coils as primary coils
   Separate CPT power supply.

3. Separate set of primary coils
   Actuator power amplifiers as CPT power supply

4. Separate set of primary coils
   Separate CPT power supply.

Furthermore, the use of iron or ferrites in the system is prohibited, since the levitation of the platform is achieved by repulsive forces between the coils on the ground and the permanent magnets on the platform. The appearance of an iron core will introduce significant attraction forces between the moving platform and the stationary part. In addition, the use of cores will limit the stroke of the system, since they will concentrate the flux within a certain physical structure, thus confining the stroke to the physical magnetic circuit. Therefore, a coreless or aircore inductive coupling is used to transfer the energy. In all cases the secondary

coil is not specified, since it will be optimized depending on the choice of the primary coil system and CPT power supply. Before the options are considered, some other aspects have to be taken into account.

- The moving platform causes the secondary coil(s) to move with respect with the primary coil(s). This will result in a changing coupling between the primary and secondary coil(s).

- To increase the power transfer capability of the CPT system, the inductances of the primary and secondary coil(s) should be compensated by a capacitance. The capacitor can be in series or in parallel with the coil resulting in a resonant circuit, so there is only a resistive load seen by the power supply. If the CPT is operated at its resonant frequency the power rating of the power supply is minimized.

- If a resonant capacitor is chosen parallel with the coil(s) in either the primary or the secondary circuit, the resonant frequency of the total system depends on the coupling between the primary and secondary coil(s) [31].

- The aimed power transfer is 250 W, which is sufficient to power several small actuators including sensors, power electronics and controllers.

Considering the resonant frequency dependence on the coupling in a parallel resonant circuit [31, 49], both the primary and the secondary circuit need a series resonance. This simplifies the CPT power supply since its operating frequency will not have to be adjusted continuously while the platform is moving. Furthermore, a series resonant circuit amplifies the voltage of the power supply [49], which will prevent the amplifier from directly delivering the voltage required to force the high frequency current through the coil.

3.1.1   Steady State Electric Circuit Analysis

In Figure 3.1 the electric circuit is shown for a CPT with a series resonant capacitor for the primary and secondary coil, where V_1 [V] is the RMS voltage of the power supply, I_1 [A] the RMS current supplied by the power supply, I_2 [A], the RMS current induced in the secondary circuit. C_1 [F] and C_2 [F] are the series resonant capacitance in the primary and secondary circuit, respectively, R_1 [Ω] the resistance of the primary coil, R_2 [Ω] is the resistance of the secondary coil, L_1 [H] and L_2 [H] are the self inductance of the primary and secondary coil respectively, k [-] is the inductive coupling factor between the primary and secondary coil and R_L [Ω] is the resistance of the load. Simplified versions of the circuit are shown in figure 3.2, where Z_R [Ω] is the reflected load of the secondary circuit on the primary circuit and Z_1 [Ω] is the load seen by the power supply.

The equations for this system for an AC voltage source with angular resonant frequency $\omega_0 = 2\pi f_0$ in rad/s are:

$$M = k\sqrt{L_1 L_2}, \tag{3.1}$$

$$V_1 = R_1 I_1 + j(\omega_0 L_1 - \frac{1}{\omega_0 C_1})I_1 - j\omega_0 M I_2, \tag{3.2}$$

$$j\omega_0 M I_1 = (R_2 + R_L)I_2 + j(\omega_0 L_2 - \frac{1}{\omega_0 C_2})I_2, \tag{3.3}$$
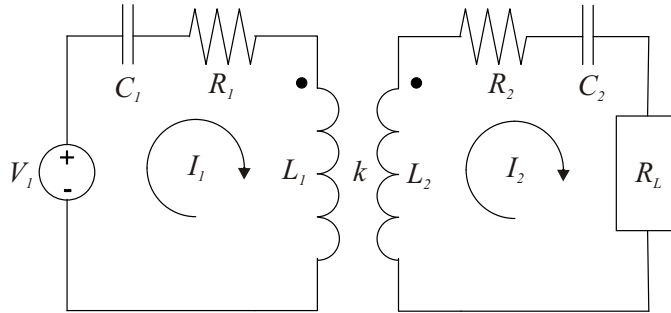
Figure 3.1: Electric circuit of the aircore contactless power transfer system
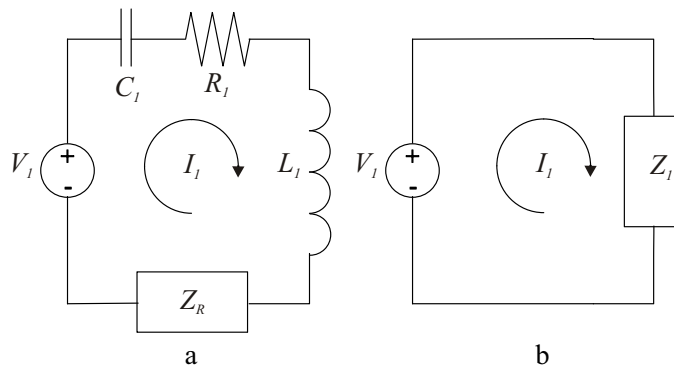
Figure 3.2: Simplified electric circuits of the aircore contactless power transfer system

where M is the mutual inductance of the primary and secondary coil.

The impedance Z_2 [Ω] of the secondary circuit is:

$$Z_2 \quad = \quad (R_2 + R_L) + j(\omega_0 L_2 - \frac{1}{\omega_0 C_2}). \tag{3.4}$$

The reflected impedance of the secondary circuit on the primary circuit as shown in Figure 3.2a can now be calculated.

$$Z_R \quad = \quad \frac{\omega_0^2 M^2}{Z_2}$$

$$Z_R \quad = \quad \frac{\omega_0^2 k^2 L_1 L_2}{(R_2 + R_L)^2 + (\omega_0 L_2 - \frac{1}{\omega_0 C_2})^2}$$

$$\left((R_2 + R_L) - j(\omega_0 L_2 - \frac{1}{\omega_0 C_2}) \right). \tag{3.5}$$

To eliminate the reflected reactance C_2 must be suitably chosen:

$$C_2 \quad = \quad \frac{1}{\omega_0^2 L_2}, \tag{3.6}$$

$$Z_R \quad = \quad \frac{\omega_0^2 k^2 L_1 L_2}{(R_2 + R_L)}. \tag{3.7}$$

Now the load on the power supply Z_1 (Figure 3.2b) can be calculated.

$$Z_1 \quad = \quad R_1 + j(\omega_0 L_1 - \frac{1}{\omega_0 C_1}) + Z_R \tag{3.8}$$

Similarly to C_2, the capacitance of C_1 is chosen to eliminate the reactance of the load on the power supply:

$$C_1 \quad = \quad \frac{1}{\omega_0^2 L_1}, \tag{3.9}$$

$$Z_1 \quad = \quad R_1 + \frac{\omega_0^2 k^2 L_1 L_2}{(R_2 + R_L)}. \tag{3.10}$$

By substituting Eq. 3.6 into Eq. 3.3 the relation between I_1 and I_2 becomes:

$$I_2 \quad = \quad G I_1, \tag{3.11}$$

$$G \quad = \quad \frac{j\omega_0 M}{R_2 + R_L + j(\omega_0 L_2 - \frac{1}{\omega_0 C_2})}$$

$$G \quad = \quad j\frac{\omega_0 M}{R_2 + R_L}, \tag{3.12}$$

where $|G|$ [-] is a gain relating the current I_2 to I_1 and Eq. 3.12 shows that I_2 leads I_1 by 90 degrees. Now the power that is transferred to the load P_{out}, the power supplied by the power supply P_{in} and the efficiency of the total system η [-] can

be calculated:

$$P_{in} = I_1^2 Z_1, \tag{3.13}$$

$$P_{out} = |G|^2 I_1^2 R_L, \tag{3.14}$$

$$\eta = \frac{P_{out}}{P_{in}} = \frac{|K|^2 R_L}{Z_1},$$

$$\eta = \frac{R_L \omega_0^2 k^2 L_1 L_2}{(R_1 R_2 + R_1 R_L + \omega_0^2 k^2 L_1 L_2)(R_2 + R_L)}. \tag{3.15}$$

By rewriting Eq. 3.14 it is possible to calculate the voltage V_1 and the current I_1 of the power supply for a desired power on the load:

$$I_1 = \sqrt{\frac{P_{out}}{|G|^2 R_L}}, \tag{3.16}$$

$$V_1 = \sqrt{\frac{P_{out} Z_1^2}{|G|^2 R_L}}. \tag{3.17}$$

From Eq. 3.6 and 3.9 it is clear that the resonant frequency of the circuit does not depend on the coupling, since the choice of the resonant capacitors only depends on the inductance of the coils. In reality the two series resonant capacitors will not cancel the inductances of the primary and secondary coil completely. Therefore, the load seen by the power supply will not be purely resistive. The load seen by the power supply Z_1 does depend on the coupling. This implies that the power transfer capability of the system depends on the coupling as well.

3.1.2 CPT Topology Selection

To study the effect on efficiency of each parameter in Eq. 3.15 each parameter has been varied while others were kept constant. The nominal values of each parameter are shown in Table 3.1. In Figure 3.3 the efficiency is plotted vs. the variation of each parameter. In reality, it is not possible to change only a single parameter, e.g. if the inductance of a coil is increased by adding more turns, its resistance will increase as well. However, it does give a feeling of the influence of each parameter on the power transfer efficiency.

It can be concluded that a higher inductance and higher frequency increase the efficiency, R_1 and R_2 should be sufficiently small, k should be as high as possible and that there is an optimal R_L. The optimal R_L can be found by differentiating Eq. 3.15 with respect to R_L:

$$\frac{d\eta}{dR_L} = \frac{\omega_0^2 M^2 (R_1 R_2^2 + R_2 \omega_0^2 M^2 + R_1 R_L^2)}{(R_2 + R_L)^2 (R_1 R_2 + R_1 R_L + \omega_0^2 M^2)^2}. \tag{3.18}$$

Next, the derivative is set equal to zero and solved for R_L to find the optimum:

$$R_L^{opt} = \frac{1}{R_1} \sqrt{R_1 R_2 (R_1 R_2 + \omega_0^2 M^2)} \tag{3.19}$$

Therefore, the actuator power amplifiers cannot be used as power supply for the CPT, since they only operate up to several kHz. A separate high-frequency

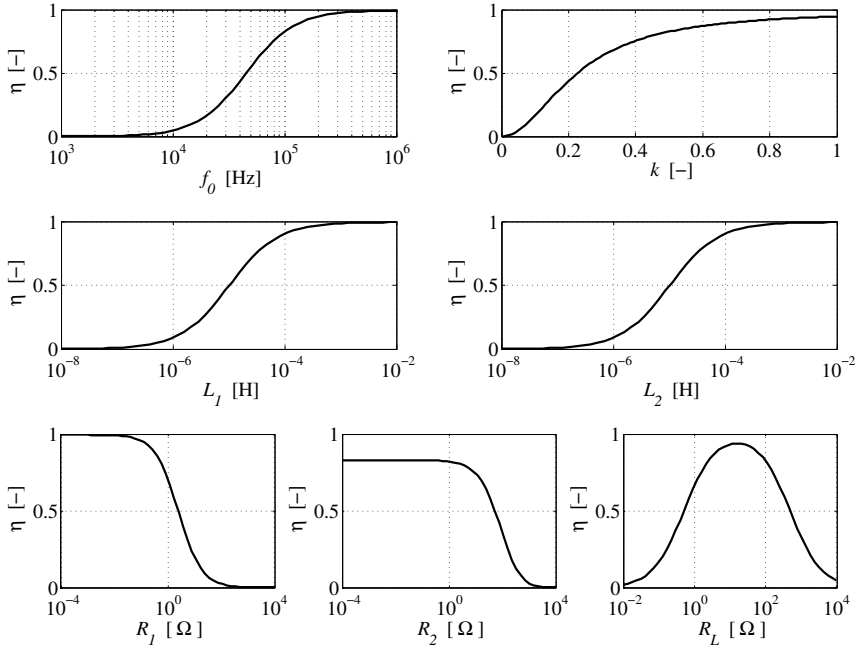Figure 3.3: Effect of electric circuit parameters on efficiency

Table 3.1: Nominal values of electric circuit parameters used in Figure 3.3

Parameter	Value	Dimension
ω_0	$2\pi f_0$	rad s^{-1}
f_0	100	kHz
L_1	50	μH
L_2	50	μH
k	0.5	-
R_L	100	Ω
R_1	0.5	Ω
R_2	0.5	Ω

power supply must be used that operates at a frequency higher than approximately 50 kHz.

Nevertheless it still might be possible to use the actuator coils as primary CPT coils. An actuator coil typically has a high inductance (>0.5 mH) and from Eq. 3.12-3.15, it can be concluded that a higher inductance increases efficiency. However, the transfer of large amounts of power at a high frequency using a high inductance coil requires a special design of the primary coil.

A high voltage will be necessary to force the current in the coil. The voltage will partly be generated by the power supply, but mostly by the resonance of the capacitor and the coil. The voltage over the coil and the capacitor can be several kV which requires special attention in the design. The power supply will be limited to approximately $+/-$ 200 V which is the maximum operating voltage of commonly available power MOSFETs.

In addition, high frequency effects such as skin effect and especially proximity effect will be large for a high inductance coil [48] at higher operating frequencies. These effects will have to be taken into account by using litz wire. If the disadvantages of using a high inductance actuator coil (high voltage, large skin and proximity effect) as primary coil can be managed, it is preferable over using a separate set of primary coils for the CPT system, since it is more restrictive for the actuator design. Therefore, the chosen CPT topology is the second topology mentioned: actuator coils as primary coils with separate CPT power supply.

3.1.3   Geometry of the CPT coils

To verify the feasibility of the use of actuator coils as primary coils, a preliminary design of a CPT system is tested. First, a possible primary coil is chosen, which can also be used as actuator coil. The actuator coil design is not yet fixed, since the shape and size of the actuator coil will depend on the final planar actuator design, so the choice of the actuator coil is somewhat arbitrary.

The actuator coil is chosen keeping in mind that the planar actuator will have a long stroke movement in a 2D plane. Therefore, it is convenient to start with a shape that is symmetrical in 2D: a square for instance. The cross-section of the coil bundle is chosen square as well and large enough to fit a couple of hundred windings to create a high-inductance coil (>0.5 mH). The corresponding dimensions of the primary coil and their values in Figure 3.4 and Table 3.2 respectively.

From literature ([35, 36, 37]), it is known that flat spiral coils have good coupling and that they are tolerant to misalignments of the primary and secondary coil centers. However, in this case of a moving platform the secondary coil will move over several primary coils and, depending on the trajectory of platform, different coils will be switched on as CPT primary coil and as actuator coil. From Eq. 3.10, it is clear that a changing coupling will result in a changing impedance seen by the power supply. In addition, the coupling should be as high as possible to improve efficiency and the maximum output power. Therefore, the requirements of the secondary coil are the following:

1. Maximize the coupling of the primary and secondary coil.

2. Minimize the dependence of the coupling on the position of the secondary coil with respect to the primary coil.
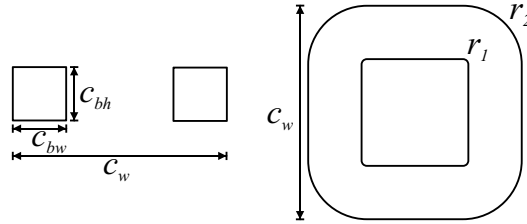
Figure 3.4: Primary and secondary coil geometry parameters

Table 3.2: Dimensions of primary and secondary coil

| | Primary coil | | Secondary coil | |
Parameter	Value	Dimension	Value	Dimension
c_w	60.0	mm	130.0	mm
c_{bw}	10.0	mm	30.0	mm
c_{bh}	10.0	mm	2.0	mm
r_1	1.0	mm	1.0	mm
r_2	11.0	mm	31.0	mm

To keep the total number of secondary coils in the final design limited, the range of each secondary coil should be sufficient to move from one primary coil to the next while allowing continuous transfer of power from one or more primary coils during its movement. If this is not possible, there should be multiple secondary coils that are spatially shifted in phase, which will only add more complexity and weight to the final design.

The primary coil is modeled in the finite element package Maxwell 10 3D Optimetrics from Ansoft [30]. Several secondary coil shapes are evaluated e.g. round, square and rectangular. The highest coupling is attained when the secondary coil is very flat, confirming the literature regarding spiral coils. The shape with the highest coupling is also a square. The maximum coupling is obtained when the secondary coil has approximately the same size as the primary coil (up to 0.62). However, in this configuration the coupling degrades very fast when the centers of the secondary and primary coil are misaligned. The worst-case coupling position for the secondary coil is when one quarter of the secondary coil overlaps each primary coil. The challenge is to find a shape of the secondary coil that has a high and fairly constant coupling while moving from one primary coil to the next. Several geometries have been tested by doing a parametric search in Maxwell 3D Optimetrics and a promising geometry is shown in Figure 3.5. The dimensions of the secondary coil are listed in Table 3.2, according to the parameter definitions in Figure 3.4.

The drawing in Figure 3.5 shows one secondary coil above nine primary coils. The black square shows the area in which the center of the secondary coil can move while maintaining good coupling with the middle primary coil. The secondary
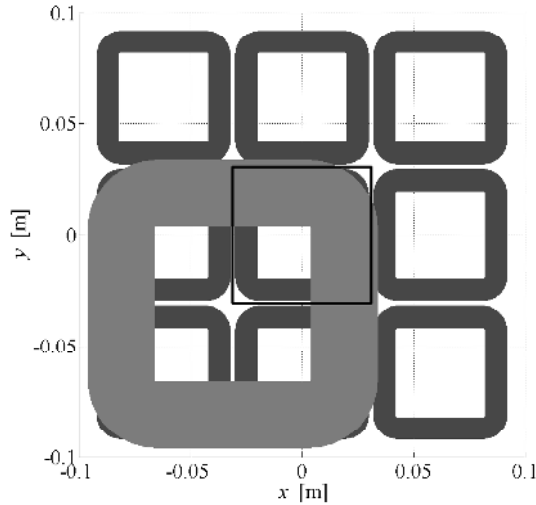
Figure 3.5: Secondary coil above 9 primary coils

Table 3.3: Measured electric circuit parameters of the CPT setup

	Primary 1	Primary 2	Primary 3	Secondary
Inductance	980 μH	944 μH	878 μH	49 μH
Resistance	5.6 Ω	5.7 Ω	5.1 Ω	0.3 Ω
Capacitance	0.73 nF	0.76 nF	0.82 nF	14.1 nF
Resonance	190 kHz	190 kHz	189 kHz	191 kHz

coil is situated in the bottom-left corner of the area of interaction with the middle primary coil. The coupling between the primary coil and the secondary coil within that area is calculated with Maxwell 3D 10 Optimetrics.

Three primary coils and one secondary coil were manufactured and matched with capacitors according to Eqs. 3.6 and 3.9 to obtain a resonant frequency of ca. 190 kHz. The frequency has been chosen this high to obtain an aimed efficiency above 90% within the voltage limits of the power electronics. Another practical problem is the availability of capacitors, which make only a limited number of values practical. The electric circuit parameters of these four circuits are listed in Table 3.3. The coupling with primary coil 1 and the secondary coil is measured at different positions and compared to the simulated values using FEM. The results are shown in Figure 3.6, where (0,0) corresponds with the center of the black square in Figure 3.5, which is the position where the centers of the primary and secondary coil are aligned. Figure 3.6 shows that the FEM predictions are very close to the measured values.
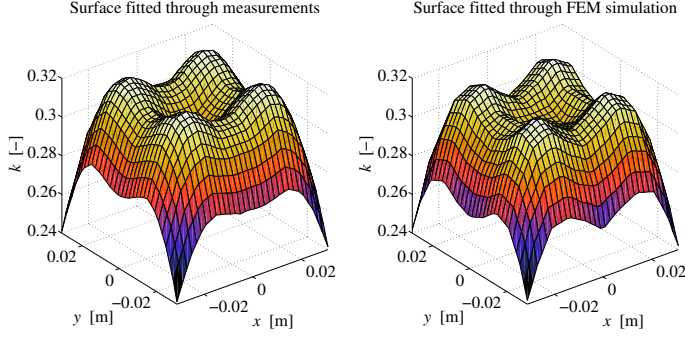
Figure 3.6: Coupling between primary and secondary coil

3.2 CPT Simulations

3.2.1 Simulation of Electric Circuit Differential Equations

To simulate the electrical transient, first the differential equations of the system shown in Figure 3.1 have to be defined:

$$u_1 = R_1 i_1 + L_1 \frac{di_1}{dt} + \frac{1}{C_1} \int_0^t i_1 d\tau - M \frac{di_2}{dt}, \tag{3.20}$$

$$M \frac{di_1}{dt} = (R_2 + R_L) i_2 + L_2 \frac{di_2}{dt} + \frac{1}{C_2} \int_0^t i_2 d\tau, \tag{3.21}$$

where i_1 [A] is the current in the primary circuit, i_2 [A] the current in the secondary circuit and u_1 [V] the voltage supplied by the power supply, which are all functions of time. The differential equations are transformed to a state-space notation for simulation of the electrical transient. First, the state is defined:

$$\underline{x} = \begin{bmatrix} x_1 & x_2 & x_3 & x_4 \end{bmatrix}^T, \tag{3.22}$$

$$\begin{bmatrix} x_1 \\ x_2 \\ x_3 \\ x_4 \end{bmatrix} = \begin{bmatrix} \int_0^t i_1 d\tau \\ i_1 \\ \int_0^t i_2 d\tau \\ i_2 \end{bmatrix}, \tag{3.23}$$

$$\underline{u} = \begin{bmatrix} u_1 \end{bmatrix}, \tag{3.24}$$

$$\underline{y} = \begin{bmatrix} i_1 & i_2 \end{bmatrix}^T. \tag{3.25}$$
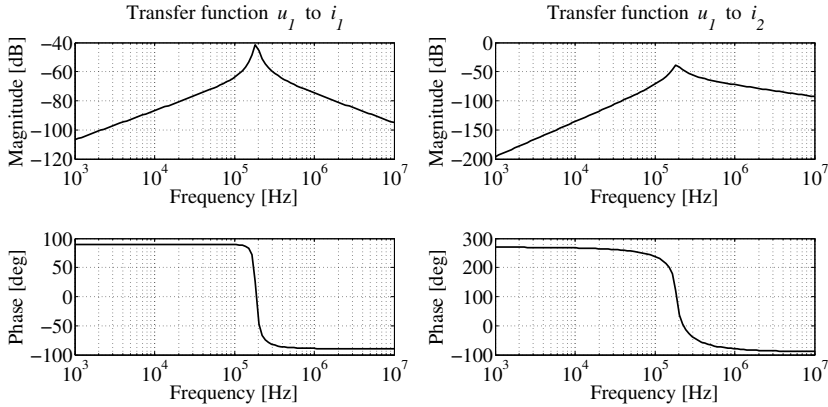
Figure 3.7: Transfer functions of CPT system

Next, the state-space model is calculated:

$$\underline{A} = \begin{bmatrix} 0 & 1 & 0 & 0 \\ \frac{L_2}{C_1\alpha} & \frac{L_2 R_1}{\alpha} & \frac{M}{C_2\alpha} & \frac{M(R_2+R_L)}{\alpha} \\ 0 & 0 & 0 & 1 \\ \frac{M}{C_1\alpha} & \frac{M R_1}{\alpha} & \frac{L_1}{C_2\alpha} & \frac{L_1(R_2+R_L)}{\alpha} \end{bmatrix}, \tag{3.26}$$

$$\underline{B} = \begin{bmatrix} 0 & \frac{L_2}{\alpha} & 0 & \frac{M}{\alpha} \end{bmatrix}^T, \tag{3.27}$$

$$\underline{C} = \begin{bmatrix} 0 & 1 & 0 & 0 \\ 0 & 0 & 0 & 1 \end{bmatrix}, \tag{3.28}$$

$$\underline{D} = \begin{bmatrix} 0 & 0 \end{bmatrix}^T, \tag{3.29}$$

$$\alpha = M^2 - L_1 L_2. \tag{3.30}$$

The power supply is a voltage source that outputs a square-wave voltage u_1. A square-wave is chosen, since the maximum voltage is less than for a sine wave to obtain the same RMS value and to transfer the same amount of power. In addition, a square-wave is easier to obtain. Moreover, a resonant circuit is used, so the current will be approximately sinusoidal, since all other frequencies will be filtered out by the resonance. This is clear when the transfer functions of u_1 to i_1 and i_2 are studied, which are shown in Figure 3.7. These transfer functions have been calculated using the parameters of primary circuit 1 with the secondary circuit.

To transfer 250 W of power to a 50 Ω resistor, the needed RMS sinusoidal voltage is calculated from Eq. 3.17. Next, the 191 kHz square-wave voltage is calculated by multiplying the RMS sine wave voltage by $\sqrt{2}\frac{\pi}{4}$. A square-wave voltage u_1 is supplied by the power supply for 0.35 ms and the corresponding input and output power are calculated by solving the state-space model. Again the parameters of primary circuit 1 and the secondary coil, listed in Table 3.3, are used in the simulation. The frequency of the square-wave is 1 kHz higher than
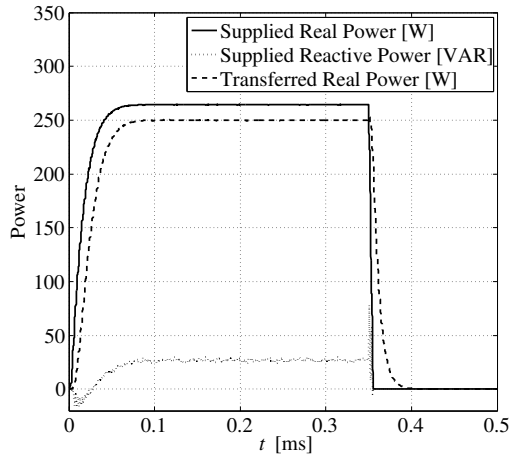
Figure 3.8: Real and reactive power from the square-wave voltage source and transferred real power to the load resistor

the resonant frequency of the circuit, since the square-wave voltage source needs an inductive load to switch properly. This results in a small phase shift between the square-wave voltage and the current, which means that, besides real power, there is some reactive power in the system as well. The reactive power does not contribute to the power transfer. The real and reactive power from the square-wave voltage source and the transferred real power to the load resistor (there is no reactive power in case of a resistor) are shown in Figure 3.8. Within 70 μs the power transfer is reaching steady state and the transferred real power is indeed 250 W with an efficiency of approximately 95 %, which does not include losses in the power electronics.

3.2.2 Simulation of the Combined Electrical and Mechanical Transient

The platform with the secondary coil is moving and the coupling between the primary and secondary coil will change during this movement. Therefore, not all parameters of the differential equation in the previous section are constant. The coupling factor k will change depending on the position according to Figure 3.6, which shows the coupling for different positions. The impedance Z_1 seen by the power supply will change as well, so the voltage u_1 of the power supply will have to be adjusted in order to keep transferring the desired power.

The best way to control the transferred power is by controlling the current i_2 in the secondary coil. However, if the current in the secondary coil is not known, the system is not observable and it is not possible to control current i_2 explicitly by adjusting the square-wave voltage u_1 using the state-space model. Since the moving load is not connected to the fixed world it is not likely that data about i_2 is available for the power supply.

From the steady-state equations it is possible to relate the RMS voltage V_1 to
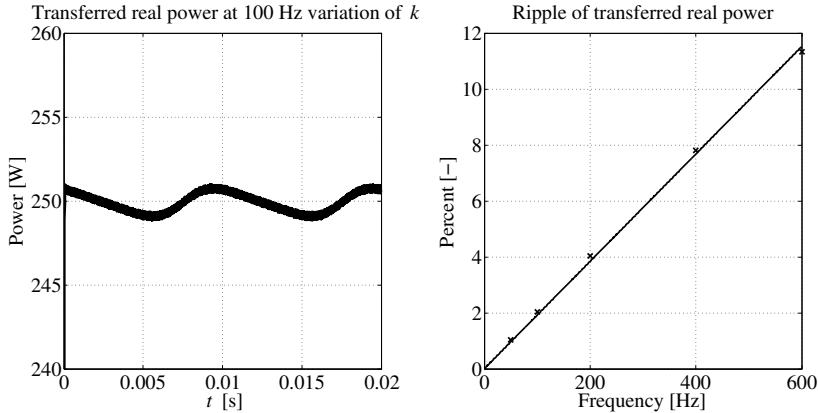
Figure 3.9: Ripple of transferred real power

the transferred power (Eq. 3.17). In order to use this equation the system has to be in steady state. In the previous section it is shown that it takes 70 μs for the system to reach steady state, while operating at 191 kHz. The variations of k are related to mechanical movement which will be in a frequency range typically up to 50-100 Hz. It would, therefore, be obvious to assume that the power transfer remains quasi-static due to the relatively slowly changing k. If this is valid, then the steady-state equation Eq. 3.17 can be used to adjust the voltage.

To test this assumption, the state-space model is solved with a sinusoidally time-varying k at different frequencies with the same parameters used in the previous section. The minimum and maximum of the sinusoidal variation of k are the values from Figure 3.6 ($0.24 < k < 0.32$).

The voltage is adjusted according to Eq. 3.17 to compensate for the variations of k and the result is shown in Fig 3.9. The average power transfer is not completely without transient, since the changing k results in a ripple of the transferred power. From the plot it can be concluded that at low-frequency variations of k, the power transfer can be assumed quasi-static.

3.2.3 Forces between the Primary and Secondary Coil

Since the contactless power transfer system is supposed to be used in high precision motion systems, it is important to investigate possible disturbance forces. The force between two coils can be calculated by the gradient of the mutual inductance between the coils as [26]:

$$\underline{F} \quad = \quad -i_1 i_2 \nabla M \tag{3.31}$$

The maximum force between the coils is obtained when the absolute value of the product of i_1 and i_2 reaches its maximum. The gradient of the coupling is calculated using FEM simulations within the area of the black square of Figure. 3.5. During the simulation in Section 3.2.1, the maximum absolute value of the product of i_1 and i_2, when transferring 250 W, is 3.44 A^2. The gradient of the coupling
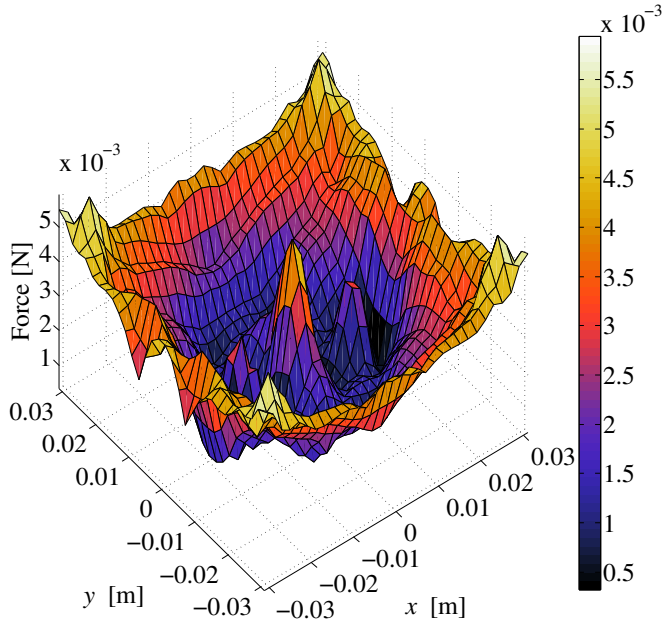
Figure 3.10: Amplitude of the force vector between primary and secondary coil

within the area of the black square is multiplied by 3.44 and the 2-norm of the result is taken to retrieve the amplitude of the force vector acting between the primary and secondary coil.

In Figure 3.10, the force vector amplitude is shown within the area of the black square of Figure. 3.5. The force amplitude is never higher than 6 mN. Moreover, the product of i_1 and i_2 is a sine function with a frequency that is twice the frequency of the square-wave power supply. In this case, it implies that the force oscillates between +/-6 mN at a frequency of 382 kHz. From the low force amplitude and especially the high frequency of the force amplitude oscillation, it can be concluded that the CPT system will not cause any noticeable mechanical disturbance on the moving part of the machine.

3.3   Experimental Verification of the CPT

3.3.1   Description of the Test Setup

An experimental setup was built to test the CPT design, which consists of an array of three stationary primary coils that are fixed in a row on top of a ceramic structure. The ceramic structure is used to allow heat from the coils to be conducted to the iron base frame and at the same time to prevent eddy current losses in the iron base frame.

The primary coils are made of litz wire. Each bundle of litz wire consists of 60 individually isolated strands of 71 μm and the strands are wrapped together with
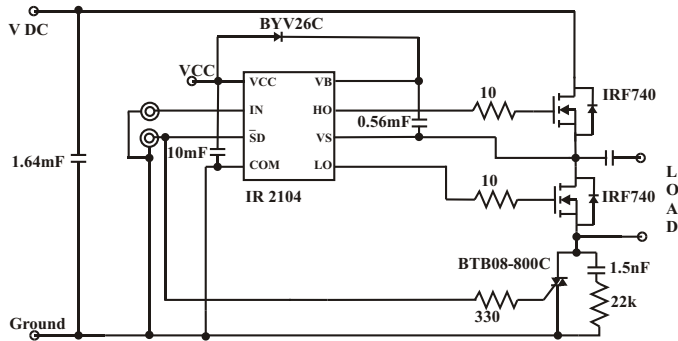
Figure 3.11: Half-bridge power supply of the primary resonant circuit

a layer of cotton. The strand size has been chosen after examining the AC losses using the method described in [48]. The turns of the coil are fixed by glue that has been applied during the winding process. Approximately 120 turns fitted in the cross-section, resulting in a 0.3 filling factor.

Each primary coil is connected in series with a resonant capacitor. Each resonant circuit is driven by a separate half-bridge power supply shown in Figure 3.11, that applies a square-wave voltage of 191 kHz over the resonant circuit.

The secondary coil is made of litz wire with 100 strands of 100 μm and is fixed onto a ceramic plate that is bolted to the mover of a linear actuator. Again ceramic material is used for heat conduction and the minimization of eddy current losses. The linear actuator can move the secondary coil over the three primary coils. The position of the secondary coil with respect to the array of primary coils is measured by the encoder of the linear actuator. A picture of the experimental setup is shown in Figure 3.12.

An overview of the electric circuit parameters of the primary coils, the secondary coil and the corresponding series capacitors can be found in Table 3.3. The secondary circuit is then connected to a full-bridge diode rectifier with a 100 μF capacitor to generate a DC output. The DC output of the rectifier is connected to a 50 Ω resistor.

All subsystems are connected to a DS1103 dSpace system running the control program at 8 kHz. This way the DC bus voltage of the primary coil power supplies is controlled as well as which of the primary coil power supplies is enabled. The position of the linear actuator is controlled using a PID controller running on the dSpace system. Depending on the position of the linear actuator the dSpace system enables the primary coil that is completely overlapped by the secondary coil.

The primary coil activation is controlled by a multi-port switch. The multi-port switch has four active coil states, state 1 enables the power supply of the first primary coil, state 2 and 3 enable the power supply of the second and third primary coil, respectively. State 4 disables all power supplies and this state is used for switching from one power supply to the next.
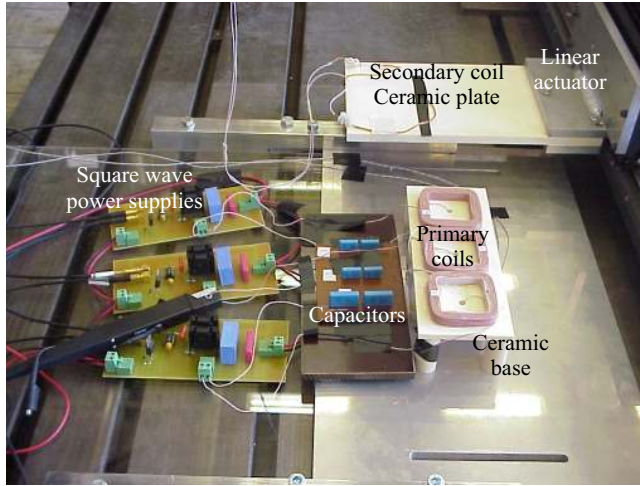
Figure 3.12: Picture of experimental CPT setup

When the secondary coil moves out of range of primary coil 1 (active coil state 1), the active supply is switched off (active coil state 4) and one sample time later the second supply is switched on (active coil state 2). For one sample time, none of the power supplies is active (active coil state 4), which is necessary to allow the triac in the power supply that is switched off to block the circuit after the current in the resonant circuit is damped. The triac prevents current flowing through the circuit due to the back-EMF induced by a neighboring active primary coil, when the power supply is switched off. There is no other control mechanism in the power electronics, and the system operates without any measurement on the secondary site, except for the position of the secondary coil.

3.3.2 Results

The secondary coil is moving over all three primary coils following a sinusoidal position reference, which represents a total displacement of 18 cm (i.e. the amplitude of the sinewave is 9 cm). The frequency of the sinusoidal position reference is 2 Hz, so in one second the secondary coil makes two cycles (one cycle implies moving from primary coil 1 over primary coil 2 to primary coil 3 and back). The coupling between the primary coils and the secondary coil is measured along the trajectory. In Figure 3.13 the coupling between the three primary coils and the secondary coil is shown along the 18 cm of the secondary coil trajectory.

The voltage and current from the DC bus supply as well as the voltage and current to the 50 Ω load resistor are measured and shown in Figure 3.14 and 3.15, respectively. The cycle is clearly visible from the Active Coil plot, which represents the state of the active coil multi-port switch. The secondary coil reaches a maximum speed of 1.1 m/s over the second primary coil. Due to this speed the secondary coil is in range of the second primary coil for only 60 ms. When the active coil state reaches 4, all power supplies are switched off and no current is drawn from the DC bus supply.
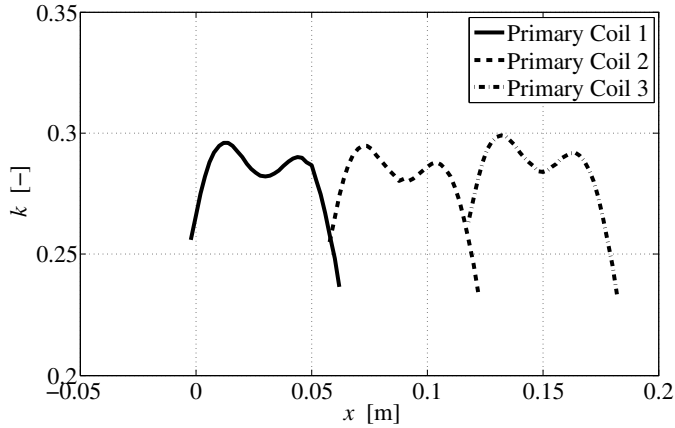
Figure 3.13: Measured coupling between the three primary coils and the secondary coil

Table 3.4: Measured values of the CPT to a 50 Ω load resistor

Variable	RMS Value	Dimension
V_{DCbus}	452	V
I_{DCbus}	0.66	A
P_{in}	301	W
V_{load}	115	V
I_{load}	2.3	A
P_{out}	265	W
η	88	%

By calculating the RMS values of the voltages and currents the power from the DC bus supply P_{in} as well as the power to the 50 Ω load resistor P_{out} and the efficiency η according to Eq. 3.15 can be calculated. This calculation includes losses in the power electronics. The values are listed in Table 3.4.

The variation in coupling is clearly visible in the current and voltage waveforms of the load. This suggests that the power transfer can be further smoothed by measuring the coupling and changing the voltage of the DC bus supply according to Eq. 3.17. Therefore, a step-down converter with a bandwidth of 1 kHz is connected to the DC bus supply to regulate the DC bus voltage by changing the duty-cycle of a 25 kHz PWM signal. The step-down converter could operate up to 200 V, so the maximum power is only 50 W.

From comparing the voltage and current waveforms from Figure 3.15 and Figure 3.17, it is clear that the variation of coupling can be compensated by adjusting the DC bus voltage accordingly, as is shown in Figure 3.16. The ripple of the
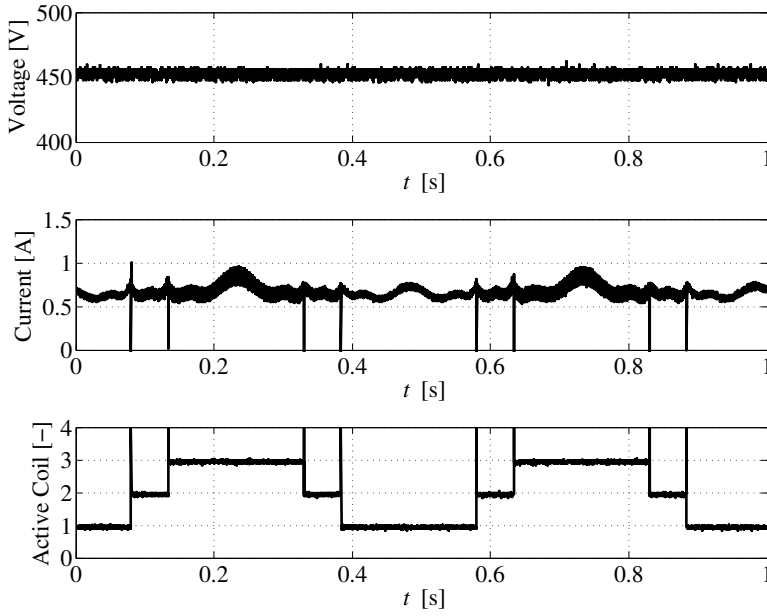
Figure 3.14: Measured voltage, current and active primary coil of the DC bus supply

Table 3.5: Measured values of the CPT to a 50 Ω resistor with DC bus voltage compensation

Variable	RMS Value	Dimension
V_{DCbus}	187	V
I_{DCbus}	0.27	A
P_{in}	50	W
V_{load}	49	V
I_{load}	0.95	A
P_{out}	47	W
η	93	%
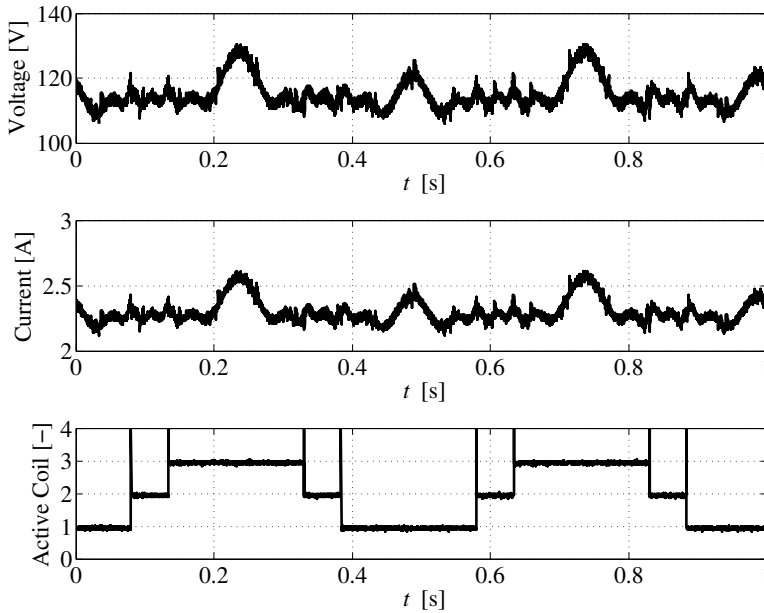
Figure 3.15: Measured voltage, current and active primary coil of the 50 Ω load resistor

voltage and current of the 50 Ω load resistor has been greatly reduced.

3.3.3   Durability of the CPT System

The durability of the CPT system is determined by the thermal properties of the system and the quality of the isolation between the windings. The voltage over the primary coil when transferring 265 W can be calculated by:

$$u_{coil} \quad = \quad L_1 \frac{di_1}{dt}. \tag{3.32}$$

Since the primary circuit is powered by a half-bridge power supply, the RMS voltage over the primary circuit is half the RMS value of the DC bus voltage. The power drawn from the DC bus supply is almost equal to the power put into the primary circuit, so the RMS current through the primary coil is twice the current from the DC bus supply. From the value of I_{DCbus} in Table 3.4 it follows that the peak value of the primary coil voltage equals ($\sqrt{2}\, 4\pi f_0 L_1 I_{DCbus} =$) 2.1 kV. Each coil has about 120 windings so each winding has a peak voltage drop of 18 V, which is rather high. This has to be taken into account when the final design is chosen, both by using a proper number of windings and by selecting the right isolation of the wires.

The resistance of the primary circuit (R_1) is about 5.5 Ω. The ohmic losses P_{loss} [W] in the primary circuit can be calculated by:

$$P_{loss} \quad = \quad (2I_{DCbus})^2 R_1, \tag{3.33}$$
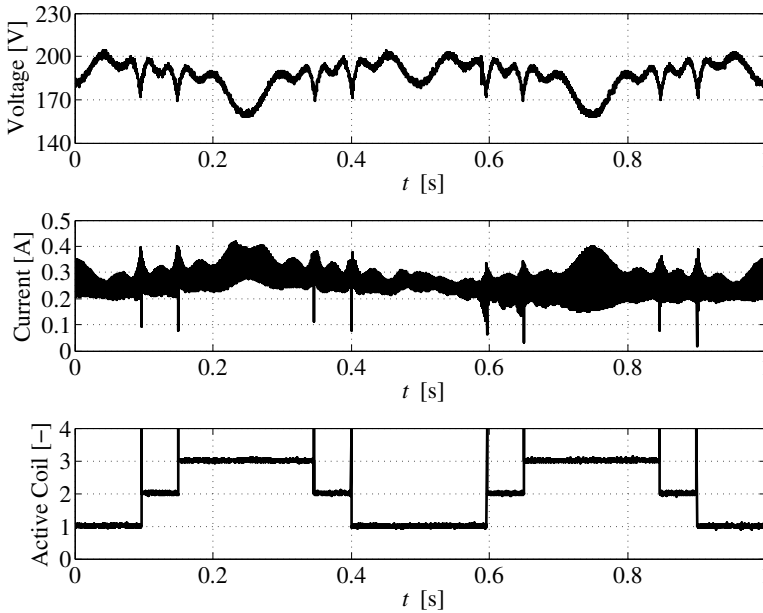
Figure 3.16: Measured voltage, current and active primary coil of the DC bus supply with DC bus voltage compensation

which equals about 10 W of heat that is dissipated in the active primary coil. On the secondary side the losses in in the secondary coil are negligible since the resistance of the secondary circuit is only 0.3 Ω, resulting in a loss of $0.3 \times 2.3^2 = 1.6$ W. Moreover, due to the planar geometry of the secondary coil, the generated heat can easily be removed by either convection or conduction.

To investigate the durability of the CPT system the power transfer is continued for 30 minutes, while transferring 250 W continuously to the load. Meanwhile the temperatures of the primary coils, the resonant capacitors and the power electronics is monitored as is the power that is transferred to the 50 Ω load resistor. A fan is installed for additional cooling by blowing air over the power supplies and coils and the temperature of the components is monitored using a thermal camera. The secondary coil is moved over the three primary coils with the same sinusoidal trajectory as is discussed in the previous section. The frequency of the sinusoidal trajectory is lowered from 2 Hz to 0.5 Hz in order to give the thermal camera time to adjust during the movement of the secondary coil. This implies that the outer coils will dissipate most of the heat, since the second primary coil is only active for 0.48 s of each 2 s cycle.

In Figure 3.18, the input power from the DC bus supply and the output power, transferred to the 50 Ω load resistor is shown during the 30 minute experiment. The efficiency of the power transfer varies between 88.8 % and 89.8 % and the total energy transferred is 450 kJ. In the same figure, the hotspots in the components of the setup, i.e. primary coils, resonant capacitors and power electronics components
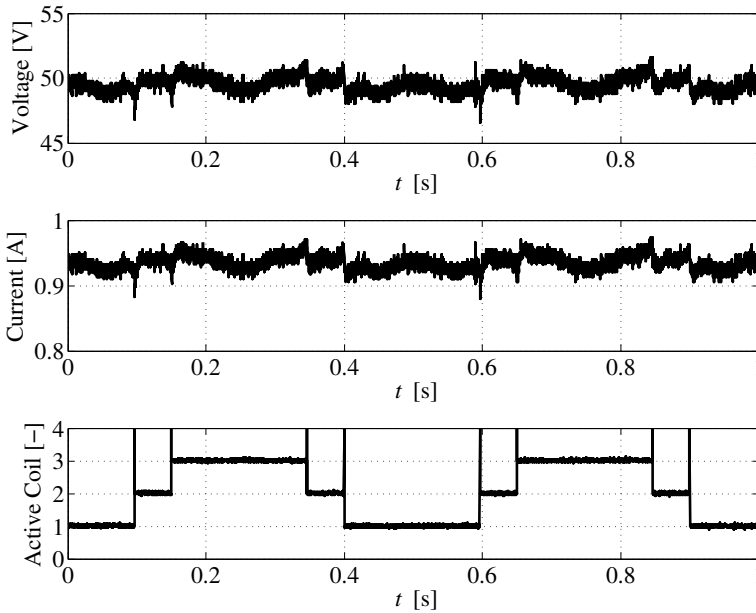
Figure 3.17: Measured voltage, current and active primary coil of the 50 Ω load resistor with DC bus voltage compensation

of the half-bridge power supply, during the measurement are shown. The highest temperature measured is 37.6 °C at the surface of the outer primary coil. The coils reach steady-state temperature after approximately 15 minutes. The power electronics components and resonant capacitors reach steady-state temperature earlier.

From this experiment it can be concluded that there are no thermal problems to be expected from the CPT power electronics. The current density of the coils during power transfer is much lower (ca. 1.5 A/mm^2) than the maximum current density during levitation (ca. 10 A/mm^2), so if the thermal design of the planar actuator is good, it will be sufficient for the CPT as well.

3.4 Power Electronics on the Platform

All simulations and tests in this chapter have been performed using a resistive load of 50 Ω. Of course, in reality, the loads on the platform will not behave like a perfectly resistive load. Moreover, the different systems on the platform require different fixed voltages with varying power demands. The motors in the manipulator will need a power amplifier to provide the necessary currents. These (commercially available) power amplifiers need either a AC input (220 V, 50 Hz) or a DC input. Since the high frequency output of the secondary circuit needs to be rectified anyway, a power amplifier with a DC input is more convenient. To
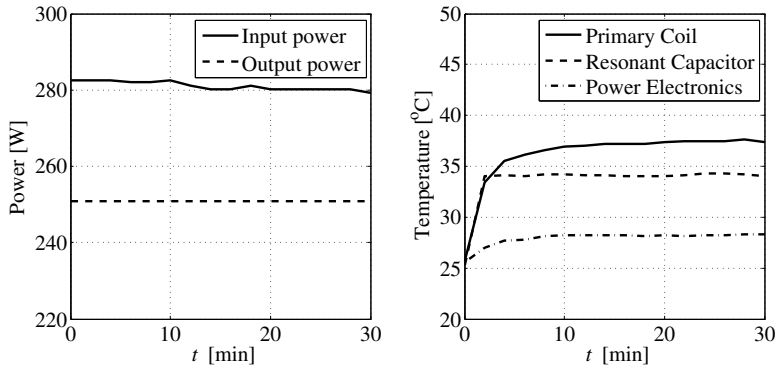
Figure 3.18: Measured input and output power

prevent problems with high voltages, the DC voltage is fixed at 59 V, which is sufficient to power a wide range of commercially available power amplifiers and motors. The voltage has to remain fairly stable (ca. 10% variation) and this DC bus sees the largest power variations such as short periods of high power when the motors are accelerating.

Furthermore, there are electronic subsystems, e.g. the wireless control system, on the platform that will need high quality voltages at different levels: +5 V for the logic and +/- 15 V for the analog systems such as op-amps and AD/DA-converters. These voltage levels need to be very stable and accurate within 5% or better. Finally, this system has to be as simple and lightweight as possible.

The proposed solution is a rectifier with a large DC bus capacitor that is capable of handling variations in the power requirements and that can buffer enough energy to ensure stable operation during the transition from one primary coil to the next. In that period no energy can be transferred to the secondary side and all energy is drawn from the DC bus capacitor, which results in a voltage drop of the DC bus voltage. On the other hand, the capacitor should be able to buffer the energy delivered back from the motors, if they are braking, which could result in a voltage increase.

When power is transferred to the secondary side, the voltage over the DC bus capacitor is rising, so when a certain voltage (the upper threshold voltage) is reached, the power transfer should be stopped to prevent an over voltage. When the voltage drops, due to the energy used by the systems on the secondary side, the power transfer should resume at a lower threshold voltage. If the upper and lower threshold voltages are close, e.g. 57.5 V and 58.5 V, the DC bus capacitor can be directly used as the power supply of the motor power amplifiers.

To control the voltage of the DC bus capacitor, it is necessary to enable and disable the power transfer on the secondary side, preferably without communication with the primary side. From Eq. 3.10, it is clear that the power supply sees a high impedance when the load R_L is zero and a low impedance when the load is high.

Therefore, the power transfer can be stopped by shorting the secondary circuit,

which will result in a high impedance on the primary side. However, the power transfer will not be zero, so some power will be dissipated in the components on the secondary side. From efficiency point of view, it is beneficial to open the secondary circuit (R_L approaches ∞), since there will not flow any current in the secondary circuit. This requires special adaptations in the primary square-wave voltage source, since it will have to shut-down when the impedance becomes very low (no power transfer). In addition, it will have to detect when to resume the power transfer. This all becomes easier if there is communication between the primary and secondary side. Even if there is a wireless link available, for safety reasons it is better to rely on a control scheme without communication.

The voltages for the electronics are realized by DC-DC converters from Traco which can operate with an input voltage of 18-75 V and output the required +5 V (TEN 5-4811WI) and +/-15 V (TEN 5-4823WI) with an accuracy of +/-2%. There is an additional +12 V DC-DC converter that is isolated from the other outputs to operate the electronics needed to short the secondary circuit. A schematic of the secondary side power supply for the platform is shown in Figure 3.19.

Apart from the already discussed rectifier, DC bus capacitor and AC switch to short the secondary circuit, the power supply consists of a adjustable voltage divider that measures the DC bus voltage, an op-amp comparator with adjustable hysteresis to select the upper and lower threshold of the DC bus capacitor voltage and an optocoupler that can drive the AC switch directly. The AC switch consists of four diodes and a MOSFET that only conducts if the MOSFET is conducting. Heatsinks are placed on the diodes of the rectifier and on the components of the AC switch, since they conduct currents of up to 2.5 A. A small fan is powered by the 12 V converter to provide airflow over the heatsinks for additional cooling.

3.5   Conclusions

In this chapter, a new contactless power transfer system based on an inductive coupling between a primary coil and a secondary coil has been presented that can transfer power continuously in a large area. One of the key characteristics of the approach has been the relatively small position dependence of the coupling ($< 25\%$) between the primary and secondary coil, allowing significant misalignments between the coils. In fact, the relative displacement between the coils can be so large that the secondary coil can move from one primary coil to the next without passing through an area with low coupling, which enables infinite stroke in the x-y plane.

Simulations and measurements have shown that a design with a small variation of the coupling and a series resonant topology is not affected by mechanical movement. On the other hand, the force between the contactless power transfer coils is at a very high frequency and of low magnitude, so it does not induce disturbances in the mechanics. Since small variations of the coupling do not affect the behavior, the system is tolerant to short stroke movements in other directions.

By keeping the average coupling high enough (> 0.2), an efficient power transfer of up to 90% at significant power levels of 265 W maximum has been achieved. Although the coupling is low compared to regular transformers, the efficiency can
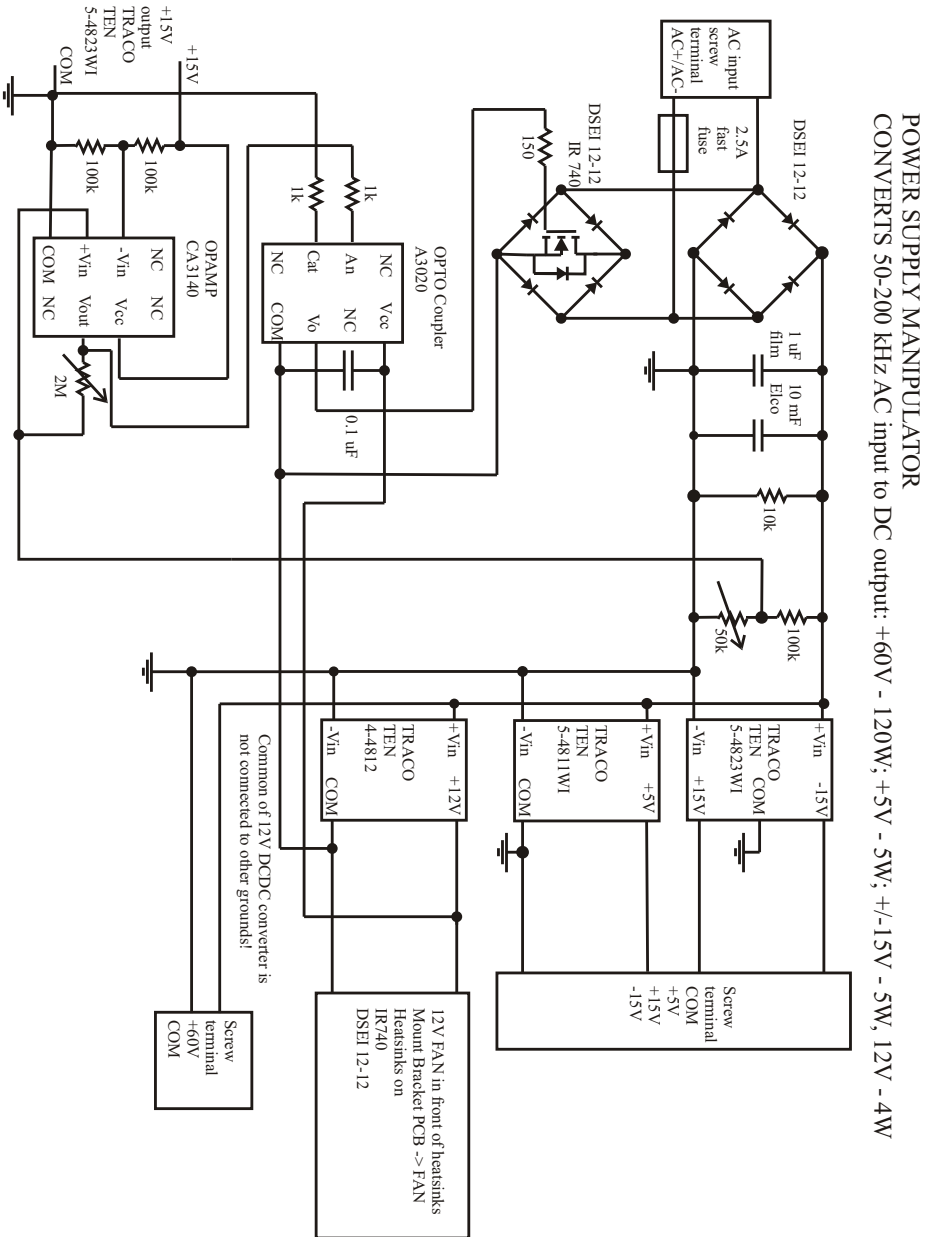
Figure 3.19: Secondary side power supply schematic.

still be high by choosing the appropriate inductances and frequency as it has been shown by the measurements. However, the relatively low coupling limits the maximum power that can be transferred because of practical limitations of the components, in this case the high voltage in the resonance. Finally, a power supply has been presented that converts and buffers the energy from the secondary coil to supply the motor power amplifiers and electronics on the secondary side.

Optimization of the Planar Actuator with CPT

After the discussion of the planar actuator models and the contactless power transfer system in Chapter 2 and Chapter 3, respectively, the two subsystems are now integrated. In this chapter, it is discussed how both systems interact and which parameters are critical for the integration. Optimization variables, constraints and objectives as well as additional considerations are discussed, that finally result in a topology that is best suited to integrate both functions. Finally, the geometry of the secondary coil is optimized to obtain a high coupling with low position dependence with the primary coil geometry that is found in the planar actuator optimization. The optimization of the planar actuator with CPT is published in [84] and [92].

4.1 Optimization Strategy

The number of variables involved in finding an optimal design is enormous, it includes magnet array topology (e.g. Halbach or N-S array), coil topology (e.g. number of phases) and the dimensions of the magnets and coils involved. Limits such as maximum current, maximum back-EMF, maximum temperature and maximum condition number should be included in the optimization problem as constraints. Moreover it is hard to make a trade-off between the different characteristics and to convert this into a single cost function.

It is difficult, if not impossible, to include topology optimization (e.g. Halbach or N-S, 2-phase or 3-phase), shape optimization (round, rectangular or square coils) and geometrical optimization (magnet height, coil height, etc.) into one optimization routine. Therefore, a practical approach would be to choose several topologies with fixed shapes and then to do a geometrical optimization for each problem to find the optimal solution.

4.1.1 Optimization Variables

Due to the complexity of the planar actuator design, the optimization is reduced to a geometric optimization for a fixed coil topology and fixed magnet topology. The Halbach magnet topology is fixed by the number of poles in the array (e.g. 8×8 or 9×9) and the pole pitch. The coil topology is fixed by the number of phases in the coil array, which is determined by the electrical degrees between each coil with the pole pitch being equal to 180 electrical degrees.

It is possible to use rectangular coils if the magnet array is 45 degrees rotated with respect to the coil array [5, 6, 9, 10, 11, 12]. However, as rectangular coils can only generate forces in two directions, there are two orthogonal orientations of rectangular coils necessary to generate forces in three directions. This results in an irregular pattern of coils that complicates the contactless power transfer to
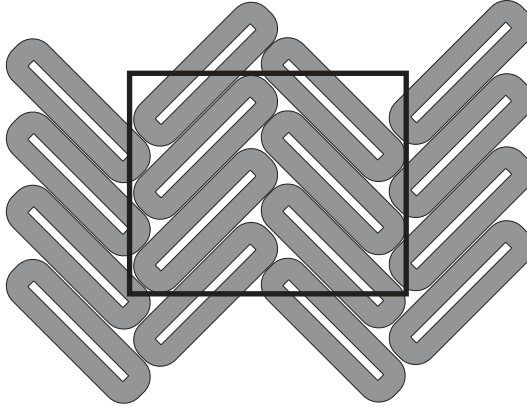
Figure 4.1: Array of rectangular coils and secondary coil outline

a single secondary coil. A single secondary coil would either have to be large, resulting in a low coupling (ca. 0.1). This is depicted in Figure 4.1, where an approximate outline of the secondary coil is given. It is clear that the number of rectangular coils within the outline is approximately six or even slightly higher, which causes the low coupling for a single rectangular coil and the secondary coil. Such a low coupling would make it difficult to transfer the desired amount of power within the voltage and current limits of the components. Although it does not necessarily mean that the efficiency will be lower as well, it will be more difficult to maintain a high efficiency. Another possibility is to use an array of spatially shifted secondary coils, optionally in combination with multiple primary coils. Unfortunately, this will make the power transfer system very complicated, since it requires more components to work together. In addition, the size of the power transfer system would be larger, which results in a larger construction, more problems with stiffness and a higher levitated mass.

Therefore, only topologies, with square or round coils are taken into account in the optimization. The N-S array is not considered as a possible array in this optimization, since it produces less force than the Halbach array [9, 10]. Although the Halbach array weighs more than the N-S array, since it consists of more magnets, the additional force that can be generated ultimately leads to higher accelerations of the full system. The variables that cannot be included in an optimization routine are varied by means of a parametric search. For a certain set of variables the geometric optimization is carried out and by comparing the results for the different topologies in the set a final selection is made.

The following variables are included by means of parametric search:

1. **Pole pitch τ**
   The size of the magnet array depends on the pole pitch (τ) and the number of poles. The pole pitch is varied in steps of 5 mm, while keeping the size of the magnet array between approximately 300×300 mm and 500×500 mm, e.g. for 10×10 poles the minimum pole pitch is 30 mm and the maximum pole pitch is 50 mm.

2. **Number of magnet poles**
   Besides the pole pitch, the number of poles determines the size of the magnet array. In addition, the number of poles together with the number of phases in the coil array determines the number of coils that are covered by the magnet array. Since the outer dimensions of the platform are bounded as is the pole pitch, the number of poles included in the parametric search are: 7×7, 8×8, 9×9 and 10×10.

3. **Coil phases**
   Three different coil phase systems are considered in the optimization, with coils that are spaced apart 225 degrees, 240 degrees and 270 degrees, respectively. A minimum number of coils is necessary to guarantee controllability of the planar actuator. In addition, the more coils that are contributing to the force and torque vector on the platform, the lower the maximum dissipated heat in a single coil, while the overall power consumption to levitate the weight remains approximately the same.

Since τ represents 180 electrical degrees, a coil that is shifted 240 electrical degrees has a maximum coil width (c_w) of $\frac{240}{180}\tau$. With the topology and the pole pitch defined the remaining variables that are included in the optimization are:

1. **Magnet ratio r_m**
   The magnet ratio between the width of the N-S magnets in the Halbach array (m_w) and the pole pitch τ is defined by:

   $$r_m \quad = \quad \frac{m_w}{\tau}. \tag{4.1}$$

2. **Coil bundle ratio r_c**
   The ratio between the coil bundle width c_{bw} and the coil width c_w is defined by:

   $$r_c \quad = \quad \frac{c_{bw}}{c_w}. \tag{4.2}$$

3. **Magnet height m_h**
   The height of the magnets is included in the optimization.

4. **Coil bundle height c_{bh}**
   The height of the coil bundle is included in the optimization.

The geometrical variables are shown in Figure 4.2.

4.1.2 Optimization Constraints

The optimization of the planar actuator is subject to several constraints. The constraints are divided into geometrical constraints and thermal constraints. In addition, there are other considerations that are not hard constraints, but will be taken into account when deciding which final topology will be chosen. First, the constraints are discussed.
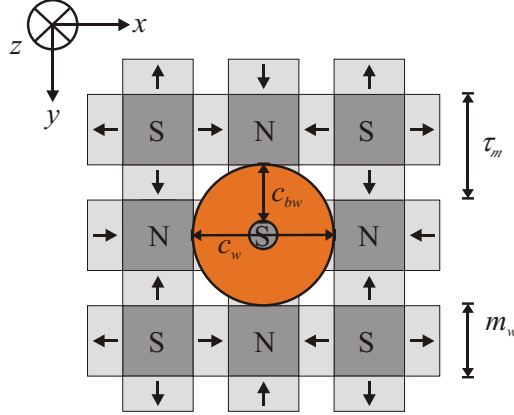
Figure 4.2: Halbach array and a round coil with a coil width of 240 electrical degrees

1. $m_w < \tau$
   There is a geometrical constraint on the magnet width m_w: the magnet width can never be larger than the pole pitch.

2. $2c_{bw} < c_w$
   The coil bundle width c_{bw} has a geometrical constraint, since it can never be larger than half the coil width.

3. $T_{ct} <$120 °C
   The magnets are made of NdFeB, which will suffer from demagnetization if the temperature rises above 120 °C. Therefore, the temperature of the top surface of the litz wire coil should not exceed that temperature. Moreover, the hot-spot temperature of the coil is almost equal to the top surface temperature and the thermal stability of the litz wire coil is guaranteed up to 125 °C. This constraint also ensures that the coils will not get damaged. The thermal model described in Section 2.5 is used to calculate T_{ct}

4.2   Optimization Objective

The total weight of the levitated system, F_z, results in a high power dissipation in the coils. Therefore, the losses in the coils should be minimized. Since the planar actuator consists of a large set of modular coils with separate amplifiers, it is in fact a combination of many 1 DOF actuators. Due to the fact that from an electromagnetic point of view this system is linear (no iron, no saturation), the principle of superposition is valid for force calculation. Moreover, optimization of $|\underline{F}|$ means an optimization of F_z. To achieve this, a single coil is placed underneath the magnet array with the center of the coil aligned with a magnet pole, where it only generates lift force. Then the required current, i_c, in the coil is calculated to compensate F_z. The optimization routine then minimizes the resulting resistive

losses, P_{loss}, in that single coil:

$$P_{loss} = \min_{Ki_c = F_z} i_c^2 R, \qquad (4.3)$$

where K is the constant that expresses the force per Ampère.

4.2.1 Additional Considerations

Besides the losses and temperatures, there are practical issues that affect the optimal design, which is the total levitated mass, the availability of power amplifiers, the control complexity, the integration of the contactless power transfer and the manufacturability of all components.

Control Complexity

The planar actuator is over-actuated so there are a large number of coils to generate the desired force and torque on the platform. The controller should be able to calculate all these coil currents within one sample time. In addition, the topology should be controllable, i.e. the condition number of the coupling matrix $\underline{K}$ should be sufficiently low, as it is discussed in Section 2.2.2.

Levitated Mass and Stiffness

The moving platform should be stiff in order to prevent flexible modes and resonances, which will limit the performance. In general, the stiffness of the platform reduces when it becomes larger and additionally the mass increases. Since mechanical resonant frequencies scale with $\sqrt{\frac{k}{m}}$, a higher mass, m [kg], and a lower stiffness, k [N/m], result in resonances at lower frequencies. Therefore, the platform should be reasonably small, stiff and light. The levitated mass is estimated by the total mass of the magnets, a glue filling in between the Halbach magnets, an aluminum backplate with a thickness of 10 mm behind the magnets and a total load of the manipulator of 6 kg.

Power Amplifier Specification

The choice of the number of turns N for the primary coil depends on the maximum number of Ampère-turns that are necessary to levitate and accelerate the platform and the amplifier used to supply the current. In addition, the power amplifiers use switching electronics to control the current in the coil. If the inductance becomes to low (< 0.5 mH), the switching results in significant current ripples that reduce the performance of the system. Furthermore, power amplifiers work at a certain voltage u_{ext}, which has to be sufficient to overcome the back-EMF due to the movement of the magnet array, the resistive losses in the coils and the voltage drop due to the time-derivative of the current in the coil:

$$u_{ext} = Ri + L\frac{di}{dt} + E_{EMF} \qquad (4.4)$$

If the number of turns in the coil is too large, resulting in an inductance over 10 mH, the back-EMF will be too high for the amplifier to generate the desired

$\frac{di}{dt}$. Finally, the number of turns fixes the wire dimensions used to wind the coil. This is a practical concern, since not every diameter wire is readily available. Moreover, the filling factor for litz-wire will increase if the wire bundle diameter is larger. If the bundle diameter is larger, the thickness of the isolation around the bundle consumes a smaller percentage of the diameter, thereby increasing the filling factor. In the optimization, the maximum continuous current of the amplifier is set to 5 A and this specification is used to calculate the number of turns in primary coil. This value gives reasonable numbers and is a good start to compare the different topologies.

Contactless Power Transfer

The contactless power transfer is influenced by the optimization of the planar actuator, since the inductance of the actuator coil determines part of the CPT characteristics. The inductance L and hence, the number of turns N, is an important characteristic. The power transfer occurs at a high frequency ($f_0 =$50-200 kHz) and the RMS voltage over the coil in the resonant circuit is set by these parameters according to:

$$V_{coil} \quad = \quad 2\pi f_0 L I_1, \tag{4.5}$$

where I_1 is the RMS current through the coil. A high inductance results in a high resonant voltage and thus a high voltage over each winding. Several other factors determine the behavior of the CPT, such as secondary coil inductance, load impedance and resonant frequency as discussed in Chapter 3. However, an estimate of the expected resonant voltage over the primary coil is done to verify the feasibility for contactless power transfer. The main problem is the resonant voltage, so this is the parameter of interest. The inductance of the secondary coil is adapted to match the following CPT characteristics:

- Resonant frequency of 100 kHz,

- Load impedance of 25 Ω (purely resistive),

- Input square-wave voltage of $\pm$ 200 V,

- Output power of 250 W,

- Coupling of 0.2.

The geometry of the primary coil follows from the optimization and the inductance of the primary coil geometry is calculated using FEM analysis [30]. Finally, the number of turns cannot be too large for the CPT coils, since its parasitic capacitance of the coil increases with the number of turns. The parasitic capacitance is in parallel with the coil inductance and the resonant frequency of the two should be at a much higher frequency than the resonant frequency of the CPT series resonant circuit.

4.2.2   Optimization Approach

The optimization of the planar actuator is split in two parts: a geometrical optimization and a parametric search.

1. **Geometrical optimization**
   For each topology that is considered the optimal dimensions of the coils and magnets are calculated to minimize the loss in a single coil according to Eq. 4.3.

2. **Parametric search**
   Using the dimensions from the geometrical optimization, the behavior of the full planar actuator is calculated using a combined analytical-numerical model from which the thermal and CPT characteristics are derived.

Geometrical Optimization

The Lorentz force principle is used to calculate the force, $\underline{F}_c$, that is applied on the coil by numerically integrating the outer product of the current density in the coil, $\underline{J}_c$, and the magnetic flux density, $\underline{B}_m$, in the volume of the coil, V_c, generated by the magnet array:

$$\underline{F}_c = \int_{V_c} \underline{J}_c \times \underline{B}_m dV_c. \tag{4.6}$$

The magnetic field density can be calculated using the surface charge model as described in Chapter 2. However, to save calculation time, an analytical spatial harmonics representation of the magnetic field is used as described in [9, 10]. Moreover, only the first harmonic of the magnetic field is included in the analysis. Higher harmonics do not greatly effect the optimal dimensions [10]. The change of the dimensions by using more accurate models (by using higher harmonics or surface charge) is in the order of the manufacturing tolerances of the coil and is, therefore, not necessary to include. The surface charge model is only used to verify the outcome of the numerical Lorentz force calculation after optimization using the first order harmonic model.

A sequential quadratic programming routine (*fmincon* in Matlab) is used to find the optimal dimensions which minimizes the power dissipation in the single coil. The geometrical constraints are included as bounds in the optimization routine. Since the pole pitch and coil width are fixed, the bounds do not depend on the optimization variables. Since it is easier to manufacture round coils than square coils and the shape of the square coil converges to almost round coils during initial tests, it was decided to only consider round coils in the optimization.

Parametric Search

The geometrical optimization is done for several topologies as is discussed in Section 4.1.1. Using the dimensions from the geometrical optimization, the combined analytical-numerical model described in Chapter 2 is used to calculate the behavior of the full planar actuator including end-effects. The model predicts the currents necessary in each coil to lift the platform at a grid of points in the workspace of the
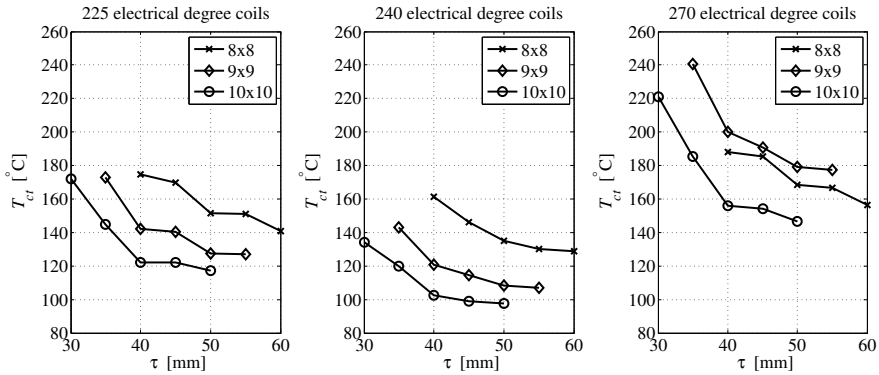
Figure 4.3: Coil surface temperatures for different topologies with $n \times n$ magnet poles

planar actuator. From that analysis the worst-case power dissipation in the actual planar actuator is calculated, assuming a 0.3 filling factor of the coil and an airgap of 2 mm. The filling factor of 0.3 was measured for the litz wire coils discussed in Chapter 3. Since this was the first experience with manufacturing aircore litz wire coils, it is anticipated that this is the minimum value for the filling factor, which might be slightly conservative.

The dimensions of the coil and the dissipated power are fed into a thermal model of the planar actuator coils to calculate the surface temperature of the coil. Since not all topologies will satisfy the thermal constraint ($T_{ct} < 120°C$), this results in a set of solutions. Finally, the values, which are important for the additional considerations are calculated. These considerations determine which of these solutions is most feasible.

4.3   Optimization Results

First, the corresponding coil surface temperatures are analyzed for the three different coil phase systems and different number of magnet poles, of which the dimensions are optimized. The results are shown in Figure 4.3. It is clear that increasing the pole pitch leads to lower coil surface temperatures.

The temperature constraint specified in Section 4.1.2 of a maximum surface temperature of 120 °C, rules out most of the topologies. Only for the coils of 240 electrical degrees (3-phase), a significant set stays below the temperature constraint. The other coil topologies are neglected for the remainder of the optimization.

The topologies that satisfy the coil surface temperature constraint are now compared using different characteristics, such as the parameters related to the power amplifier specifications, the contactless power transfer, the control complexity and the mechanical construction. These parameters are listed in Table 4.1 and Table 4.2. From the resonant voltages it can be concluded that a higher inductance

Table 4.1: Electrical parameters for different 3-phase topologies

magnet poles	τ	Inductance	Resistance	Resonance
9×9	50 mm	2.15 mH	1.6 Ω	1.87 kV RMS
9×9	55 mm	2.87 mH	1.7 Ω	2.50 kV RMS
10×10	35 mm	0.76 mH	1.1 Ω	0.66 kV RMS
10×10	40 mm	0.97 mH	1.1 Ω	0.85 kV RMS
10×10	45 mm	1.37 mH	1.2 Ω	1.20 kV RMS
10×10	50 mm	1.89 mH	1.4 Ω	1.65 kV RMS

Table 4.2: Mechanical parameters for different 3-phase topologies

magnet poles	active coils	τ	magnet mass	total mass
9×9	8×8	50 mm	16.0 kg	27.6 kg
9×9	8×8	55 mm	19.6 kg	32.4 kg
10×10	9×9	35 mm	8.8 kg	18.2 kg
10×10	9×9	40 mm	11.7 kg	22.1 kg
10×10	9×9	45 mm	15.0 kg	26.6 kg
10×10	9×9	50 mm	18.8 kg	31.7 kg

will lead to a higher resonant voltage. The voltages are over 1 kV for the topologies with 9×9 magnets and from Table 4.2 it is clear that these topologies result in a heavy platform that needs to be levitated. The topologies with 10×10 magnets have lower surface temperatures and lower resonant voltages and are, therefore, a more suitable design choice. However, this comes at a cost of higher control complexity, since seventeen (81-64) more active coils are necessary to control the platform at any position. This additional control complexity can be handled by the controller, so this will not pose a problem. The condition number of the coupling matrix $\underline{K}$ of the 10×10 topologies varies between 13.5 for τ=35 mm and 9.3 for τ=50 mm, which are well below the upper limit of 100, as it is discussed in Section 2.2.2. The surface temperature (see Figure 4.3) decreases only marginally, if the pole pitch is increased from 40 mm to 50 mm, but the levitated mass increases tremendously. Finally, it was found that the inductance was small enough for all topologies to operate the amplifiers at 60V. Therefore, the final choice is a 3-phase system with 10×10 magnet poles and a pole pitch of 40 mm, since it is the best tradeoff between temperature, resonant voltage and total levitated mass. The dimensions of the final topology are: r_m =0.64, r_c =0.41, m_h =10.3 mm and c_{bh} =11.3 mm.

4.4 Optimization of the Contactless Power Transfer System

Now, the geometry of the primary coil is fixed by the optimization of the planar actuator, the secondary coil geometry can be optimized. As discussed in Chapter 3,

the geometry of the secondary coil much be such that the position dependence of the coupling is minimized, while maintaining a fairly high coupling in the entire workspace. Moreover, the workspace must be large enough to allow the secondary coil to move from one primary coil to the next without a sharp decline in coupling.

From the shape of the coupling variation (see Figure 3.6), it is clear that the largest variations occur along the diagonal of the workspace. Furthermore, the lowest coupling is found at the far corner of the workspace, where the secondary coil, in principle, can retrieve power from four coils (see also Figure 3.5).

The following optimization approach is used to find the optimal geometry of the secondary coil.

1. **Geometrical optimization**
   First, the coupling at the far corner of the workspace is maximized by optimizing the dimensions c_w, c_{bw}, r_1 and r_2 with a fixed coil bundle height $c_{bh} = 1$ mm using the sequential nonlinear programming method within Ansoft Maxwell 3D Optimetrics [30]. For a definition of the parameters see Figure 3.4.

2. **Parametric search**
   Using the geometry from the geometrical optimization as a starting point, the dimensions are varied by means of a parametric search to minimize the position dependency of the coupling along the diagonal of the workspace.

With an airgap of 2 mm the maximum obtainable coupling is 0.22 at the corner of the workspace. The resulting geometry from the geometrical optimization is shown in Figure 4.4. Then the coupling is calculated along the diagonal of the workspace, where the outer position $(x, y = -27$ mm) is shown in the figure and position $(x, y = 0$ mm) corresponds with the position where the centers of the coils are aligned. The corresponding coupling is shown in Figure 4.6, where it is clearly visible that when the centers of the coils are aligned, the coupling is even lower than at the corner of the workspace. This effect is undesired and, therefore, a parametric search is necessary that takes into account the variation of the coupling in the workspace. For several geometries the coupling along the diagonal was calculated and the best one is shown in Figure 4.5 with the corresponding coupling plotted in Figure 4.6. The cost function to determine which of the geometries in the parametric search is best is:

$$f = -\text{mean}(\underline{k}) + \text{std}(\underline{k})\frac{\text{mean}(\underline{k}_0)}{\text{std}(\underline{k}_0)}, \tag{4.7}$$

where $\underline{k}$ is the coupling vector containing the coupling values at different positions along the diagonal and $\underline{k}_0$ is the coupling vector that corresponds with the geometry from the geometrical optimization. The standard deviation of the coupling vector is weighted to give it approximately the same weight in the cost function as its mean value. Although a cost function is defined, this problem was solved by means of a parametric search, since it was not possible to implement this optimization in Ansoft Maxwell 3D Optimetrics. The final topology has the dimensions: $c_w = 115$ mm, $c_{bw} = 27.5$ mm, $r_1 = 2.5$ mm and $r_2 = 30$ mm.
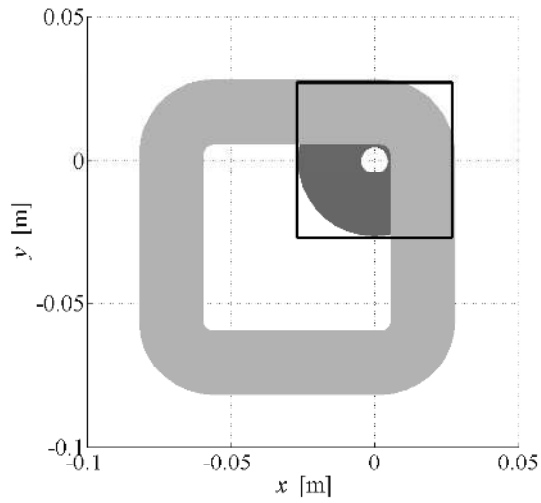
Figure 4.4: Secondary coil with round primary coil optimized at the far corner of the workspace
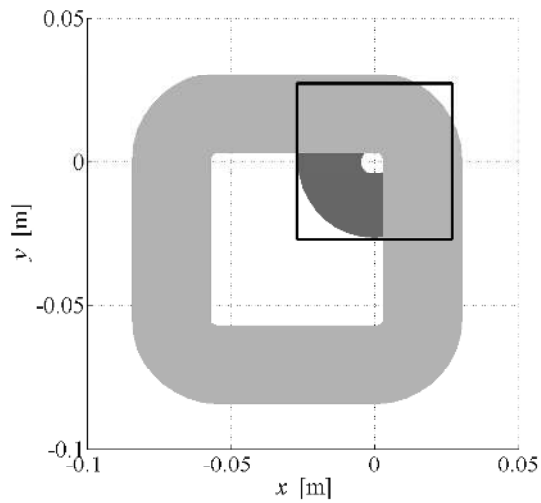
Figure 4.5: Secondary coil with round primary coil optimized over the entire workspace
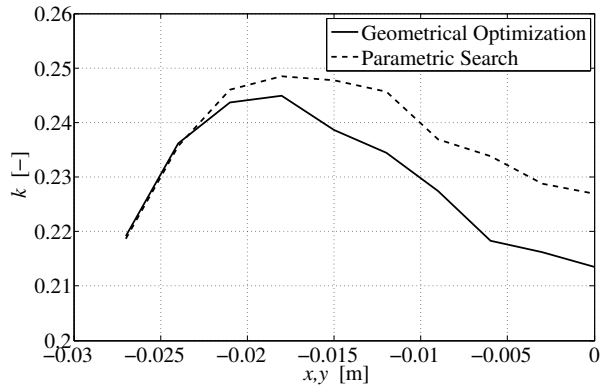
Figure 4.6: Coupling between the secondary and primary coil along the diagonal of the workspace

4.5   Conclusions

The optimization of the planar actuator in combination with contactless power transfer has been discussed in this chapter. Due to the large number of variables involved, the optimization has been carried out as a combination of a geometrical optimization of a single coil for a large number of topologies and a parametric search to compare the overall behavior of the optimized topologies to come to a final design. It has been found that using litz wire for the coils of the planar actuator introduces significant thermal problems. From the various topologies considered, only a small number satisfied the thermal constraint of 120°C maximum coil top surface temperature. The final topology has been chosen based on considerations of the mechanical properties, control complexity, power amplifier specifications and the contactless power transfer characteristics. The secondary coil geometry has been optimized to obtain a high coupling with a low position dependency with the primary coil geometry found in the planar actuator optimization.

CHAPTER 5
DYNAMIC SYSTEM EQUATIONS BASED ON LAGRANGE

On top of the floating platform with the contactless planar actuator, a manipulator is placed, which can move independently from the planar actuator. The design of the manipulator is shortly discussed in this chapter, but the focus in this chapter lays on the dynamic equations that describe the behavior of the full system.

The dynamic equations are derived using Lagrangian mechanics in stead of using the Newton-Euler approach. In general, Newton's laws are formulated for a single body, but extension to multiple bodies is possible. In that case, the physical coordinates and all forces that act on each separate body in the system including interconnecting forces between the bodies have to be included in the analysis to describe the motion of the multi-body system. The interconnections between the bodies result in kinematic constraints and often these interacting forces between the bodies are not of interest [51].

In a Lagrangian approach, the entire system is considered instead of the separate bodies, thereby eliminating the need to calculate the interacting forces. The physical coordinates are replaced with a minimal set of generalized coordinates that capture the variations in the system, which do not necessarily have a physical meaning. The method is based on energy stored in the system, which in case of mechanics concerns kinetic energy of the moving masses and potential energy stored in the gravitational field and elastic deformations. The energy in the system can change due to non-conservative generalized forces, which represent losses such as friction and externally applied forces or torques. In case of electromagnetics, the energy is stored in the magnetic fields, e.g. in coils, iron and permanent magnets. The non-conservative generalized forces in the electromagnetic domain are dissipative losses in conductors and voltages that are applied by external sources such as batteries or power amplifiers [53]. The dynamics of the system are then derived by considering the virtual work that is done by virtual variations of the generalized coordinates as a result of the non-conservative generalized forces.

First, the coordinate transformations and generalized coordinates are discussed that define the position of each body. Second the equations of the multi-body dynamics are derived using Lagrange. With these equations it is possible to predict the forces and torques that act on the bodies when they are moving along a certain trajectory. Second, the dynamic equations are extended into the electromagnetic domain, to include the interaction between magnets and coils that create the forces and torques that act on the bodies. This results in a comprehensive set of dynamic equations that describes the full system both in the mechanical and electromagnetic domain and the interaction of the two domains from the changes in energy in the system. Finally, the equations of motions are validated in an experimental setup and the non-rigid body dynamics are identified by measurements. The equations of motion and the experimental verification are published in [90] and [97].
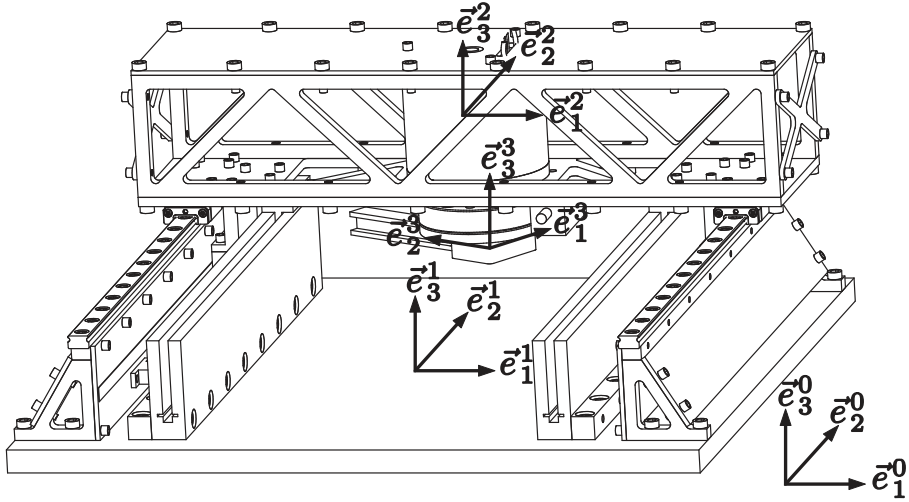
Figure 5.1: Coordinate systems in the manipulator

5.1   Manipulator

The manipulator is designed to represent a real industrial-like system, with actuators and sensors that are commonly used in machines and robots. Such a design will prove the suitability of the developed concepts in an industrial environment. Moreover, the manipulator is designed to minimize the necessary mass, since this mass will have to be levitated.

The manipulator on top of the platform is an H-drive with two ironless linear actuators attached to a beam. In the center of the beam a rotary motor is assembled with an arm attached to it. The tip of this arm can be positioned anywhere in the x-y plane between the two horizontal linear legs by combining the translation of the beam and the rotary movement of the arm. A drawing of the H-drive is shown in Figure. 5.1.

The linear actuators are ironless 3-phase synchronous motors and the rotary drive is a slotless 3-phase synchronous motor, which do not suffer from cogging and reluctance effects. The actuator properties are listed in Table 5.1.

The position of each linear actuator is measured with incremental encoders which have a 1 μm resolution. The angle of the rotary motor is measured with a 40 μrad resolution. The beam, which connects the linear actuators, is assumed sufficiently stiff in order to consider it rigid. In addition, the bearings are assumed ideal, therefore, movements of the beam in directions other than the movement direction of the linear actuators are considered impossible. Although effects such as limited bearing stiffness are important for the tuning of the position controllers, the previous assumptions can be made, since the goal of the dynamic model is to predict feedforward compensation due to acceleration of the bodies.

Table 5.1: Actuator properties

Property	Linear motor	Rotary motor
Motor constant	8.1 N/A	0.11 Nm/A
Peak current	4.4 A	15.3 A
Continuous current	1.23 A	2.71 A
Continuous force	10 N	-
Continuous torque	-	0.28 Nm

5.2 Coordinate Transformations

The manipulator consists of three separate bodies. The platform, magnet tracks and bearings together are the first body with mass, m_1. The second body is the beam and has a mass, m_2. The rotor of the rotary motor together with the arm form the last body with mass, m_3. Each body has a local coordinate system attached to it (see Figure 5.1), which is used for describing the position and orientation with respect to the global coordinate system. Each coordinate system consists of three orthogonal unit vectors:

$$\underline{\vec{e}}^i \quad = \quad \begin{bmatrix} \vec{e}_1^i & \vec{e}_2^i & \vec{e}_3^i \end{bmatrix}^T \text{ for } i = 0, \ldots, 3, \qquad (5.1)$$

where $\underline{\vec{e}}^0$ is the global coordinate system, fixed to the world and can, therefore, not move, $\underline{\vec{e}}^1$ is placed in the geometrical center of the magnet array, $\underline{\vec{e}}^2$ is located in the geometrical center of the beam and $\vec{e}^3$ is attached to geometrical center of the rotary arm.

5.2.1 Generalized Coordinates

In general, a body has 6 degrees of freedom (DOF) if it is not subject to any constraints. In presence of constraints, each constraint removes one degree of freedom. The minimum required set of coordinates to describe the position and orientation of each body are a set of n generalized coordinates, $\underline{q}$. So $\underline{q}$ is a $(n \times 1)$ vector. The floating platform has 6 DOF due to its complete freedom with respect to the fixed world. Furthermore, the manipulator adds 1 DOF due to the translation of the beam and 1 DOF due to the rotational movement of the rotary motor. The beam is considered rigid and roller bearings are assumed to be infinitely stiff, so they do not allow other movements of the beam than the one in the $\vec{e}_2^1$-direction. Therefore, only 1 DOF is added by the beam. The column of generalized coordinates for the manipulator on the floating platform is:

$$\underline{q} = \begin{bmatrix} x & y & z & \theta & \psi & \phi & y_{LM} & \phi_{RM} \end{bmatrix}^T. \qquad (5.2)$$

Here x, y and z [m] denote the geometric center of the magnet array of the contactless planar actuator and θ, ψ and ϕ [rad] are the rotation parameters of the platform around the geometric center of the magnet array. y_{LM} [m], is the displacement of the beam w.r.t. to its median position, while ϕ_{RM} [rad] is the rotation
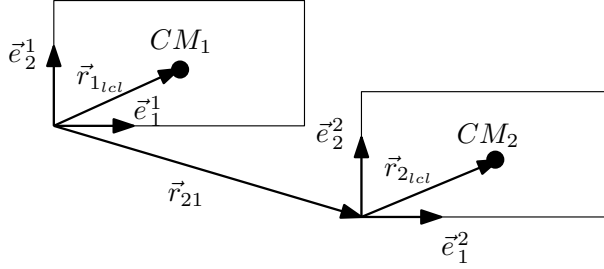
Figure 5.2: Body fixed vectors

angle of the rotary motor. Now the position vector of the center of mass, $\vec{r}_{CM_i}$, can be written in terms of $\underline{q}$.

This definition is used, since the location of the center of mass and the origin of the body-fixed coordinate system do not coincide.

5.2.2 Position of the Bodies

Using this choice for the generalized coordinates, the positions of the center of mass of each body are rewritten in terms of $\underline{q}$:

$$
\begin{aligned}
\vec{r}_{CM_1} &= \vec{r}_1 + \vec{r}_{1_{lcl}} \\
&= \begin{bmatrix} x & y & z \end{bmatrix} \underline{\vec{e}}^0 + \begin{bmatrix} x_{1_{lcl}} & y_{1_{lcl}} & z_{1_{lcl}} \end{bmatrix} \underline{\vec{e}}^1,
\end{aligned} \tag{5.3}
$$

$$
\begin{aligned}
\vec{r}_{CM_2} &= \vec{r}_1 + \vec{r}_{21} + \begin{bmatrix} 0 & y_{LM} & 0 \end{bmatrix} \underline{\vec{e}}^1 + \vec{r}_{2_{lcl}} \\
&= \begin{bmatrix} x & y & z \end{bmatrix} \underline{\vec{e}}^0 + \begin{bmatrix} x_{21} & y_{21} + y_{LM} & z_{21} \end{bmatrix} \underline{\vec{e}}^1 \\
&\quad + \begin{bmatrix} x_{2_{lcl}} & y_{2_{lcl}} & z_{2_{lcl}} \end{bmatrix} \underline{\vec{e}}^2,
\end{aligned} \tag{5.4}
$$

$$
\begin{aligned}
\vec{r}_{CM_3} &= \vec{r}_1 + \vec{r}_{21} + \vec{r}_{32} + \vec{r}_{3_{lcl}} \\
&= \begin{bmatrix} x & y & z \end{bmatrix} \underline{\vec{e}}^0 + \begin{bmatrix} x_{21} & y_{21} + y_{LM} & z_{21} \end{bmatrix} \underline{\vec{e}}^1 \\
&\quad + \begin{bmatrix} x_{32} & y_{32} & z_{32} \end{bmatrix} \underline{\vec{e}}^2 + \begin{bmatrix} x_{3_{lcl}} & y_{3_{lcl}} & z_{3_{lcl}} \end{bmatrix} \underline{\vec{e}}^3,
\end{aligned} \tag{5.5}
$$

where $\vec{r}_{i_{lcl}}$ denotes a body-fixed vector which describes the position of the center of mass of a body w.r.t. its local coordinate system (see Figure 5.2) and $\vec{r}_{ji}$ denotes a body fixed vector which describes the relative position of body j w.r.t. body i.

The position vector of each coordinate system is defined by:

$$
\vec{r}_1 = \begin{bmatrix} x & y & z \end{bmatrix} \underline{\vec{e}}^0, \tag{5.6}
$$

$$
\vec{r}_2 = \begin{bmatrix} x & y & z \end{bmatrix} \underline{\vec{e}}^0 + \begin{bmatrix} x_{21} & y_{21} + y_{LM} & z_{21} \end{bmatrix} \underline{\vec{e}}^1, \tag{5.7}
$$

$$
\begin{aligned}
\vec{r}_3 &= \begin{bmatrix} x & y & z \end{bmatrix} \underline{\vec{e}}^0 + \begin{bmatrix} x_{21} & y_{21} + y_{LM} & z_{21} \end{bmatrix} \underline{\vec{e}}^1 \\
&\quad + \begin{bmatrix} x_{32} & y_{32} & z_{32} \end{bmatrix} \underline{\vec{e}}^2.
\end{aligned} \tag{5.8}
$$

5.2.3   Orientation of the Bodies

The orientation of each body is described by means of Tait-Bryant angles. The orientation of body i is the result of subsequent rotations θ_i, ψ_i and ϕ_i about the local $\vec{e}_1^{\,i}$, $\vec{e}_2^{\,i\alpha}$ and $\vec{e}_3^{\,i\beta}$ axis, respectively. By the use of rotation matrices, $\underline{A}^{ji}$ the transformation from one coordinate system to another can now be made:

$$
\begin{aligned}
\vec{e}^{\,i\alpha} &= \underline{A}^{\alpha 0}\vec{e}_1^{\,i} \\
&= \begin{bmatrix} 1 & 0 & 0 \\ 0 & \cos(\theta_i) & \sin(\theta_i), \\ 0 & -\sin(\theta_i) & \cos(\theta_i) \end{bmatrix} \vec{e}_1^{\,i},
\end{aligned}
\tag{5.9}
$$

$$
\begin{aligned}
\vec{e}^{\,i\beta} &= \underline{A}^{\beta\alpha}\vec{e}_2^{\,i\alpha} \\
&= \begin{bmatrix} \cos(\psi_i) & 0 & -\sin(\psi_i), \\ 0 & 1 & 0 \\ \sin(\psi_i) & 0 & \cos(\psi_i) \end{bmatrix} \vec{e}_2^{\,i\alpha},
\end{aligned}
\tag{5.10}
$$

$$
\begin{aligned}
\vec{e}^{\,j} &= \underline{A}^{j\beta}\vec{e}_3^{\,i\beta} \\
&= \begin{bmatrix} \cos(\phi_i) & \sin(\phi_i) & 0 \\ -\sin(\phi_i) & \cos(\phi_i) & 0 \\ 0 & 0 & 1 \end{bmatrix} \vec{e}_3^{\,i\beta},
\end{aligned}
\tag{5.11}
$$

$$
\begin{aligned}
\vec{e}^{\,j} &= \underline{A}^{ji}\vec{e}^{\,i} \\
&= \underline{A}^{j\beta}\underline{A}^{\beta\alpha}\underline{A}^{\alpha i}\vec{e}^{\,i},
\end{aligned}
\tag{5.12}
$$

$$
\underline{A}^{ji} = \begin{bmatrix} C(\psi_i)C(\phi_i) & C(\theta_i)S(\phi_i)+S(\theta_i)S(\psi_i)C(\phi_i) & S(\theta_i)S(\phi_i)-C(\theta_i)S(\psi_i)C(\phi_i) \\ -C(\psi_i)S(\phi_i) & C(\theta_i)C(\phi_i)-S(\theta_i)S(\psi_i)S(\phi_i) & S(\theta_i)C(\phi_i)+C(\theta_i)S(\psi_i)S(\phi_i) \\ S(\psi_i) & -S(\theta_i)C(\psi_i) & C(\theta_i)C(\psi_i), \end{bmatrix},
\tag{5.13}
$$

where C and S represent the sine and cosine functions respectively. The rotation matrices are now written in terms of $\underline{q}$:

$$
\underline{A}^{10}(\theta_1, \psi_1, \phi_1) \Rightarrow \underline{A}^{10}(\theta, \psi, \phi),
\tag{5.14}
$$

$$
\underline{A}^{20}(\theta_2, \psi_2, \phi_2) \Rightarrow \underline{A}^{20}(\theta, \psi, \phi),
\tag{5.15}
$$

$$
\underline{A}^{30}(\theta_3, \psi_3, \phi_3) \Rightarrow \underline{A}^{30}(\theta, \psi, \phi + \phi_{RM}),
\tag{5.16}
$$

5.3   Model of the Multi-Body Dynamics

The derivation of the multi-body model is done by using Lagrange's equations [51, 52, 53]. These equations eliminate the need for computing all interacting forces between different bodies. Only external forces and constraint forces of interest have to be taken into account. The equation of Lagrange has the following form [51]:

$$
\left(\frac{d}{dt}\left(\frac{\partial T}{\partial \dot{\underline{q}}}\right) - \frac{\partial T}{\partial \underline{q}} + \frac{\partial V}{\partial \underline{q}} \right)^T = \left(\underline{Q}^{nc}\right) + \underline{W}\lambda,
\tag{5.17}
$$

where T [J] is the kinetic energy, V [J] the potential energy, $\underline{Q}^{nc}$ the vector with non-conservative generalized forces and $\underline{W}\lambda$ are the constraint equations. The various components in this equation will be discussed in this section.

5.3.1 Moments of Inertia

In order to calculate the kinetic energy due to the rotations of the system, for each body the inertia matrix with respect to its axis of rotation needs to be determined. For all three bodies, the inertia matrix is estimated with respect to the origin of each body-fixed coordinate system. These inertia matrices have to be expressed with respect to the axis of rotation by means of the Huygens-Steiner formula:

$$_{CM_i}^i \underline{J} = {}_{O_i}^i \underline{J} - m_i \left(\underline{r}_{i_{lcl}}^T \underline{r}_{i_{lcl}} \underline{I} - \underline{r}_{i_{lcl}} \underline{r}_{i_{lcl}}^T \right) \quad \text{for } i = 1, \dots, 3, \qquad (5.18)$$

$$\underline{r}_{i_{lcl}} = \begin{bmatrix} x_{i_{lcl}} & y_{i_{lcl}} & z_{i_{lcl}} \end{bmatrix}^T, \qquad (5.19)$$

where $_{CM_i}^i \underline{J}$ [kgm^2] is the inertia matrix of body i with respect to its center of mass, $_{O_i}^i \underline{J}$ is the estimated inertia matrix of body i with respect to the origin O_i of the body-fixed coordinate system $\underline{\vec{e}}^i$ and $r_{i_{lcl}}$ is the vector with the coordinates of the center of mass of body i in coordinate system $\underline{\vec{e}}^i$ with origin O_i.

5.3.2 Angular Velocity

The angular velocity, $^{ji}\vec{\omega}$ [rad/s], of coordinate system $\underline{\vec{e}}^j$ with respect to $\underline{\vec{e}}^i$, is determined using the additive property [51]. This property states that all relative angular velocities of a body can simply be summed in order to achieve the total angular velocity. This way the angular velocity of body 1 can be written as the sum of the angular velocities caused by its three rotations

$$^{10}\vec{\omega} = \dot{\theta}\vec{e}_1^0 + \dot{\psi}\vec{e}_2^{0\alpha} + \dot{\phi}\vec{e}_3^{0\beta} \qquad (5.20)$$

$$= \begin{bmatrix} \dot{\theta} + \dot{\phi}\sin(\psi) \\ \dot{\psi}\cos(\theta) - \dot{\phi}\cos(\psi)\sin(\theta) \\ \dot{\phi}\cos(\psi)\cos(\theta) + \dot{\psi}\sin(\theta) \end{bmatrix}^T \underline{\vec{e}}^0 \qquad (5.21)$$

Because body 2 can not rotate with respect to body 1 the following holds:

$$^{20}\vec{\omega} = {}^{10}\vec{\omega}. \qquad (5.22)$$

Finally, body 3 rotates about $\vec{e}_3^2$ with angle ϕ_{RM}, which results in:

$$^{30}\vec{\omega} = \dot{\theta}\vec{e}_1^0 + \dot{\psi}\vec{e}_2^{0\alpha} + \dot{\phi}\vec{e}_3^{0\beta} + \phi_{RM}\vec{e}_3^2 \qquad (5.23)$$

$$= \begin{bmatrix} \dot{\theta} + (\dot{\phi} + \dot{\phi}_{RM})\sin(\psi) \\ \dot{\psi}\cos(\theta) - (\dot{\phi} + \dot{\phi}_{RM})\cos(\psi)\sin(\theta) \\ (\dot{\phi} + \dot{\phi}_{RM})\cos(\psi)\cos(\theta) + \dot{\psi}\sin(\theta) \end{bmatrix}^T \underline{\vec{e}}^0 \qquad (5.24)$$

5.3.3 Kinetic and Potential Energy

The next step in the Lagrangian approach is to define the energy available in the system. The kinetic energy of the system is the sum of the translational and rotational kinetic energies of each body:

$$T = \frac{1}{2} \sum_{i=1}^{3} \left(m_i \dot{\vec{r}}_{CM_i} \cdot \dot{\vec{r}}_{CM_i} + {}^{i0}\vec{\omega} \cdot {}_{CM_i}^i J \cdot {}^{i0}\vec{\omega} \right), \qquad (5.25)$$

where m_i denotes the mass of body i, $^{i0}\vec{\omega}$ is the angular velocity of body i with respect to the fixed world and $_{CM_i^i}J$ is the inertia matrix of body i with respect to its center of mass.

The total potential energy of the system is the sum of the potential of the gravitational forces acting on each body and the energy stored in the system in spring-elements. Because there are no springs in the manipulator and no flexibility, i.e. rigid body, is included in the model the potential energy equation reduces to:

$$V = -\sum_{i=1}^{3} m_i \vec{g} \cdot \vec{r}_{CM_i}, \tag{5.26}$$

$$\vec{g} = \begin{bmatrix} 0 & 0 & -9.81 \end{bmatrix} \underline{\vec{e}}^0, \tag{5.27}$$

with $\vec{g}$ the gravitational acceleration vector.

5.3.4   Non-Conservative Generalized Forces

Since the platform will be floating, there is no friction except for air-drag acting on the floating platform, which is so small that it is neglected. In addition, there is friction in the bearings of the beam and the arm. However, the friction in the bearings is between the bodies, and does not effect the system. According to Newton's third law, the resulting force due to friction on the entire system is zero. Therefore, the electromagnetic suspension and propulsion will only have to compensate gravity and the forces and torques due to accelerations of the beam and the arm. For these reasons, friction is not included in the model.

Usually, actuator forces and torques are included in the dynamic equations together with friction and damping, as external non-conservative forces. In this case, the forces and torques of the 6 DOF electromagnetic suspension and propulsion, the forces of the linear motors and the torque of the rotary motor could be included as non-conservative generalized forces. However, since the trajectories are known and the electromagnetic suspension and propulsion only has to compensate the inertial forces and torques, it is more straightforward to include the forces and torques as constraint forces and torques. This results in an inverse dynamic analysis without a column of external forces and torques $\underline{\tau}$ and simplifies the calculation because only the constraint equation has to be solved. Therefore, the column with non-conservative generalized forces is zero:

$$\underline{Q}^{nc} = \underline{0} \tag{5.28}$$

5.3.5   Constraint Equations

The six DOF of the planar actuator, the position of the beam and rotation of the arm are measured and are following a prescribed trajectory in a feedback loop. Therefore, all motions are prescribed and can be included in the equations as driving constraints. From this formulation, the necessary forces to realize these trajectories are calculated. All constraints are included as velocity constraints and are written as:

$$\underline{h}_{nh} = \begin{bmatrix} \underline{\dot{q}} - \underline{\dot{u}}(t) \end{bmatrix} = \underline{0}, \tag{5.29}$$

where $\underline{u}$ is the column with measured positions of the platform, the beam and the arm. Because all velocity components appear as terms which are linear in the generalized coordinates, the constraints are rewritten as:

$$\underline{W}^T(\underline{q}, t)\underline{\dot{q}} + \underline{\tilde{w}}(\underline{q}, t) = \underline{0}, \tag{5.30}$$

where $\underline{W}(\underline{q}, t)$ is a (8×8) matrix which represents the velocity dependent components and has all ones on the diagonal in this case. The component $\underline{\tilde{w}}(\underline{q}, t)$, a (8×1) column with the remaining components that do not depend on $\underline{\dot{q}}$, i.e. $\underline{\dot{u}}$

Lagrange Multipliers

In order to incorporate the constraint equations in the equations of Lagrange, a (8×1) vector, $\underline{\lambda}$, of so called Lagrange multipliers is introduced. The Lagrange multipliers represent the constraint forces and torques:

$$\underline{\lambda} = [F_x \quad F_y \quad F_z \quad T_x \quad T_y \quad T_z \quad F_{LM} \quad T_{RM}]^T, \tag{5.31}$$

where F_x, F_y, F_z, T_x, T_y and T_z are the 6 DOF forces and torques of the platform, F_{LM} is the force of the beam and T_{RM} is the torque of the arm, which are necessary to realize the motion profile $\underline{u}$.

5.3.6 Equations of Motion

The equations of motion now follow from the equations of Lagrange:

$$\left(\frac{d}{dt}\left(\frac{\partial T}{\partial \underline{\dot{q}}}\right) - \frac{\partial T}{\partial \underline{q}} + \frac{\partial V}{\partial \underline{q}}\right)^T = \underline{W}\lambda. \tag{5.32}$$

The equations of Lagrange together with the constraint equations (Eq. 5.30) completely describe the dynamics of the system. In order to solve the equations they are rewritten and combined. Therefore, first the equations of Lagrange without constraints (i.e. $\underline{W}\lambda = \underline{0}$) are put in the following form:

$$\underline{M}(\underline{q})\underline{\ddot{q}} + \underline{H}(\underline{q}, \underline{\dot{q}}) = \underline{S}(\underline{q})\underline{\tau}, \tag{5.33}$$

where $\underline{M}(\underline{q})$ is the mass-matrix, $\underline{H}(\underline{q}, \underline{\dot{q}})$, a matrix with centripetal, Coriolis, friction and gravitational terms and $\underline{S}(\underline{q})$, the distribution of external forces and torques, $\underline{\tau}$. In this case, there are no external forces and torques so:

$$\underline{S}(\underline{q})\underline{\tau} = \underline{0}. \tag{5.34}$$

The next step is differentiating the constraint equations (Eq. 5.30) with respect to time:

$$\underline{W}^T(\underline{q}, t)\underline{\ddot{q}} + \underline{\bar{w}}(\underline{q}, \underline{\dot{q}}, t) = \underline{0}, \tag{5.35}$$

where

$$\underline{\bar{w}}(\underline{q}, \underline{\dot{q}}, t) = \frac{\partial \underline{\tilde{w}}(\underline{q}, t)}{\partial t} \quad + \left(\frac{\partial \underline{W}^T(\underline{q}, t)}{\partial t} + \frac{\partial \underline{W}^T(\underline{q}, t)\underline{\dot{q}}}{\partial \underline{q}} + \frac{\partial \underline{\tilde{w}}(\underline{q}, t)}{\partial \underline{q}}\right)\underline{\dot{q}}. \tag{5.36}$$

The total dynamics is now written as:

$$
\begin{bmatrix} \underline{M}(\underline{q}) & -\underline{W}(\underline{q},t) \\ \underline{W}^T(\underline{q},t) & \underline{0} \end{bmatrix} \begin{bmatrix} \underline{\ddot{q}} \\ \underline{\lambda} \end{bmatrix} + \begin{bmatrix} \underline{H}(\underline{q},\underline{\dot{q}}) \\ \underline{\bar{w}}(\underline{q},\underline{\dot{q}},t) \end{bmatrix} = \begin{bmatrix} \underline{0} \\ \underline{0} \end{bmatrix}. \tag{5.37}
$$

Next, an expression is derived for the Lagrange multipliers, which are the required forces and torques to realize a certain trajectory of the platform and manipulator. From Eq. 5.37 an expression for the generalized accelerations, $\underline{\ddot{q}}$, is now derived as:

$$
\underline{\ddot{q}} = \underline{M}^{-1}(\underline{q}) \left(-\underline{H}(\underline{q},\underline{\dot{q}}) + \underline{W}(\underline{q},t)\underline{\lambda} \right). \tag{5.38}
$$

Using this equation in the second line of Eq. 5.37 and solving for $\underline{\lambda}$ results in:

$$
\begin{aligned}
\underline{\lambda} &= \left(\underline{W}^T(\underline{q},t)\underline{M}^{-1}(\underline{q})\underline{W}(\underline{q},t) \right)^{-1} \tag{5.39} \\
&\quad \left(\underline{W}^T(\underline{q},t)\underline{M}^{-1}(\underline{q})\underline{H}(\underline{q},\underline{\dot{q}}) - \underline{\bar{w}}(\underline{q},\underline{\dot{q}},t) \right). \tag{5.40}
\end{aligned}
$$

So an expression for $\underline{\lambda}$ is now available in terms of $\underline{q}$, $\underline{\dot{q}}$ and t.

5.4 Extension of Lagrange into the Electromagnetic Domain

So far, only the mechanical energy in the system is considered without taking the energy in the magnets and coils into account. However, the forces and torques acting on the bodies in the system are the direct result of changes in the electromagnetic energy. There are four electromechanical conversions in the system:

1. **6 DOF planar actuator (PA)**
   This system contains a moving magnet array with 320 permanent magnets interacting with 81 stationary coils.

2. **Linear Motor 1 ($LM1$)**
   This is a ironless 3-phase motor with three moving coils and a static magnet array.

3. **Linear Motor 2 ($LM2$)**
   This is a ironless 3-phase motor with three moving coils and a static magnet array.

4. **Rotary Motor (RM)**
   This is a slotless 3-phase motor with 8 rotating magnet poles and a 3-phase stationary coil array.

5.4.1 Electromagnetic Energy for a Single Coil with a Single Magnet

The first step is to model a magnet as a single current loop, which in fact converts each permanent magnet into a single winding coil with a static current [53]. The energy stored in the electromagnetic field U_{em} [J] in a system with one coil and one magnet can then be written as [50, 53]:

$$
U_{em} = \frac{1}{2} L_c {i_c}^2 + L_{mc} i_m i_c + \frac{1}{2} L_m {i_m}^2 \tag{5.41}
$$

If no demagnetization of the permanent magnet occurs and temperature effects are neglected, the current i_m [A], representing the magnetization, is constant. In addition, the self inductances of the coil L_c [H = J/A^2 = Wb/A = Vs/A] and the current loop representing the magnet L_m [H] are assumed constant, because of the absence of iron and saturation. Then, the only varying parameters are the current in the coil and the mutual inductance L_{mc} [H] of the coil and the current loop. The mutual inductance L_{mc} [H] is given by [26]:

$$L_{mc} = \frac{N}{i_m i_c} \int_{V_c} \underline{A}_m \cdot \underline{J}_c dV_c, \tag{5.42}$$

where N [-] is the number of turns of the coil, V_c [m^3] the volume of the coil, $\underline{J}_c$ [A/m^2] the current density vector in the coil and $\underline{A}_m$ [J/(Am) = Wb/m = Vs/m] the magnetic vector potential corresponding with the magnetic field density $\underline{B}_m$ [T = Wb/m^2] of the current loop representing the magnets ($\underline{B}_m = \nabla \times \underline{A}_m$), [53]) only. This vector potential can either be calculated using analytical solutions of the Maxwell equations or by means of finite element analysis. Since the energy stored in the magnets does not change, neither with time, if temperature effects are neglected, nor with position or orientation, it is possible to eliminate this term:

$$U_{em} = \frac{1}{2} L_c i_c{}^2 + L_{mc} i_m i_c. \tag{5.43}$$

Now this equation is compared with Eq. 2.2, which is repeated here for clarity:

$$U_{em} = \frac{1}{2} \Lambda_c i_c + \Lambda_m i_c. $$

From Eq. 5.43 and Eq. 2.2 it can be concluded that the energy associated with the mutual inductance of current loops representing the magnet and the coil $L_{mc} i_m i_c$ is the same as the energy due to the flux linkage of the coils as a result of the field of the magnet $\Lambda_m i_c$ [J] and, therefore, the following holds:

$$\begin{aligned}
\Lambda_m &=& L_{mc} i_m, \\
&=& \frac{N}{i_c} \int_{V_c} \underline{A}_m \cdot \underline{J}_c dV_c. \tag{5.44}
\end{aligned}$$

5.4.2   Electromagnetic Energy in the System

With the basic equations from the previous section it is now possible to derive the electromagnetic energy in the system using the same assumptions:

$$\begin{aligned}
U_{em}^{sys} &=& U_{em}^{PA} + U_{em}^{LM1} + U_{em}^{LM2} + U_{em}^{RM}, \tag{5.45} \\
U_{em}^{PA} &=& \underline{\Lambda}_m^{PA} \cdot \underline{i}^{PA} + \frac{1}{2} \underline{L}^{PA} \underline{i}^{PA} \cdot \underline{i}^{PA}, \tag{5.46} \\
U_{em}^{LM1} &=& \underline{\Lambda}_m^{LM1} \cdot \underline{i}^{LM1} + \frac{1}{2} \underline{L}^{PA} \underline{i}^{LM1} \cdot \underline{i}^{LM1}, \tag{5.47} \\
U_{em}^{LM2} &=& \underline{\Lambda}_m^{LM2} \cdot \underline{i}^{LM2} + \frac{1}{2} \underline{L}^{PA} \underline{i}^{LM2} \cdot \underline{i}^{LM2}, \tag{5.48} \\
U_{em}^{RM} &=& \underline{\Lambda}_m^{RM} \cdot \underline{i}^{RM} + \frac{1}{2} \underline{L}^{PA} \underline{i}^{RM} \cdot \underline{i}^{RM}, \tag{5.49}
\end{aligned}$$

where $\underline{\Lambda}_m$ is a vector with flux linkages in each coil, due to the field of the magnet array, $\underline{i}$ is a vector with coil currents, $\underline{L}$ is a matrix with self inductance and mutual inductances of the coils and $\underline{R}$ is a matrix with the coil resistances. It is assumed that the flux linkages $\underline{\Lambda}_m$ only depend on the position of the coils with respect to the magnets and that other effects (saturation, eddy-currents, etc) are negligible and do not affect $\underline{\Lambda}_m$. In addition, the coils are assumed to be linear so that $\underline{L}$ and $\underline{R}$ do not depend on the current. These assumptions are the same as the ones made in Chapter 2 to derive the forces and torques on the planar actuator.

This expression for the electromagnetic energy can now be included in the Lagrange equation. First, a new vector of generalized coordinates is defined:

$$\underline{q}_{em} = \left[\begin{array}{ccccc} \underline{q}^T & \left(\underline{c}^{PA}\right)^T & \left(\underline{c}^{LM1}\right)^T & \left(\underline{c}^{LM2}\right)^T & \left(\underline{c}^{LM3}\right)^T \end{array} \right]^T, \qquad (5.50)$$

where $\underline{c}$ is a vector with the time integral of the coil currents of each subsystem. Then, the lagrange equation becomes:

$$\frac{d}{dt}\left(\frac{\partial T}{\partial \underline{\dot{q}}_{em}}\right) - \frac{\partial T}{\partial \underline{q}_{em}} + \frac{\partial V}{\partial \underline{q}_{em}} + \frac{d}{dt}\left(\frac{\partial U_{em}^{sys}}{\partial \underline{\dot{q}}_{em}}\right) - \frac{\partial U_{em}^{sys}}{\partial \underline{q}_{em}} = \left(\underline{Q}^{nc}\right)^T, \qquad (5.51)$$

where the constraint term $\underline{W}\lambda$ is omitted but the term with non-conservative generalized forces $\left(\underline{Q}^{nc}\right)^T$ reappears. This term includes all the external amplifier voltages ($\underline{u}_{ext}$ [V]) on the coils and the dissipation in the coils due to the internal resistance:

$$\left(\underline{Q}^{nc}\right)^T = \left[\begin{array}{c} \underline{0} \\[2ex] \underline{u}_{ext}^{PA} - \underline{R}^{PA}\underline{\dot{c}}^{PA} \\[2ex] \underline{u}_{ext}^{LM1} - \underline{R}^{LM1}\underline{\dot{c}}^{LM1} \\[2ex] \underline{u}_{ext}^{LM2} - \underline{R}^{LM2}\underline{\dot{c}}^{LM2} \\[2ex] \underline{u}_{ext}^{RM} - \underline{R}^{RM}\underline{\dot{c}}^{RM} \end{array} \right]. \qquad (5.52)$$

The first term in $\underline{Q}^{nc}$ could also include eddy current damping or mechanical damping but this is assumed to negligible and, therefore, the $\underline{Q}^{nc}$ entry related to the mechanical part is $\underline{0}$. The electromagnetic equivalent of potential energy V is a capacitor, but except for negligible parasitic effects, capacitors are not present in the electromechanical conversion and are, therefore, not considered. When these equations are worked out, the set of equations is found for the full dynamics including the electromechanical interaction according to Eq. 5.53. The inputs of the total system are the voltages that are applied on the terminals of the coils. Furthermore, it is clear that for all coils the entire voltage equation is included in the dynamic equations (compare with Eq. 4.4). Finally, it is shown that the mechanical forces and torques of each coil originate from the spatial jacobian of the flux linkage multiplied by the current in the coil itself. In addition, the same jacobian multiplied with derivative of the positions and orientations gives the back-EMF in the voltage equations. In Appendix A, the equations are worked out for a simple example. The only drawback is the large number of DOF involved (8+81+3+3+3=98), which

$$
\begin{bmatrix} \underline{0} \\[4pt] \underline{u}_{ext}^{PA} \\[4pt] \underline{u}_{ext}^{LM1} \\[4pt] \underline{u}_{ext}^{LM2} \\[4pt] \underline{u}_{ext}^{RM} \end{bmatrix} = \begin{bmatrix} \underline{M}(\underline{q}) & \underline{0} & \underline{0} & \underline{0} & \underline{0} \\[4pt] \underline{0} & \underline{L}^{PA} & \underline{0} & \underline{0} & \underline{0} \\[4pt] \underline{0} & \underline{0} & \underline{L}^{LM1} & \underline{0} & \underline{0} \\[4pt] \underline{0} & \underline{0} & \underline{0} & \underline{L}^{LM2} & \underline{0} \\[4pt] \underline{0} & \underline{0} & \underline{0} & \underline{0} & \underline{L}^{RM} \end{bmatrix} \begin{bmatrix} \ddot{\underline{q}} \\[4pt] \ddot{\underline{c}}^{PA} \\[4pt] \ddot{\underline{c}}^{LM1} \\[4pt] \ddot{\underline{c}}^{LM2} \\[4pt] \ddot{\underline{c}}^{RM} \end{bmatrix} + \begin{bmatrix} \underline{H}(\underline{q},\dot{\underline{q}}) \\[4pt] \underline{0} \\[4pt] \underline{0} \\[4pt] \underline{0} \\[4pt] \underline{0} \end{bmatrix}
$$

$$
+ \begin{bmatrix} 0 & -\frac{\partial \underline{\Lambda}_m^{PA}}{\partial \underline{q}} & -\frac{\partial \underline{\Lambda}_m^{LM1}}{\partial \underline{q}} & -\frac{\partial \underline{\Lambda}_m^{LM2}}{\partial \underline{q}} & -\frac{\partial \underline{\Lambda}_m^{RM}}{\partial \underline{q}} \\[8pt] \left(\frac{\partial \underline{\Lambda}_m^{PA}}{\partial \underline{q}}\right)^T & \underline{R}^{PA} & \underline{0} & \underline{0} & \underline{0} \\[8pt] \left(\frac{\partial \underline{\Lambda}_m^{LM1}}{\partial \underline{q}}\right)^T & \underline{0} & \underline{R}^{LM1} & \underline{0} & \underline{0} \\[8pt] \left(\frac{\partial \underline{\Lambda}_m^{LM2}}{\partial \underline{q}}\right)^T & \underline{0} & \underline{0} & \underline{R}^{LM2} & \underline{0} \\[8pt] \left(\frac{\partial \underline{\Lambda}_m^{RM}}{\partial \underline{q}}\right)^T & \underline{0} & \underline{0} & \underline{0} & \underline{R}^{RM} \end{bmatrix} \begin{bmatrix} \dot{\underline{q}} \\[4pt] \dot{\underline{c}}^{PA} \\[4pt] \dot{\underline{c}}^{LM1} \\[4pt] \dot{\underline{c}}^{LM2} \\[4pt] \dot{\underline{c}}^{RM} \end{bmatrix} \qquad (5.53)
$$

requires solving 106 differential equations simultaneously. Of course, the result of the Lagrangian approach corresponds with the analysis done in Chapter 2 from Eq. 2.33 to Eq. 2.49, which basically only discusses the following part of Eq. 5.53:

$$
\begin{bmatrix} \underline{F} \\ \underline{T} \end{bmatrix} = \begin{bmatrix} \frac{\partial \underline{\Lambda}_m^{PA}}{\partial \underline{x}} \\[8pt] \frac{\partial \underline{\Lambda}_m^{PA}}{\partial \underline{y}} \\[8pt] \frac{\partial \underline{\Lambda}_m^{PA}}{\partial \underline{z}} \\[8pt] \frac{\partial \underline{\Lambda}_m^{PA}}{\partial \underline{\theta}} \\[8pt] \frac{\partial \underline{\Lambda}_m^{PA}}{\partial \underline{\psi}} \\[8pt] \frac{\partial \underline{\Lambda}_m^{PA}}{\partial \underline{\phi}} \end{bmatrix} \begin{bmatrix} \dot{\underline{c}}^{PA} \end{bmatrix} = \underline{K} N \underline{i} \qquad (5.54)
$$

$$\underline{E}_{EMF} = \begin{bmatrix} \dfrac{\partial \underline{\Lambda}_m^{PA}}{\partial \underline{x}} \\[1.2em] \dfrac{\partial \underline{\Lambda}_m^{PA}}{\partial \underline{y}} \\[1.2em] \dfrac{\partial \underline{\Lambda}_m^{PA}}{\partial \underline{z}} \\[1.2em] \dfrac{\partial \underline{\Lambda}_m^{PA}}{\partial \underline{\theta}} \\[1.2em] \dfrac{\partial \underline{\Lambda}_m^{PA}}{\partial \underline{\psi}} \\[1.2em] \dfrac{\partial \underline{\Lambda}_m^{PA}}{\partial \underline{\phi}} \end{bmatrix}^T \begin{bmatrix} \dot{x} & \dot{y} & \dot{z} & \dot{\theta} & \dot{\psi} & \dot{\phi} \end{bmatrix}^T . \tag{5.55}$$

The beauty of deriving the dynamic equations using Lagrange is that with one comprehensive analysis all system dynamics can be included, even from different domains, i.e. mechanical and electromagnetic. In addition, it is a top-down approach (everything is derived from the total energy in the system), while in Chapter 2 a bottom-up approach is used (superposition of Lorentz actuators). Finally, the energy approach derived using Lagrange has close resemblance with the virtual work method that is often used to calculate forces and torques in electromagnetic systems.

5.4.3   Application of the Full System Dynamic Equations

The system of differential equations describing the dynamics of both the mechanics and electromagnetics is useful for analyzing the energy flow in the system. For a certain desired trajectory it is possible to calculate the forces and torques on the bodies, which result in coil currents by applying the commutation law (Eq. 2.34). The trajectories give rise to back-EMF voltages in the coils and together with the currents predicted by the commutation law, the external voltages are calculated from the electrical equations. In Chapter 2, all these items have been discussed separately for the planar actuator.

However, with the equations derived in this chapter, the interaction and energy flow can be calculated directly for the full system. By solving all states of Eq. 5.53, the combined power input from the power amplifiers to the coils is found, which is necessary to specify the required output of the main power supply of the planar actuator and the power supply on the platform for the motors of the manipulator. Moreover, the conversion of electromagnetic energy to mechanical energy is verified, thereby validating the correctness of the calculations of the coil currents and flux linkages, by comparing the product of back-EMF and current with the product of force and speed as well as torque and angular speed.

It is recommended that a Lagrangian approach is used for the design itself, instead of verifying the correctness of various other models afterwards as has been done in this thesis. The multi-level contactless motion system is complicated due to the moving center of mass of the system. With this approach it is possible to include knowledge of the motion profile and duty-cycle of a dedicated application in the design, which results in realistic topologies without the need to make very
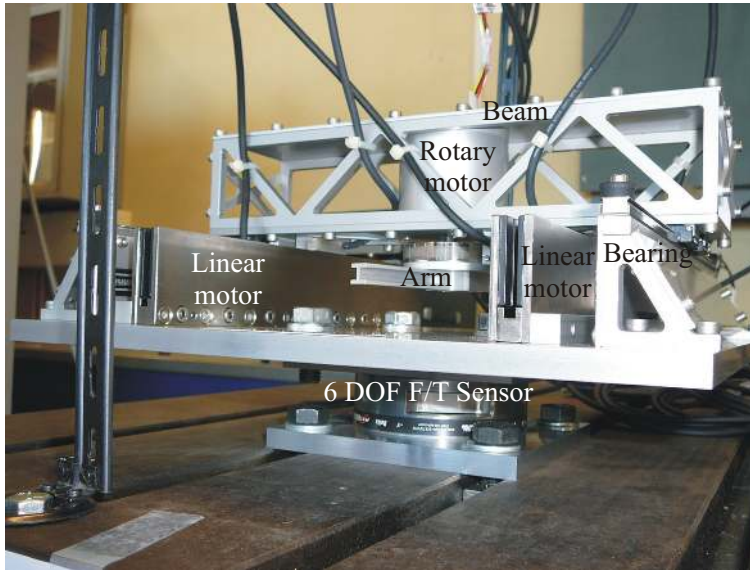
Figure 5.3: Experimental setup with the manipulator mounted on top of a 6 DOF F/T sensor

conservative thermal estimates. A set of differential equations of the full system dynamics enhances the understanding of the system and it is easily suitable for extensions, e.g. including and controlling non-rigid body modes [79] or non-linear electromagnetic effects [26]. However, a separate model will always be necessary to calculate the Jacobian of the flux-linkages, which can be either analytical, numerical or a combination of the two.

5.5 Experimental Verification of the Equations of Motion

A real manipulator is built and this experimental setup is used for verification purposes. The manipulator is placed on a 6 DOF F/T sensor (ATI Delta SI-165-15) which can measure forces and torques in three directions. The beam and the arm of the manipulator are moving and the trajectories and the resulting forces and torques on the sensor underneath the platform are measured. The measured reaction forces and torques are equal in magnitude to the forces and torques necessary to stabilize the platform in case it is floating. An aluminum plate replaces the planar actuator platform. A photo of the experimental setup is shown in Figure 5.3.

5.5.1 Identification of Non-Rigid Body Dynamics

The derived multi-body dynamics model assumes that all bodies are rigid, therefore, frequency response function measurements of the three motors and of the 6 DOF F/T sensor are done using Spectral Dynamics SigLab 20-42 to verify

this assumption.

Identification of the 6 DOF F/T Sensor

For the 6 DOF F/T sensor a force or torque is applied using a impuls hammer for one direction at a time. The impuls hammer has a analog voltage output proportional to the applied force and, in the case of a torque, an arm is introduced to convert the applied force to an applied torque. The forces and torques are applied at the bottom plate of the manipulator.

The 6 DOF F/T sensor has six analog outputs and each analog output is proportional with the applied force or torque in a particular direction. The frequency response function (FRF) between the output voltage of the impuls hammer and the output voltage of the 6 DOF F/T sensor is then determined using the Siglab spectrum analyzer. The measured frequency response functions are shown in Figure 5.4. The main resonances of the 6 DOF F/T sensor are around 400 Hz for F_x and F_y and 800 Hz for F_z, which is outside the measured range. The resonances of T_x, T_y, and T_z are about 150 Hz. Furthermore, a lot of other resonances are visible starting around 80 Hz, which are related to the mechanical construction of the manipulator.

Furthermore, it is visible that at low frequencies the gain of the 6 DOF F/T sensor frequency response functions is not equal to 0 dB but slightly lower. This implies that there is a gain in the sensor measurements and that the sensor was not properly calibrated by the manufacturer. Static measurements showed that the gain was approximately 0.7.

Identification of the Motors

The frequency response functions of the 3-phase current amplitude to position of the linear motors and the rotary motor are measured as well. First, the motor is moved along a constant velocity trajectory with a low bandwidth (i.e. 10 Hz) PD controller. Then band-limited white noise is added to the control signal of the PD controller and the frequency response function between the noise and the control signal with noise is measured which is equal to the sensitivity of the plant. The frequency response function of the plant is obtained from the measured sensitivity function and the known controller function.

All motors are treated as single-input-single-output (SISO) systems and their corresponding frequency response functions are shown in Figure 5.5, Figure 5.6 and Figure 5.7. The frequency response function of the linear motors (Figure 5.5 and Figure 5.6) are almost completely identical, which is logical considering the fact that the motors are of the same type and connected through a stiff beam. Therefore, each motor delivers half of the force F_{LM} on the beam. Furthermore, a lot of resonances are visible from 80 Hz which are most likely related to the limited stiffness of the bearings and the bearing supports. The resonances show some resemblance with the resonances measured at the 6 DOF F/T sensor.

The frequency response function of the rotary motor (Figure 5.7) has a first resonance at approximately 400 Hz and has a much better characteristic than the linear motors. The resonance is due to the limited stiffness of the axle between the rotor of the motor and the encoder ring.
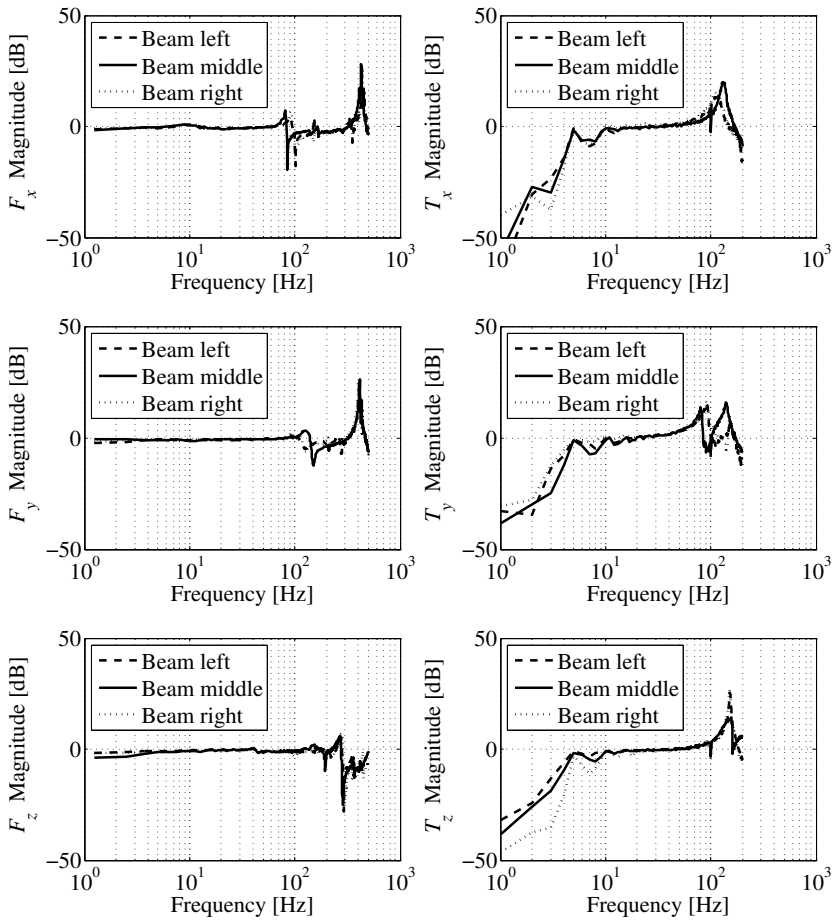
Figure 5.4: Measured frequency response function magnitude of force and torque input to measurement of the 6 DOF F/T sensor
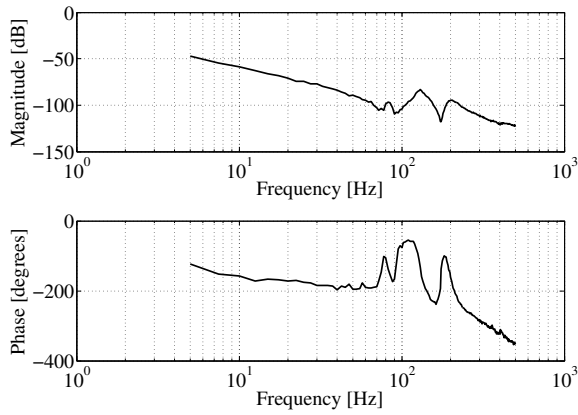
Figure 5.5: Measured frequency response function of motor current amplitude to position of linear motor 1
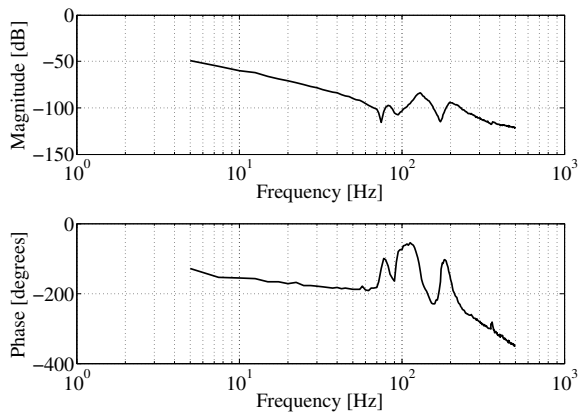

Figure 5.6: Measured frequency response function of motor current amplitude to position of linear motor 2
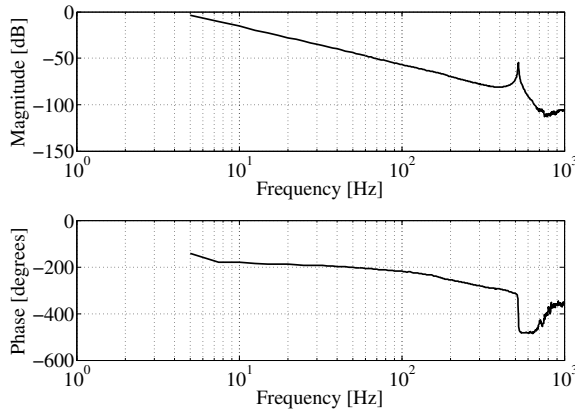
Figure 5.7: Measured frequency response function of motor current amplitude to rotation of the rotary motor

Validity of the Rigid-Body Assumption

These measurements show that the first resonances due to flexibilities in the system occur at 80 Hz, which implies that the rigid body assumption is only valid up to this frequency. Therefore, all measurements are filtered offline using a fourth order butterworth filter with a cut-off frequency of 80 Hz and the anti-causal filtering function *filtfilt* in Matlab to eliminate phase-lag by the butterworth filter. The linear motors each have a SISO PID controller with a bandwidth of 20 Hz and a first order low-pass filter at 70 Hz to limit the excitation of unmodeled non-rigid-body dynamics. The rotary motor has a PID controller with a bandwidth of 50 Hz and a first order low-pass filter at 300 Hz. More advanced control strategies can be incorporated but they are not within the scope of this research project [82].

5.5.2   Verification of the Constraint Forces and Torques

The trajectories of $\underline{q}$ are zero except for the movement y_{LM} of the beam and ϕ_{RM} of the arm. The measured trajectories are now applied as inputs for the multi-body model, which is used to calculate the necessary constraint forces and torques in order to keep the platform in the original position. Since the movement of the beam is in the $\vec{e}_2^1$ direction, the force in the $\vec{e}_2^1$-direction (F_y) and the torque around the $\vec{e}_1^1$-axis (T_x) are dominant. The model predictions and the measured values of F_y, T_x and T_z are shown in Figure 5.8. The torque around the $\vec{e}_3^1$-axis (T_z) is associated with the applied torque by the rotary motor that drives the arm. From the predicted and measured values in Figure 5.8 it can be concluded that the model predictions and measurements of F_y and T_x match well, although the relative errors are still in the range of 5-10%. The remaining errors are caused by inaccurate model parameters such as mass and moments of inertia, since these parameters are estimated from the CAD model. Moreover, it was found that the 6 DOF F/T sensor was not properly calibrated, so the model parameters were not adjusted using the measurement data. The measured torque around the $\vec{e}_3^1$-
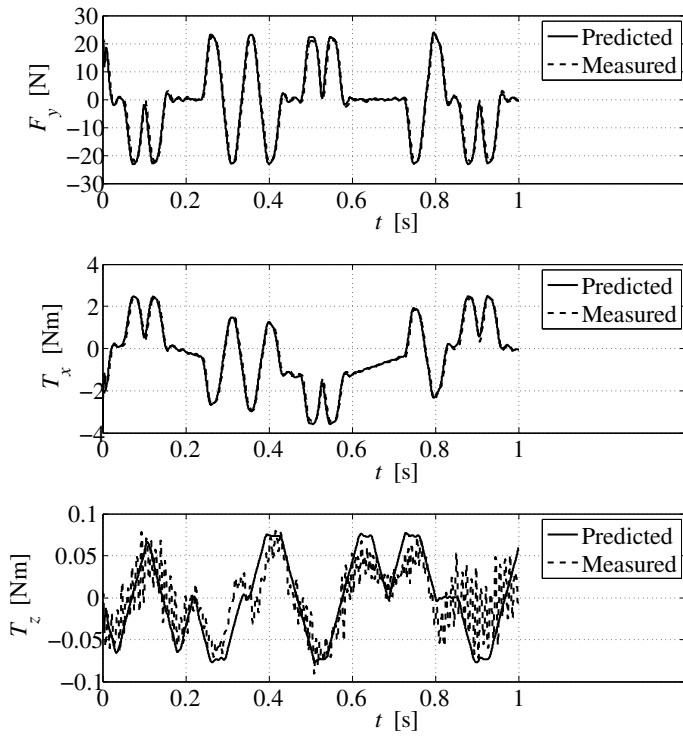
Figure 5.8: Prediction and measurement of the force in $\vec{e}_2^1$-direction, the torque around the $\vec{e}_1^1$-axis and the torque around the $\vec{e}_3^1$-axis

axis T_z looks very similar to the model predictions, however, the values are in the same range as the noise on the sensor signal in that direction. Therefore, it is not possible to draw strong conclusions from these measurements.

5.6   Conclusions

In this chapter, the dynamics of the system have been described. First, the manipulator that is put on top of the planar actuator has been discussed.

Second, the multi-body dynamics of the manipulator on top of a floating platform have been modeled using a Lagrangian approach. The model is suitable to describe the interaction between the manipulator and the electromagnetic suspension and propulsion of the planar actuator and can predict the forces and torques necessary to move the planar actuator with manipulator along a certain trajectory.

Third, the Lagrangian approach has been extended into the electromagnetic domain, which allows to include the dynamic equations of the coil currents and the electromechanical interaction between coil currents and moving magnets into a single set of dynamic equations together with the equations of the multi-body dynamics. The result is a comprehensive framework, suitable for transient simulation of the system, which is much more elegant than putting the results of all separate systems together. It has been used to specify the requirements for the power amplifiers that drive the coils in the electromagnetic suspension and the motors. In addition, the correctness of the calculation of coil currents and flux linkages has been checked with the full dynamic model by validating the conversion of electrical energy to mechanical energy.

The model describes the dynamics in both the mechanical as electromagnetic domain of the contactless planar actuator with a moving center of mass and can be easily extended to include and control non-rigid body dynamics or non-linear electromagnetic effects. It is recommended to use this comprehensive model for the design itself instead of verification afterwards, in future applications with known motion profiles and duty-cycles.

Finally, the manipulator multi-body dynamics have been verified with measurements, which showed that the rigid-body assumption is valid up to 80 Hz. Additionally, the capability of the model to predict the forces and torques necessary to move the multi-level contactless motion system along a certain trajectory has been validated.

WIRELESS CONTROL SYSTEM

The manipulator on top of the floating platform needs to be controlled in synchronization with the electromagnetic suspension and propulsion. Furthermore, in order to ensure accurate positioning of the tool center point (TCP) in 3D space, it is necessary to know the position of the platform and the position of the TCP of the manipulator, i.e. the tip of the arm of the manipulator with respect to the platform in real-time. Finally, the movement of the contactless planar actuator and of the manipulator will influence each other, which requires feedforward compensation. The realization of these functions requires a real-time wireless communication link between the ground controller of the electromagnetic suspension and propulsion and the floating platform. Ideally, the controller of the manipulator is located on fixed world, together with the controller of the electromagnetic suspension and propulsion, which requires the entire control loop of the manipulator to be wireless.

As discussed in Section 1.2.3, in existing literature regarding wireless control, the standard wireless protocols for data transmission are used that are designed for high data throughput, not for a small delay. Observers or predictors are used to estimate the delay [64, 69, 71, 72, 74] and theory is developed to prove stability [73, 75]. Although these techniques can improve the performance of the feedback loop, it will never work better than greatly reducing the delay itself. The inverted pendulum wireless control loops discussed in [59, 65] show errors in the range of 10 degrees (0.2 rad) or worse with wireless communication delays of at least several milliseconds, which is not realistic for a high precision application.

In this chapter, a first attempt is made to define a protocol that reduces the transmission delay to a minimum. First, it is investigated, which factors are important for wireless real-time communication in motion control applications both in qualitative as in quantitative sense. Then the protocol itself is described as well as how it is implemented. Finally, measurements are presented that show the behavior of the wireless real-time communication in a motion control system. The proposed real-time wireless link is published in [89, 91, 96].

6.1 Technical Background

First, the requirements for a real-time wireless link are discussed, which are then compared with the characteristics of currently existing wireless techniques. Finally, a choice is made for the wireless channel and the protocol.

6.1.1 Requirements for a Real-Time Wireless Link

There are three characteristics that are very important for a real-time wireless link:

1. **Accuracy**
   The accuracy of the wireless link has to be sufficient to send high precision position information.

2. **Delay** δ
   The delay or latency is the time necessary to transmit data from the transmitter to the receiver. This has to be as short and constant as possible.

3. **Datarate** d_r
   The datarate is the amount of data that can be sent per second over the wireless channel.

Accuracy

In high precision systems, position is measured in micrometers or even nanometers. For a linear motor with a stroke of one meter and an accuracy of 1 μm, this implies a precision of 20 bits. This prohibits the use of fully analog techniques, since it will be difficult, if not impossible, to maintain the precision. Therefore, the information should be sent digitally.

Delay

A major issue is the definition of real-time, which has different meaning, depending on the application. In motion control, closed loop delay is one of the characteristics that determines the performance (i.e. bandwidth) of the controlled system. To investigate the influence on the control bandwidth a stabilizing lead-lag-filter with a zero at one-third of the bandwidth and a pole at three times the bandwidth is assumed. This results in approximately 50° phase lead at the control bandwidth [54] and with a phase margin of 30°, the following holds for the maximum bandwidth f_{bw} for a given closed loop delay δ_{cl}:

$$f_{bw} \quad = \quad \frac{50 - 30}{360 \; \delta_{cl}} \tag{6.1}$$

In a plant the delay due to the sensor delay, actuator delay and computing time is typically 1 ms, so adding another 1 ms by the wireless links reduces the maximum controller bandwidth from 56 Hz to 28 Hz. Since there are two wireless links in the loop, the maximum permissable delay for one link is only 500 μs. In high precision motion systems, with closed loop bandwidth requirements up to several hundreds of Hertz, this delay is still unacceptable, so a further reduction of the delay is desirable. However, the requirement of 500 μs is used as a start to benchmark the suitability of existing wireless techniques for wireless motion control.

Delay can be split into two parts:

1. **Static Delay**
   This type of delay is always the same and is caused by processing of the data in the protocol and the limited datarate. This can be kept small by using a simple protocol with small data packets and a wireless channel with a high datarate.

2. **Stochastic Delay**

   This is delay that is not constant but varies in time, mainly due to the retransmission of wrongly received data. The variation of the total delay is called jitter and is caused by this stochastic delay, which is purely related to the protocol. Moreover, retransmission of data from a previous controller sample time is not useful for control applications, since it is better to receive the next data packet than to waste time by retransmitting the old one. Other phenomena such as routing also contribute to stochastic delay.

Datarate

The datarate of the wireless channel directly influences the delay: if the datarate is doubled than the time needed to transmit a packet through the wireless channel will halve. The datarate strongly depends on the frequency of the electromagnetic wave used to transmit the data and the modulation technique, e.g. in optical systems datarates of Gbps are possible, the currently available WLAN operates at 54 Mbps.

The datarate necessary to realize a wireless motion control system needs to be estimated. Each position measurement is about 20 bits accurate (1 μm resolution for a 1 m stroke). The sample frequency f_s of the controller is at least 1 kHz, although higher frequencies are increasingly common (up to 20 kHz in nm stages). A significant amount of actuators are single phase or 3-phase motors, which require one or two current setpoints, respectively, estimated at 10 bit per setpoint. If the commutation of the 3-phase motor is done locally, only one current amplitude setpoint is necessary. Finally, several enable and status bits are necessary to operate a motor. The manipulator consists of three 3-phase motors and from this discussion it is assumed that 64 bits of data per packet is sufficient to transmit the necessary information. However, in wireless data transfer additional bits are necessary to encode the data into packets. Assuming, that about two times the number of data bits is required and that 64 bits of data is sent at 2 kHz, the required datarate is finally estimated at 256 kbps.

6.1.2 Characteristics of Existing Wireless Techniques and Protocols

Several wireless techniques are currently available that send digital information, such as Bluetooth, WLAN, DECT, and Zigbee [55, 57, 58, 61]. Usually these protocols have strong links to the hardware implementation, but in principle any medium could be used to transmit the bits. All of these techniques operate in the 2.4GHz ISM frequency band and their characteristics are listed in Table 6.1. From this table it is clear that all techniques have sufficient bandwidth. However, none of the techniques is able to meet the minimum delay specification of 500 μs. Another interesting characteristic is the difference between WLAN TCP/IP and WLAN UDP/IP. The delay for TCP/IP is about ten times higher than for UDP/IP. This is caused by the fact that UDP/IP is designed for streaming video transfer over internet and does not use packet retransmission, i.e. wrongly received packets are not sent again. To meet the delay specification of 500 μs, it is necessary to develop a new protocol.

Table 6.1: Characteristics of several wireless communication techniques

Communication technique	Bandwidth	Minimum delay
Bluetooth	1 Mbps [55]	7 ms [56, 65]
IEEE 802.11b WLAN (TCP/IP)	11 Mbps [57]	20-25 ms [56]
IEEE 802.11b WLAN (UDP/IP)	11 Mbps [57]	1.78 ms [59]
Zigbee	250 kbps [61]	15 ms [60]
DECT	384 kbps [58]	3-24 ms [58]

6.2 Implementation of a Custom Protocol

The delay requirement of the wireless system can only be met by means of a custom protocol with small packets that only consist of data and a minimum of additional overhead. Packet retransmission is omitted, since it is undesired in control applications, i.e. only the most recent data is relevant. This is not valid, if the wireless link is fast enough to send multiple packets within one controller sample time. However, this is certainly not the case with existing technologies. Considering that wireless motion control is confined to a machine or system, routing is omitted, since the inclusion of such a wireless control system needs to be incorporated from the start of the machine design. A smart use of channels and the limited range of transmission media enables routing on a hardware level.

6.2.1 Structure of the Packets

The wireless link must transmit 64 bits of data in a packet. How this data is acquired will be discussed later in this section. As discussed previously, the packet must be as small as possible to minimize the delay of the transmission. However, some overhead is absolutely necessary to ensure the correct transmission of the data:

1. **Start bits**
   The beginning of the packet is marked with sixteen start bits that are the same for every packet. This ensures that the beginning of each packet is recognized by the receiver.

2. **CRC-16**
   To verify the validity of the data bits a 16 bit key is sent with the data to perform a cyclic redundancy check (CRC). CRC is a polynomial code, which means that bit strings are treated as a representations of polynomials with coefficients of 0 and 1 only. The CRC-algorithm is an error detection code and can be put in the following general form:

$$M(x)x^n = Q(x)K(x) + R(x). \tag{6.2}$$

Here $M(x)$ is the original message polynomial, 64 bits of data, $K(x)$ is the key polynomial, with degree n. The bits of $M(x)x^n$ are the original message with n zeros appended at the end. $R(x)$ is the remainder polynomial, which

is the CRC. In communication, the sender attaches the n bits of R after the original message bits of M and sends it to the receiver. The receiver takes M and R and checks whether $M(x)x^n - R(x)$ is divisible by $K(x)$. If it is, then the receiver assumes the received message bits are correct. From measurements at different data rates, a CRC-16-IBM ($n = 16$) code was found to be required to detect all errors. CRC-16-IBM is also used in USB. The key polynomial is $1 + x^2 + x^{15} + x^{16}$.

3. **8b10b encode**
   The data transmission is asynchronous, which implies that the transmitter and the receiver do not operate with the same clock. Therefore, the clock rate of the transmission needs to be recovered. To be able to do so, there must be sufficient transitions between zeros and ones in the bitstream of the transmission. The 8b10b encoding guarantees that there are no more than three consecutive zeros or ones in the bitstream to accommodate the clock-recovery. The number of bits, however, increases with 25%.

4. **Error detection bits**
   Since the packet is very small, it is expected that a maximum of 1 bit per packet will be wrong. A Hamming code of 7 bits is added to the packet, which can correct a single erroneous bit and detect two.

Based on this structure of the packet, the total packet size n_p will be:

$$16 \text{ Start} + 1.25 \times (64 \text{ Data} + 16 \text{ CRC}) + 7 \text{ Hamming} = 123 \text{ bits}. \qquad (6.3)$$

As can be concluded from the description of the packet, its structure is very basic and stripped of anything that is not absolutely necessary. Although it seems simple, such an approach is not documented in literature, but offers great advantages for real-time motion control by minimizing the delay.

6.2.2   Hardware

The implementation of such a protocol requires a transceiver without any embedded protocol. A lot of transceiver chips for standard techniques (WLAN, bluetooth, DECT, Zigbee) have parts of the protocol embedded in the hardware and are, therefore, unsuitable for the development of custom protocols. Unfortunately, any protocol is strongly related to its hardware implementation so this is also included in the discussion.

Optical techniques such as laser and infrared are not considered, since they require line-of-sight (LOS). This is hard to achieve for a platform that has a long-stoke movement in a plane. The advantage of optical systems is a high bandwidth and low bit-error-rates (BER), due to the limited interference, but the LOS requirement makes it more difficult to implement. In a system with a purely rotating or linear movement, optical systems are more feasible.

Another option is to use an inductive coupling to transmit a high frequency signal to a moving target [38, 66], which could be added to the power transfer signals. However, since the active coil depends on position of the moving multi-level contactless motion system, switching is necessary and this would interrupt
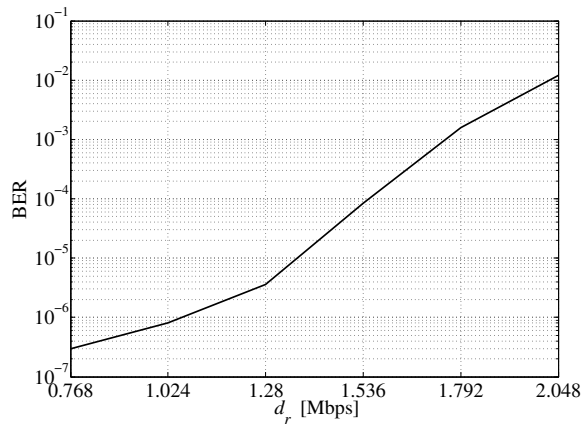
Figure 6.1: BER measurement of ML2724SK-02 transceiver

the data transfer. Therefore, radio waves are an attractive choice for the wireless data transfer, in particular the unlicensed 2.4 GHz ISM band.

There are not many commercially available radio transceivers that have no embedded protocol, so the choice is limited. Moreover, RF design requires specific skills and is time consuming. To overcome these issues a ready-to-use RF starters kit (ML2724SK-02 from Micro-Linear [62]) is used that is based on a 1.5 Mbps FSK transceiver. If the transceiver is used as a transmitter it converts zeros and ones on the input to an RF antenna signal. When the transceiver is used as receiver, the RF antenna signal is converted back to zeros and ones on the output. Due to filtering of the RF signal, variation of the time of each bit (jitter) and noise, not all bits are received correctly. In Figure 6.1 the bit-error-rate (BER) is measured at different datarates. Since the packetsize is 123 bits, datarates higher than 1.5 Mbps are unacceptable due to the high BER. Moreover, this measurement is done with only one link. In the final setup the transmission will be full-duplex, i.e. simultaneously transmitting and receiving in two directions, so there will be two transmitters and two receivers, which will interfere with each other. Therefore, it is expected that the BER in the full-duplex system will be worse than this measurement.

High-gain, directional antennas are used to limit the interference between the channels and the influence of other 2.4 GHz transmitters in the lab such as the WLAN router, since the transmitter and receiver will only be one or two meters apart. The transceiver has a adjustable amplifier to change the RF signal strength from the antenna. To prevent clipping of the signal, the gain is automatically adjusted by a microcontroller. This hardware choice of the wireless communication channel is by no means optimal, but given the commercial availability it is the best option.

The protocol itself is implemented on an FPGA (Xilinx Spartan IIE [63]). An FPGA is chosen, since it allows parallel execution of code. Moreover, integer arithmetic is very fast due to the use of interconnected logic gates. In addition, it can execute several threads at different clock rates, making the FPGA a flexible
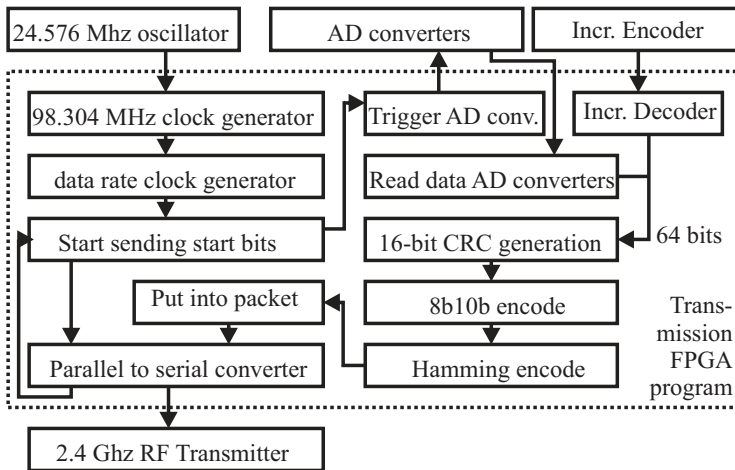
Figure 6.2: Schematic of FPGA transmitter protocol

development platform. The communication between the FPGA and the outside world (sensors, amplifiers and DSP) is done by means of digital IO and AD/DA conversion.

Transmitter Protocol

Several operations are performed by the FPGA to send data by one of the wireless transmitters (Figure 6.2). First, the sending of the start bits to the parallel-to-serial converter is started. While these bits are being sent, the DA converters are triggered and the data is acquired from the AD converters or the incremental decoder. In a single clock cycle, a CRC-16 is calculated from this data, the 64 bits and CRC bits together, are 8b10b encoded, followed by the calculation of the Hamming correction parity bits. This data is added to the packet behind the start bits, just before all start bits are sent. Finally, the rest of the packet is put into the parallel-to-serial converter, driving the transmitter with this serial data. The timing of this A/D trigger assures that the most recent data is sent. The parallel-to-serial converter triggers the transmission of the next packet.

Receiver Protocol

To retrieve the data correctly from the receiver and to deal with the asynchronous reception, a 16x oversampling and clock recovery algorithm has been implemented. The clock recovery is required because the oscillator (24.756 MHz) of the transmitter will never have exactly the same oscillation frequency as the oscillator at the receiver. Oversampling is also a necessity caused by each received bit period deviating from the average value (jitter). A Moore state machine [68] is used as the oversampling algorithm (Figure 6.3). When 9 consecutive samples are recognized with the same value, it is recognized as a valid input-bit. This algorithm
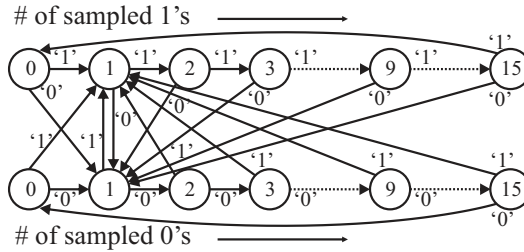
Figure 6.3: Moore state machine for the oversampling algorithm

also automatically recovers the clock from the data, hence it is known as a DCR (Digital Clock Recovery) circuit. This oversampling algorithm also compensates for the jitter (variations in bit duration). However, the algorithm only works properly when sufficient logical transitions are present in the data. To ensure sufficient logical transitions, an 8b10b encode has been applied.

While each bit is being received using the oversampling algorithm, each bit is concatenated into a 16-bit register like a sliding window. The data in the register is compared with the start bits. When the data in the shift register is equal to the start bits, a signal is generated which will trigger the data processing of the rest of the packet. The rest of the packet is put in an array of 107 bits. This is followed by a Hamming correction decode, which is able to correct a single erroneous bit. Afterwards, this data is 8b10b decoded, which leaves 80 bits. For the first 64 bits of this array a CRC is calculated, which is compared with the last 16 bits. Equality of the CRC means that the first 64 data bits are valid, and are thus sent to the output port. When a whole packet has been received (valid or not), a signal will trigger the search for the start bits of the following packet. False packets are ignored, due to the useless nature of data retransmission in motion control and the previous valid data is held at the output port. The entire protocol is visualized in Figure 6.4.

Expected Performance

Using the packet size n_p [bits] and the datarate d_r [bits/s] of the data transmission, the delay in a single wireless link δ_{sl} [s] is estimated:

$$\delta_{sl} \quad = \quad \frac{3n_p}{2d_r}, \tag{6.4}$$

where the factor $\frac{3}{2}$ is added to take the sample and hold characteristic of the transmission into account. Besides the delay due to datarate limit, there is additional delay that is introduced by the AD/DA conversions and the buffers in the digital IO. In addition, the sample frequency f_s [Hz] is calculated by:

$$f_s \quad = \quad \frac{d_r}{n_p}. \tag{6.5}$$

Since a wireless control system consists of two links the additional closed loop delay added by the two links is double the single link delay. In Table 6.2 the additional
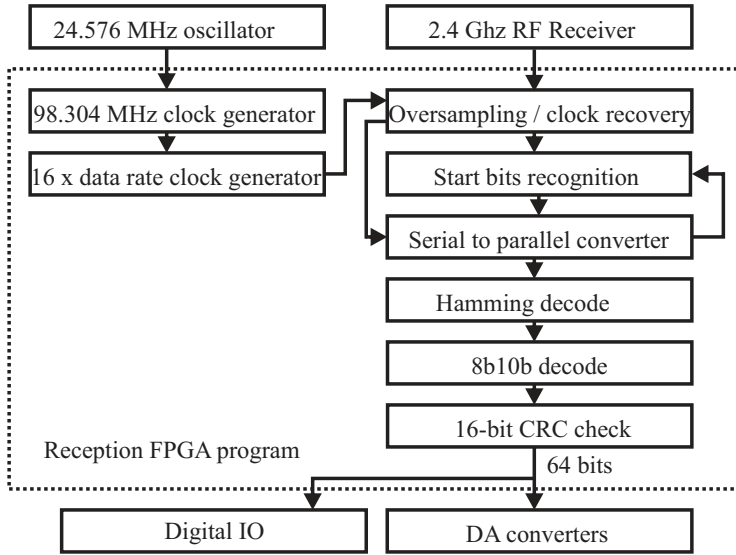
Figure 6.4: Schematic of FPGA receiver protocol

Table 6.2: Delay and sample frequency for different datarates

d_r	δ_{wl}	f_s
0.768 Mbps	480 μs	6.24 kHz
1.024 Mbps	360 μs	8.33 kHz
1.280 Mbps	288 μs	10.4 kHz
1.536 Mbps	240 μs	12.5 kHz

closed loop delay δ_{wl} and sample frequency f_s are listed for different datarates d_r, considering only the delay due to the limited datarate and the sample and hold.

6.3   Identification of Wireless Control System Performance

Measurements concerning the packet loss have been executed to evaluate the performance of communication and delay measurements have been done to determine the effects of the wireless communication compared to wired solutions. A position error measurement determines the performance in the control loop.

6.3.1   Packet Loss Measurements

In Figure 6.5, the packet loss ratio, which is the ratio between the number of non-correctable erroneous packets and the total number of received packets, has been measured for four different datarates. In addition, the ratio between the number of corrected packets, which had a single bit error that is corrected by the
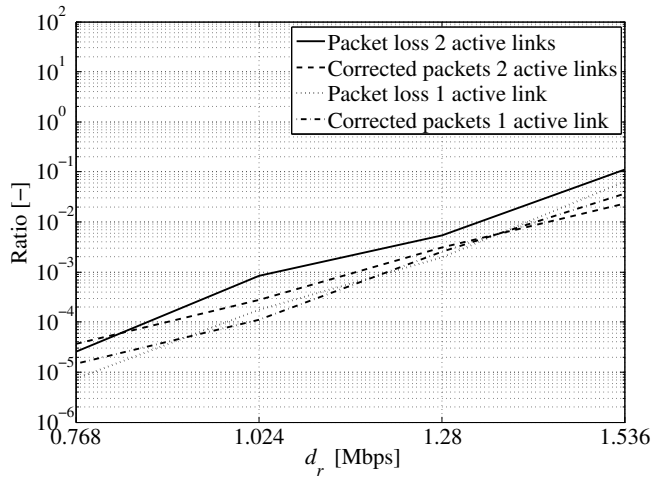
Figure 6.5: Measured packet loss ratio and packet correction ratio

Hamming code, and the total number of received packets is plotted. This measurement was performed in the laboratory with a WLAN router and other transmitters in the area. Due to the high gain antennas it is unlikely that other transmitters will deteriorate the packet loss. The results show the difference in performance between one active link and two active links, caused by the interference between the links. The figure shows that up to about half of the packets which contained an error are corrected. Consideration should be made what is preferred for a specific plant: a rather large packet loss with the advantage of a very short delay, or a smaller packet loss ratio with a larger delay.

6.3.2   frequency Response Function and Delay Measurements

To test the wireless control system, a closed loop wireless control system has been built, in which a three-phase synchronous rotary motor of the manipulator is controlled. The controller DSP (dSpace DS1103) generates analog voltage signals, representing the motor current references, which are sent over the first wireless link to the input of the power amplifier of the motor. The position of the rotor is measured by means of an incremental encoder. The signals from this sensor are decoded to a 16 bit position, which is sent over the second wireless link and is read by the controller DSP using a 16 bit digital IO. The frequency response functions of the setup at different data rates have been measured using a Siglab spectrum analyzer. These 'wireless' frequency response functions are compared with the frequency response function of the same control system without the wireless communication (wired). Figure 6.6 shows that the wireless system has no effect on the gain of the system. However, at high frequencies the gain decreases with respect to the wired system, which is related to the fact that the commutation is done by the controller. The additional delay at this frequency influences the accuracy of the commutation and an error in the commutation results in a lower gain. This can be improved by implementing the commutation on the FPGA,
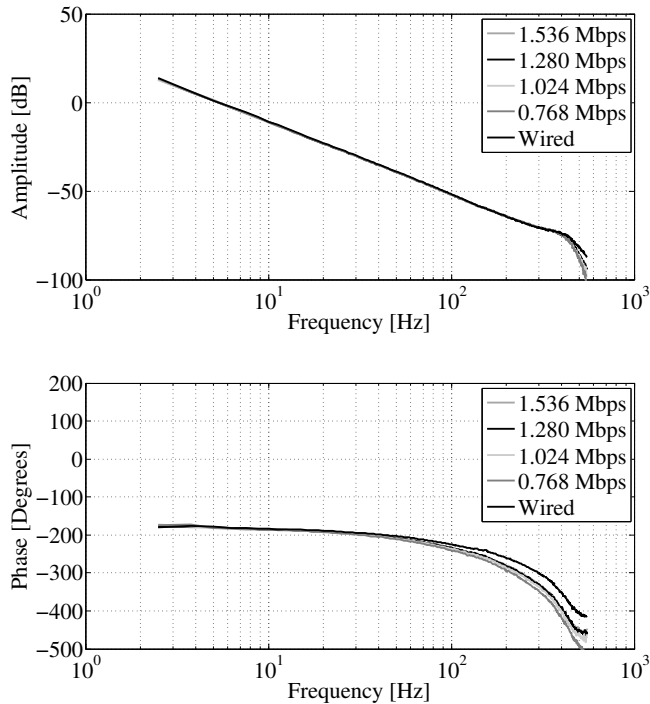
Figure 6.6: Measured rotary motor frequency response functions of current amplitude to position with the wireless link at different datarates

and only sending the current amplitude over the wireless link. The phase shift increases when the datarate decreases, which is consistent with the extra communication delay involved. From the phase shift in the frequency response functions, the delay is calculated for each datarate. These delays are variable as shown by the probability density distributions in Figure 6.7, which is caused by the absence of synchronization between controller DSP and FPGA's. The jitter defined as the difference between the maximum and minimum delay, is listed in Table 6.3 for each datarate and is at least 133 μs. This is significant, so synchronization should be a main issue in future improvements. The mean delays are rather consistent with the estimated delays, but slightly higher due to the A/D conversion times, buffers and unsynchronized operation of the wireless system with the controller DSP. The variable delay can be reduced by synchronizing the wireless link and the controller, i.e. start sending a packet with current setpoints directly after the controller finished calculating the setpoint values and transmit the latest position data just before the controller starts with the next sample.

At the highest datarate, the average of the additional closed loop delay is just 270 μs. This delay is about 15 times shorter compared with the UDP/IP WLAN 802.11b solution [59], while just a fraction of the datarate is used (1.536 Mbps against 11 Mbps). The jitter is reduced by a factor 4 compared to [59]. The proposed protocol and UDP/IP WLAN do not guarantee correct reception of the
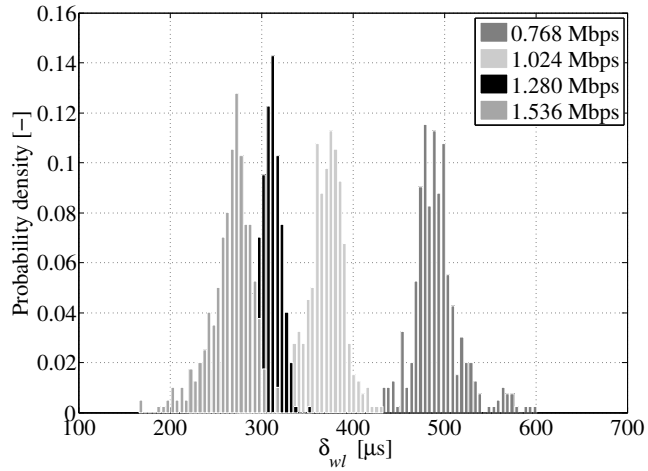
Figure 6.7: Measured additional closed loop delay probability density at different datarates

Table 6.3: Jitter for different datarates

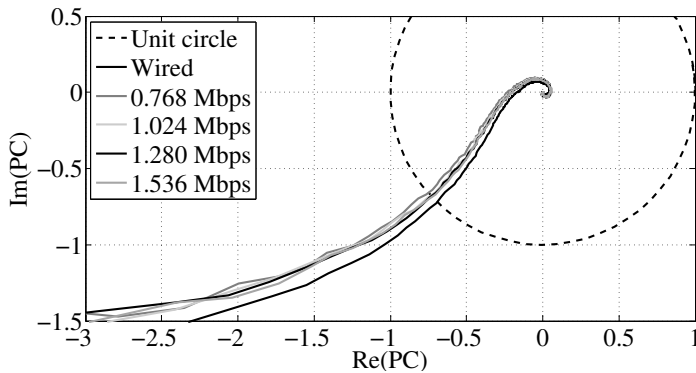| δ_r	jitter
0.768 Mbps	175 μs
1.024 Mbps	157 μs
1.280 Mbps	133 μs
1.536 Mbps	154 μs

Figure 6.8: Nyquist plot of wired and wireless open loop frequency response function PC

data, since packet retransmission is not included, and both have error correction built in, which makes them comparable. In all cases, the additional closed loop delay remains below the 1 ms specification.

6.3.3   Position Error Measurement

To determine the effects of the wireless communication on the control loop performance, the position error of the arm in a wired closed loop system has been compared with the position error of the arm in the wireless closed loop systems. A PID controller is implemented that realizes a position loop bandwidth of 30 Hz, defined as the 0 dB crossing of the gain of the open loop frequency response function PC. The phase margin is 46 degrees and the gain margin is 15 dB, if the delay of the wireless link is omitted. Due to the added delay in the loop, the phase and gain margin of the wireless loops are less and depend on the datarate of the wireless link. In Figure 6.8 the Nyquist plot of the open loop frequency response function of the system is shown for the wired case and for the wireless case at different datarates.

If a packet loss occurs, additional delay is induced in the loop which is equal to the sample time of the controller plus the time delay between sending and receiving a packet. In Figure 6.9, the Nyquist plot of the open loop frequency response function is shown including two sequential packet losses. In this case, all systems are stable but the margins have been reduced to approximately 30 degrees and 10 dB, while the maximum gain of the sensitivity is approaching 6 dB. Now it is possible to evaluate how many consecutive packets should be lost in order to cross -1 in the Nyquist plot. Taking into account the packet loss ratio measured in Figure 6.5 and assuming a uniform distribution for the occurrence of packet loss, it can be calculated that instability will occur once every 1×10^{19} seconds in the worst-case.

The position error of the arm is plotted in Figure 6.10 for different data rates. Because the FPGA's and the DSP run at different sample frequencies (f_s, see Table 6.2 and 8000 Hz, respectively) and no synchronization is present in the
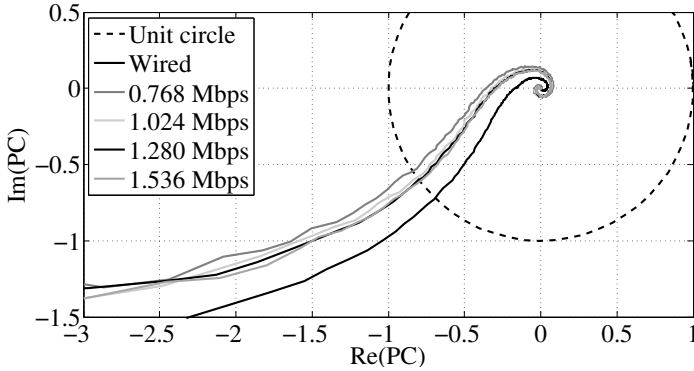
Figure 6.9: Nyquist plot of wired and wireless open loop frequency response function PC with two consecutive packets lost

wireless system, harmonics of the difference frequency are present in the position error of the wireless closed loop systems. At a datarate of 0.768 Mbps the error amplitude is significant higher than at higher data rates, because $\frac{d_r}{n_p} = 6244$ Hz < 8000 Hz. The large packet loss at 1.536 Mbps introduces significant spikes on the position error. These reading are confirmed by the maximum position error. Table 6.4 shows the maximum position error in milliradians. From Figure 6.10 and Table 6.4, it is concluded that the wireless control system performs best at a datarate of 1.280 Mbps.

The error in the wireless system suffers from a lot of chattering, which is not visible for the wired system. The error of the wired system is smooth, which indicates that it is related to unmodeled dynamics. The chattering on the error of the wireless system reduces significantly when the velocity of the arm is zero. It is likely that this effect is related to the commutation and to the jitter in the control loop. If the velocity is close to zero, the angle of the rotor hardly changes during one sample time and therefore, the phase currents that are commutated depending on the position do not change during the sample time. It suggests that the control behavior will be improved by implementing the commutation locally at the FPGA, while only sending the current amplitude command from the controller over the wireless link. In addition, the variable delay or jitter in the loop due to the wireless communication will have less effect on the performance when the velocity is small. This can be improved by synchronizing the wireless data transfer and the controller. FFT analysis shows that the frequencies present in the chattering are related to the difference frequency between the controller frequency and the wireless transmission sample frequency. In Figure 6.11, the frequency content of the measured position error with a wireless link running at 1.280 Mbps is shown. The harmonic with the highest amplitude is located at about 2.4 kHz, which is the difference frequency between the link $(10.4 - 8.0 = 2.4$ kHz$)$. The second highest amplitude is found at 3.2 kHz which is the aliased representative of double the difference frequency $(8 - 2.4 \times 2 = 3.2$ kHz$)$. Similar derivations can be done for higher harmonics.
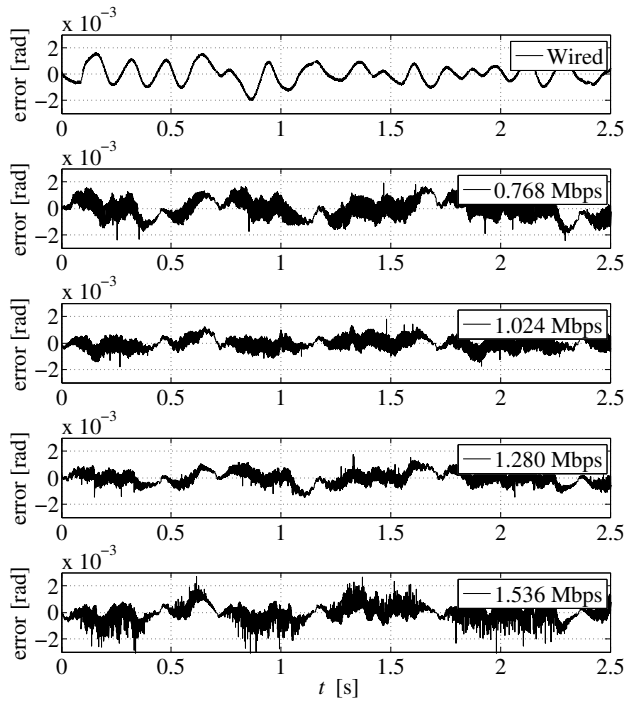
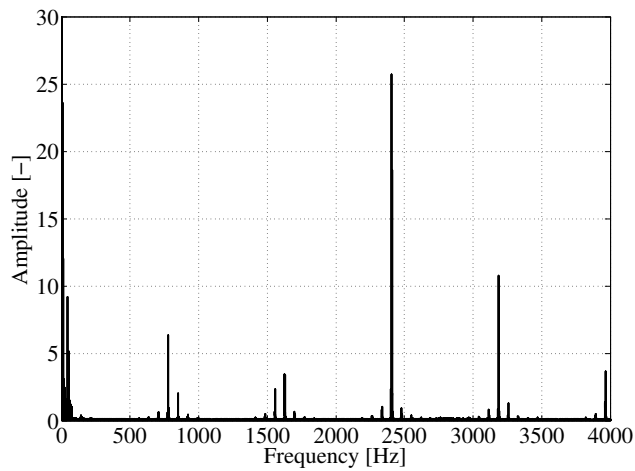Figure 6.10: Position error of the rotating motor

Figure 6.11: FFT of the 1.280 Mbps position error measurement

Table 6.4: Maximum position error for different datarates

Control system	Maximum position error
wired	2.0367 mrad
0.768 Mbps	4.0180 mrad
1.024 Mbps	2.8486 mrad
1.280 Mbps	2.5788 mrad
1.536 Mbps	5.5010 mrad

Table 6.5: Data allocation within the data packets

Manipulator to controller	Controller to manipulator
3 positions of 20 bits each	3 current amplitudes of 16 bit each
1 bit motor 1 enabled	1 bit enable motor 1
1 bit motor 2 enabled	1 bit enable motor 2
1 bit motor 3 enabled	1 bit enable motor 3
	1 bit enable homing
63 bits	52 bits

6.4 Implementation of the Wireless System on the Manipulator

From the initial tests with a single motor the final wireless control system for the entire manipulator is derived. The first requirement is that all information should fit within the 64 bit of data in the packet. The commutation and the position measurement is done locally by the FPGA, which implies that the controller only needs to send three current amplitudes, one for each motor, that are converted to 3-phase current commands to the amplifiers. The allocation of data in the data packets is shown in Table 6.5. To save space on the manipulator platform, all communication is implemented on a single FPGA board. A schematic of the wireless control system is shown in Figure 6.12. Since the same protocol and packets are used as in the tests with one motor, the performance of the system in terms of packet loss and delay will be the same. The datarate of the link is 1.28 Mbps, which is the best trade-off between delay, jitter and packet loss.

6.5 Conclusions

A new protocol and implementation for low-latency wireless communication has been presented that is suitable for wireless motion control and that overcomes the unsuitability of currently existing wireless communication protocols. The additional closed-loop delay has been reduced to 300 microseconds which is more than 10 times smaller than other known methods. This low delay has been realized
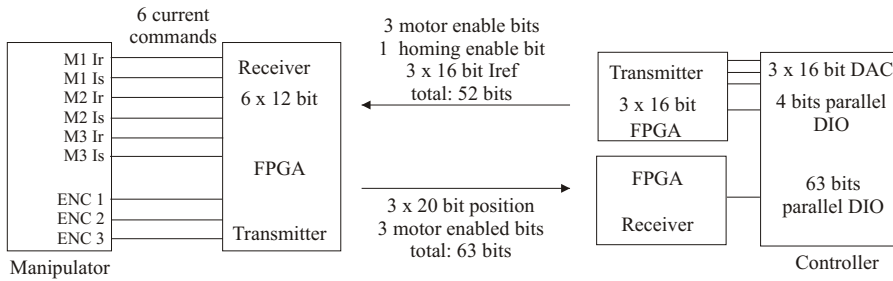
Figure 6.12: Schematic of the wireless control system communication of the manipulator

with low datarates up to 1.536 Mbps. Since the delay in this protocol is inversely proportional to the datarate, much lower delays and lower packet loss ratios can be easily obtained by optimizing the wireless channel, e.g. higher datarates, lower BER, optical communication.

The behavior of a wireless motion system, consisting of an arm driven by a 3-phase ironless rotary motor and a PID controller with a 30 Hz bandwidth position loop, has been shown. The stability of the system is demonstrated using Nyquist analysis of the open loop frequency response function. Errors have been shown in the range of several millirad compared to 10 degrees (0.2 rad) or worse in previously presented wireless control loops [59, 65]. The behavior of the wireless motion control system can be further improved by adding synchronization between the wireless communication link and the position controller to reduce jitter, which is already improved by a factor 4 compared to [59]. Finally, the implementation for the wireless control system communication of the manipulator has been presented, which is used in the system prototype.

In the previous chapters the subsystems of the multi-level contactless motion system are discussed. The final design of the contactless planar actuator with integrated contactless power transfer is discussed in Chapter 4, the manipulator in Chapter 5 and the wireless control system in Chapter 6. In this chapter the experimental setup is discussed that integrates all subsystems into a single system. First, design aspects that have not yet been discussed are explained. Then, the performance of all aspects of the final multi-level contactless motion system prototype, i.e. commutation, thermal properties, measurement system, contactless power transfer, wireless motion control and long stroke movement, is shown with measurements. The experimental verification of the commutation algorithm is published in [87] and the experimental results of the final multi-level contactless motion system prototype are published in [86].

7.1 Design Choices of the Experimental Setup

Several issues of the final prototype are not yet addressed such as the mechanical construction and stiffness, the final layout of the coils, the measurement systems and the power amplifiers.

7.1.1 Measurement System

The measurement of the six DOF of the platform without contact and with long-stroke in the x-y plane is not trivial. The conventional method for measuring large displacements with high accuracy is a laser interferometer measurement system. However, this system requires the angles of the measurement surface to be orthogonal with the laser beam within 1 mrad. Since this is a prototype, it is not yet possible to guarantee such angle accuracy. Moreover, a laser interferometer works like an encoder, so it cannot measure absolute positions. Therefore, there is always a necessity for an additional absolute measurement system that is more tolerant to angles. Finally, laser triangulator sensors from Micro-Epsilon with a bandwidth of 2.5 kHz and 400 μs delay are selected for the x-, y- and ϕ- (yaw) measurement. The y- and ϕ-measurement is done by means of a 100 mm stroke (ILD 2200-100, 5 μm resolution, 30 μm linearity), while the x-measurement is done within a 200 mm range (ILD 2200-200, 10 μm resolution, 60 μm linearity). The resolution is equal to the peak noise level on the sensor output and the linearity is the maximum deviation from the true value within the range of the sensor.

With a tilt angle of the target of 5°, these sensors have an error less than 0.12% of the measuring range, (120 μm and 240 μm respectively). The measuring range is also called full scale output or FSO. This allows for large yaw angles to be measured with a reasonable accuracy. Due to the use of round coils as discussed in Chapter 4, the planar actuator is able to rotate with large angles around the z-axis and this measurement system is capable of measuring angles of a few degrees.
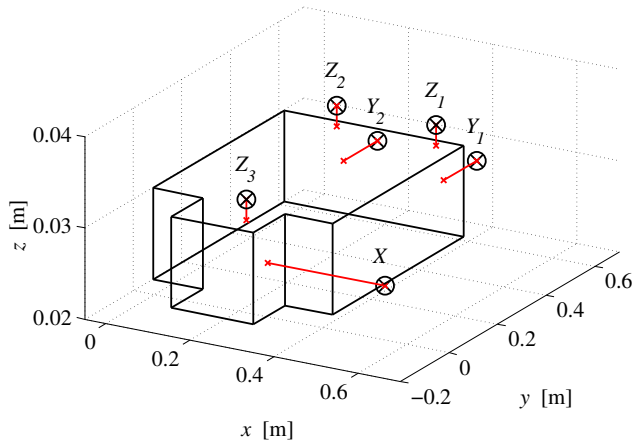
Figure 7.1: Platform with sensor system

The stroke in the z-direction is only 2 mm, so it is more straightforward to measure the height z, pitch ψ and roll θ. Since the platform will have a smooth aluminum surface, it makes a fine target for eddy current sensors. In this case ECL100-U8B eddy current sensors (10 kHz bandwidth, 0.16 μm resolution, 5 μm linearity) from Lion Precision are used, which operate with an excitation frequency of 1 MHz.

The platform has additional surface area that acts as target for the sensors. The platform with the sensors is shown in Figure 7.1 with a factor 20 zoom in z-direction, where the y-laser triangulator sensors are labeled Y_1 and Y_2, the x-laser triangulator sensor is labeled X and the three eddy current sensors are labeled Z_1, Z_2 and Z_3, respectively. The markers with circle show the absolute position of the sensors and the readout of each sensor is the intersection point of the line of measurement and the surface of the manipulator plate. From these intersection points the position of the magnet array in the global coordinate frame is retrieved. All absolute positions are related to the CAD drawings of the system so the absolute accuracy is only as accurate as the mechanical manufacturing and mounting tolerances which are in the order of 50-100 μm. Additionally, the manipulator plate surface is used as a target for the sensors which is of course not completely flat.

Commutation

The positions of the coils are defined in the global coordinate frame and the position of the magnet array in the global coordinate frame is measured. The calculation of the forces and torques depends on the position of the coil with respect to the magnet array so this information is necessary for the commutation algorithm. Since the prototype consists of round coils, the orientation of the magnet array and the coils with a large yaw angle does not affect the commutation algorithm as long as the transformation between the global coordinate frame and the local
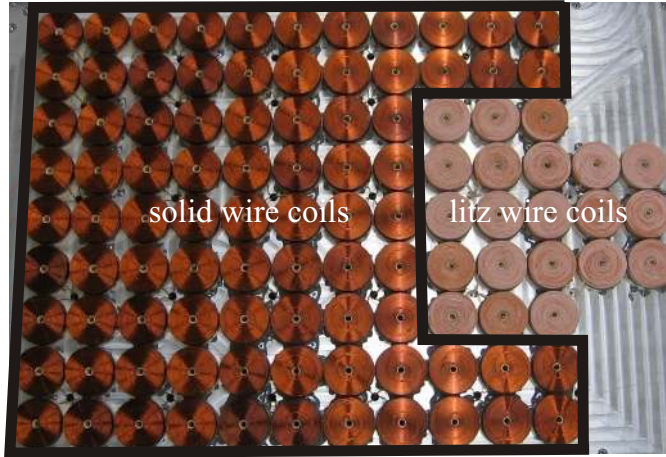
Figure 7.2: Coil array before casting

magnet array coordinate frame is properly defined. The commutation algorithm uses the position of the coils in the magnet array coordinate frame so the coordinate transformation described in Section 5.2 are used to calculate the required positions. As long as the measurement system can reconstruct the large rotations around the z-axis, the planar actuator can realize large rotations, due to the use of round coils and the proper coordinate transformations.

7.1.2 Coil Array Layout

In principle, the stroke of the planar actuator is only limited by the number of coils that are on the fixed world and the measurement system. Since the measurement system can only measure an area of 100×200 mm, the coils are only placed to accommodate such a workspace. In this case, it requires a coil array of 9×11 coils. Moreover, the secondary coil, which picks up power from the primary coils, is only active in a small range of the coil array. Therefore, not all coils need to be made from litz-wire, which limits the manufacturing risks. In Figure 7.2 the coil array is shown before casting and the sections with solid wire coils and litz wire coils are marked. All the coils have the same dimensions, although the tolerances on the dimensions of the litz wire coils are slightly higher.

All coils are fixed around ceramic tubes and the height of the top surface of each coil is measured by a 3D measurement machine from Zeiss (CALYPSO 4.4.06.04). Using the measurement of the height of each coil, all coils are cast into a epoxy resin containing 60% aluminum oxide powder (RenCast CW 5156-1 / Ren HY 5158 [10]). Finally, the cast surface is milled down to 0.2 mm above the highest coil. This way the coils are completely covered and protected from damage by contact between the magnet array and the coils. In addition, it ensures that the bonding between the wires of the coils remains good, which is especially a problem for the hand-wound litz wire coils. Also, it creates a smooth surface for the airgap.

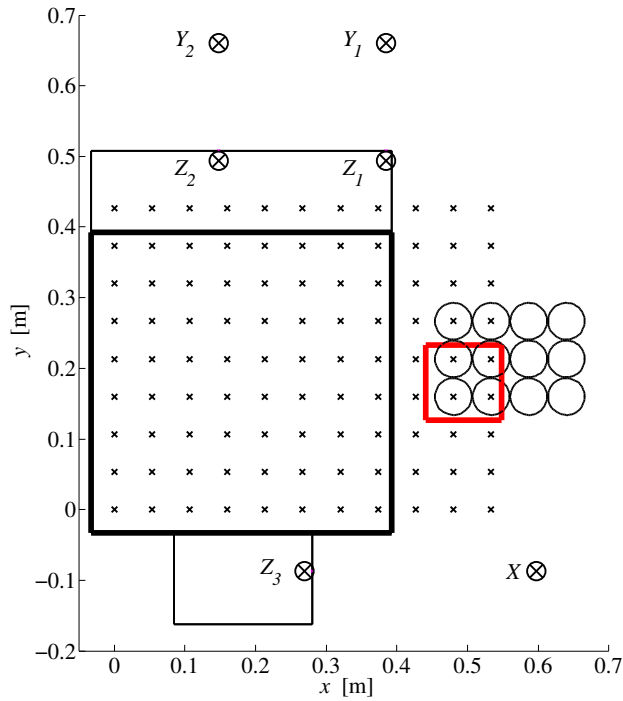In Figure 7.3, a schematic representation of the system is shown in the global

Figure 7.3: Schematic representation of the coil array and magnet array

coordinate frame. The small crosses are coils that are active in the electromagnetic suspension and propulsion, if the magnet array (large black square) is in range, while the circles represent coils that transfer power if they are overlapped by the secondary coil (small square). As it is clear from the schematic representation, only six litz wire coils have both functions. The origin of the global coordinate system is located on the central axis of the coil in the bottom left corner at the height of the resin surface. The magnet plate is now in its zero position, where the center of the bottom left magnet pole is aligned with the central axis of the bottom left coil.

7.1.3   Mechanical Construction and Stiffness

The final design of the contactless planar actuator consists of a 10×10 Halbach magnet array with round coils. The total levitated weight was estimated to be 22.1 kg resulting in a worst-case steady-state coil temperature of 102 °C. It is desirable to reduce this temperature by means of reducing the levitated mass. The initial assumption was to glue the magnets to a support plate of solid aluminum with a thickness of 10 mm, which would have a mass of 4.9 kg. Instead of solid aluminum, aluminum honeycomb material (Alcan Alucore-10) is used, which is much lighter and still has a relatively high stiffness. To realize a 30 Hz bandwidth of the PID position control loop assuming rigid body motion, the first eigenmode

Table 7.1: Aluminum honeycomb Alcan Alucore-10 properties

Parameter	Alucore	Aluminum	Unit
Density	450	2700	kg/m^3
Young's Modulus	8.9	70	GPa
Shear Modulus	3.4	27	GPa
Poisson's ratio	0.33	0.33	-

of the magnet plate has to be at least 300 Hz. Two aluminum honeycomb plates of 10 mm thickness are used. One plate $425 \times 425 \times 10$ mm is the magnet plate, to which all the magnets that form the Halbach array are glued. The other plate is slightly larger and is used as a basis for the manipulator. Since it is not possible to create a hole in a honeycomb plate, all mounting holes (if necessary with thread) are realized by means of solid aluminum inserts with the holes, which are glued into the honeycomb plate. The magnet plate and the manipulator plate are finally glued and bolted together to create a stiff and light platform.

To identify the flexible modes of the platform, a modal analysis is performed using the FEM package Algor for mechanical modal analysis with the properties of Alucore listed in Table 7.1. The density of Alucore is six times lower than regular aluminum, however, the stiffness is eight times less as can be concluded from Table 7.1. The total height of the two aluminum honeycomb plates glued together is 21 mm and the 11.37 kg of the magnets is added as a dummy mass that does not add to the stiffness of the platform. The resulting first eigenmode occurs at 309 Hz. The total the platform including magnets, glue and aluminum inserts is 13.7 kg, a reduction of 2.4 kg compared to the initial estimate.

The additional load of the manipulator was estimated at 6 kg (see Section 4.2.1), however, the manipulator, FPGA with wireless link, secondary coil with power supply, mounting supports and cables have a mass of 6.8 kg as is shown in Table 7.2. The total levitated weight thus becomes 20.5 kg, which is 1.6 kg or 7% less than the initial estimate. This will reduce required current by the same factor and the dissipated power in the coils with 14% $((1 - \frac{1.6}{22.1})^2)$.

The base of the coil block is a large aluminum block, which acts as a heat sink with channels for water cooling and as a base frame for the sensors. In addition, all coils are cast using a resin and are therefore completely embedded into the structure. Therefore, it is assumed that all non-rigid body effects are negligible compared to the platform with the manipulator. The construction of the coil block, the manipulator, and the planar actuator platform has been carried out by the GTD workshop of the Eindhoven University of Technology (Gemeenschappelijke Technische Dienst).

7.1.4 Power Amplifiers

From the models described in Chapter 2, the required Ampère-turns in the coils to move the planar actuator are derived. For a given number of Ampère-turns i_{at}, coil cross-section and filling factor, the dissipation is independent of the number of

turns N in the coil (Eq. 2.37). For a coil with N turns and current i, the following holds [26, 53]:

$$u_{ext} = R_s N^2 i + L_s N^2 \frac{d}{dt} i + \underline{K} N \underline{v}, \tag{7.1}$$

where u_{ext} is the power amplifier voltage, R_s, the resistance of the coil with a single winding, L_s, the inductance of the coil with a single winding. Next, the Ampère-turns i_{at} and the power P_{ext} of the power amplifier are considered:

$$i = \frac{i_{at}}{N}, \tag{7.2}$$

$$\begin{aligned} P_{ext} &= u_{ext} i \\ &= R_s i_{at}^2 + L_s \left(\frac{d}{dt} i_{at} \right) i_{at} + \underline{K} \underline{v} i_{at}. \end{aligned} \tag{7.3}$$

Since i_{at}, $\frac{d}{dt} i_{at}$ and $\underline{v}$ only depend on the required forces, torques and motion profile and the power of the power amplifier is fixed, the choice of N is a trade-off between voltage and current output of the power amplifier and manufacturing trade-offs. The power amplifier voltage should be high enough to realize the desired current loop bandwidth ($\frac{di}{dt}$) and the current should be low enough to meet the power amplifier specifications. The preferred PWM amplifiers for this application are Prodrive PADC3AX52/6 (with permission of ASML) which have excellent SNR, low offset and good linearity. Moreover, they have a digital interface, so current setpoints can be transmitted without offsets or gain errors. The maximum continuous current for this power amplifier is 1.8 A and the peak current is 6 A with a voltage of $+/- 52$ V. The maximum continuous Ampère-turns for levitation only for the final topology is 1123 Ampère-turns and during 10 m/s^2 acceleration in x- and y-direction it is 2412 Ampère-turns.

Solid Wire Coils

The solid wire coils have 684 turns of 0.56 diameter copper wire, which has been selected, to match well with the desired geometry of the coil. This results in a filling factor of 0.7, a resistance of 4.4 Ω, an inductance of 8.1 mH, a back-EMF of 10.3 V if the magnet array moves at 1 m/s and a minimum $\frac{di}{dt}$ of 3.2 A per millisecond with 52 V of power amplifier voltage. The peak power amplifier current is 3.5 A and the continuous power amplifier current is 1.64 A, which is within the power amplifier specifications. The bandwidth of the current loop, defined as the frequency where the open loop gain equals 0 dB, is measured to be 1.8 kHz.

Litz Wire Coils

For the litz wire coils, a second aspect is of importance. The coil should not only operate in the range of the current loop bandwidth, but also at much higher frequencies to transfer power. At high frequencies, the capacitance of the wires becomes visible as a parasitic capacitance in parallel with the inductance. The resonant frequency of the coil, due to the parasitic capacitance, should be much higher than the frequency of the power transfer. The parallel capacitance increases

if the number of wires increases. In addition, the bundle diameter of litz wire, i.e. the number of strands should not be too small, otherwise the filling factor will be very low. Moreover, the inductance should not be too high, otherwise the resonant voltage over the coil will be too large. Additionally, the inductance should be high enough for the amplifiers to realize a stable current loop >0.5 mH. Finally, a trade-off is chosen with 240 turns of 100×71 μm strands resulting in an inductance of 1.0 mH, a resistance of 1.0 Ω at frequencies within the current bandwidth and a back-EMF of 3.6 V at 1 m/s. The continuous current of the power amplifier is 4.7 A and the peak current is 10.1 A. This current specification does not match with the PADC3AX52/6, so the litz wire coils are fed with PWM Bosch Rexroth NYCe4000-NY4120 power amplifier (7 A continuous, 20 A peak). The power amplifier voltage is the same as for the regular coils, so the current loop has a higher bandwidth for the litz wire coils. The filling factor is 0.4, which is 33% higher than the worst-case estimate, which reduces the copper losses by the same percentage.

Finally, the resonant frequency due to the parasitic capacitance of the litz wire coil is measured to be 440 kHz, however, this parasitic capacitance is dominated by the capacitance between the aluminum coil block and the litz wire coil itself. The maximum voltage over the coil in the series resonance during power transfer is 1.5 kV, which results in a 6.25 V drop per turn and a maximum voltage between two adjacent turns of 125 V. The litz wire isolation allows voltages up to 150 V, so no isolation failures are expected. The litz wires from the supply to the coil terminals have additional teflon isolation which can withstand voltages up to 2.5 kV.

Contactless Power Transfer

The series resonance of the contactless power transfer with the litz wire coil occurs at 158 kHz. The coil is driven by a square-wave voltage source which is similar to the one described in Section 3.3, Figure 3.11, except that the square-wave reference is generated by a circuit based on the NE555 oscillator, with an adjustable frequency. The frequency is lower than the 191 kHz with a similar topology discussed in Section 3.3, which is caused by the additional inductance of the cable between the square-wave voltage source and the coil. In addition, the triac is replaced by a mechanical relay (Finder 66.22 DPDT), that either connects the coil to the square-wave voltage source when the litz wire coil is in power transfer mode, or to the current loop power amplifier if not. The frequency of the power transfer is about one third of the resonant frequency of the coil due to the parasitic capacitance. This difference is large enough, although it already gives rise to oscillations at 440 kHz, when the square-wave voltage switches polarity.

The power stages of the PWM power amplifier and of the square-wave voltage source are very similar since it consists of a MOSFET bridge (either half or full) that switches with a high frequency up to 200 kHz. For the current loop however, the duty-cycle is varied to realize the desired current. In case of the voltage source, the duty-cycle is fixed. It would make a lot of sense to combine the two functions into one driver with two modes, which would also make the mechanical relay obsolete. However, since it takes time and money to design such an integrated

Figure 7.4: Magnet array

driver, this solution is not yet applied in this setup.

7.1.5 Electromagnetic Aspects

The first aspect to be discussed is the type of magnets used in the Halbach magnet array. The magnet array is made of VACODYM 665HR [29], a product of Vacuumschmelze, who manufactured and glued the magnets. In [10] it is thoroughly discussed why these magnets are suitable to be used in a planar actuator and the same analysis is valid for this prototype. The magnet array is shown in Figure 7.4.

Another issue is eddy current damping, which is caused by the magnet array moving above the aluminum underneath the coils. An analysis is performed in [10], which resulted in a distance of 17.4 mm between the magnet array (25 mm pole pitch) and the aluminum with a damping force of about 3 N at 1 m/s. Since the maximum speed is the same and all properties of the magnet array in the design scale with the pole pitch it is sufficient to estimate the distance by $\frac{40}{25} \times 17.4 = 27.8$ mm to obtain a similar damping force.

7.1.6 Realized Prototype

Due to mechanical tolerances and manufacturing preferences the magnets and coils do not have the exact same dimensions as the ones calculated in Chapter 4. The real dimensions are listed in Table 7.2. All position sensors, the wireless control system and coil amplifiers are connected to a dSpace multiprocessor board, where a single DS1005 board is carrying out all calculations, analog I/O and digital I/O and a slave DS1005 board is responsible for the digital RS485 communication with the Prodrive power amplifiers. The current setpoints to the Bosch power amplifiers are sent by analog voltage references. The communication with the wireless link is explained in Section 6.4 and Figure 6.12. The sample time of the dSpace system is 330 μs, which is the time it takes to transfer all current setpoints

Table 7.2: Dimensions of the final prototype

Parameter	Symbol	Value	Dimension
Pole pitch	τ	40.0	mm
Halbach magnet width	d	14.0	mm
Magnet height	m_h	10.0	mm
Coil width	c_w	51.0	mm
Coil bundle width	c_{bw}	21.1	mm
Coil bundle height	c_{bh}	11.4	mm
Platform mass	m_p	13.7	kg
Manipulator mass	m_m	4.2	kg
Additional mass	m_a	2.6	kg
Levitated mass	m	20.5	kg

to the amplifiers using the RS485 channels. The reading of the sensors, calculation of the position references, controller outputs and coil currents and safety checks take about 250 μs. The current setpoints of sample n are calculated, while the values of sample $n-1$ are transferred to the amplifiers. Although the delay in the loop is about 1.2 ms (sensor 0.4 + calculation 0.33 + RS485 0.33 + current loop 0.1), it still makes sense to run the algorithm as fast as possible, since it adjusts the coil currents necessary for a certain force and torque as often as possible, depending on the position and orientation.

7.2 Verification of the Commutation Algorithm

The look-up tables are calculated for the final prototype and implemented in the commutation algorithm as discussed in Section 2.4 using 2D look-up tables with a grid points spacing of 0.5 mm in x- and y-direction. An advantage of round coils is that they are axisymmetric, which cancels out the volume dependent term of the torque around the z-axis K_{T_z}. This makes the look-up table commutation algorithm even more efficient. The commutation is verified by mounting the magnet array on a 6 DOF Force/Torque (F/T) sensor (JR3 45E15A4-163S 100N10) that is fixed in a x-y robot. The robot moves the magnet array over the coil array while the commutation algorithm calculates the currents that are necessary to realize the desired forces and torques. The position of the magnet array is measured by the linear encoders of the x-y robot, which have a resolution of 1 μm. The measured forces and torques at different positions above the coil array are compared with the desired values to verify the performance of the commutation algorithm. In Figure 7.5, a photo of the experimental setup is shown with the relevant parts. All coils are now embedded in resin to create a smooth surface, so they are not visible as in Figure 7.2, which was made before casting.

The magnet plate is moved within the workspace (200 x 80 mm) to 1071 grid points that are spaced 4 mm apart. At every position two measurements are done. First, a zero measurement is done, i.e. the reading of the 6 DOF F/T sensor is
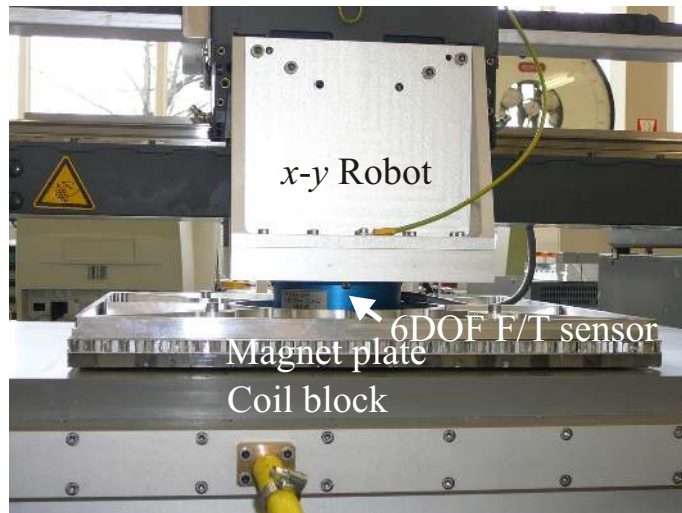
Figure 7.5: Experimental setup for verifying the commutation algorithm

measured with a zero current setpoint to all power amplifiers. Second, the current setpoints are sent to the power amplifiers to create 50 N in all three directions and zero torque around the three axes. Both the zero measurement and the load measurement are done at a static position for half a second with a sample time of 330 microseconds and then the mean of each period is used as the measured value. The magnet plate is kept at the same position by the x-y robot during this process. Then the robot moves the magnet plate to the next grid point, where the process is repeated. The airgap between the coil block surface and the magnet array is 2 mm. The measured forces and torques by the 6 DOF F/T sensor are shown in Figure 7.6 and Figure 7.7, respectively.

As is clear from Figure 7.6 and Figure 7.7, the commutation algorithm is capable of calculating the currents necessary to realize the desired forces and torques on the magnet array. The force has a peak error of 3% and an RMS error of 1.3%, while the maximum torque error is 0.15 Nm. This peak torque error corresponds with a force of 0.72 N on the perimeter of the magnet array, which is 1.5% of 50 N. In addition, some variations are visible in the surfaces that are fitted through the measurement points. These variations show some periodicity, which is related to the spacing of the coils. Both in x- and y-direction, the coils are space 53.33 mm apart and the variation of the errors is related to this distance. The errors have several causes, which are:

1. Mechanical tolerances of the coils. The standard deviations of the coil height, coil inner diameter and coil outer diameter are 52 μm, 12 μm and 409 μm, respectively.

2. Mechanical tolerances of the magnet plate. The magnets are 50 μm accurate and the plate is about 100 μm deformed due to the gravity and forces between the magnets.
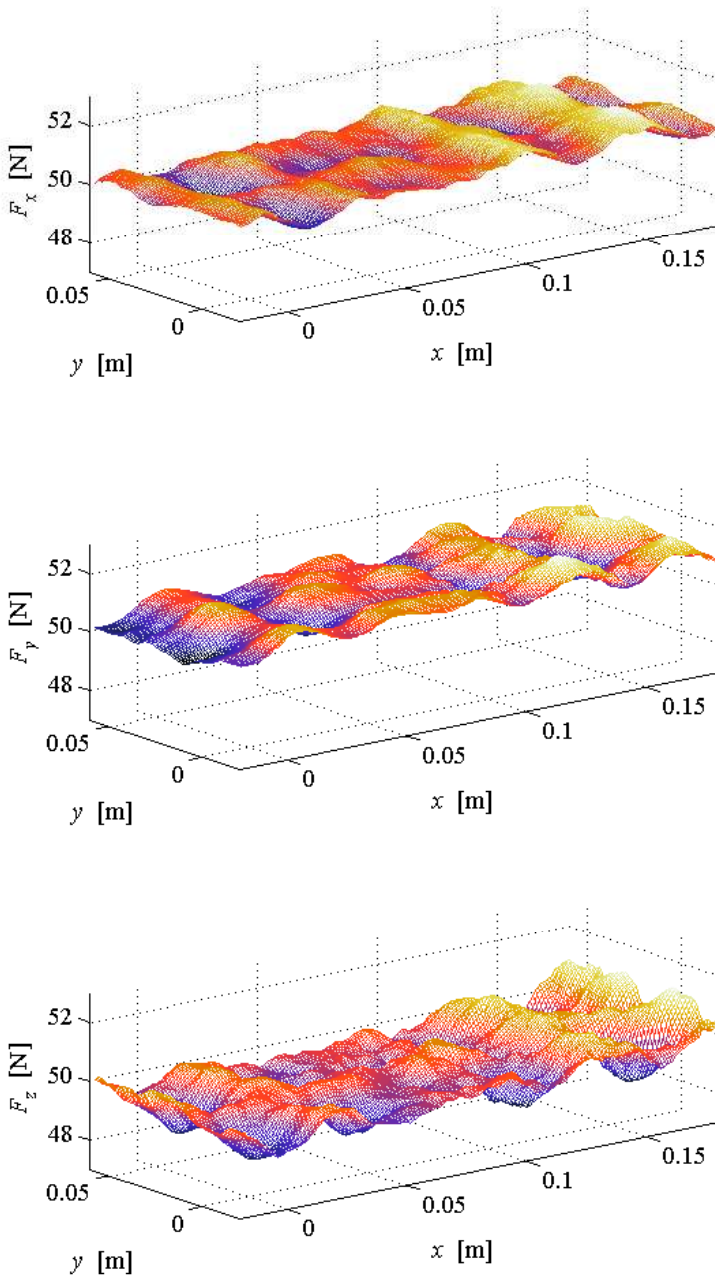
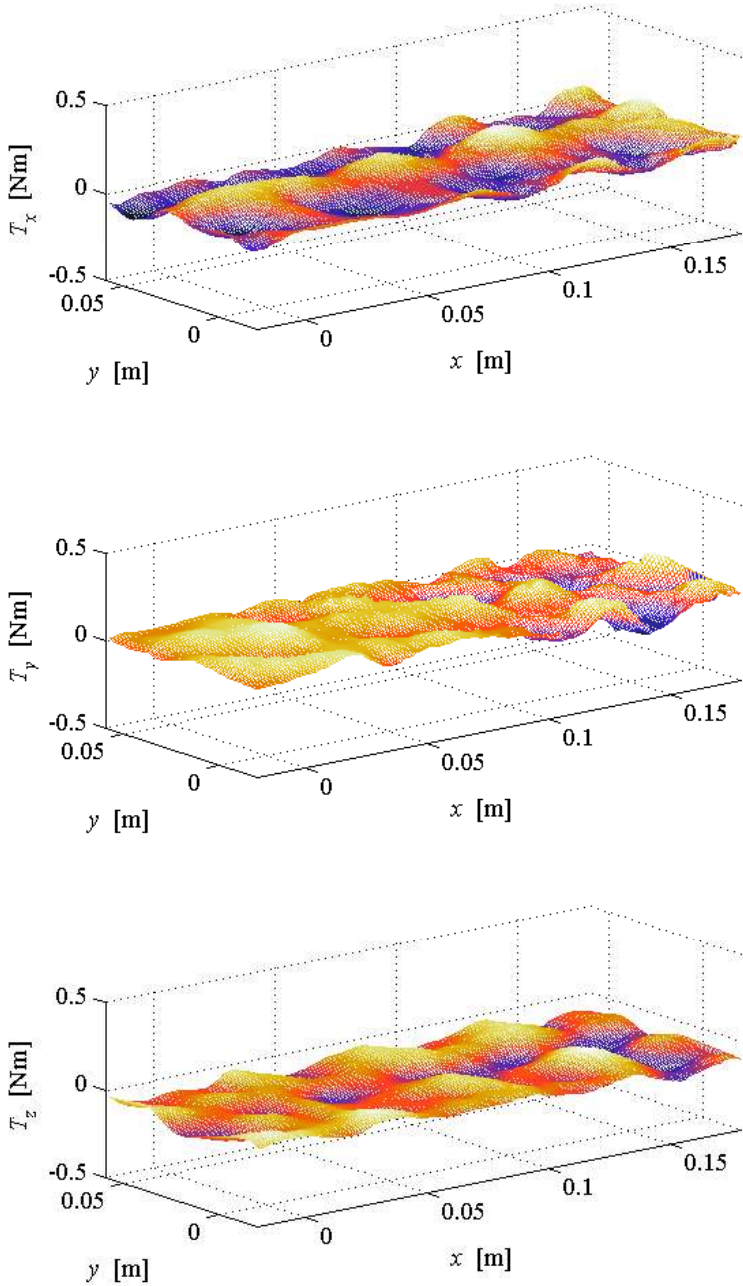Figure 7.6: Measured forces on the magnet plate

Figure 7.7: Measured torques on the magnet plate

3. The magnetization of the magnets is not perfectly uniform and the magnetization vector is not completely perpendicular to the magnet surface. In addition, the look-up tables are calculated with a model assuming $\mu_r = 1$, while in reality the value is equal to 1.03.

4. The alignment and position of the coordinate systems of the robot, the magnet plate, the coil block and the 6 DOF F/T sensor is not perfect.

All these factors contribute to the errors, so it is hard to distinguish which effect is dominant. Although the position measurement in this experiment has a resolution of 1 μm, the absolute position accuracy of this measurement is very dependent on the absolute positions of all the coordinate systems involved and this accuracy is limited by the manufacturing and mounting tolerances as it is discussed in Section 7.1.1. The errors are corresponding with the accuracy of the models used, as it is discussed in Section 2.1.4 and Section 2.4.5.

7.3 Thermal Verification

In Chapter 4, the worst-case temperature of the litz wire coils was estimated at 102°C. However, as discussed in the previous section, the weight is reduced by 7%, which results in a significant reduction of the required Ampère-turns to lift the platform. In addition, the filling factor of the litz wire coil is increased by 33%, hereby lowering the dissipated power in the coils. The gravity force on the platform is approximately $20.5 \times 9.81 = 201$ N and this has been rounded to 210 N to include controller forces. Now the platform is lifted at the worst-case position, which results in the highest continuous current in one of the litz wire coils. The required current in the litz wire coil to realize this force with an airgap of 1 mm above the resin surface is 4.22 A. The coil resistance at 20° is 1.02 Ω and together with the parameters listed in Table 2.2 this results in a predicted maximum coil temperature of 80°C and a surface temperature of 76°C. The temperature distribution of the coil block surface is measured while applying the currents necessary to produce 210 N of lift at the worst-case position. The measurements have been performed with a FLIR ThermaCAM S45 infrared camera and the steady-state temperature distribution is shown in Figure 7.8. The maximum surface temperature is 71.1°C, which is about 5°C lower than the prediction of the thermal model. The error of the estimated temperature increase is about 10%, which is due to the fact that the thermal properties of the coil, the cooling and the natural convection are hard to estimate. From Figure 7.8, it is clear that the coils are grouped in a two-dimensional 3-phase system, since there are two coils that are hardly active between the coils with the highest dissipation and the commutation algorithm puts most current in the coils that are most efficient in providing lift.

In the design of the planar actuator, the worst-case continuous power dissipation was the starting point of the design. Since there was no experience in building electromechanical actuation systems with litz wire coils, everything should work even in a worst-case scenario. However, in normal applications, the planar actuator is continuously moving from point to point. To investigate the thermal behavior during movement, a motion profile is applied between nine points distributed equally over the entire workspace with an acceleration of 10 m/s^2 in both
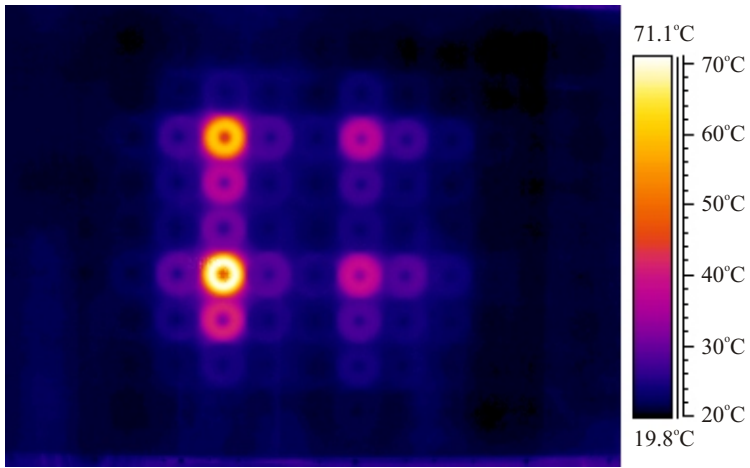
Figure 7.8: Measured steady-state temperature distribution with levitation only at worst-case position
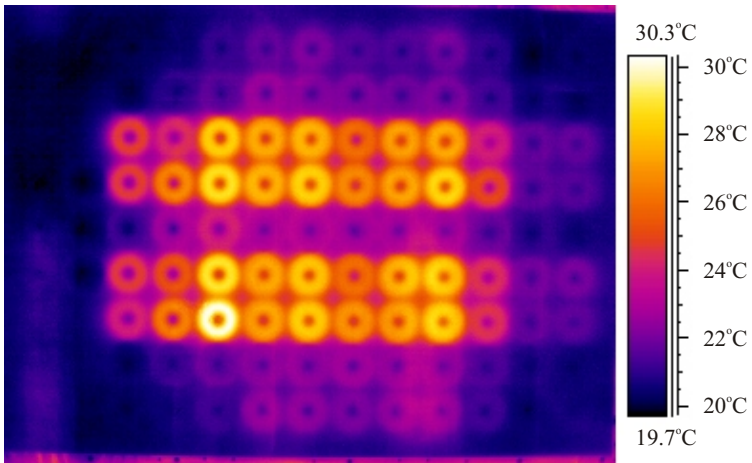

Figure 7.9: Measured steady-state temperature distribution with levitation and motion profile

x- and y-direction, where 30% of the time the platform is either accelerating or braking. The currents required to generate the desired forces for levitation and propulsion and zero torque are put into the coils, while the temperature distribution is monitored using the infrared camera. After four hours, steady state is reached and the resulting temperature distribution is shown in Figure 7.9.

It is clear that the thermal load is more evenly distributed over the coils and that the temperature rise is much less than in the worst-case situation. The initial temperature estimate in the design was, therefore, very conservative and it shows that with a proper thermal design which includes the duty-cycle it is possible to create a electromechanical system with litz wire coils. The main problem in the thermal design is the limited conduction coefficient of the coil and the low filling factor of 0.4 but as can be concluded from Figure 7.9, this does not necessarily have to result in extreme temperatures. Another way of looking at it is that much higher acceleration or levitated mass is possible with the same configuration.

7.4 Closed-Loop Control of the Planar Actuator

The commutation algorithm is verified and it is capable of generating the desired forces and torques on the platform. In addition, the thermal behavior of the coils is checked and the temperatures are well below the maximum allowable values. The next step is to check the behavior of the planar actuator in the position control loop.

7.4.1 Behavior of the Measurement System

During initial tests with operating the planar actuator in the position control loop, vibrations were visible in the x-, y- and ϕ-directions. Since the commutation algorithm was checked without variation in the angles, the coordinate transformations and the position and orientation reconstruction of the measurement system were checked. After the checks, it was possible to manually move the platform in the x-y plane, including large rotations around the z-axis, without significant force and torque ripples when the x-, y- and ϕ-position controllers were turned off. Therefore, the cause must be an effect of the laser triangulator sensors that does not affect the commutation algorithm, but somehow causes vibrations when the sensors are used in a position control loop. Additional short-stroke eddy current sensors were placed instead of the X, Y_1 and Y_2 laser triangulator sensors as is shown in Figure 7.10.

With the additional eddy current sensors it was possible to use the position measurement of the eddy current sensors to control the position of the platform in the plane, while simultaneously measuring the position in the plane with the laser triangulator sensors to find out the cause of the vibrations. All six DOF of the platform are controlled with 10 Hz bandwidth PD controllers.

The platform was moved with small steps of 0.1 mm in the x-direction using the eddy current sensors for the control. The resulting position in the plane is shown for both the eddy current sensors as well as the laser sensors in Figure 7.11. It is clearly visible that a change in the x-position does also create a change in y and ϕ in case of the laser triangulator sensor, an effect which is not visible for the eddy
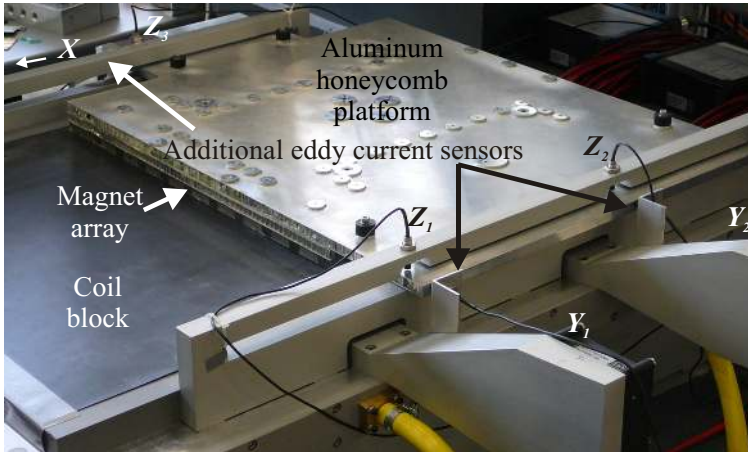
Figure 7.10: Platform with sensor system and additional eddy current sensors
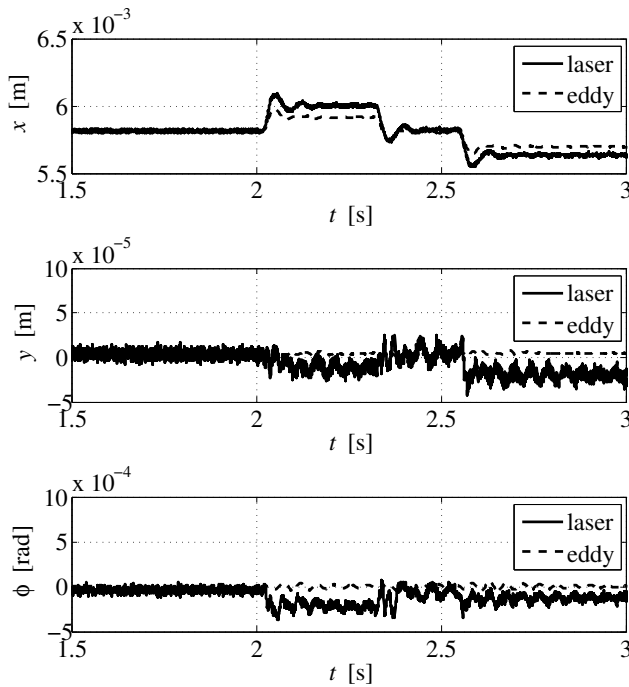

Figure 7.11: Measured position of the platform with eddy current sensors and laser triangulator sensors
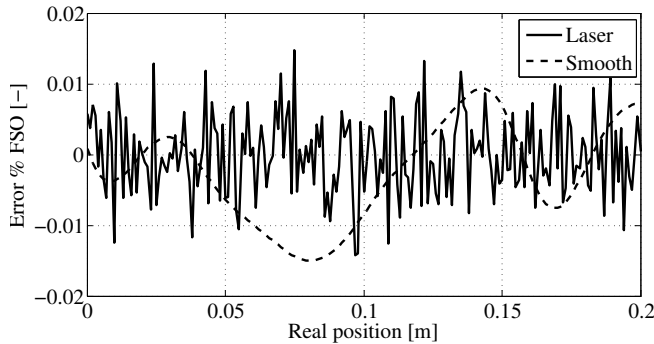
Figure 7.12: Sensor error as a percentage of the full-scale output (FSO) at different positions for a laser triangulator and a smooth behavior of other sensor types

current sensors. In addition, the error in the ϕ measurement propagates in the x-measurement. This effect is caused by the changes in reflection of the measurement surface when the platform moves in x-direction. Although the y-position does not change, the laser beam of the Y_1 and Y_2 sensors reflects at a different position and this causes a different y- and ϕ-measurement at that position.

When the calibration certificate of the laser triangulator sensor is studied it is visible that the sensor reading varies heavily within the measurement range. Although this chattering stays well within the linearity specification of the sensor, its fast changing behavior results in vibrations in the control loop. Effectively, the resolution of the sensor is completely dominated by the fast changes in linearity of the sensor. If the variation of the sensor error at different positions was more smooth, it would not have been a problem. This is illustrated in Figure 7.12, where two error behaviors are depicted with approximately the same linearity. The one labeled *Laser* resembles the behavior of the laser triangulator sensor, while the one labeled *Smooth* corresponds with the behavior of other sensors like the eddy current sensor. The accuracy itself is good enough for commutation algorithm to decouple the forces and torques.

Tests with the laser triangulator sensors showed that it is possible to measure a single DOF and control the platform in a stable way. This is possible because differences in reflections are limited since there is no long stoke motion perpendicular to the laser beam and the variations do not propagate much to the measurement of other DOF. Therefore, the long stroke x-position will be measured by the laser triangulator sensors, while y and ϕ are measured by the additional eddy current sensors.

7.4.2   Auto-Alignment of the Commutation Algorithm

As discussed previously, the absolute accuracy of the sensor system is limited to the mechanical tolerances in the manufacturing and assembly of the system. Moreover, additional eddy current sensors are added to measure the position of the platform in the x-y plane. The mounting of these sensors is done with aluminum
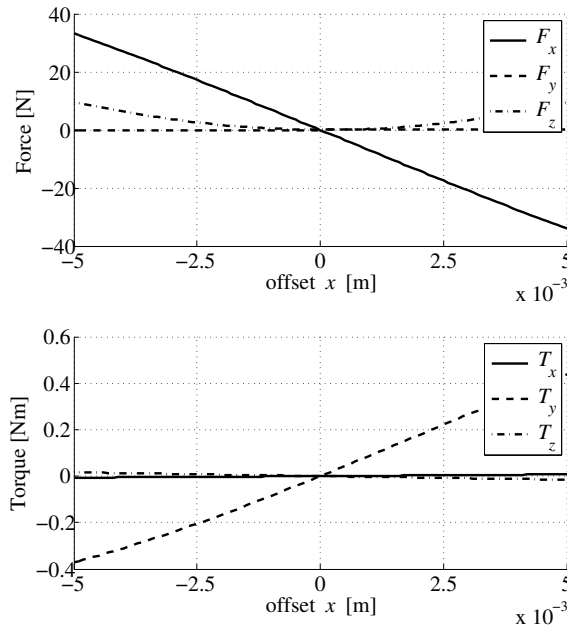
Figure 7.13: Force and torque errors for a measurement offset in x

mounts that are fixed to the coil block with double-sided tape. The absolute position of these additional sensors is anything but accurate and this results in errors in the actual forces and torques that are generated by the commutation algorithm. Even worse, the absolute position of the additional eddy current sensors might even change due to external forces such as gravity or vibrations, since the double-sided tape does not make a stiff connection.

To overcome this problem an auto-alignment algorithm is incorporated that can estimate the error of the measurement system in all six DOF and adds offsets to the measured positions and angles to remove the errors due to the measurement system. For each DOF the commutation algorithm is evaluated with a range of offsets in that particular DOF. The desired F_z is 134 N, which is necessary to lift the platform and all other force and torque setpoints for the commutation algorithm are zero. The currents, that are calculated by the commutation algorithm are fed into an inverse model without that offset to predict what forces and torques would act on the platform and what the difference is with the desired values. The result of such a simulation for a range of offsets in x is shown in Figure 7.13, from which it can be concluded that a measurement offset in x strongly affects F_x, and to a lesser extend F_z and T_y.

Similar simulations can be performed for the other DOF, where a similar conclusion can be drawn, i.e. a measurement offset in one DOF most strongly affects the corresponding force, or torque. This implies that when the force and torque errors are known the sign and quantity of the measurement error for each DOF can be estimated with a first order approximation based upon the simulated behavior.
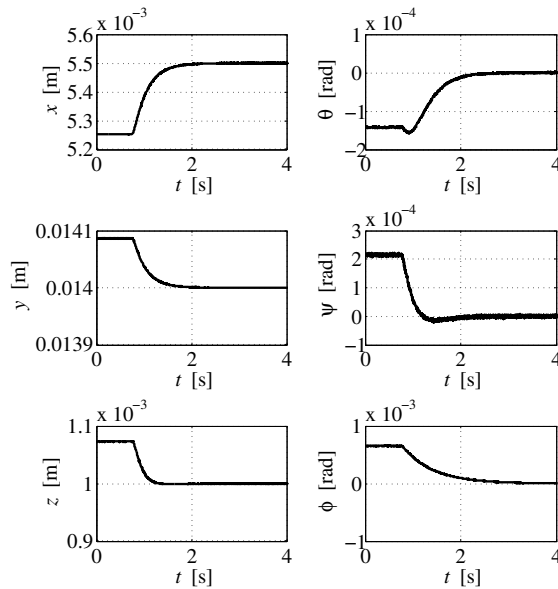
Figure 7.14: Position and orientation of the platform during auto-alignment

Suppose the error of F_x is estimated to be 20 N, then the measurement error in x is approximately -2.8 mm, according to Figure 7.13.

Now the problem is, how to estimate the force and torque errors of the commutation algorithm. If the platform is controlled by a PD controller, steady-state errors will not be compensated and these errors will remain visible. If the speed is zero, i.e. no D-action, the gain of the PD controller multiplied by the error is a good estimate of the force or torque error for each DOF. Since this estimation requires steady-state, it is not advisable to immediately correct the offset at once during one sample time of the controller. Therefore, the predicted correction is multiplied by a gain of 0.001, to force the alignment to be gradually. The position of the platform and the forces and torques from the controllers are monitored during this process and the result is shown in Figure 7.14 and Figure 7.15. From the figures is it clear that the position converges to the setpoint of the controller (x=5.5 mm, y=14 mm, z=1 mm, $\theta = \psi = \phi$ =0 rad), while the output of the controllers go to values close to zero except for F_z, which has to compensate the weight of the platform ($13.7 \times 9.81 = 134.4$ N). The controller outputs do not reduce to zero exactly, since the commutation algorithm does not decouple the forces and torques perfectly, so the remaining error is due to the deviations in the estimate of $\underline{K}$.

The analysis presented here does not prove global convergence of the auto-alignment procedure, since only deviations of one DOF at a time were studied, while the other five DOF were without errors in the calculations. To prove global convergence it should be shown that for each offset in the measurement system at
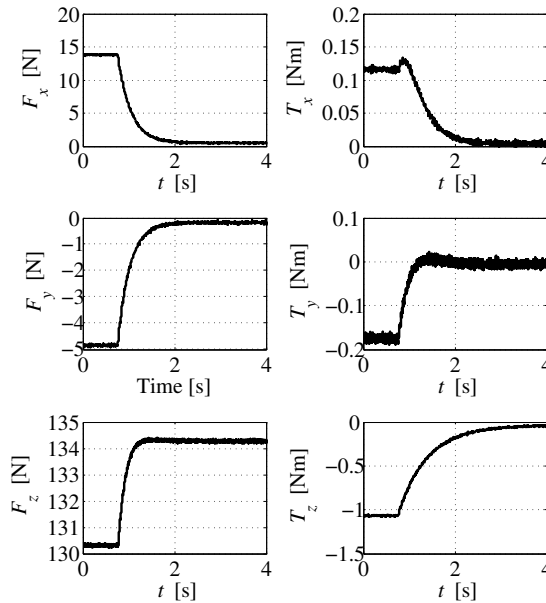
Figure 7.15: Controller forces and torques during auto-alignment

every position in the workspace, the errors of the forces and torques only reach zero if all offsets are zero. Furthermore, this first order approximation must hold throughout the entire workspace.

7.4.3   Closed-Loop Control with Short-Stroke Eddy Current Sensors

With the additional eddy current sensors and after auto-alignment of the commutation algorithm, the planar actuator performance can be evaluated for small displacements. To investigate the performance of the planar actuator and the accuracy and quality of the decoupling, a step of 0.1 mm is applied in the x-direction, while the errors and controller outputs for all six DOF are monitored. Although a step in the position reference is not useful for motion control, due to the infinite acceleration required, it is used here for identification purposes in combination with a saturation on the additional controller force of 25 N. In Figure 7.16 the response in x-direction is shown and the errors of all other DOF. The corresponding force and torque outputs of the controllers are shown in Figure 7.17. The errors show that there is cross-coupling between the degrees of freedom but it is limited. In addition, it is visible that there is a position dependent force ripple, since the static errors depend on the x-position, which is clearly visible for z and the rotation around the x-axis, θ. The static errors are nevertheless in the sensor noise, which is less than 1 μm RMS and 10 μrad RMS. The x-controller outputs a peak force of almost 20 N, but the reaction in y- and z-direction are about 0.2 N, which shows that the cross-coupling is about 1%. The torques <0.1 Nm are small,
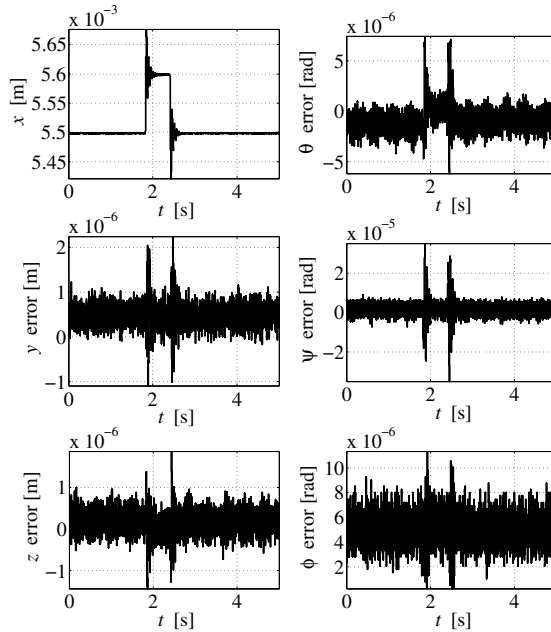
Figure 7.16: Response for all DOF of the planar actuator on a 0.1 mm step identification in x-direction

considering that the platform measures 425×425 mm and has a mass of 13.7 kg and moments of inertia of 0.2 kgm^2 around the x- and y-axis and 0.4 kgm^2 around the z-axis.

7.5 Behavior of the System

The final prototype is shown in Figure 7.18, which is the same system as shown in Figure 7.10 but with the manipulator, power amplifiers, secondary coil, power supply and wireless communication system added. The block scheme of the control architecture of the multi-level contactless motion system is shown in Figure 7.19, where the feedforward and the feedback controller on the ground calculate the desired forces and torques ($\underline{F}_d^{PA}$, $\underline{T}_d^{PA}$, F_d^{LM} and T_d^{RM}) for the motion system. The commutation algorithms convert the desired forces and torques to coil currents for the coils and the current setpoints for the manipulator beam ($\underline{i}^{LM}$) and the arm ($\underline{i}^{RM}$) are transferred to the manipulator by the wireless link. The power amplifiers convert all current setpoints to coil currents, which result in actual forces and torques in the motion system by means of the electromechanical conversion. The measured position of the beam and the arm is sent to the ground controller by the wireless link and it is combined with the measured trajectories of the contactless planar actuator. More advanced control strategies are possible, however, that is not within the scope of this thesis [82].
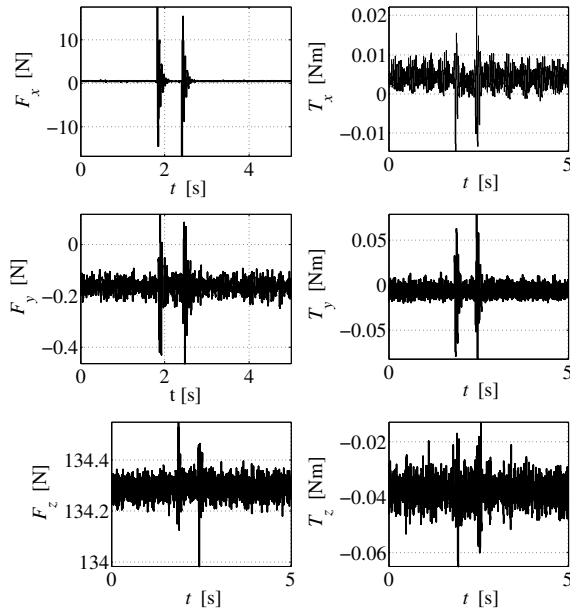
Figure 7.17: Controller output for each DOF of the planar actuator during a 0.1 mm step identification in x-direction
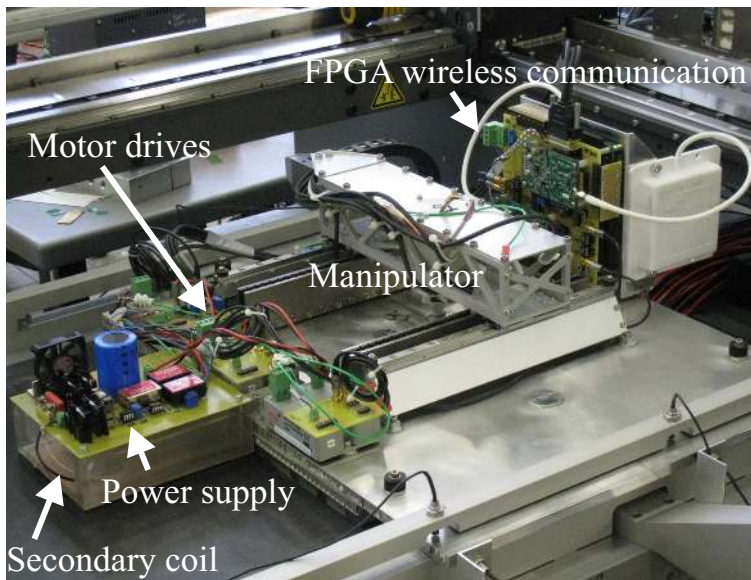

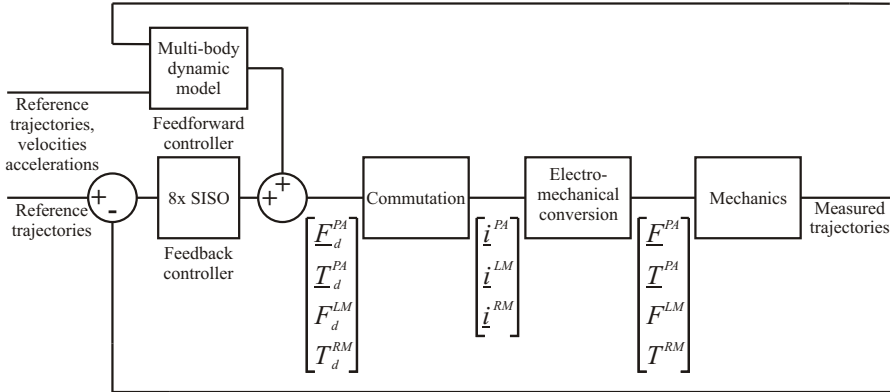Figure 7.18: Final prototype of multi-level contactless motion system

Figure 7.19: Block scheme of the control architecture of the multi-level contactless motion system, where the desired forces and torques ($\underline{F}_d^{PA}$, $\underline{T}_d^{PA}$, F_d^{LM} and T_d^{RM}) are calculated by the feedforward and the feedback controller and, additionally, the current setpoints $\underline{i}^{LM}$ and $\underline{i}^{RM}$ as well as the measured trajectory of the manipulator beam (LM) and the arm (RM) are sent by the wireless link

7.5.1 Power Transfer

The power is transferred to the manipulator using an inductive coupling at a high frequency. The square-wave high frequency driver is fed by a DC bus power supply of which the output voltage and output current are measured. The square-wave driver has a 50% duty-cycle and runs at 158 kHz which is equal to the resonant frequency of the primary coil including 5 m connection cable and the resonant capacitor on the driver. This connector cable introduces additional inductance and significant resistance at that frequency (7 Ω) but unfortunately it is necessary to keep everything in the test setup easily accessible. In a true industrial design this cable should be omitted.

On the secondary side, the energy is stored in a 10 mF capacitor that is kept between two voltages by a hysteresis comparator. When the upper threshold (58.5 V) is reached the power transfer is shut down by short-circuiting the secondary coil. This results in a high impedance for the primary coil driver and drops the power transfer to a few Watts. When the capacitor voltage drops to the lower threshold (57.5 V) the power transfer is resumed. The storage capacitor is used to directly power the motor drives on the platform and to supply three DC-DC converters that generate the required low voltages on the platform (+12 V, +/-15 V, +5 V) for the electronics. The entire topology is discussed in Section 3.4. The power consumption of the electronics is constant (5 W), while the power to the power amplifiers of the motors is varying. This power is found by measuring the capacitor voltage and the current that flows to the motor drives from the capacitor.

The power flow is measured in two situations at low and high power output. In Figure 7.20 the output to the power amplifiers is 15 W and 5 W to the electronics and the input power is 41 W. The efficiency of the power transfer is slightly less than 50%. It is visible from the rising voltage of the capacitor and the current
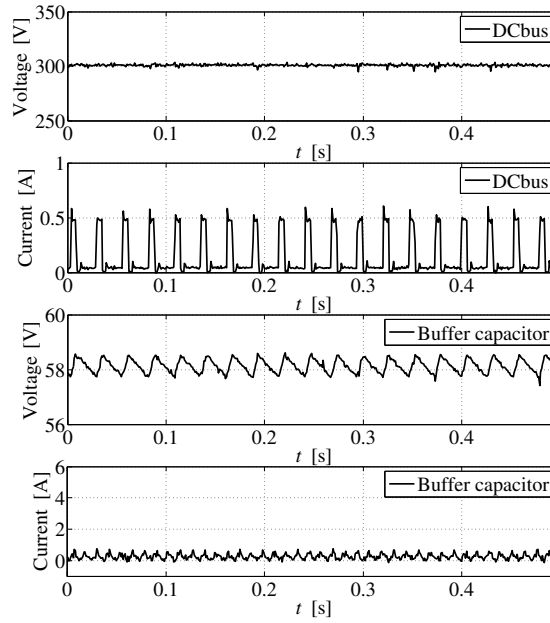
Figure 7.20: Measured voltage and current input from the DC bus supply and voltage and current output of the CPT buffer capacitor at low power
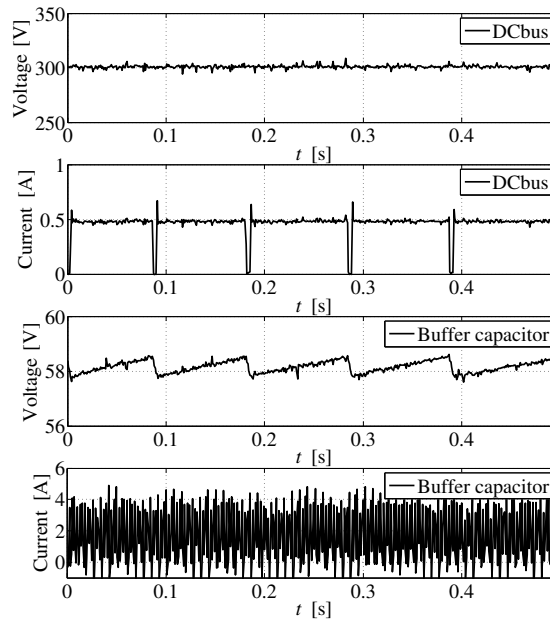

Figure 7.21: Measured voltage and current input from the DC bus supply and voltage and current output of the CPT buffer capacitor at high power

pulses from the DC bus supply that the capacitor is charged in short pulses and that the power transfer is stopped till the capacitor is discharged to the lower voltage threshold. The current to the power amplifiers is fluctuating, however, these fluctuations are at the switching frequency of the power amplifier (32 kHz), while the current probe output is sampled every 330 μs. Due to aliasing the variations appear to have a lower frequency.

The primary coil still draws current when no power is transferred to the buffer which is caused by the fact that the primary circuit still draws some current. With more intelligent power management this problem can be solved.

When a higher output power is required, the power transfer to the storage capacitor is mostly enabled and the discharge periods are very short, as shown in Figure 7.21. The input power is 139 W and the continuous output power is 100 W which yields an efficiency of 72%, while the peak output power is 300 W. In a previous test setup discussed in Section 3.3, where the CPT system was not integrated with the electromagnetic suspension and propulsion, efficiencies up to 90% are achieved. The reason that the efficiency is lower in this system are the losses in the long power cables, oscillations due to parasitic capacitance, the idle power when no power is transferred and eddy current losses in the aluminum water cooling block, which is located 15 mm underneath the coil.

7.5.2   Manipulator Movement

First, the platform is lifted at the position shown in Figure 7.22 using additional eddy current sensors instead of laser triangulator sensors Y_1, Y_2 and X. The commutation algorithm of the planar actuator decouples the 6 DOF, so each DOF is controlled using a PD position controller with a bandwidth of 10 Hz. The setpoint for the controllers is a static position. The measurement of the position and orientation of the platform is done with eddy current sensors, so only short-stroke movements are possible. The torque needed to control the arm of the manipulator ($J = 1 \times 10^{-4}$ kgm^2) is very low but the 10 m/s^2 acceleration of the manipulator beam (1.5 kg) requires a significant force of the linear motors. Moreover, the beam is not located in the center of gravity of the platform as is shown in Figure 7.23, so the gravity force and acceleration force create disturbance torques.

The error of the planar actuator is measured without any compensation of the reaction forces and torques, which is shown in Figure 7.24, where θ is the rotation around the x-axis, ψ the rotation around the y-axis and ϕ the rotation around the z-axis. The corresponding controller forces and torques are shown in Figure 7.25, which clearly shows the reaction of the beam acceleration force in the x-direction and the changing torque around the y-axis due to the combined effect of the acceleration force and changing position of the gravity force of the beam. Since the planar actuator is controlled using a low-bandwidth PD-controller, the errors caused by the reaction forces and torques are clearly visible.

Next, the controller forces of the linear motors of the beam and the corresponding position dependent torque are used as a feedforward in the planar actuator controllers. The effect of the feedforward action on the error and the controller forces and torques is shown in Figure 7.26 and Figure 7.27, respectively. The errors are reduced in all directions, but especially for x and ψ which are the DOF associated
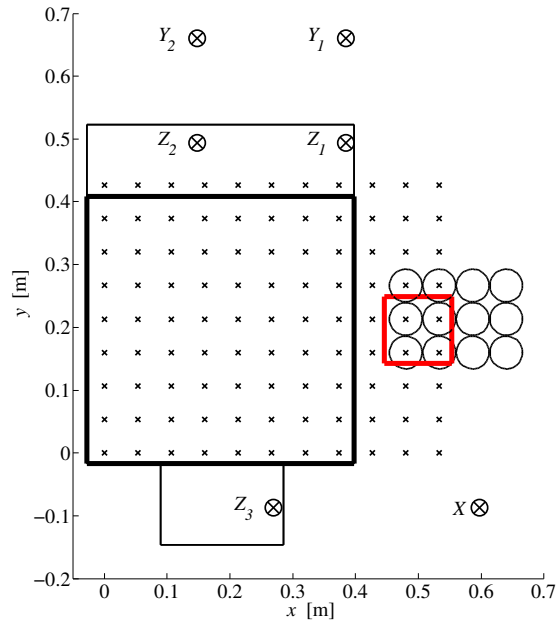
Figure 7.22: Schematic representation of the experimental setup at position $x = 0.005$ m
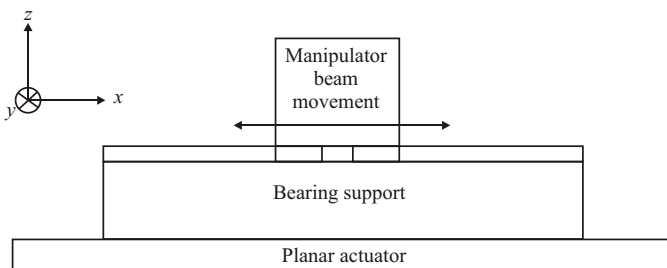

Figure 7.23: Schematic 2D representation of contactless planar actuator with manipulator
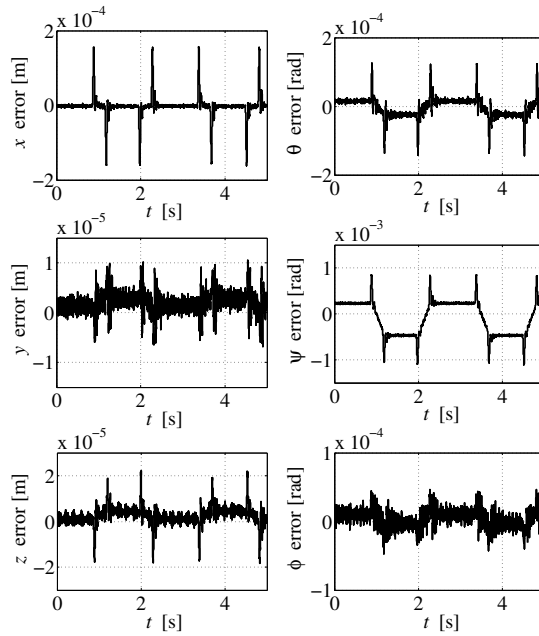
Figure 7.24: Measured errors of the planar actuator during movement of the manipulator without compensation
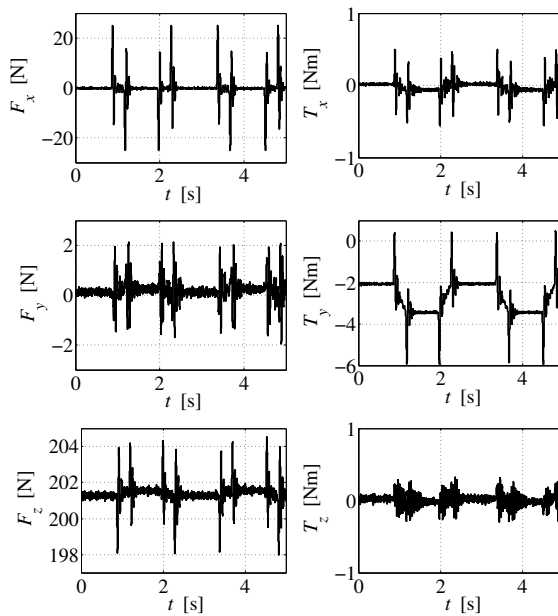

Figure 7.25: Controller forces and torques of the planar actuator during movement of the manipulator without compensation
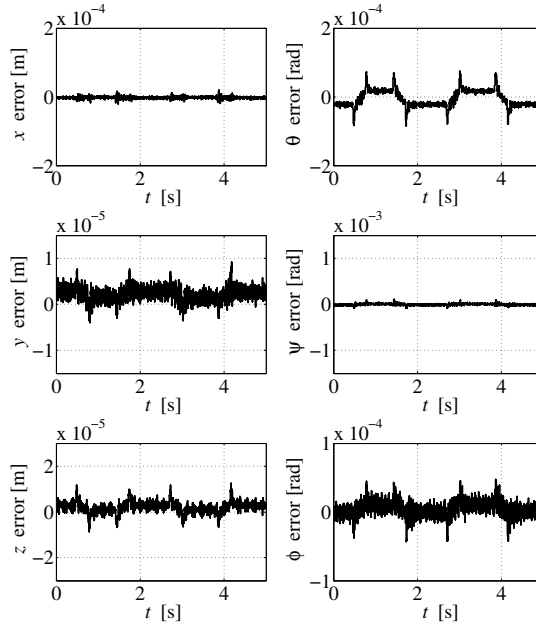
Figure 7.26: Measured errors of the planar actuator during movement of the manipulator with compensation

with the disturbances. This compensation can only be done if the manipulator controller is synchronized in real-time with the planar actuator controller. This implies that the delay between sending and receiving of current commands of the manipulator motors and the position measurements is smaller that the sample time of the controller. This proves the effectiveness of the wireless motion control system.

7.5.3   Long Stroke Movement

The system behavior has been demonstrated at a static position without any long stroke movement of the planar actuator. The next step is to move the planar actuator in the x-direction in such a manner that the secondary coil will move in range of a different primary coil. As discussed in Section 7.4.1, it is possible to measure the x-position with the long-stroke laser triangulator sensor X, while y and ϕ are measured using the additional eddy current sensors instead of the laser triangulator sensors Y_1 and Y_2.

In Figure 7.22 at position $x = 0.005$ m, the coil in the middle of the left row of three (coil 86) is energized. If the planar actuator moves to the right, there is a point at position $x = 0.0125$ m, where both coil 95 (which is on the right side of coil 86) and coil 86 are in range of the secondary coil as is shown in Figure 7.28. The final position of the planar actuator is shown in Figure 7.29, where coil 86 is out of range. The switching of the power transfer is done with mechanical relays, so to prevent that two coils are active at the same time, a dead time of 30 ms
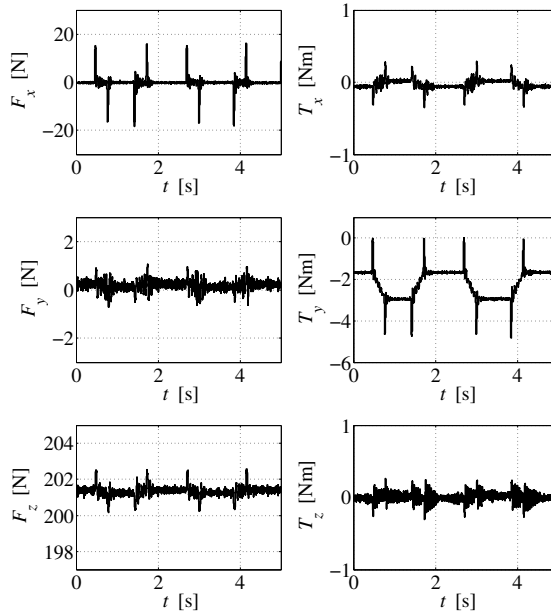
Figure 7.27: Controller forces and torques of the planar actuator during movement of the manipulator with compensation

is incorporated between switching one off and the other one on. In addition, a dead zone of 1 mm in position is added to prevent continuous switching, so coil 86 is switched off and coil 96 is switched on at position $x = 0.013$ m and the opposite occurs at position $x = 0.012$ m. When the mechanical relay (DPDT) disconnects the coil from the square-wave voltage source, it reconnects the coil to the power amplifier to allow the coil to be active in the electromagnetic suspension and propulsion, if it is in range of the magnet array.

In Figure 7.30, the measured absolute position of the planar actuator and the manipulator beam is shown, as well as the local position of the manipulator beam with respect to the platform. The manipulator beam is continuously moving between three different points with a third order position reference. The planar actuator is moved in long stroke between three x-positions, the other 5 DOF have a constant reference. The errors of the planar actuator during these movements are shown in Figure 7.31 and the corresponding forces and torques from the controller are shown in Figure 7.32.

Due to the limited resolution of the laser sensor, the overall noise levels are much higher, which are amplified by the vibrations due to movement of the manipulator. Although the reaction forces and torques are compensated, the amplitude of the error in x-direction is about the same as when the eddy current sensors are used without compensation (see Figure 7.24). The errors in the other directions become larger as well, which is related to the cross-coupling in the planar actuator. The decoupling of forces and torques is not perfect, so variations in
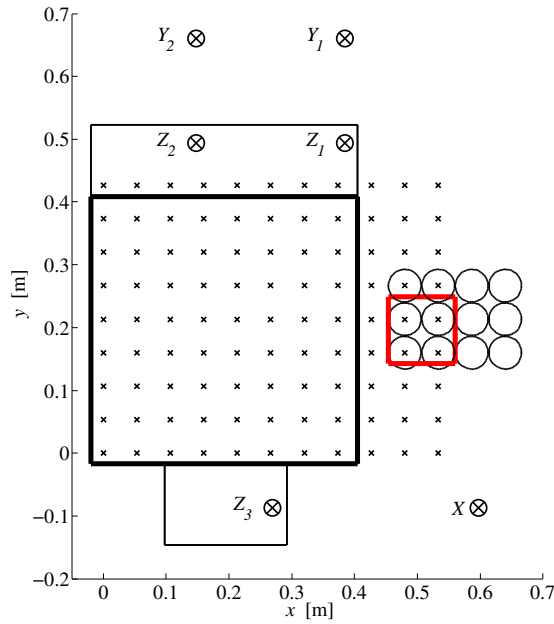
Figure 7.28: Schematic representation of the experimental setup at position $x = 0.0125$ m
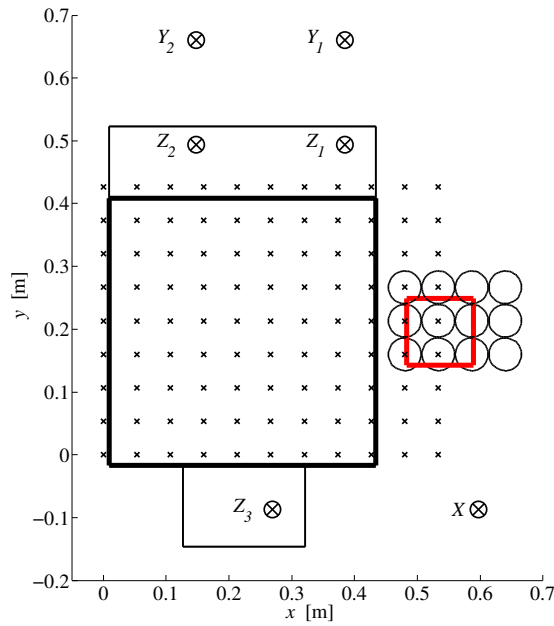

Figure 7.29: Schematic representation of the experimental setup at position $x = 0.0415$ m
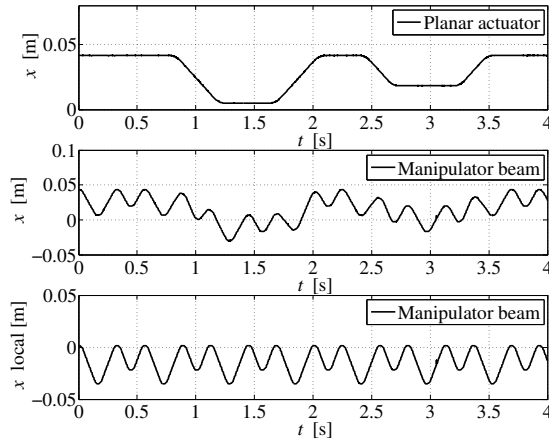
Figure 7.30: Measured x-position of the planar actuator (x) and manipulator beam (x) in the global coordinate frame $\vec{e}^{\,0}$ and the local displacement (x local) of the manipulator beam with respect to the planar actuator in coordinate frame $\vec{e}^{\,1}$

the control force in x will also influence the other forces and torques in the magnetic bearings. Finally, the error in y does also depend on the x-position (there is no integrative action), a result of cross-coupling. This cross-coupling occurs due to limited model precision in the commutation algorithm, mechanical tolerances and measurement errors.

The behavior of the contactless power transfer during the long stroke movement is shown in Figure 7.33, where the voltage and current of the DC bus supply and the buffer capacitor on the platform are shown, together with the active primary coil and the acceleration of the manipulator beam in the $\vec{e}^{\,1}$ frame. Energy is drawn from the DC bus supply during charging of the buffer capacitor on the platform, which is visible from the current pulses from the DC bus supply. The sequences of charging and discharging are clearly visible from the increasing and decreasing of the capacitor voltage, respectively.

The acceleration of the manipulator beam is also shown and that shape corresponds with the current drawn from the buffer capacitor. It is visible that decelerations of the manipulator beam requires less power than acceleration, which is related to the electromechanical energy conversion. Finally, the enabled primary coils is shown, including the 30 ms deadtime between switching off and on. In the deadtime the buffer voltage drops to a lower value than during normal operation. The drop depends on the energy consumption of the manipulator within the 30 ms deadtime. The first occurrence is at the same moment of maximum acceleration of the manipulator beam, and the voltage drops from 58 V to 55 V. During the second primary coil transition, the manipulator beam moves at constant speed and less energy is needed, resulting in a voltage drop of 58 V to 57 V. The peak output power is 208 W and the continuous output power is only 20 W, while the average input power is 47 W and the peak input power is 140 W.
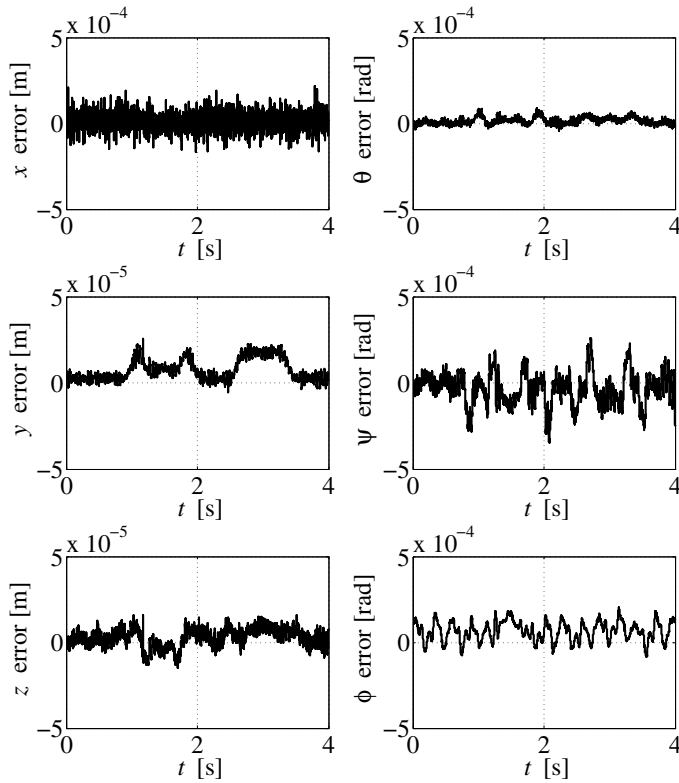
Figure 7.31: Measured errors of the planar actuator during long stroke movement in the x-direction of the planar actuator and the manipulator beam (see Figure 7.30)
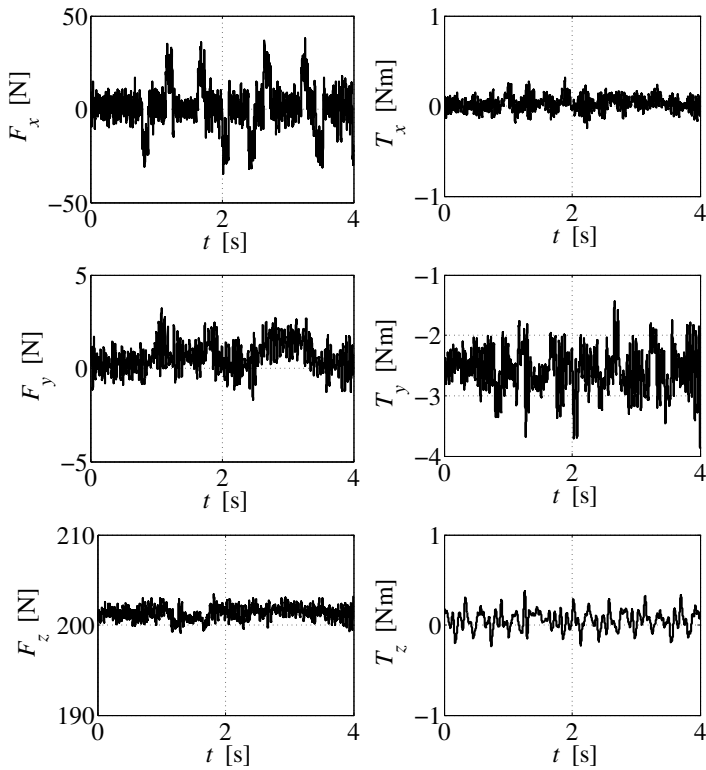
Figure 7.32: Controller output of the planar actuator during long stroke movement in the x-direction of the planar actuator and the manipulator beam (see Figure 7.30)
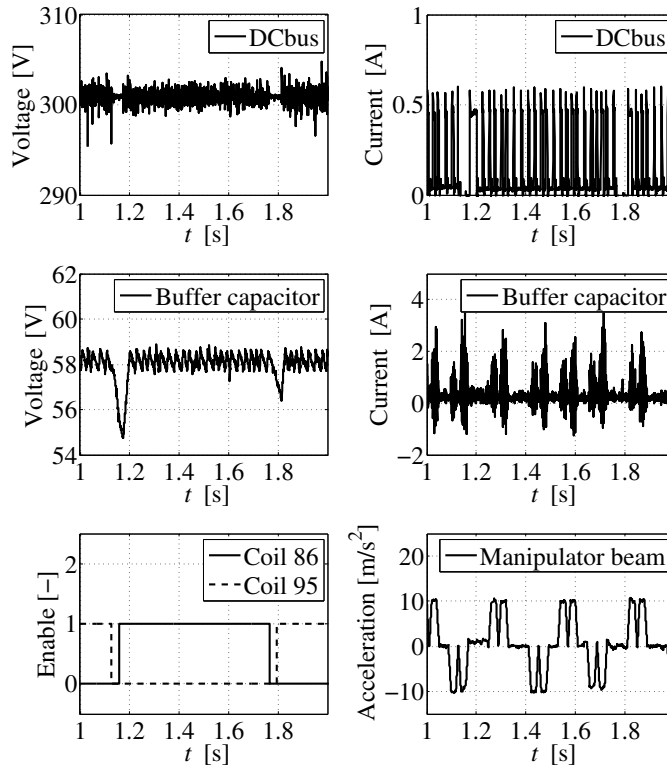
Figure 7.33: Measured voltage and current input from the DC bus supply and voltage and current output of the CPT buffer capacitor during long stroke movement of the planar actuator and the manipulator beam in the x-direction (see Figure 7.30), including the enabled primary coil and the acceleration of the manipulator beam in the $\vec{\underline{e}}^1$ frame

7.5.4   Limitations of the Mechanical Relays

As already discussed, the laser triangulator sensors are not suitable to measure the long-stroke movement due to the variations in the reflection of the lasers at different positions of the target surface. However, there are additional problems related to the mechanical relays. As it turned out, the relays do not have a high impedance at high frequencies. While at frequencies up to several kHz, the absolute value of the impedance of an open contact is in the mega-Ohm range. Since the relay can be represented as a capacitor of approximately 500 pF, at high frequencies, the absolute value of the impedance quickly drops to several kilo-Ohms. This results in currents that are induced in the loop of the coil and the relays, which causes additional losses. Moreover, the induced voltages in the litz-wire coils due to the current flowing in the power transferring primary coil can reach peak values up to 140 V. Since the induced voltages have the same frequency as the power transfer they are filtered using a first order LC-low-pass filter with a cut-off frequency at 30 kHz, which prevents the voltages to reach the Bosch amplifiers which are rated up to 90 V.

A more elegant solution would be to integrate the power amplifier and the power transfer square-wave voltage source into one system. The power stage of a PWM based power amplifier should be able to switch at frequencies in the same range as the power transfer (< 200 kHz). If the unit acts as an power transfer driver, it will change to a 50% duty-cycle square-wave voltage source. An AC switch of the same type as used in the power supply to short the secondary circuit (see Section 3.4) could be used to switch the resonant capacitor in series with the coil if the power transfer mode is enabled. This resonant capacitor should of course be switched out of the circuit if the driver is used as a current source. The main problem is to design a switch that can withstand the high voltages in the resonant circuit. However, high voltage, i.e. up to 2 kV, diodes and MOSFET/IGBTs exist, or can be realized by using components in series. Another advantage of such a solution is the increased power management capabilities combining fast solid state switching and the option of including improved power management in the FPGA, which will boost the efficiency of the power transfer.

7.6   Conclusions

A significant number of design aspects of the contactless planar actuator with manipulator system have been discussed. From these aspects, it has become clear that a lot of components in the system influence each other.

The look-up table based commutation algorithm for the decoupling of forces and torques on a 6 DOF magnetically levitated contactless planar actuator with moving magnets that includes end-effects, which has been presented in Section 2.4, has been validated. The method is verified with measurements and can realize the desired forces and torques within a peak error of 3% and an RMS error of 1.3%. The maximum torque error has been found to be 0.15 Nm. This is consistent with the error estimation of the model and the commutation presented in Section 2.1 and Section 2.4, respectively.

The worst-case surface temperature during levitation has been measured to be

71.1°C, which is 30°C lower than the prediction in Chapter 4. This is realized by reducing the weight of the support structure by using aluminum honeycomb material and by a 33% increase of the litz wire coil filling factor. The prediction of the model presented in Section 2.5 has been found to be within the 10% error that was estimated. An auto-alignment procedure has been described that can correct the absolute static errors in the measurement system, due to misalignment and tolerances of the assembled setup. However, errors due to sensor noise, limited linearity and the mechanical tolerances of the coils and magnets and magnetization tolerances of the magnets persist.

The behavior of the planar actuator with this commutation algorithm has been demonstrated in closed loop control. Due to the remaining errors in the commutation algorithm, crosstalk between the 6 DOF has been identified to be of the same order as the errors in the commutation algorithm itself. Static levitation has been shown with errors smaller than 1 μm RMS and 10 μrad RMS using 6 DOF measurement with eddy current sensors.

Finally, the behavior of the multi-level contactless motion system, i.e. the contactless planar actuator with manipulator including contactless power transfer and wireless motion control, has been demonstrated with measurements. It has been shown that the disturbance forces and torques of the manipulator can be effectively countered using the wireless control loop in combination with feedforward.

The long stroke laser triangulator measurement system in the x-y-plane, which has been chosen for its ability to measure a large rotation around the z-axis of up to 5 degrees, has turned out to give a lot of problems. Long stroke movement can only be controlled in one direction with this type of sensor. If a large rotation around the z-axis is not important, the measurement system can be replaced with a laser interferometer based system. Otherwise, a new measurement system needs to be developed.

The contactless power transfer has been able to transfer up to 100 W of power to the platform with a maximum efficiency of 72% and an efficiency around 50% at lower power levels. In a previous test setup discussed in Section 3.3, where the CPT system was not integrated with the electromagnetic suspension and propulsion, efficiencies up to 90% are achieved. The reason that the efficiency is lower in this system are the losses in the long power cables, oscillations due to parasitic capacitance, the idle power when no power is transferred and eddy current losses in the aluminum water cooling block, which is located 15 mm underneath the coil.

The efficiency can be further improved by better power management and by designing an integrated power amplifier and square-wave voltage source. Due to time and budget restraints, a mechanical relay is used to switch the coil from the power amplifier to the high frequency square-wave voltage source. This mechanical relay causes additional losses and is very slow, resulting in long switching dead-times, which interrupt the power transfer. A more elegant solution would be to integrate the power amplifier and the square-wave voltage source into one system. The power stage of a PWM based power amplifier should be able to switch at frequencies in the same range as the contactless power transfer (< 200 kHz). If the unit acts as a square-wave voltage source, it will change to a 50% duty-cycle square-wave voltage source. This requires a reprogramming of the FPGA-logic that is available in most modern power amplifiers.

Conclusions and Recommendations

A multi-level contactless motion system has been investigated in this thesis on a system level, integrating three contactless subsystems, i.e. six DOF electromagnetic suspension and propulsion, contactless power transfer (CPT) to a moving platform and wireless real-time communication between the ground controller and the plant processes on the platform into a single system. This research has resulted in a fully operational prototype, which has been successfully tested.

Three different levels of the electromagnetic spectrum are involved, i.e. six DOF electromagnetic suspension and propulsion generating forces and torques (<3 kHz), contactless power transfer (50-200 kHz), and real-time wireless communication (2.4 GHz). These three techniques facilitate the design of high precision machines with greater complexity, accuracy and flexibility, either by removing cable slabs by means of integrating wireless real-time communication and contactless power transfer or by removing physical contact altogether by including 6 DOF electromagnetic suspension and propulsion. The analysis in this thesis has provided a novel framework for understanding the behavior of the subsystems and their interaction in the full system.

The conclusions are grouped according to objectives formulated in Chapter 1. Finally, an outlook toward further developments is given.

8.1   System Integration

The system integration of the multi-level contactless motion system has been the focus of this thesis and has proven not to be an easy task. At the start of this research it was not sure whether subsystems of the system were feasible whatsoever (reliable CPT with infinite stroke in the x-y plane, real-time wireless communication) and the first working prototype of a contactless planar actuator [10, 12] had yet to be built.

Due to the different operating frequencies of the 6 DOF electromagnetic suspension and propulsion (<3kHz) and the contactless power transfer (50-200 kHz), the actuator coils also had to be able to work as primary coils at higher frequency. This requires the use of litz wire to limit the eddy current losses at high frequencies at a cost of a lower filling factor of copper in the coil cross-section, i.e. higher DC resistance. This results in higher dissipation of the contactless planar actuator compared to regular solid wire or foil coils for a given topology. Since this has been the first time to use litz wire as actuator coils, a lot of attention has been given to the thermal problems. Conservative estimates were initially used for the filling factor based upon the first litz wire coil prototypes (0.3) and for the levitated mass (solid aluminum). In the realization, the filling factor has been increased to 0.4 by using high quality custom made litz wire and the levitated mass has been reduced with 2.4 kg by using aluminum honeycomb for the support structure of the multi-level contactless motion system. Additionally, keeping weight as low

as possible has been important for all aspects of the system, from electronics to electromechanics and mechanics.

The high operating frequency of the CPT requires parasitic effects that are normally not considered in actuator design, to be taken into account. These effects include parasitic inductance in cables as well as the capacitance of the coil, the capacitance between the coil and other structural components, as well as eddy currents induced in structural components.

Removing cables for power and data transfer to the moving parts in this motion system has eliminated the inflexibility, vibrations, hysteresis and friction disturbances associated with cable slabs. The moving mass of the cable slab is taken out of the system, which can be significant depending on the thickness of the cables and the structural requirements of the cable slab. However, more power electronics are necessary on the moving part to convert the high frequency AC input to the required DC voltage levels and to operate the electromechanical actuators on the moving platform. Electronics for the real-time wireless communication also increase the mass. The mass of all the additional electronics is, therefore, added to the moving mass. Whether the total moving mass is reduced or increased depends on the application. In the prototype, the additional mass of the electronics accounts for 2.2 kg, which might be reduced by 0.5 kg by further miniaturization. However, a self supporting cable slab with long stoke in the x-y plane might have a similar mass.

The dynamic equations of the multi-level contactless motion system have been derived using Lagrange in the mechanical and the electromagnetic domain. The result is a set of differential equations that describes the system behavior, including voltages and currents of the coils, forces and torques from the electromechanical conversion and the motion of the bodies in the system as a result of the applied forces and torques. In this research, the Lagrangian system model has been used to verify the different models that describe separate subsystem (electromechanical conversion, voltage equation for the power amplifiers, equations of motion). However, it is recommended to use this type of model from the initial phase of the design of similar systems, now the working principle of a multi-level contactless motion system has been shown. It is very suitable for visualizing the interactions in the system and for the inclusion of non-rigid body dynamics or non-linear electromagnetic effects. Furthermore, it is a useful model for deriving multiple-input-multiple-output (MIMO) control strategies for the motion system and to include the control of non-rigid body modes.

Due to the uncertainty with respect to filling factor and levitated mass, the topology of the contactless planar actuator has been chosen with a worst-case thermal scenario. Now the properties of the litz wire coils are known better and construction with honeycomb aluminum has been explored it is possible to use a less conservative approach for the topology selection. For a certain application (stroke, moving mass, acceleration) with a known motion profile for the multi-level contactless motion system, the duty-cycle of the coils can be explored using the Lagrangian system model. With this information the thermal loading of the coils will be known more accurately, so a topology can be chosen that is more appropriate for the application. By combining the geometry optimization of a single coil, the look-up table commutation algorithm, the Lagrangian system model

and the thermal model it is possible to evaluate the behavior of a multi-level contactless motion system in an efficient manner.

Although much attention has been given to the thermal behavior of the 6 DOF electromagnetic suspension and propulsion coils, the thermal properties of the multi-level contactless motion system itself and the measurement system have not been included in the research. Moreover, not much is known about the thermal behavior of the aluminum honeycomb material. It is recommended to perform a thermal analysis of the full structure.

8.2 Contactless Power Transfer

The most important contactless power transfer (CPT) requirement is infinite stroke in the x-y plane, while being able to transfer power efficiently at any position. In addition, it should be tolerant to small variations of the airgap and small rotations. This level of unconstrained movement has not been achieved before for contactless power transfer.

A new design approach has been taken, which focussed on minimizing the position dependency of the coupling between the primary and secondary coil. In addition, the workspace of the secondary coil is selected large enough to enable it to move from one primary coil to the next one without large variations in coupling ($<25\%$ in the initial prototype, $<12\%$ in the final prototype). The only requirement for the mean value of the coupling is that it must be high enough (>0.2) to transfer the desired continuous power.

The design has been tested to transfer 250 W continuously for up to 30 minutes with an efficiency up to 90%. Furthermore, it has been shown that realistic mechanical movements, i.e. velocities up to 10 m/s, do not influence the power transfer.

8.3 Real-time Wireless Communication

Until now, wireless communication was based on protocols that were developed for high data throughput. The delay between sending and receiving of the data packets cannot be reduced to less than several milliseconds due to the protocol overhead, even if the datarate of the wireless communication is increased. For high performance motion control applications, the total closed loop delay, including calculation time of the controller and delays in the sensors and actuators, should preferably be less than 1 ms.

In this thesis, a new protocol has been presented that is optimized for transmitting data packets with a small delay. It has been implemented on an FPGA and 2.4 GHz transceivers with a datarate up to 1.5 Mbps. Measurements showed that is it possible to transmit and receive data packets with less than 100 μs delay, which is more than ten times faster than UDP/IP WLAN at 11 Mbps. The additional closed loop delay of the wireless communication in the control loop is 300 μs, which includes full duplex data transmission (2×100 μs), sample and hold delay and delay in the logic.

Moreover, the delay is directly related to the datarate. So by increasing the

datarate by a factor ten, the delay will decrease by a factor ten. Since the current transceiver has a relatively low datarate, much can be improved. Besides a limited datarate, the disadvantage of this transceiver if the rather high bit-error-rate (BER), resulting in a packet loss of 1%. A redesign of the wireless channel with other radio-transceivers or with optical systems such as laser or infrared is recommended. Some preliminary results with infrared communication are discussed in [81].

The wireless system has been successfully implemented in a wireless position control loop where data packets were sent every 96 μs. Variation of the closed loop delay was visible in the measurements, since the sample time of the controller did not match the sample time of the wireless link. A synchronized operation of the two systems would enhance the performance of the position control loop by reducing jitter. The maximum variation of the closed loop delay or jitter is 133 μs, which introduces chattering in the position feedback loop and has a significant impact on the error. However, the jitter is still a factor 4 smaller than in UDP/IP WLAN.

8.4   Contactless Planar Actuator

The analysis of the contactless planar actuator is an extension of the work of Helm Jansen [10] and Nelis van Lierop [12] and the electromagnetic models are based upon their work. A new commutation algorithm based on a smart use of compact look-up tables has been developed to accurately predict the behavior of all coils in the range of the magnet array including those that are not completely overlapped by the magnet array. If these coils are included in the control of the planar actuator, the controllability is improved or the number of coils necessary to control the planar actuator at all positions in the workspace can be reduced.

In addition, it makes the use of window functions to force smooth switching obsolete, since smooth switching is guaranteed by the decay of the magnet flux density as the magnet array moves out of range of a particular coil. However, the smoothing window function [10, 12] can be used in combination with the look-up table based commutation, if desired.

This look-up table based commutation algorithm can also include higher harmonics of the flux density distribution into the commutation algorithm, which improves the accuracy compared to only the first harmonic in [10, 12]. The look-up tables have to be calculated offline for a given geometry of coils and magnets and their accuracy depends on that of the model. The look-up tables could also be constructed from measurements. In this case, the peak force error has been found to be 3%, with an RMS error of 1.3% and a peak torque error of 0.15 Nm, which corresponds with the error of the model used to calculate the look-up tables. In closed loop, an accuracy of 1 μm and 10 μm has been shown during static levitation using a 6 DOF eddy current measurement system.

An auto-alignment procedure that can estimate absolute position errors of the measurement system is proposed. It uses the output of the PD-controller to estimate the difference between the desired forces and torques and the actual forces and torques generated by the currents from the commutation algorithm. The auto-alignment corrects the position and orientation measurement by adding

offsets to the measured values and it effectively eliminates cross-coupling due to measurement errors. Unfortunately, it only works when the system is at standstill, since the estimation assumes steady-state. A possible improvement would be to extend the capabilities to enable alignment during movement. Finally, it is not proven that this method is globally converging at every position in the workspace, so this should be further investigated.

The use of round coils, due to their symmetry around the z-axis, in combination with the look-up table based commutation algorithm enables full rotation around the z-axis of the planar actuator platform. However, this requires that the full rotation can be measured accurately.

8.5 Realization of a Prototype

A prototype of the multi-level contactless motion system has been successfully built and tested. The topology of the six DOF electromagnetic suspension and propulsion has been chosen based upon a worst-case thermal scenario, i.e. litz wire coil filling factor of 0.3 and a solid aluminum support structure. The worst-case surface temperature has been estimated to be 102°C. However, the filling factor of the litz wire coils has been increased to 0.4 and the total levitated mass has been reduced by 1.6 kg which reduced the worst-case temperature surface prediction to 75°C. In the prototype the worst-case temperature was measured to be 71.1°C. Furthermore, it was shown that during movement of the levitated platform with accelerations of 10 m/s^2 in both x- and y-direction the steady-state maximum temperature drops to almost 30°C. This is caused by the fact that the thermal loading of the coils is spread both spatially and in time. The following conclusions can be drawn regarding the selection of the six DOF electromagnetic suspension and propulsion topology:

1. A 6 DOF electromagnetic suspension and propulsion system with litz wire coils is feasible.

2. The worst-case dissipation during levitation design criterion is very conservative.

3. The levitated mass or acceleration can be increased.

4. A lower number of coils can be used to achieve similar or better performance, especially when the duty-cycle is considered from the start of the design.

The long stroke laser triangulator measurement system in the x-y-plane has been chosen for its ability to measure a large rotation around the z-axis of up to 5 degrees. However, it gave rise to vibrations if used in a control feedback loop. Long stroke movement could only be controlled in one direction with this type of sensor. If a large rotation around the z-axis is not important, the measurement system can be replaced with a laser interferometer based system. Otherwise, a new measurement system needs to be developed. An improved long stroke sensor system will enable a better identification of the dynamics and cross-coupling within the system.

The contactless power transfer has been able to transfer up to 100 W of power to the platform with a maximum efficiency of 72% and an efficiency around 50% at lower power levels. In a previous test setup discussed in Section 3.3, where the CPT system was not integrated with the electromagnetic suspension and propulsion, efficiencies up to 90% are achieved. The reason that the efficiency is lower in this system are the losses in the long power cables, oscillations due to parasitic capacitance, the idle power when no power is transferred and eddy current losses in the aluminum water cooling block, which is located 15 mm underneath the coil.

The efficiency of the CPT can be improved by better power management and by designing an integrated power amplifier and square-wave voltage source. Now, a mechanical relay is used to switch the coil from the power amplifier to the high frequency energy transfer driver. This mechanical relay causes additional losses and is very slow, resulting in long switching deadtimes, which interrupt the power transfer. A better solution would be to combine the power amplifier and the square-wave voltage source into one system. Power stages of currently existing advanced PWM based power amplifier are able to switch at frequencies up to 200 kHz. If the unit operates in power transfer mode, it will change to a 50% duty-cycle square-wave voltage source. This functionality can easily be included in the FPGA-logic that is available in most modern power amplifiers.

All motion controllers of the 8 DOF multi-level contactless motion system were located on the fixed world, where the wireless real-time communication enabled wireless motion control of the 2 DOF of the manipulator. The small delay in the wireless link enabled a synchronized behavior of the total system, where real-time position information is used to compensate the reaction forces and torques between the planar actuator and the manipulator.

8.6   Thesis Contributions

The major scientific and technological contributions of this thesis can be summarized as follows:

- *Comprehensive Lagrangian framework for motion systems with a six DOF electromagnetic suspension and propulsion, which gives good insight into the transient interaction between the mechanical and the electromagnetic domain.* Dynamic equations based upon Lagrange are common for mechanical system and have been applied for simple electromechanical conversions such as a linear or rotary motor with a single mechanical DOF. This has been the first application to a system with a large number of DOF in both domains, 8 DOF in the mechanical domain and 90 DOF in the electromagnetic domain.

- *The modeling, building and testing of a inductive contactless power transfer system that can transfer power efficiently and continuously with unlimited stroke in the x-y plane and short stroke movements in other directions.* Previously presented inductive solutions have limited stroke or can not transfer power continuously at any position.

- *First application of real-time wireless motion control with a closed loop delay that is small enough for realistic motion systems.* In literature there are applications of standard wireless protocols used for wireless motion control. However, these standard wireless communication protocols introduce communication delays in the control loop of several milliseconds. In this thesis, a new protocol and implementation have been used, which reduced the wireless communication delay with a factor 10 compared to the fastest standard wireless communication protocol based upon radio waves.

- *New real-time commutation algorithm for contactless planar actuator with moving magnets that includes end-effects and full rotation around the z-axis.* Previously presented methods were based on simplified analytical methods that could only include the first harmonic of the magnetic field in real-time. The commutation method presented in this thesis has proposed a smart use of compact look-up tables that can include higher harmonics and end-effects in the real-time commutation.

- *Modeling, building and testing of a multi-level contactless motion system.* In this thesis, the first working prototype of a multi-level contactless motion system is presented that integrates six DOF electromagnetic suspension and propulsion with contactless power transfer and wireless motion control, which each occupy a different range in the electromagnetic frequency spectrum. The system can operate without mechanical or electrical contact with the fixed world.

8.7 Outlook Towards Future Developments

Based on the results that have been presented in this thesis, the following projections for future developments are done.

8.7.1 Measurement System on the Floating Platform

Further enhanced functionality of the contactless planar actuator such as rotation around the z-axis and multiple actuators above a single coil block is possible. The controller and commutation algorithm are suitable for realizing this, but the limitation is the measurement system. The reason is that the measurement system is located on the fixed world, while the object, which position should be measured, is moving over large distances. A real-time wireless link enables a different approach by placing the sensors on the floating platform. In combination with a measurement grid or other reference on the fixed world, the position and orientation in the x-y plane can be measured and the other DOF can be found by measuring the height of the platform above the coil block at three positions. The real-time wireless link can send the measured positions with a small delay to the ground controller that controls the currents in the suspension coils. Of course, to operate the sensors and electronics of the wireless communication, power is necessary on the floating platform.

8.7.2 Cableless Motion Systems

In this thesis, the contactless power transfer and wireless motion control have been studied in combination with 6 DOF electromagnetic suspension and propulsion. The combined use of contactless power transfer and wireless motion control provides a powerful technique to completely remove cables in wide variety of applications. In most machines, rotating and linear motors are present, where a cable connects the moving part with the fixed world. A cableless solution will increase reliability, repeatability, accuracy, acceleration and velocity of those machines. Moreover, guiding cables into a vacuum is difficult, so cableless solutions might be applicable then as well. Since the electromagnetic suspension and propulsion is based on repulsive forces, the use of iron is prohibited in the application discussed in this thesis. In other systems, this might not be a problem, so the maximum continuous power can be considerably enhanced if iron or ferrites are used to increase the coupling between the primary and secondary coils. A project with industry is in progress to investigate these type of motion systems. The current status of this project includes two stacked linear drives with contactless power transfer by means of elongated primary coils, while the position control loop is collocated at each linear drive, since real-time wireless control is not yet incorporated [76]. Another project has been started to investigate the integration of a linear synchronous actuator and contactless power transfer [77].

8.7.3 Further System Integration

Since this thesis presents the first attempt of integrating contactless power transfer and electromagnetic suspension and propulsion as well as real-time wireless control, the results enable further system integration. With the new commutation algorithm that includes end-effects it is possible to control magnet arrays that are not perfectly periodic. This makes it possible to build a square magnet array with a hole in the center, where the secondary coil can be placed. By including the coil within the structure, the size of the total structure becomes smaller and stiffness can be increased. Other options include an array of round coils with a hexagonal packing arrangement, thereby increasing the area that is filled with copper, making the coil array more compact.

Furthermore, the real-time wireless link can be used to improve the power management and control the power flow of the contactless power transfer. This will boost the efficiency of the power transfer. In addition, the power control method presented in this thesis can be kept as a hardware safety method or backup, if the wireless communication is offline. Finally, the motors and sensors of the manipulator on the floating platform are still connected with cables to the power amplifiers and the electronics of the real-time wireless communication, respectively. A truly cableless design would also make these cables obsolete as discussed in the previous section.

8.7.4 Control of Non-Rigid Body Modes

Because the number of coils used to control the 6 DOF of the planar actuator is much larger than six, the system is highly overactuated and additional constraints are necessary to calculate the current in each coil. So far, the currents in the

coils have been calculated using the pseudo-inverse, which minimizes the 2-norm of the current vector. Other transformations can be done such as minimizing the ∞-norm, which will limit the dissipation in a single coil. This choice is especially interesting for reducing the thermal stresses in the litz wire coils. Another option is to include the force distribution over the magnet array, which enables the possibility of controlling non-rigid body modes, i.e. the shape deformation of the platform.

The Lagrangian system model can be extended to include non-rigid body modes [79]. This can only be implemented if these modes can be measured, either by a grid of sensors on the fixed world, or directly by strain gages on the platform. The real-time wireless link can send this information to the controller on the fixed world. A project has already been started to research and demonstrate a planar actuator with nanometer accuracy. Non-rigid body modes are an important factor in this project [80].

8.7.5 Electromagnetic Compatibility

In industrial applications, every machine has to comply with electromagnetic compatibility standards. Due to the use of several frequency levels of the electromagnetic spectrum in the multi-level contactless motion system, electromagnetic compatibility is an important issue towards industrial applications. Since the work presented in this thesis is a proof of principle, this should be further investigated. Electromagnetic compatibility becomes even more important, if high accuracy is required, since electromagnetic interference will give rise to unwanted measurement noise.

8.7.6 Ceiling Robots

In this thesis, a multi-level contactless motion system is described that is based on repulsive Lorentz forces between permanent magnets and coils without the use of iron. In this case, the mover is placed above the stator. However, if iron is incorporated in the structure, a similar system can be built based upon attractive forces. Then, the mover is suspended underneath an iron ceiling with a 6 DOF electromagnetic suspension and long stroke propulsion in the plane. This requires the incorporation of non-linear electromagnetic effects that are associated with iron in the Lagrangian system model. For a contactless motion system, contactless power transfer and wireless motion control should be included as well. The contactless power transfer will have to be adapted for operation with an iron core. A project has been started to research such a topology [78].

APPENDIX A
LAGRANGIAN DYNAMIC SYSTEM EQUATIONS EXAMPLE

For a system with a permanent magnet and two coils, the dynamic equations of the system are derived using Lagrange including the electromagnetic domain. The permanent magnet has a mass m and can move in one direction x. The positive x-direction is in the opposite direction of the gravity vector. Underneath the permanent magnet there are two coils with a current i_1 and i_2, an inductance L_1 and L_2 and mutual inductance M_{12}, resistance R_1 and R_2 and a flux linkage $\Lambda_1(x)$ and $\Lambda_2(x)$, respectively. Each coil is connected to a power amplifier that can realize a certain voltage over the terminal of each coil (u_1 and u_2).

First, some definition are made:

$$\underline{q}_{em} = \begin{bmatrix} x & c_1 & c_2 \end{bmatrix}^T, \tag{A.1}$$

$$i_1 = \dot{c}_1, \tag{A.2}$$

$$i_2 = \dot{c}_2. \tag{A.3}$$

Then, the energy functions are defined:

$$T = \frac{1}{2}m\dot{x}^2, \tag{A.4}$$

$$V = -m|\vec{g}|x, \tag{A.5}$$

$$U_{em} = \Lambda_1 \dot{c}_1 + \frac{1}{2}L_1 \dot{c}_1^2 + \Lambda_2 \dot{c}_2 + \frac{1}{2}L_2 \dot{c}_2^2 + M_{12}\dot{c}_1\dot{c}_2. \tag{A.6}$$

Finally, the vector with non-conservative forces is derived:

$$\underline{Q}^{nc} = \begin{bmatrix} 0 & u_1 - R_1\dot{c}_1 & u_2 - R_2\dot{c}_2 \end{bmatrix} \tag{A.7}$$

This is the Lagrange equation of motion including the electromagnetic energy:

$$\frac{d}{dt}\left(\frac{\partial T}{\partial \dot{\underline{q}}_{em}}\right) - \frac{\partial T}{\partial \underline{q}_{em}} + \frac{\partial V}{\partial \underline{q}_{em}} + \frac{d}{dt}\left(\frac{\partial U_{em}}{\partial \dot{\underline{q}}_{em}}\right) - \frac{\partial U_{em}}{\partial \underline{q}_{em}} = \left(\underline{Q}^{nc}\right)^T. \tag{A.8}$$

The components in the Lagrange equation are now calculated:

$$\frac{d}{dt}\left(\frac{\partial T}{\partial \underline{\dot{q}}_{em}}\right) = \begin{bmatrix} m\ddot{x} \\ 0 \\ 0 \end{bmatrix}, \tag{A.9}$$

$$\frac{\partial T}{\partial \underline{q}_{em}} = \begin{bmatrix} 0 \\ 0 \\ 0 \end{bmatrix}, \tag{A.10}$$

$$\frac{\partial V}{\partial \underline{q}_{em}} = \begin{bmatrix} -m|\vec{g}| \\ 0 \\ 0 \end{bmatrix}, \tag{A.11}$$

$$\frac{d}{dt}\left(\frac{\partial U_{em}}{\partial \underline{\dot{q}}_{em}}\right) = \begin{bmatrix} 0 \\ \frac{d\Lambda_1}{dx}\dot{x} + L_1\ddot{c}_1 + M_{12}\ddot{c}_2 \\ \frac{d\Lambda_2}{dx}\dot{x} + L_2\ddot{c}_2 + M_{12}\ddot{c}_1 \end{bmatrix}, \tag{A.12}$$

$$\frac{\partial U_{em}}{\partial \underline{q}_{em}} = \begin{bmatrix} \frac{d\Lambda_1}{dx}\dot{c}_1 + \frac{d\Lambda_2}{dx}\dot{c}_2 \\ 0 \\ 0 \end{bmatrix}. \tag{A.13}$$

Finally, the results are combined to one set of equations that describe the full dynamics of the system:

$$\begin{bmatrix} 0 \\ u_1 \\ u_2 \end{bmatrix} = \begin{bmatrix} m & 0 & 0 \\ 0 & L_1 & M_{12} \\ 0 & M_{12} & L_2 \end{bmatrix} \underline{\ddot{q}}_{em} + \begin{bmatrix} -m|\vec{g}| \\ 0 \\ 0 \end{bmatrix} +$$

$$\begin{bmatrix} 0 & -\frac{d\Lambda_1}{dx} & -\frac{d\Lambda_2}{dx} \\ \frac{d\Lambda_1}{dx} & R_1 & 0 \\ \frac{d\Lambda_2}{dx} & 0 & R_2 \end{bmatrix} \underline{\dot{q}}_{em}. \tag{A.14}$$

Appendix B
List of Symbols

Symbol	Quantity	Unit
δ	Delay	s
δ_{cl}	Closed loop delay	s
δ_{sl}	Single link communication delay	s
δ_{wl}	Wireless closed loop communication delay	s
η	Efficiency	-
ϕ	Rotation around z-axis	rad
ϕ_{RM}	Manipulator arm rotation	rad
λ	Lagrangian multipliers vector	-
Λ	Flux linkage	Wb, J/A, Vs
$\underline{\Lambda}$	Flux linkage vector	Wb, J/A, Vs
Λ_c	Flux linkage due to coil current	Wb, J/A, Vs
Λ_m	Flux linkage due to magnet	Wb, J/A, Vs
μ_0	Permeability of vacuum	H/m, J/(mA^2)
μ_r	Relative permeability	-
ρ	Resistivity	Ωm
ρ_c	Volume charge density	A/m^2
σ_c	Surface charge density	A/m
θ	Rotation around x-axis	rad
$\underline{\Sigma}$	Singular value matrix	-
τ	Pole pitch	m
ψ	Rotation around y-axis	rad
Ψ	Magnetic scalar potential	A
ω	Radial frequency	rad/s
$\vec{\omega}$	Angular velocity vector	rad/s
A	Area	m^2
$\underline{A}_m$	Magnetic vector potential due to magnet	J/(Am), Wb/m
$\underline{A}$	Rotation matrix	-
$\underline{B}$	Magnetic flux density vector	T,Wb/m^2
B_r	Remanent magnetization	T,Wb/m^2
c	Condition number	-
$\underline{c}$	Charge vector	C
C	Capacitance	F
c_{bh}	Coil bundle height	m
c_{bw}	Coil bundle width	m
c_w	Coil width	m
d	Halbach magnet width	m
d_{alox}	Height of aluminum oxide disc	m
$\underline{dl}$	Wire filament vector	m
d_{pin}	Width of aluminum oxide pin	m
d_r	Datarate	bps

$\vec{\underline{e}}$	Coordinate frame	-
E_{EMF}	Back-EMF	V
$\underline{E}_{EMF}$	Back EMF vector	V
f_0	Resonant frequency	Hz
f_{bw}	Controller bandwidth	Hz
f_c	Filling factor	-
f_s	Sample frequency	Hz
F	Force	N
$\underline{F}$	Force vector	N
$\underline{F}_c$	Force vector acting on coil	N
$\underline{F}_d$	Desired force vector	N
$\underline{F}_m$	Force vector acting on magnet	N
g	Airgap	m
$\vec{g}$	Gravitational vector	m/s^2
h	Convection coefficient	W/(m^{2}K)
$\underline{h}$	Constraint equations vector	-
$\underline{H}$	Magnetic field strength vector	A/m
i	Current	A
$\underline{i}$	Current vector	A
I	RMS current	A
i_{at}	Current Ampère-turns	A turns
$\underline{i}_{at}$	Current Ampère-turns vector	A turns
i_c	Coil current	A
$\underline{J}$	Moment of inertia matrix	kgm^2
$\underline{J}_c$	Current density vector	A/m^2
k	Thermal conductivity	W/(mK)
k	Inductive coupling	-
$\underline{k}$	Inductive coupling vector	-
k	Stiffness	N/m
$\underline{K}$	Coupling matrix	N/A or Nm/A
$\underline{K}_F$	Force coupling vector	N/A
$\underline{K}_T$	Torque coupling vector	Nm/A
L	Inductance	H, J/A^2
$\underline{L}$	Inductance matrix	H
l_c	Average coil turn length	m
L_s	Inductance of single winding coil	H
m	Mass	kg
M	Mutual inductance	H
$\underline{M}$	Magnetization vector	A/m
$\underline{M}$	Mass matrix	kg or kgm^2
m_h	Magnet height	m
n	Number	-
n_p	Packet size	bits
$\underline{n}$	Normal vector	-
N	Number of turns	-
P	Power	W
p	Heat generation	W/m^3

P_{ext}	Power output power amplifier	W
Q	Heat flow	W
$\underline{Q}_{nc}$	Non-conservative generalized forces vector	-
q	Heat flow density	W/m^2
$\underline{q}$	Generalized coordinates vector	-
R	Coil resistance	Ω
R	Thermal resistance	K/W
$\underline{R}$	Resistance matrix	Ω
$\vec{r}$	Position vector	m
$\underline{r}$	Position coordinate vector	m
r_1, r_2	Coil radius	m
r_c	Coil ratio	-
r_m	Magnet ratio	-
R_s	Resistance of single winding coil	Ω
t	Time	s
T	Kinetic energy	J
T	Temperature	K or °C
$\underline{T}$	Torque vector	Nm
$\underline{T}_c$	Torque vector acting on coil	Nm
$\underline{T}_d$	Desired torque vector	Nm
$\underline{T}_m$	Torque vector acting on magnet	Nm
u	Voltage	V
u_{ext}	Power amplifier voltage	V
$\underline{u}_{ext}$	Power amplifier voltage vector	V
U	Energy	J
V	Potential Energy	J
V	RMS voltage	V
V_c	Coil volume	m^3
$\underline{v}$	Velocity vector	m/s or rad/s
$\underline{\bar{w}}, \underline{\tilde{w}}$	Constraint vector	-
$\underline{W}$	Constraint matrix	-
x	Cartesian coordinate	m
y	Cartesian coordinate	m
y_{LM}	Manipulator beam displacement	m
z	Cartesian coordinate	m
Z	Impedance	Ω

Bibliography

The references are grouped per topic: contactless planar actuator [1]-[30], contactless power transfer [31]-[50], Lagrangian dynamics [51]-[54], wireless motion control [55]-[75], related research [76]-[82] and publications with work from this thesis [83]-[97].

[1] A.J. Hazelton, M.B. Binnard, J.M. Gery: *Electric Motors and Positioning Devices Having Moving Magnet Arrays and Six Degrees of Freedom*, US Patent 6,208,045, March 2001. Cited at page: 4, 171

[2] M.B. Binnard: *Six Degree of Freedom Control of Planar Motors*, US Patent Application US 003/0085676 A1, May 2003. Cited at page: 4

[3] T.C. Teng: *Methods and Apparatus for Initializing Planar Motor*, US Patent US 6,777,896 B2, August 2004. Cited at page: 4

[4] T. Ueta, B. Yuan, T.C. Teng: *Moving Magnet Type Planar Motor Control*, US Patent Application US 2003/0102722 A1, June 2003. Cited at page: 4

[5] Frissen et al.: *Displacement Device*, US Patent Application, US 2004/0017116 A1, January 2004. Cited at page: 4, 69

[6] J.C. Compter: Electro-Dynamic Planar Motor, *Precision Engineering*, Vol. 28, Issue 2, pp. 171-180, April 2004. Cited at page: 4, 69

[7] J.C. Compter, P.C.M. Frissen: *Displacement Device*, International Patent WO 2006/075291 A2, July 2006. Cited at page: 4

[8] W. Potze, P.C.M. Frissen: *Method for Controlling an Electic Motor, Control Unit and Electric Motor*, International Patent WO 2006/054243 A2, May 2006. Cited at page: 4, 21, 22

[9] J.W. Jansen, C.M.M. van Lierop, E.A. Lomonova, A.J.A. Vandenput: Modeling of Magnetically Levitated Planar Actuators with Moving Magnets, *IEEE Transactions on Magnetics*, Vol. 43, No. 1, pp. 12-25, May 2007. Cited at page: 4, 11, 13, 22, 69, 70, 75

[10] J.W.Jansen: *Magnetically Levitated Planar Actuator with Moving Magnets, Electromechanical Analysis and Design*, Eindhoven University of Technology, PhD Thesis, 2007. Cited at page: 4, 8, 11, 13, 17, 18, 21, 22, 69, 70, 75, 121, 126, 155, 158

[11] C.M.M. van Lierop, J.W. Jansen, A.A.H. Damen, P.P.J. van den Bosch: Control of Multi-Degree-of-Freedom Planar Actuators, *Proceedings of the IEEE International Conference on Control Applications*, Munich, Germany, pp. 2516-2521, October 2006. Cited at page: 4, 18, 21, 22, 69

[12] C.M.M. van Lierop: *Magnetically Levitated Planar Actuator with Moving Magnets, Dynamics, Commutation and Control Design*, Eindhoven University of Technology, PhD Thesis, 2007. Cited at page: 4, 8, 18, 21, 22, 69, 155, 158

[13] B.A. Sawyer: *Magnetic positioning device*, U.S. Patent 3,376,578, April 1968. Cited at page: 4

[14] K. Kahlen, I. Voss, R.W. De Doncker: Control of multi-dimensional drives with variable pole pitch, *Proceedings of the IEEE Industry Applications Society 37th Annual Meeting*, Vol. 4, pp. 2366-2370, 2002. Cited at page: 4

[15] T. Asakawa: *Two-dimensional precise positioning device for use in a semi-conductor manufacturing apparatus*, U.S. Patent 4,535,278, August 1985. Cited at page: 4

[16] W.E. Hinds: *Single plane orthogonally moveable drive system*, U.S. Patent 4,654,571, March 1987. Cited at page: 4

[17] N. Fujii, M. Fujitake: Two-dimensional drive characteristics by circular shaped motor, *IEEE Transactions on Industrial Applications*, Vol. 35, No. 4, pp. 803809, July 1999. Cited at page: 4

[18] B.V. Jayawant: Electromagnetic suspension and levitation techniques, *Proceedings of the Royal Society of London*, Vol. A, No. 416, pp. 245320, April 1988. Cited at page: 4

[19] J.L. Coulomb: A Methology for the Determination of Global Electromechanical Quantities from a Finite Element Analysis and its Application to the Evaluation of Magnetic Forces, Torques and Stiffness, *IEEE Transactions on Magnetics*, Vol. MAG-19, No. 6, November 1983. Cited at page: 12

[20] J.L. Coulomb, G. Meunier: Finite Element Implementation of Virtual Work Principle for Magnetic or Electric Force and Torque Computation, *IEEE Transactions on Magnetics*, Vol. MAG-20, No. 5, September 1984. Cited at page: 12

[21] J. Penman, M.D. Grieve: Efficient Calculation of Force in Electromagnetic Devices, *IEE Proceedings*, Vol. 133, Pt. B, No. 4, July 1986. Cited at page: 12

[22] D.L. Trumper, W. Kim, M.E. Williams: Design and Analysis Framework for Linear Permanent-Magnet Machines, *IEEE Transactions on Industry Applications*, Vol. 32, No. 2, March/April 1996. Cited at page: 11, 13, 22

[23] J. de Boeij, M. Steinbuch, H.M. Gutiérrez: Mathematical Model of the 5-DOF Sled Dynamics of an Electrodynamic Maglev System with a Passive Sled, *IEEE Transactions on Magnetics*, Vol. 41, No. 1, pp. 460-465, January 2005. Cited at page: 22

[24] J. de Boeij, M. Steinbuch, H.M. Gutiérrez: Real-Time Control of the 3-DOF Sled Dynamics of a Null-Flux Maglev System With a Passive Sled, *IEEE Transactions on Magnetics*, Vol. 42, No. 5, pp. 1604-1610, May 2006. Cited at page: 21, 22

[25] G. Akoun and J.P. Yonnet: 3D Analytical Calculation of the Forces Exerted between Two Cuboidal Magnets, *IEEE Transactions on Magnetics*, Vol. 20, No. 5, pp.1962-1964, May 1984. Cited at page: 15, 16

[26] E.P. Furlani: *Permanent Magnet and Electromechanical Devices*, San Diego CA, USA, Academic Press, 2001. Cited at page: 12, 15, 16, 55, 90, 94, 124

[27] B.N. Datta: *Numerical Linear Algebra and Applications*, Pacific Grove CA, USA, Brooks/Cole Publishing Company, 1995. Cited at page: 18, 20

[28] Bakker Magnetics: *BM Permanent Magnetic Materials Brochure*, Son, The Netherlands, 2005. Cited at page: 13

[29] Vacuumschmelze: *Vacodym, Vacomax, Selten-Erd-Dauermagnete*, Hanau, Germany, 2006. Cited at page: 13, 126

[30] Ansoft: *Maxwell 10 User's Guide*, Pittsburgh PA, USA, 2003. Cited at page: 50, 74, 78, 171

[31] C. Wang, G.A. Covic, O.H. Stielau: Power Transfer Capability and Bifurcation Phenomena of Loosely Coupled Inductive Power Transfer Systems, *IEEE Transactions on Industrial Electronics*, Vol. 51, No. 1, pp. 148-157, February 2004. Cited at page: 44, 171

[32] N. Tesla: *Apparatus for transmitting electrical energy* U.S. patent number 1,119,732, December 1914. Cited at page: 5

[33] A. Esser, H.C. Skudelny: A new approach to power supplies for robots, *IEEE Transactions on Industry Applications*, Vol. 27, No. 5, pp. 872-875, September 1991. Cited at page: 5

[34] A. Esser, A. Nagel: Contactless high speed signal transmission integrated in a compactrotatable power transformer, *Proceedings of the 5th European Conference on Power Electronics and Applications*, Vol. 4, pp. 409-414, September 1992. Cited at page: 5, 7

[35] C. Fernandez, O. Garcia, R. Prieto, J.A. Cobos, S. Gabriels, G. Van der Borght: Design Issues of a Core-less Transformer of a Contact-less Application, *Proceedings of the 17th Annual IEEE Applied Power Electronics Conference and Exposition*, Vol.1, pp. 339-345, 2002. Cited at page: 5, 49

[36] R. Mecke, C. Rathge: High Frequency Resonant Inverter for Contactless Energy Transmission over Large Airgap, *Proceedings of the 25th Annual IEEE Power Electronics Specialist Conference*, pp. 1737-1743, 2004. Cited at page: 5, 49

[37] T. Bieler, M. Perrottet, V. Nguyen, Y. Perriard: Contactless Power and Information Transmission, *IEEE Transactions on Industry Applications*, Vol. 38, No. 5, pp. 1266-1272, September/October 2002. Cited at page: 5, 49

[38] H.M.W. Goossens, G.L.M. Jansen, P.H.J. Van den Bosch, A. Molenaar: *Uni-directional Power and Bi-directional Data Transfer over a Single Inductive Coupling*, International Patent Application, WO 2005/015766A1, February 2005. Cited at page: 5, 7, 105

[39] E. Abel, S.M. Third: Contactless Power Transfer - An Exercise in Topology, *IEEE Transactions on Magnetics*, Vol. MAG-20, No. 5, September 1984. Cited at page: 5

[40] G.L.M. Jansen: *2-Dimensional Displacement Device*, International Patent Application, WO 2005/013464 A1, February 2005. Cited at page: 5

[41] S. Adachi, F. Sato, S. Kikuchi: Considerations of Contactless Power Station with Selective Exitation to Moving Robot, *IEEE Transactions on Magnetics*, Vol. 35, No. 5, pp. 3583-3585, September 1999. Cited at page: 5

[42] F. Sato, J. Murakami, H. Matsuki, S. Kikuchi, K. Harakawa, T. Satoh: Stable Energy Transmission to Moving Loads Utilizing New CLPS, *IEEE Transactions on Magnetics*, Vol. 32, No. 5, pp. 5034-5036, September 1996. Cited at page: 5

[43] F. Sato, H. Matsuki, S. Kikuchi, T. Seto, T. Satoh, H. Osada, K. Seki: A New Meander Type Contactless Power Transmission System - Active Excitation with a Characteristics of Coil Shape, *IEEE Transaction on Magnetics*, Vol. 34, No. 4, pp. 2069-2071, July 1998. Cited at page: 5

[44] G.A. Covic, G. Elliott, O.H. Stielau, R.M. Green, J.T. Boys: The Design of a Contact-less Energy Transfer System for a People Mover System, *Proceedings of the IEEE International Conference on Power System Technology*, Vol. 1, pp. 79-84, December 2000. Cited at page: 5

[45] H. Ayano, K. Yamamoto, N. Hino, I. Yamato: Highly-Efficient Contact-less Electrical Energy Transmission System, *Proceedings of the 28th Annual Conference of the IEEE Industrial Electronics Society*, Vol 2, pp. 1364-1369, November 2002. Cited at page: 5

[46] K. Hatanaka, F. Sato, H. Matsuki, S. Kikuchi, J. Murakami, M. Kawase, T. Satoh: Power Transmission of a Desk with a Cord-Free Power Supply, *IEEE Transactions on Magnetics*, Vol. 38, No. 5, pp. 3329-3331, September 2002. Cited at page: 5

[47] S.Y.R. Hui, W.C. Ho: A New Generation of Universal Contactless Battery Charging Platform for Portable Consumer Electronic Equipment, *Proceedings of the 35th Annual IEEE Power Electronics Specialists Conference*, pp. 638-644, 2004. Cited at page: 5

[48] C.R. Sullivan: *Computationally Efficient Winding Loss Calculation with Multiple Windings, Arbitrary Waveforms and Two-Dimensional or Three-Dimensional Field Geometry*, *IEEE Transactions on Power Electronics*, Vol. 16, No. 1, pp. 142-150, January 2001. Cited at page: 49, 57

[49] J.O. Bird: *Electrical Circuit Theory and Technology*, Oxford, UK, Newnes, Reed Elsevier plc, 2000. Cited at page: 44

[50] F.W. Grover: *Inductance Calculations*, New York, USA, Dover, 1964. Cited at page: 89, 171

[51] B. de Kraker, D.H. van Campen: *Mechanical Vibrations*, Maastricht, The Netherlands, Shaker Publishing, 2001. Cited at page: 81, 85, 86, 171

[52] S. E. Lyshevski: *Electromechanical Systems, Electric Machines, and Applied Mechatronics*, Boca Raton, CRC Press, 2000. Cited at page: 85

[53] J.I. Neimark, N.A. Fufaev: *Dynamics of Nonholonomic Systems*, Providence, American Mathematical Society, 1972. Cited at page: 81, 85, 89, 90, 124

[54] G.F. Franklin, J.D. Powell, A. Emami-Naeini: *Feedback Control of Dynamic Systems*, Reading, Addison-Wesley, 1994. Cited at page: 102, 171

[55] *Bluetooth Specification*, `http://www.bluetooth.com/`. Cited at page: 6, 103, 104, 171

[56] N. Golmie: *Wireless Personal Area Networks*, IEEE P802.15-01/317r0, 2001. Cited at page: 6, 104

[57] IEEE: *IEEE Standard 802.11-1997*, `http://www.ieee.org/`, 1997. Cited at page: 6, 103, 104

[58] A. Heron, N. MacDonald: Video Transmission over a Radio Link using H.261 and DECT, *Proceedings of the International Conference on Image Processing and its Applications*, pp. 621-624, April 1992. Cited at page: 6, 103, 104

[59] N.J. Ploplys, P.A. Kawka, A.A. Alleyne: Closed-Loop Control over Wireless Networks, *IEEE Control Systems Magazine*, Vol. 24, No. 3, pp. 58-71, 2004. Cited at page: 6, 101, 104, 111, 117

[60] W.C. Craig: Zigbee: *Wireless Control That Simply Works*, Zigbee Alliance ZigBee Alliance `http://www.51zigbee.com/uploadfile/jh2.pdf`, 2004. Cited at page: 104

[61] The Zigbee Alliance: *The ZigBee Specification*, `http://www.zigbee.org/`. Cited at page: 6, 103, 104

[62] Microlinear: ML2724SK-02 High Power 2.4GHz Radio Starter kit Design. Cited at page: 106

[63] Xilinx: *Spartan IIE*, `http://www.xilinx.com/support/documentation/data_sheets/ds077.pdf`. Cited at page: 106

[64] S. Behnke, A. Egorova, A. Gloye, R. Rojas, M. Simon: Predicting Away Robot Control Latency, *Lecture Notes in Computer Science*, Vol. 3020/2004, pp. 712-719, August 2004. Cited at page: 6, 101

[65] J. Eker, A. Cervin, A. Horjel: Distributed Wireless Control Using Bluetooth, *Proceedings of the IFAC Conference on New Technologies for Computer Control*, Hong Kong, China, November 2001. Cited at page: 6, 101, 104, 117

[66] J. Hirai, T.W. Kim, A. Kawamura: Wireless Transmission of Power and Information for Cableless Linear Motor Drive, *IEEE Transactions on Power Electronics*, Vol. 15, No. 1, pp. 21-26, January 2000. Cited at page: 7, 105

[67] C. Hochel-Winter: *Industrial Wireless LANs with Siemens SCALANCE W*, Product Analysis, ComConsult Research, 2004. Cited at page: 6

[68] C.H. Roth: *Fundamentals of Logic Design*, Fourth Edition, Boston, PWS Publishing Co., 1992. Cited at page: 107

[69] W.J. Kim, K. Ji, A. Ambike: Networked Real-Time Control Strategies Dealing with Stochastic Time Delays and Packet Losses, *Proceedings of the American Control Conference*, pp. 621-626, Portland OR, USA, June 2005. Cited at page: 6, 101

[70] M. Kintner-Meyer, R. Conant: Opportunities of Wireless Sensors and Controls for Building Operation, *Energy Engineering*, Vol 102, No. 5, pp. 27-48, 2005. Cited at page: 6

[71] J. Nillson: *Real-Time Control Systems with Delays, Department of Automatic Control*, Lund Institute of Technology, PhD Thesis, 1998. Cited at page: 6, 101

[72] J. Nilsson, B. Bernhardsson, B. Wittenmark: Stochastic Analysis and Control of Real-Time Systems with Random Time Delays, *Automatica*, Vol. 34, No. 1, pp. 57-64, 1998. Cited at page: 6, 101

[73] M. Tabbara, D. Nesic, A.R. Teel: Input-Output Stability of Wireless Networked Control Systems, *Proceedings of the 44th IEEE Conference on Decision and Control*, pp. 209-214, Seville, Spain, December 2005. Cited at page: 6, 101

[74] Y. Uchimura: Wireless Network Based Identification and Control with Variable Time Delay, *Proceedings of the IEEE International Workshop on Advanced Motion Control*, pp. 336-341, March 2008. Cited at page: 6, 101

[75] W. Zhang, M.S. Branicky, S.M. Philips: Stability of Networked Control Systems, *IEEE Control Systems Magazine*, pp. 84-99, Februari 2001. Cited at page: 6, 101, 171

[76] J.J.H. Paulides, L. Encica, J.W. Jansen, R.A.J. van der Burg, J.L. Horijon, E.A. Lomonova: Robot Architecture for a Contactless Industrial Pick-and-Place Machine, *Proceedings of the 11th International Conference on Electrical Machines and System*, CDROM, Wuhan, China, October 2008. Cited at page: 162, 171

[77] D.C.J. Krop, E.A. Lomonova: A study on the integration of contactless energy transfer in the end teeth of a PM synchronous linear motor, *Abstracts of 53rd Annual Conference on Magnetism and Magnetic Materials*, Austin, TX, USA, November 2008, and *Applied Physics*, under review, 2008. Cited at page: 162

[78] E.A. Lomonova: *Autonomous Ceiling Robots*, SenterNovem, IOP-TTI, EMVT08207, 2008. Cited at page: 163

[79] M.G.E. Schneiders, M.J.G. van de Molengraft, M. Steinbuch: Modal Framework for Closed-Loop Analysis of Over-Actuated Motion Systems *Proceedings of the 2004 ASME International Mechanical Engineering Congres*, pp. 1-6, Anaheim, California, USA, November 2004. Cited at page: 94, 163

[80] P.P.J. van den Bosch, E.A. Lomonova: *Advanced Single-Stage Planar Actuator*, SenterNovem, Pieken in de Delta, PID07055, 2008. Cited at page: 163

[81] M. Gajdusek, A.A.H. Damen, P.P.J. van den Bosch: Infrared wireless data transfer for real-time motion control *Proceedings of the IFAC Workshop on Programmable Devices*, accepted, 2009. Cited at page: 158

[82] M. Gajdusek, J. de Boeij, A. Damen, P. van den Bosch: Contactless Planar Actuator with Manipulator - Experimental Setup for Control, *Proceedings of the 6th International Symposium on Linear Drives for Industry Applications* (LDIA2007), CDROM, Lille, France, September 2007. Cited at page: 98, 139, 171

[83] J. de Boeij, E. Lomonova, J.L. Duarte, A.J.A. Vandenput: Contactless Power Supply for moving sensors and actuators in high-precision mechatronic systems with long-stroke power transfer capability in the x-y plane, *Sensors and Actuators A: Physical*, Vol. 148, Issue 1, pp. 319-328, 2008. Cited at page: 43, 171

[84] J. de Boeij, E. Lomonova, A.J.A. Vandenput: Optimization of Contactless Planar Actuator with Manipulator, *IEEE Transactions on Magnetics*, Vol 44, No. 6, pp. 1118-1121, June 2008. Cited at page: 69

[85] J. de Boeij, E. Lomonova, A.J.A. Vandenput: Modeling of Ironless Permanent Magnet Planar Motor Structures, *IEEE Transactions on Magnetics*, Vol. 42, No. 8, pp. 2009-2016, August 2006. Cited at page: 11

[86] J. de Boeij, E. Lomonova, J.L. Duarte: Contactless Planar Actuator with Manipulator: a Motion System without Cables and Physical Contact between the Mover and the Fixed World, *Proceedings of the IEEE Industry Applications Society 43st Annual Meeting*, CDROM, Edmonton AB, Canada, October 2008. Cited at page: 119

[87] J. de Boeij, E. Lomonova: Experimental Verification of Look-Up Table Based Real-Time Commutation of 6-DOF Planar Actuators, *Proceedings of the 11th International Symposium on Magnetic Bearings* (ISMB11), pp. 496-501, Nara, Japan, August 2008. Cited at page: 119

[88] J. de Boeij, E. Lomonova, A.J.A. Vandenput: Look-Up Table Based Real-Time Commutation of 6-DOF Planar Actuators, *Proceedings of the 16th Interrernational Conference on Control Applications* (CCA2007), pp. 1118-1123, Singapore, October 2007. Cited at page: 11

[89] J.W. Jansen, C.C.M. van Lierop, J. de Boeij, E.A. Lomonova, J.L. Duarte, A.J.A. Vandenput: Moving Magnet Multi-DOF Planar Actuator Technology with Contactless Energy and Data Transfer, *Proceedings of the 6th International Symposium on Linear Drives for Industry Applications* (LDIA2007), CDROM, Lille, France, September 2007. Cited at page: 101

[90] B. Zuurendonk, J. de Boeij, M. Steinbuch, E. Lomonova: Modeling of Disturbance Forces of a x-y Manipulator on a Floating Platform, *Proceedings of the 6th International Symposium on Linear Drives for Industry Applications* (LDIA2007), CDROM, Lille, France, September 2007. Cited at page: 81

[91] J. de Boeij, E. Lomonova, J.L. Duarte, A.J.A Vandenput: Contactless Planar Actuator with Manipulator, *Proceedings of the 12th European Conference on Power Electronics and Applications* (EPE2007), pp. 1-9, Aalborg, Denmark, September 2007. Cited at page: 101

[92] J. de Boeij, E. Lomonova, A.J.A. Vandenput: Optimization of Contactless Planar Actuator with Force and Torque Disturbances, *Proceedings of the 16th Conference on the Computation of Electromagnetic Fields* (COMPUMAG 2007), pp. 935-936, Aachen, Germany, June 2007. Cited at page: 69

[93] J. de Boeij, E. Lomonova, A.J.A. Vandenput: Contactless Energy Transfer to a Moving Actuator, *Proceedings of the IEEE Industry Applications Society 41st Annual Meeting*, Vol. 4, pp. 2020-2025, Tampa FL, USA, October 2006. Cited at page: 43

[94] J. de Boeij, E. Lomonova, A.J.A. Vandenput: Contactless Energy Transfer to a Moving Load Part I: Topology Synthesis and FEM simulation, *Proceedings of the International Symposium on Industrial Electronics*, Vol. 2, pp. 739-744, Montreal, Canada, July 2006. Cited at page: 43

[95] J. de Boeij, E. Lomonova, J.L. Duarte, A.J.A. Vandenput: Contactless Energy Transfer to a Moving Load Part II: Simulation of Electrical and Mechanical Transient, *Proceedings of the International Symposium on Industrial Electronics*, Vol. 2, pp. 745-750, Montreal, Canada, July 2006. Cited at page: 43

[96] J. de Boeij, M.H. Haazen, P. Smulders, E. Lomonova: Low-Latency Wireless Data Transfer for Motion Control, *IEEE Transactions on Control Systems Technology*, under review, 2008. Cited at page: 101

[97] B. Zuurendonk, J. de Boeij, M. Steinbuch, E. Lomonova: Modeling of disturbance forces of a x-y manipulator on a floating platform, *Electromotion*, Vol. 15, No. 2, pp. 81-87, 2008. Cited at page: 81, 171

Samenvatting

In het ontwerp van machines worden de acceleratie en snelheid van bewegende delen vaak beperkt door mechanische lagering voor geleiding and kabels for het overbrengen van vermogen en informatie. Deze factoren begrenzen niet alleen het werkgebied en de functionaliteit van de machine maar verstoren daarbij ook de beweging van het bewegende deel, waarmee de betrouwbaarheid, snelheid en nauwkeurigheid gereduceerd worden. Dit proefschrift concentreert zich op het verwijderen van deze beperkingen en het effect hiervan op het systeemontwerp van de machine. Drie verschillende contactloze technieken kunnen in één bewegingssysteem worden samengevoegd om de barrières die worden opgeworpen door lagers en kabels te doorbreken:

- Zes vrijheidsgraden elektromagnetische lagering en aandrijving,

- Contactloze vermogensoverdracht,

- Draadloze besturingstechniek.

Elke contactloze techniek werkt in een apart frequentiegebied van het elektromagnetische spectrum, vandaar de titel "Multi-Level Contactless Motion System" ("Op verscheidene niveaus contactloos bewegingssysteem"). De elektromagnetische lagering en aandrijving maken gebruik van permanente magneten en spoelen, die een stroomlus hebben met een bandbreedte van enkele kHz. De vermogensoverdracht is gebaseerd op een inductieve koppeling en wisselstromen in een frequentiegebied van 50-200 kHz. Tenslotte wordt de data verstuurd met een radio die werkt op 2.4 GHz. Het is mogelijk om met nog hogere frequenties te werken, vooral wanneer optische systemen gebruikt worden voor de data transmissie.

Dit proefschrift presenteert theorie en technologie die noodzakelijk is om een op meerdere niveaus contactloos bewegingssysteem, alsmede de drie subsystemen en hun interactie in het globale systeem te beschrijven en te realiseren. Het gaat dan om het integreren van een contactloze planaire actuator met bewegende magneten, zes graden van vrijheid en een lange slag in het x-y vlak, contactloze vermogensoverdracht naar het bewegende platform en draadloze onvertraagde draadloze communicatie tussen de regelaars op de vaste wereld en de processen op het platform. Op het platform bevindt zich een manipulator met twee lineaire motoren die een brug aandrijven en een roterende motor waaraan een arm is bevestigd, waarbij iedere motor is uitgerust met een incrementele encoder.

The elektromagnetische interactie tussen de spoelen en de magneten is gemodelleerd om de koppeling van iedere spoel te voorspellen, waarmee met koppeling de hoeveelheid kracht en koppel per eenheid stroom bedoeld wordt. Als deze koppeling van alle spoelen bekend is, kunnen de stromen uitgerekend worden die nodig zijn om de gewenste krachten en koppels op de planaire actuator uit te oefenen met behulp van de pseudo-inverse van de koppelingsmatrix. Een commutatie algoritme gebaseerd dit op model en gebruikmakend van interpolatie matrices wordt gepresenteerd dat deze berekeningen in een zeer korte tijd kan uitvoeren. Met deze methode is het mogelijk om de koppeling van de spoelen aan de rand van de magneetplaat mee te nemen, ook al gedragen deze zich anders vanwege de eind-effecten

van het magnetisch veld. Daarnaast is volledige rotatie om de z-as mogelijk wanneer ronde spoelen worden gebruikt. Een thermisch model wordt gepresenteerd dat de hoogst mogelijke spoeltemperatuur kan schatten voor een gegeven stroom.

De contactloze vermogens overdracht is onderzocht met de nadruk op het effect van een grote mechanische beweging op het elektrische systeem. De vermogensoverdracht is gebaseerd op een inductieve koppeling tussen een primaire en een secondaire spoel. The primaire spoel kan kracht en koppel leveren op de planaire actuator als het in de buurt van de magneetplaat is of het is een primaire spoel van een luchtkern transformator als het in de buurt is van de secondaire spoel. Vanwege de hoge frequentie van de contactloze vermogensoverdracht moeten de primaire spoelen van litze draad worden gemaakt, wat de weerstand op hoge frequenties laag houdt maar de weerstand in het geval van gelijkstroom verhoogt. Dit heeft weer tot gevolg dat de thermische dissipatie in de planaire actuator groter wordt. Door de variatie van de inductieve koppeling tussen de primaire spoel en de secondaire spoel klein te houden in een groot gebied en tegelijkertijd de gemiddelde waarde hoog genoeg te houden om een significante vermogensoverdracht te realiseren, is het mogelijk om efficient en continu in het gehele werkgebied van de planaire actuator vermogen over te dragen.

Met de modellen die de contactloze planaire actuator en de contactloze vermogensoverdracht beschrijven is het mogelijk om een geschikte topologie te vinden van een contactloze planaire actuator met contactloze vermogensoverdracht binnen de geometrische en thermische beperkingen. De uiteindelijke topologie is niet alleen gekozen op basis van deze geometrische en thermische beperkingen maar ook door de elektrische eigenschappen van de vermogensoverdracht, regelbaarheid en mechanische afwegingen zoals stijfheid en leviterende massa inclusief de manipulator in beschouwing te nemen. Aangezien dit de eerste keer is dat litze draad wordt gebruikt voor een elektromechanisch aandrijfsysteem, is een conservatieve schatting van de eigenschappen gebruikt in de analyze.

De dynamische vergelijkingen van het systeem zijn afgeleid met behulp van Lagrange, zowel voor het mechanische als voor het elektromagnetische domein. Deze set vergelijkingen verschaft een complete beschrijving van het elektromechanische systeem en het is gebruikt ter verificatie van andere modellen. Het wordt aanbevolen om deze methode te gebruiken voor de analyse en het ontwerp van vergelijkbare systemen in combinatie met het commutatie algoritme, aangezien het een transiënte analyse verschaft dat bewegingstrajecten, regelwetten, spoelstromen en versterkerspanningen kan samenvoegen. De systeemdynamica kan worden uitgebreid met flexibele modes of niet-lineaire elektromagnetische effecten.

Bestaande draadloze communicatie systemen ondervinden een tijdsvertraging van enkele milliseconden en dat is onacceptabel voor de besturing van hoogwaardige bewegingssystemen. De oorzaak van deze significante tijdsvertraging is het protocol dat meestal is geoptimaliseerd voor een hoge data doorvoersnelheid, niet voor een kleine tijdsvertraging. Een nieuw protocol wordt voorgesteld en is geïmplementeerd op een FPGA met een 2.4 GHz radio dat the tijdsvertraging in de communicatie significant terugbrengt met een factor 10 vergeleken met de snelste bestaande draadloze radio communicatie protocollen.

Een prototype van een op meerdere niveaus contactloos bewegingssysteem is gebouwd en succesvol getest. De haalbaarheid van dit concept is aangetoond.

Acknowledgements

Curriculum Vitae

Jeroen de Boeij was born on July 14th 1980 in Vlijmen, the Netherlands. After finishing his secondary education at the Stedelijk Gymnasium 's-Hertogenbosch, he started his study Mechanical Engineering at the Eindhoven University of Technology (TU/e) in September 1998. He received his B.Sc degree in February 2002 and his MSc degree in November 2004, both with great appreciation.

From January 2003 till August 2004 he carried out his traineeship and his MSc thesis research at the Florida Institute of Technology, were he was appointed as a research assistant. He worked on stabilizing the dynamics of an EDS Maglev testtrack for launching, a project sponsored by NASA and the US Navy, which was awarded with the Peter Kemmey Memorial Student Scholarship at the 12th Electro Magnetic Launch Symposium in May 2004. His MSc thesis was titled "Real-time Control of an Electrodynamic Maglev System", which was awarded with the second Mignot graduation prize in April 2005.

In February 2005 he started as a PhD student in the group of Electromechanics and Power Electronics at the Electrical Engineering Faculty at the TU/e. He worked on the topic of "Multi-Level Contactless Motion System" of which this thesis is the result.